UNIVERSITY OF THESSALY
SCHOOL OF ENGINEERING

DEPARTMENT OF MECHANICAL ENGINEERING
LABORATORY OF FLUID MECHANICS & TURBOMACHINERY

DOCTORAL THESIS

FIRST PRINCIPLES STUDY OF THE STATIC ARRANGEMENT OF A PLASMA FACING COMPONENT IN THE FORM OF A CAPILLARY POROUS SYSTEM (CPS)

by
Lefteris Th. Benos

Physics Degree, Aristotle University, Thessaloniki, Greece
MSc in State-of-the-art Design and Analysis Methods in Industry, Department of Mechanical Engineering, University of Thessaly, Volos, Greece

Thesis
Submitted in partial fulfillment of the requirements
for the degree of Doctor of Philosophy in Mechanical Engineering

Volos, January 2018

ii

The approval of the current Thesis by the Department of Mechanical of the Engineering School of the University of Thessaly does not imply acceptance of the author's beliefs (Law 5343/32 – art. 202, paragraph 2). Also the views and opinions expressed herein do not necessarily reflect those of the European Commission.

Approved by the members of the Examination Committee:

1st member (supervisor)	Dr. Nikos Pelekasis, Professor Dept. of Mechanical Engineering University of Thessaly
2nd member	Dr. Dimitris Valougeorgis, Professor Dept. of Mechanical Engineering University of Thessaly
3rd member	Dr. Vasilis Bontozoglou, Professor Dept. of Mechanical Engineering University of Thessaly
4th member	Dr. Nikolaos Andritsos, Professor Dept. of Mechanical Engineering University of Thessaly
5th member	Dr. Stergios Yiantsios, Professor Dept. of Chemical Engineering Aristotle University of Thessaloniki
6th member	Dr. Kyriakos Hizanidis, Professor Dept. of Electrical and Computer Engineering National Technical University of Athens
7th member	Dr. Giuseppe Mazzitelli, Management of Large Experiment Facilities (FTU) in ENEA

v

vi

To the memory of my beloved father.
You taught me so much about life and values and always supported the decisions I
made. You are part of the reason I am where I am today.

Acknowledgements

Nuclear fusion has been called "the Holy Grail of the energy field". Thus, the choice of an attractive energy source because of its virtually inexhaustible supply of fuel, the promise of minimal adverse environmental impact and its inherent safety motivated me to undertake this study. Therefore, I wholeheartedly enjoyed the challenge of examining and researching a controversial issue that will greatly impact the whole world in the next decades.

For the completion of this Thesis, I would like to thank the members of my advisory committee. First and foremost, I am most grateful to my supervisor professor Nikos Pelekasis for trusting me such a crucial topic and for learning by his side too many computational techniques which are going to be useful in my future scientific career. Thanks also extended to the professors of the University of Thessaly Dr. Dimitris Valougeorgis, Dr. Vasilis Bontozoglou and Dr. Nikolaos Andritsos for their crucial contribution in understanding the true meaning of Transport Phenomena. Besides, along with Dr. Nikos Pelekasis, Dr. Nikolaos Vlachos and Dr. Ioannis Sarris they introduced me to the Physics of Fluids and Computational Fluid Mechanics via the Master courses. Finally, I would like to thank professor Stergios Yiantsios, professor Kyriakos Hizanidis and Dr. Giuseppe Mazzitelli for the honor to be members of the advisory committee of my Thesis.

I would also like to thank Dr. Maria Vlachomitrou, Dr. Sotiris Kakaratzas, Dr. Kostas Efthimiou, Dr. Dimitris Dimopoulos and Dr. Alkmini Lytra for their opinions, criticism, useful remarks and also for the pleasant working environment.

Special thanks go to Dr. Nikolaos Polychronopoulos, Dr. Petros Christodoulou and Dr. Dimitris Tsokolis who attended together with me the Master and PhD studies in the University of Thessaly, for their friendship, support and encouragement throughout my studies these seven years.

In addition, this work was financially supported by the European Commission within the Association EURATOM-Hellenic Republic. I would also like to acknowledge the financial support that the Department of Mechanical Engineering of the University of Thessaly gave me via a scholarship during my master studies.

Last, but never least, I would like to express my gratitude to my unbelievably supportive wife Ioanna who had the "misfortune" to meet me as a post graduate student and then as a PhD candidate. As a matter of fact, she married me and entrusted me with being the father of her daughters Zoe and Doretta. Both my wife and Zoe demonstrated rare and amazing patience throughout my lengthy working sessions over the last years. As far as Doretta is concerned, she is the lucky one since she was born this November. Ioanna, Zoe and Doretta thank you from the bottom of my heart for everything that you are and everything you will become.

x

Summary

The present PhD thesis focuses on the modelling of alternative plasma facing components in the form of liquid metals in order to circumvent problems generated by plasma-wall interaction, namely handling the excessive heat and electric current loads generated in the bulk of the reactor and directed towards the divertor. The self-cooling and self-annealing properties of flowing liquids increase their life cycle as they interact with the scrape-off-layer of the fusion reactor.

In particular, since the concept of employing a jet-drop curtain was among the first to be investigated, a first-principle magnetohydrodynamic study was conducted for the purpose of predicting the trajectory of a liquid metal jet travelling inside an electromagnetic field. Thus, the effect of Lorentz forces, gravity and pressure drop were accounted for in a unidirectional model that assumes a small jet radius in comparison with the trajectory length. The effect of external electric potential gradients on jet deflection was ascertained in conjunction with the importance of electric stresses in modulating the jet speed and radius. Moreover, the trajectory of the ensuing droplets, by virtue of the jet break-up as a capillary instability, was also modelled in the presence of Lorentz forces as a means to capture and quantify the deflection process reported in the ISTTOK experiments under the plasma influence. Droplets, due to their small size and spherical shape, experience a stronger deflection as the analytical investigation indicated. The above picture conforms, within the proper order of magnitude, to the findings of ISSTOK experiments.

The second concept that was studied seems to be the most mature path for liquid surface plasma facing components, namely the Capillary Porous System (CPS). The CPS concept is based on the use of a porous construction with a capillary-pore "pumping" system to supply the liquid metal that coats and protects the divertor material, normally tungsten, from corrosion and thermal stresses. As a first step the CPS is modelled as a thin cylindrical disk being in contact with a reservoir that provides liquid lithium. The design provides sufficient working pressure in the supply system without applying external pressure by using solely capillary pressure as the driving force. Thus, capillarity, wetting and surface forces on the porous substrate are expected to stabilize the liquid metal against electromagnetic and thermal forces as well as drop ejection, which is a key issue for the reliability of the concept itself. Until now, lithium seems to make this proposed divertor concept highly efficient. However, liquid Ga, Sn and Sn-Li have also been considered.

Nevertheless, thus far, CPS has not been the subject of extensive modelling activity partly due to the complex flow arrangement of the limiter containing the liquid metal. In the present dissertation, a first principle approach was employed concerning the understanding of the operation of the CPS as plasma facing component. Initially, lithium is in solid state at room temperature within the mesh. The wafer is in contact with the surrounding medium via the top surface that is initially covered. Upon heating, the lithium liquefies and as a result the top cover breaks by the expanding liquid and liquid metal covers the top surface forming a protective coating. Performing a simple mass balance on lithium, relating its initial solid state to its final liquid state, the film thickness was estimated to be on the order of several microns. The numerical results, derived by

fixing the mass of the contained liquid metal, the size of the wafer and the contact point while satisfying the normal force balance confirm the above results.

The static arrangement is difficult to be achieved and more difficult to be maintained at high enough heat fluxes. Hence, once the machine is "turned on", a strong external heat pulse is expected to deplete the ultra-thin film covering the top of the porous matrix via the evaporation process. Initially, first principle heat transfer considerations were conducted by taking into account heat exhaust via thermal conduction, convection and evaporation and ignoring non-coronal radiation shielding. It was seen that an oncoming heat flux of 10 MW/m^2 would evaporate the liquid lithium film from the top of the CPS structure very quickly, thus, depleting it almost immediately. As a consequence, conduction, convection and evaporation alone cannot exhaust the high heat fluxes occurring in real experiments and some form of radiation shielding will be necessary to this end.

Capillary driven replenishment of the liquid metal film is anticipated to take place by pumping the liquid metal from the reservoir. Thus, the capillary flow of a liquid metal within a single cylindrical pore was examined as a first attempt to provide an upper bound of the convective effects within the CPS matrix. This simplified investigation overestimates the permeability of the CPS but provides the framework for studying the interplay between the different forces that act towards pushing liquid lithium out of the porous matrix or resist its motion. In the present study, the hydrodynamic problem was examined in the context of axisymmetry in order to obtain an understanding of the operation principle of the capillary pump. The finite element methodology was employed in order to assess how the pore radius affects the seepage velocity of liquid lithium. These seepage velocities along with the time needed for the liquid metal to exit the pore are going to give an estimation of the liquid metal replenishment which is of major importance during plasma operation. The numerical results indicated that upon decreasing the pore radius, the capillary rise velocity decreases linearly owing to the emergence of viscous effects along the radial direction. Since the inertial effects are insignificant for the relative small pore radius considered in this study, the numerical results considering and neglecting inertia are approximately the same with a small difference as the pore radius increases. These discrepancies occur because as the pore radius increases inertia comes into the force interplay.

The current study focuses principally on the static arrangement of the liquid metal resting onto the CPS top surface. More specifically, the effect on the static film arrangement of the reservoir overpressure, electric stresses and, the more relevant to fusion applications, jxB effects was investigated. Furthermore, since, according to the experiments, the film thickness reduces down to micron or even submicron sizes, the nature of the micro-scale liquid-solid interactions was also considered. Isothermal conditions were considered and a liquid metal layer was assumed to have been established on top of the CPS and reached an axisymmetric static arrangement. The finite element methodology was used to solve the Young-Laplace equation, which incorporates surface tension, gravity, pressure and surface forces. The layer thickness was predicted at static equilibrium as a function of the imposed pressure drop across the wafer and the wetting properties of the liquid metal. It was seen that at relatively large reservoir overpressures surface tension balances pressure forces and the liquid metal assumes the form of an almost spherical-cap drop of small radius. Gravity is out of the picture in this regime. As the pressure drop decreases the drop assumes an oblate shape and a thin film is gradually formed that entirely covers the

CPS. In this range, gravity balances pressure drop and surface tension and the film thickness is on the millimeter range, which is relatively large and has negative implications on the stability of the liquid metal layer. As the pressure drop was further decreased, the contact length exceeds any reasonable wafer length and such a balance could not be maintained for fixed contact angle. The film ends in a sharp edge, in which case a fixed contact point condition was imposed rather than a fixed contact angle. In this fashion, a static solution for even lower overpressures was obtained until ΔP almost vanishes with the film achieving submicron-size thickness and near zero contact angle. Such static arrangements have been reported in the literature and are favoured in terms of stability of the CPS against electromagnetic effects.

The nature of surface forces between the liquid metal film and the solid substrate was also considered. In this study, the classic partial wetting case, of liquid lithium with a dry substrate beyond the contact point, cannot be assumed. The envisioned static configuration at near vacuum conditions is characterized by full coverage of the CPS outer surface with the reservoir overpressure being slightly positive or negative. This consideration pertains to the situation after replenishment has taken place but without taking into account the Lorentz forces. A purely repulsive potential and a long range attractive short range repulsive potential were introduced into the previous numerical model in order to simulate the effect of the topography of the porous substrate on the static arrangement of the liquid metal.

Based on the investigation of a purely repulsive potential, no static solution was possible for positive reservoir overpressures because this kind of interaction potential cannot counterbalance a positive pressure drop across the interface. However, it is anticipated that the presence of Lorentz forces may lead to positive and very large effective reservoir overpressures, especially during off-normal events. Thus, a purely repulsive potential cannot exert a stabilizing force and is considered inappropriate for the real case of CPS static configuration.

Concerning the case of a long range attractive short range repulsive potential, since gravity is insignificant in this regime, three main regions were observed, namely the inner, the outer and the transition region with different dominant force balances. Matching between the contact and transition regions provide an estimate of the static contact angle during adhesion. For low overpressures the interface acquires a shape with fixed contact point at the pore edge and a gradually increasing contact angle in that region. Beyond a certain threshold in overpressure, corresponding to the formation of the characteristic contact angle at the pore edge that is predicted based on the interaction potential, a solution could not be obtained and a limit point was formed. The arc length continuation was used instead of simple continuation which showed the existence of a second branch of solutions which evolves towards lower overpressures and corresponds to spherical-cap film shapes of the type captured in the parametric study for relatively large overpressures. For larger overpressures than the critical one dynamic analysis is required in order to study the response pattern, that will involve the onset of a dynamic contact angle.

As a first attempt to capture the electromagnetic effects on the static arrangement, an external electric field was applied. Using the static equilibrium obtained with the top of the porous matrix fully covered and gradually increasing the electric field intensity while keeping the mass of the liquid metal within the layer constant, a sequence of shapes was

3

obtained. As a result of the electric stresses, the pole section of the layer is elongated in the field direction while the contact angle at the equator decreases in order to maintain the same amount of liquid lithium. The liquid layer thickness increases away from the contact line and its curvature increases as well. Eventually, a conical angle forms at the pole region, as a manifestation of the dominant balance between electric stresses and capillarity that determines the size of the conical angle, and a solution could not be obtained for stronger electric fields. Despite the simplified model employed here, this is a valid description of the static equilibrium at extreme conditions. It has been observed in the literature that jetting can be initiated at the pole region as a result of the dynamic evolution of this singular behavior. This process is also known to generate small droplets once the jet speed reaches a certain threshold.

Regarding the effect of the more relevant to fusion applications jxB effects, as long as the liquid metal is within the pore, jxB effects generate an additional effective overpressure that tends to pull liquid lithium out of the pore. This is called magnetic pressure whose magnitude depends on the intensity of the magnetic field, the electric current that enters the liquid metal layer and the pore radius. For small enough electric current densities the Lorentz forces only affect the static arrangement and nearly static flow conditions prevail in the porous system. In fact, the dimensionless magnetic Bond number, $Bond_m$, that relates the Lorentz forces to the surface tension forces can be viewed as a dimensionless magnetic pressure that controls this process. Based on the definition of $Bond_m$, bigger plasma currents can be tolerated by decreasing the pore radius, for fixed magnetic field strength and the liquid metal that is used as the operating fluid of the CPS, a fact that intensifies the reliability of CPS as plasma facing component. Furthermore, a critical $Bond_m$ can be found as a function of a given interaction potential which sets an upper limit in the contact angle that can be achieved at the pore edge. Below this critical value static solutions with a fixed contact point are obtained. Beyond this critical value of $Bond_m$ a new solution family was found that evolves towards lower values of $Bond_m$, with the liquid metal forming a drop outside the pore for fixed contact angle prescribed by the micro-scale liquid-solid interactions and found via an asymptotic analysis. It probably emerges after a limit point in the solution branch. Above the critical magnetic Bond number static solutions with a fixed contact point were only possible whereas a dynamic approach is required to capture the dynamic contact angle evolution in this regime.

Summary (In Greek)

Στα πλαίσια του προγράμματος της ελεγχόμενης θερμοπυρηνικής σύντηξης, ως καίριο ζήτημα αναδεικνύεται η τεχνολογία που σχετίζεται με την αλληλεπίδραση του πλάσματος και των τοιχωμάτων του αντιδραστήρα. Σε συνθήκες λειτουργίας, οι τιμές του θερμικού φορτίου αναμένονται πολύ υψηλές, κυρίως κατά την διάρκεια των ασταθειών του πλάσματος. Έτσι, τα τοιχώματα εμφανίζουν προβλήματα που σχετίζονται με την διάβρωση, τις θερμικές τάσεις κ.α. Για αυτούς τους λόγους, μια διαφορετική προσέγγιση που έχει προταθεί και διερευνάται, τόσο πειραματικά όσο και στο επίπεδο της μοντελοποίησης, είναι η αντικατάσταση των στερεών στοιχείων που έρχονται σε επαφή με το πλάσμα από υγρά μέταλλα. Η παρούσα διδακτορική διατριβή σχετίζεται με την μοντελοποίηση των προαναφερθέντων εναλλακτικών στοιχείων που καλούνται να αντιμετωπίσουν το πλάσμα και τα οποία είναι σε μορφή υγρού μετάλλου.

Μία από τις πρώτες ιδέες ήταν η χρησιμοποίηση συστοιχίας από τζετ ή σταγόνες υγρού μετάλλου. Έτσι, πραγματοποιήθηκε μία μαγνητοϋδροδυναμική μελέτη για την πρόβλεψη της τροχιάς ενός τζετ καθώς και μίας σταγόνας που κινείται μέσα σε ένα ηλεκτρομαγνητικό πεδίο. Στο μονοδιάστατο αριθμητικό μοντέλο που δημιουργήθηκε για το τζετ λήφθηκε υπόψη η επίδραση των δυνάμεων Lorentz, η βαρύτητα και η πτώση πίεσης και θεωρήθηκε ότι η ακτίνα του τζετ είναι πολύ μικρότερη από το μήκος του. Επιπλέον, μελετήθηκε η επίδραση της εξωτερικής βαθμίδας του ηλεκτρικού δυναμικού πάνω στην τροχιά του καθώς επίσης και ο ρόλος που διαδραματίζουν οι ηλεκτρικές τάσεις στην διαμόρφωση της ακτίνας του τζετ και της ταχύτητάς του. Επιπροσθέτως, αναμένονται να δημιουργηθούν σταγόνες ως αποτέλεσμα της απόσπασής τους από το τζετ εξαιτίας τριχοειδών ασταθειών. Γι` αυτό το λόγο, διερευνήθηκε αναλυτικά η τροχιά μίας σταγόνας υγρού μετάλλου παρουσία δυνάμεων Lorentz έτσι ώστε να προσομοιωθεί η εκτροπή της σταγόνας που παρατηρείται λόγω της επιρροής του πλάσματος σε πειράματα όπως αυτά στο ISTTOK. Σε αυτή τη μελέτη, η σταγόνα από υγρό μέταλλο, θεωρούμενη ως σφαιρική συνεχώς, εισέρχεται σε μία περιοχή, παρόμοια με αυτή που περιγράφθηκε προηγουμένως για το τζετ, όπου υφίστανται ένα ομοιόμορφο μαγνητικό πεδίο και μία εξωτερικά επιβαλλόμενη βαθμίδα του ηλεκτρικού δυναμικού. Στην περίπτωση των σταγόνων, όπως έδειξαν τα αναλυτικά αποτελέσματα, εξαιτίας του μικρού μεγέθους και του σφαιρικού σχήματός τους εμφανίζουν μεγαλύτερη απόκλιση από την αρχική τους πορεία σε σχέση με το τζετ. Η προαναφερθείσα εικόνα συμφωνεί σε τάξη μεγέθους με τα ευρήματα των πειραμάτων στο ISTTOK.

Η δεύτερη ερευνητική μελέτη, που καλύπτει και το μεγαλύτερο μέρος της διδακτορικής διατριβής, σχετίζεται με μία άλλη διάταξη που φαντάζει ως την επικρατέστερη, λόγω του πολύ μικρού μεγέθους της και των πειραματικών ευρημάτων. Αυτή η διάταξη καλείται CPS και είναι το ακρωνύμιο του «Capillary Porous System». Η ιδέα για το CPS βασίζεται στη χρησιμοποίηση μίας πορώδους κατασκευής, η οποία λειτουργεί ως «τριχοειδή αντλία» ώστε να παρέχει το υγρό μέταλλο που επικαλύπτει και προστατεύει τον «divertor». Η διάταξη είναι κατασκευασμένη έτσι ώστε να παρέχει την απαραίτητη βαθμίδα πίεσης (μέσω τριχοειδών δυνάμεων) για την άντληση του υγρού μετάλλου από μία δεξαμενή χωρίς την επιβολή επιπλέον εξωτερικής βαθμίδας πίεσης. Έτσι, οι τριχοειδείς και οι επιφανειακές δυνάμεις καθώς και η διαβροχή του υγρού μετάλλου στο πορώδες υπόστρωμα αναμένεται να σταθεροποιούν το υγρό στρώμα ενάντια στις ηλεκτρομαγνητικές και θερμικές δυνάμεις καθώς και να αποτρέπει την δημιουργία σταγόνων, γεγονός που αποτελεί καίρια παράμετρο για την αξιοπιστία αυτής της

5

προτεινόμενης διάταξης. Μέχρι στιγμής, το Λίθιο εμφανίζεται ως το επικρατέστερο υγρό μέταλλο για να υποστηρίξει αυτή την διάταξη. Παρόλα αυτά, και άλλα υγρά μέταλλα όπως το Γάλλιο, ο Κασσίτερος και κράματα Λιθίου-Κασσίτερου έχουν προταθεί και διερευνώνται πειραματικά.

Μέχρι στιγμής, το CPS, όσο αναφορά την μοντελοποίησή του, δεν έχει αποτελέσει αντικείμενο εκτενούς μελέτης κυρίως εξαιτίας της πολυπλοκότητας της πορώδους διάταξης που εμπεριέχει το υγρό μέταλλο. Στην παρούσα διδακτορική διατριβή, πραγματοποιήθηκε μία προσπάθεια ώστε να κατανοηθεί η λειτουργία του CPS ως διάταξη για την αντιμετώπιση του πλάσματος.

Ξεκινώντας την ανάλυση για το CPS, αρχικά το μέταλλο (θεωρήθηκε το Λίθιο ως αντιπροσωπευτικό μέταλλο) βρίσκεται σε στερεή μορφή μέσα στο πλέγμα σε θερμοκρασία δωματίου. Η πορώδης διάταξη είναι σε επαφή με το περιβάλλον ρευστό μέσω της εξωτερικής άνω επιφάνειας η οποία είναι αρχικά καλυμμένη. Κατόπιν, η άνοδος της θερμοκρασίας οδηγεί σε τήξη του στερεού Λιθίου που έχει ως αποτέλεσμα το σπάσιμο του εξωτερικού περιβλήματος από το διαστελλόμενο Λίθιο και την δημιουργία ενός πολύ λεπτού υγρού υμένα στην εξωτερική άνω επιφάνεια του CPS. Εφαρμόζοντας ένα ισοζύγιο μάζας μεταξύ της αρχικής στερεής και τελικής υγρής φάσης του Λιθίου υπολογίστηκε προσεγγιστικά ότι το πάχος του προαναφερθέντος υγρού υμένα είναι τάξεως μικρομέτρων. Τα αριθμητικά αποτελέσματα που αποκομίστηκαν, σταθεροποιώντας την μάζα του υγρού υμένα, το μέγεθος της διάταξης και θεωρώντας σταθερό το σημείο επαφής, ενώ ταυτόχρονα ικανοποιούταν το κάθετο ισοζύγιο τάσεων, επιβεβαιώνουν τα προηγούμενα αποτελέσματα.

Η προαναφερθείσα στατική διαμόρφωση είναι πολύ δύσκολο να διατηρηθεί σε πολύ μεγάλα θερμικά φορτία. Μόλις η μηχανή «ανοίξει» τα εξωτερικά θερμικά φορτία εξατμίζουν τον υγρό υμένα που βρίσκεται στην άνω επιφάνεια του CPS. Προκειμένου να προσομοιωθεί η διαδικασία της μεταφοράς θερμότητας θεωρήθηκε ότι στην απαγωγή θερμότητας συμμετέχουν η αγωγή, η συναγωγή και η εξάτμιση, ενώ αγνοήθηκε η επίδραση της ασπίδας ακτινοβολίας. Παρατηρήθηκε ότι η προσπίπτουσα θερμοροή (θεωρήθηκε ως παράδειγμα αυτή των 10 MW/m^2) θα εξατμίσει τον υγρό υμένα από την άνω επιφάνεια του CPS πάρα πολύ γρήγορα. Ως αποτέλεσμα, η αγωγή, η συναγωγή και η εξάτμιση από μόνες τους δεν επαρκούν για την απαγωγή των μεγάλων θερμικών φορτίων που αναμένονται σε πραγματικά πειράματα. Συνεπώς, και η επίδραση της ασπίδας ακτινοβολίας πρέπει να ληφθεί υπόψη.

Ο ανεφοδιασμός του υγρού υμένα στην άνω επιφάνεια του CPS λαμβάνει χώρα μέσω των τριχοειδών δυνάμεων αντλώντας το υγρό μέταλλο από μία δεξαμενή που βρίσκεται σε επαφή με την πορώδη διάταξη. Για αυτό το λόγο, εξετάσθηκε η τριχοειδής ροή του υγρού μετάλλου μέσα σε ένα κυλινδρικό πόρο σαν μία πρώτη προσπάθεια να βρεθεί ένα άνω όριο των φαινομένων συναγωγής μέσα στο πλέγμα του CPS. Αυτή η απλοποιημένη μελέτη υπερεκτιμάει την διαπερατότητα του CPS, αλλά παρέχει το πλαίσιο πάνω στο οποίο μπορεί να διερευνηθεί η αλληλεπίδραση μεταξύ των διαφορετικών δυνάμεων που βοηθούν στην άντληση του υγρού μετάλλου ή επιβραδύνουν την ροή του. Στην παρούσα έρευνα διερευνήθηκε το υδροδυναμικό πρόβλημα υπό αξονική συμμετρία έτσι ώστε να κατανοηθεί η λειτουργία του CPS ως τριχοειδής αντλία. Η μέθοδος των πεπερασμένων στοιχείων εφαρμόστηκε με σκοπό να εκτιμηθεί πώς επιδρά η ακτίνα του πόρου πάνω στην ταχύτητα διαρροής του υγρού μετάλλου. Η προαναφερθείσα ταχύτητα μαζί με το χρόνο που χρειάζεται για να εξέλθει το υγρό μέταλλο από τον πόρο δίνουν μία πρώτη

εκτίμηση της διαδικασίας του ανεφοδιασμού του υγρού υμένα στην άνω επιφάνεια του CPS, κάτι που είναι πολύ σημαντικό κατά την διάρκεια της λειτουργίας του πλάσματος. Τα αριθμητικά αποτελέσματα έδειξαν ότι μειώνοντας την ακτίνα του πόρου η ταχύτητα της ροής του υγρού μετάλλου μέσα σε αυτόν μειώνεται γραμμικά εξαιτίας της εμφάνισης ιξωδών φαινομένων κατά μήκος της ακτινικής διεύθυνσης. Εφόσον, οι αδρανειακές δυνάμεις δεν είναι σημαντικές για τις σχετικά μικρές διαστάσεις που θεωρήθηκαν στην παρούσα μελέτη, τα αποτελέσματα διατηρώντας και αγνοώντας τους αδρανειακούς όρους είναι σχεδόν όμοια με μία μικρή διαφορά καθώς μεγαλώνει η διάσταση του πόρου. Αυτή η διαφοροποίηση συμβαίνει λόγω της εισόδου της αδράνειας στο ισοζύγιο δυνάμεων καθώς η ακτίνα του πόρου μεγαλώνει.

Η παρούσα διδακτορική διατριβή επικεντρώνεται κυρίως στη στατική διαμόρφωση του υμένα από υγρό μέταλλο που διαμορφώνεται στην άνω επιφάνεια της διάταξης του CPS. Πιο συγκεκριμένα, μελετήθηκε η επίδραση πάνω στην στατική διαμόρφωση του υγρού μετάλλου της διαφοράς πίεσης μεταξύ της δεξαμενής και του περιβάλλοντος ρευστού, των ηλεκτρικών τάσεων και των ηλεκτρομαγνητικών δυνάμεων, οι οποίες είναι πιο σχετικές για τις εφαρμογές της σύντηξης. Επιπροσθέτως, σύμφωνα με τα πειράματα, το πάχος του υγρού υμένα φτάνει διαστάσεις μικρομέτρων και λιγότερο. Έτσι, διερευνήθηκε και η επίδραση των επιφανειακών δυνάμεων μεταξύ του υγρού μετάλλου και του πορώδους υποστρώματος.

Το CPS μοντελοποιήθηκε ως ένας λεπτός κυλινδρικός δίσκος ευρισκόμενος σε επαφή με μία δεξαμενή που παρέχει το υγρό Λίθιο. Θεωρήθηκαν ισοθερμικές συνθήκες και ένα λεπτό στρώμα υγρού Λιθίου θεωρήθηκε ότι έχει διαμορφωθεί στην άνω επιφάνεια του CPS και έχει στατική αξονική συμμετρία. Η μέθοδος των πεπερασμένων στοιχείων χρησιμοποιήθηκε για την επίλυση της εξίσωσης Young-Laplace στην διεπιφάνεια αερίου-υγρού μετάλλου, η οποία περιλαμβάνει δυνάμεις λόγω επιφανειακής τάσης, διαφοράς πίεσης, βαρύτητας και ενδομοριακών αλληλεπιδράσεων. Αρχικά, αγνοώντας τις ενδομοριακές δυνάμεις, το πάχος του υγρού υμένα εκτιμήθηκε ευρισκόμενο σε στατική ισορροπία ως συνάρτηση της επιβαλλόμενης βαθμίδας πίεσης κατά μήκος της διάταξης και των ιδιοτήτων σχετιζόμενων με την διαβροχή του υγρού μετάλλου στο στερεό υπόστρωμα. Παρατηρήθηκε ότι για σχετικά μεγάλες τιμές της βαθμίδας πίεσης, οι δυνάμεις λόγω επιφανειακής τάσης εξισορροπούν αυτές λόγω διαφοράς πίεσης με το υγρό μέταλλο να έχει την μορφή μιας σχεδόν ημισφαιρικής σταγόνας μικρής ακτίνας. Η βαρύτητα εδώ δεν παίζει σημαντικό ρόλο. Καθώς, όμως, η διαφορά πίεσης ελαττώνεται, η υγρή σταγόνα παίρνει πεπλατυσμένη μορφή και δημιουργείται ένας λεπτός υγρός υμένας που σταδιακά καλύπτει όλη την άνω επιφάνεια του CPS. Σε αυτό το στάδιο, η βαρυτικές δυνάμεις εξισορροπούν τις δυνάμεις λόγω διαφοράς πίεσης και επιφανειακής τάσης και το πάχος του υγρού υμένα είναι τάξεως χιλιοστών, η οποία είναι σχετικά μεγάλη και έχει αρνητικές επιπτώσεις στην ευστάθεια του υγρού υμένα. Καθώς η διαφορά πίεσης ελαττώνεται περισσότερο, το μήκος επαφής υπερβαίνει κάθε ρεαλιστικό μήκος σχετικό με την διάταξη και η στατική ισορροπία δεν μπορεί να επιτευχθεί για μία φιξαρισμένη γωνία επαφής. Έτσι, φιξάροντας το μήκος επαφής αντί για την γωνία επαφής, η στατική ισορροπία μπορεί να επιτευχθεί για ακόμα μικρότερες βαθμίδες πίεσης συγκριτικά με την προηγούμενη προσέγγιση έως ότου η διαφορά πίεσης εκμηδενίζεται και ο υγρός υμένας έχει πάχος τάξεως μικρομέτρων και γωνία επαφής σχεδόν μηδενική. Τέτοιου είδους στατικές διαμορφώσεις έχουν αναφερθεί στην βιβλιογραφία και παρουσιάζονται πιο ευσταθείς ενάντια στις ηλεκτρομαγνητικές δυνάμεις.

Κατόπιν, διερευνήθηκε η επίδραση των επιφανειακών δυνάμεων μεταξύ του υγρού μετάλλου και του πορώδους υποστρώματος. Στην παρούσα μελέτη, η κλασική περίπτωση μερικής διαβροχής του υγρού μετάλλου στο στερεό υπόστρωμα δεν μπορεί να εφαρμοστεί. Εκτιμάται ότι η στατική διαμόρφωση του υγρού μετάλλου σε συνθήκες κενού χαρακτηρίζεται από πλήρη κάλυψη της άνω επιφάνειας του CPS με την διαφορά πίεσης μεταξύ της δεξαμενής και του περιβάλλοντος πλάσματος να είναι πάρα πολύ μικρή και οι τιμές της θετικές ή αρνητικές ανάλογα με τις δυνάμεις που ασκούνται. Αυτή η μελέτη δεν λαμβάνει υπόψη τις πεδιακές δυνάμεις και σχετίζεται με την φάση στην οποία ο ανεφοδιασμός του υγρού μετάλλου που αναφέρθηκε προηγουμένως έχει ήδη λάβει χώρα. Δύο είδη δυναμικών αλληλεπίδρασης μεταξύ του υγρού μετάλλου και του πορώδους υποστρώματος διερευνήθηκαν: αρχικά ένα αμιγώς απωστικό δυναμικό και εν συνεχεία ένα δυναμικό το οποίο είναι ελκτικό ή αρνητικό ανάλογα με το αν υπερβεί ή όχι η τιμή της ευκλείδειας απόστασης μεταξύ του στερεού υποστρώματος και της διεπιφάνειας υγρού μετάλλου-αερίου κάποια συγκεκριμένη τιμή. Ο ρόλος της βαρύτητας και στις δύο περιπτώσεις δεν είναι σημαντικός.

Αναφορικά με την περίπτωση ενός αμιγώς απωστικού δυναμικού, με την διαφορά πίεσης μεταξύ δεξαμενής και περιβάλλοντος ρευστού να είναι μηδέν, η γενική εικόνα είναι αυτή ενός ομοιόμορφου υπέρλεπτου υγρού υμένα τάξεως λίγο μικρομέτρων στην άνω επιφάνεια του CPS με μικρές εσοχές στην περιοχή του πόλου. Επίσης, όσο η άπωση μεγαλώνει, το πάχος του υγρού υμένα αυξάνεται. Για πιέσεις της δεξαμενής μεγαλύτερες από τις πιέσεις του περιβάλλοντος ρευστού δεν μπορεί να επιτευχθεί στατική ισορροπία, επειδή αυτού του είδους το δυναμικό είναι μόνο απωστικό. Σε περιπτώσεις που λαμβάνονται υπόψη οι δυνάμεις Lorentz το παρών δυναμικό αλληλεπίδρασης δεν πρέπει να θεωρείται κατάλληλο για την προσομοίωση της διεργασίας αφού η παρουσία τους πιθανόν να οδηγήσει σε θετική βαθμίδα πίεσης, ιδιαίτερα κατά την εμφάνιση των ασταθειών του πλάσματος. Παρόλα αυτά, η χρησιμοποίηση αυτού του δυναμικού μας έδωσε κάποια πρώτη εικόνα για την καλύτερη κατανόηση της διεργασίας.

Όσο αναφορά την δεύτερη περίπτωση δυναμικού αλληλεπίδρασης, παρατηρήθηκαν τρεις βασικές υποπεριοχές με διαφορετικά κυρίαρχα ισοζύγια δυνάμεων (η εσωτερική, η εξωτερική και η μεταβατική περιοχή που υφίσταται μεταξύ των δύο προηγούμενων περιοχών). Ο συσχετισμός της μεταβατικής περιοχής με την περιοχή της επαφής μπορεί να δώσει μία εκτίμηση της στατικής γωνίας επαφής. Για σχετικά μικρές τιμές της διαφοράς πίεσης η διεπιφάνεια υγρού-αερίου λαμβάνει ένα σχήμα με φιξαρισμένο σημείο επαφής στο χείλος του πόρου και μία σταδιακά αύξουσα γωνία επαφής σε αυτή την περιοχή. Πέρα από κάποια οριακή τιμή της βαθμίδας πίεσης, που αντιστοιχεί στη διαμόρφωση μίας χαρακτηριστικής γωνίας επαφής στο χείλος του πόρου και προβλέπεται με βάση το δυναμικό αλληλεπίδρασης, παρουσιάστηκε ένα οριακό σημείο και η στατική διαμόρφωση δεν μπορούσε να επιτευχθεί. Σε αυτή την περίπτωση εφαρμόστηκε μία άλλου είδους αριθμητική διαδικασία αντί για την απλή συνέχεια (simple continuation), η arc length continuation που έδειξε την εμφάνιση ενός δεύτερου κλάδου λύσεων που αντιστοιχεί σε υγρούς υμένες με μεγαλύτερο πάχος. Αυτός ο δεύτερος κλάδος εξελίσσεται προς μικρότερες βαθμίδες της πίεσης και το σχήμα των υγρών υμένων αντιστοιχεί σε σχεδόν ημισφαιρικές σταγόνες παρόμοιες με αυτές που λήφθηκαν στην παραμετρική μελέτη που προαναφέρθηκε και μελετά την επίδραση σχετικά μεγάλων διαφορών της πίεσης. Για αυτές τις μεγάλες πιέσεις, μεγαλύτερες της κρίσιμης τιμής που εμφανίζεται οριακό σημείο, χρειάζεται να μελετηθεί δυναμικά το πρόβλημα.

8

Ως μία πρώτη προσπάθεια να προσομοιωθεί η επίδραση των δυνάμεων Lorentz στην προαναφερθείσα στατική διαμόρφωση, μελετήθηκε η επίδραση ενός εξωτερικά επιβαλλόμενου ηλεκτρικού πεδίου. Χρησιμοποιώντας την στατική διαμόρφωση του υγρού μετάλλου που υπολογίστηκε προηγουμένως για την περίπτωση που αυτό καλύπτει πλήρως την άνω επιφάνεια του CPS και σταδιακά αυξάνοντας την ένταση του ηλεκτρικού πεδίου, ενώ η μάζα του υγρού μετάλλου διατηρήθηκε σταθερή, λήφθηκαν μία σειρά από σχήματα που απεικονίζουν το σχήμα της στατικής διαμόρφωσης. Ως συνέπεια της επίδρασης των ηλεκτρικών τάσεων στη διεπιφάνεια, η περιοχή του πόλου επιμηκύνεται στην κατεύθυνση του ηλεκτρικού πεδίου, ενώ η γωνία επαφής μειώνεται ώστε να διατηρηθεί η ίδια ποσότητα υγρού Λιθίου. Το πάχος του υγρού υμένα αυξάνεται μακριά από την γραμμή επαφής όπως και η καμπυλότητα. Τελικά, μία κωνική γωνία δημιουργείται στην περιοχή του πόλου και καμία στατική λύση δεν μπορεί να επιτευχθεί για ισχυρότερα ηλεκτρικά πεδία. Σε αυτό το στάδιο, η βαρύτητα εξισορροπεί τις ηλεκτρικές τάσεις και αυτό το ισοζύγιο δυνάμεων καθορίζει την τιμή της κωνικής γωνίας στον πόλο. Παρά το γεγονός ότι το μοντέλο που αναπτύχθηκε είναι σχετικά απλοποιημένο, τα αποτελέσματα που αποκομίστηκαν θεωρήθηκαν έγκυρα και αντιστοιχούν σε ακραία σενάρια κατά τη διάρκεια των αστάθειων του πλάσματος. Έχει παρατηρηθεί στην βιβλιογραφία ότι στην περιοχή του πόλου μπορεί να δημιουργηθεί υγρή δέσμη υψηλής ταχύτητας (jet). Αυτή η διεργασία, όπως αναφέρεται στην βιβλιογραφία, μπορεί να δημιουργήσει μικρές σταγόνες μόλις η ταχύτητα της υγρής δέσμης υψηλής ταχύτητας υπερβεί κάποια οριακή τιμή.

Όσο αναφορά την επίδραση των πιο σχετικών με τις εφαρμογές της σύντηξης ηλεκτρομαγνητικών δυνάμεων (επίδραση jxB), όσο το υγρό μέταλλο βρίσκεται εντός του πόρου οι ηλεκτρομαγνητικές δυνάμεις δημιουργούν μία βαθμίδα πίεσης που τείνει να τραβήξει το υγρό μέταλλο έξω από τον πόρο. Αυτή η μαγνητική πίεση εξαρτάται από την ένταση του εξωτερικά επιβαλλόμενου μαγνητικού πεδίου, το ηλεκτρικό ρεύμα που εισέρχεται στο υγρό μέταλλο και την ακτίνα του πόρου. Στην πράξη ο αδιάστατος αριθμός $Bond_m$ που προέκυψε από την αδιαστατική ανάλυση και σχετίζει τις δυνάμεις Lorentz με αυτές λόγω επιφανειακής τάσης φαίνεται να ελέγχει την όλη διεργασία. Βασιζόμενοι στην σχέση για την εύρεση του $Bond_m$, ελαττώνοντας την ακτίνα του πόρου μεγαλύτερα ρεύματα πλάσματος μπορούν να ανεχθούν, γεγονός που ενισχύει την αξιοπιστία του CPS ως στοιχείο αντιμετώπισης του πλάσματος. Επιπροσθέτως, μία κρίσιμη τιμή του $Bond_m$ μπορεί να βρεθεί ως συνάρτηση του δυναμικού αλληλεπίδρασης, το οποίο εισάγει ένα ανώτατο όριο στην τιμή της γωνίας επαφής που μπορεί να επιτευχθεί στο χείλος του πόρου. Πέρα από αυτή την κρίσιμη τιμή του $Bond_m$ μία καινούργια οικογένεια λύσεων, που εξελίσσεται προς μικρότερα $Bond_m$, βρέθηκε με το υγρό μέταλλο να σχηματίζει μία σταγόνα έξω από τον πόρο με φιξαρισμένη γωνία επαφής που καθορίζεται από τις αλληλεπιδράσεις στην μικροκλίμακα μεταξύ του υγρού μετάλλου και του στερεού υποστρώματος. Η προαναφερθείσα γωνία επαφής μπορεί να προβλεφθεί από μία ασυμπτωτική ανάλυση που πραγματοποιήθηκε στα πλαίσια της παρούσας διδακτορικής διατριβής. Η καινούργια λύση ίσως να εμφανίζεται μετά από την εμφάνιση κάποιου οριακού σημείου στο διάγραμμα διακλάδωσης. Μία δυναμική μελέτη του προβλήματος χρειάζεται έτσι ώστε να εκτιμηθεί η εξέλιξη της δυναμικής γωνίας επαφής σε αυτή την περιοχή.

Contents

13

14

List of figures

15

16

List of tables

Novelty and scientific contribution of the PhD dissertation

The free surface plasma facing components constitute one of the most critical technological challenges of future fusion reactors. As can be gleaned by the relevant studies, this topic has been the subject of extensive ongoing R&D. Out of the proposed liquid metal concepts, this PhD dissertation dealt with the jet/drop curtain and, primarily, the Capillary Porous System (CPS) concepts.

Regarding the jet/drop concept pertaining to the ISTTOK experiments, the simplified model developed in the context of the present study provided a proof of principle explanation for the observed deflection from the original trajectory in a Tokamak environment. As a consequence, the results obtained corroborate the belief that employment of liquid metal drops/jets cannot be regarded as an optimal alternative plasma facing component mainly due to their strong deflection as they interact with the surrounding plasma. In addition, the results based on this first principle study reasonably conform to the findings of ISSTOK experiments.

The second concept that was investigated in the present thesis, namely the CPS concept, is the most mature path for liquid surface plasma facing components as can be deduced from the relevant literature. In this concept, capillary action is of central importance for renewing the liquid metal which is in contact with plasma. Thus far, CPS has been the subject of extensive experimental activity with encouraging findings. Nevertheless the CPS, until now, has not been the subject of extensive modelling activity partly due to the complex flow arrangement of the limiter containing the liquid metal.

This is the first time, in our knowledge, that such an in-depth theoretical analysis is presented concerning the CPS concept. As a matter of fact, this PhD dissertation tries, through first-principles studies, to deal with the major phases of the CPS operation. More specifically, it models-explains what happens during the preparation phase, that is to say before the machine is "turned on". Furthermore, a heat balance is performed pertaining to the power exhaust capabilities of the CPS configuration ignoring the non-coronal radiation shielding. Subsequently, it delves into how the replenishment occurs identifying the interplay between the different forces that act towards pushing liquid lithium out of the porous matrix or resist its motion. Finally, the current PhD dissertation studies extensively the static arrangement of the ultra-thin liquid metal film that rests onto the CPS outer surface, as a function of the reservoir overpressure, external field forces and wetting properties of the working liquid metal on the substrate.

Focusing on the vented lamp concept for a capillary porous system with capillary wicking channels for the supply of liquid metal from an internal reservoir, an extensive parametric study is performed on the effect of reservoir overpressure on the static film thickness. For large overpressures the size of the liquid meal layer decreases and the balance between surface tension and pressure drop determines the shape of the interface. Subject to nearly vacuum conditions the thickness of the protective layer was found to be on the order of micron or submicron meters in agreement with experimental observations. In this regime, the shape of the interface depends on the substrate nature and topography and assumes the form of a protrusion series, when the interpore distance is much larger than the pore radius. As the reservoir overpressure increases the liquid metal layer that coats the pore assumes a static arrangement with a fixed contact point at the pore's edge. When the

19

contact angle at the pore edge reaches a critical value predicted by the interaction potential between the liquid metal and substrate a limit point arises and the solution family turns to lower overpressures. The coating assumes the shape of a drop that has escaped the pore and coats the substrate with the above critical contact angle. Beyond the overpressure corresponding to the critical contact angle, the threshold value depends on the strength of the interaction potential, a static arrangement does not exist and a transient analysis is necessary to describe the spreading process of the operating fluid on the CPS response, possibly introducing the concept of dynamic contact angle.

The importance of the above analysis becomes evident when the effect of Lorentz forces on the static arrangement is investigated. More specifically, when an electric current enters the liquid metal layer from the surrounding plasma then, in the presence of an azimuthal magnetic field component, a Lorentz force arises whose effect is incorporated in the Maxwell stresses. The latter is decomposed in the magnetic pressure and a rotational part and the relative strength of Lorentz forces with respect to capillarity is determined by a magnetic Bond number, $Bond_m$, that acts as a dimensionless magnetic pressure. For relatively small values of $Bond_m$ the rotational part of the stresses is negligible and the effect of the magnetic pressure on the static arrangement is similar to the situation described above for the same overpressure. In particular, for small values of $Bond_m$ shapes with fixed contact point are obtained at the pore's edge with increasing contact angle and increasing length of protrusion into the plasma. Provided the interaction potential with the substrate is known, in the presence of Lorentz forces, a critical contact angle can be derived in the manner shown for the case of a general overpressure.

Upon reaching the critical value for the contact angle at the pore's edge the onset of shapes with fixed contact angle is anticipated for $Bond_m$ values lower than the corresponding critical value, $Bond_m$, as a result of a limit point in the parameter space of overpressure for fixed strength of the interaction potential. Static solutions with a fixed contact angle do not exist for larger magnetic pressures and a dynamic analysis is required in order to investigate the response at large electric currents or larger magnetic $Bond_m$. More specifically, dynamic contact angle effects should be investigated during the spreading process of the liquid metal on the substrate, in order to investigate different dynamic patterns that occur at large magnetic Bond numbers. To this end, the proper interaction potential pertaining to the liquid metal and substrate has to be introduced. The above critical $Bond_m$ number is a first threshold for the establishment of a static arrangement. For fixed operating medium, e.g. liquid lithium, magnetic field intensity and strength of the interaction potential, the above critical value is achieved for larger electric current densities as the pore size decreases. In this fashion, the critical magnetic Bond number, derived via the above analysis, can be used as a control parameter in order to interpret experimental observations of capillary porous systems.

20

Outline of the PhD Thesis

The PhD Thesis is divided into seven chapters. More specifically: Chapter 1 presents the motivation of the current study and the basic principles of Controlled Thermonuclear Fusion as well as the approaches to achieve it on Earth. Besides, the governing concepts, concerning the use of liquid metal as free surface plasma facing components, are presented with more details on Capillary Porous System (CPS). In Chapter 2 the basic aspects of wetting phenomena along with the surface forces due to the micro-scale liquid-solid interactions are discussed. In Chapter 3 the deflection of a liquid metal jet/drop in a tokamak environment is investigated with the modelling section and the main results being assembled within the same chapter since the next Chapters (4-6) are referred to the CPS configuration. In Chapter 4, the step-by-step effort is described concerning the analysis of the operation of the CPS as plasma facing component. Moreover, the modelling as well as its mathematical formulation of CPS is analyzed for all the cases considered. Chapter 5 contains the finite element methodology, the basis functions and the discretized equations which were used. In Chapter 5, the Newton-Raphson method is presented along with continuation techniques. At the end of the chapter, a subsection exists focusing on benchmark calculations and comparison with available results from the literature. The main results are demonstrated in Chapter 6 while the main conclusions based on this work are drawn in Chapter 7 along with recommendations for future work.

22

Chapter 1: Introduction

In this chapter, a literature survey is presented concerning the case of thermonuclear fusion in a Tokamak with an emphasis on liquid surfaces for fusion plasma facing components and the progress which has been achieved so far. The Capillary Porous System (CPS) is analyzed mostly because it is the subject of the current PhD dissertation. Besides, it seems to be the most mature path for liquid surface PFCs. Finally, since this work has been carried out within the framework of the EUROfusion Consortium and has received funding from the Euratom research a brief description of the program`s main objectives is presented.

1.1 The European fusion program

The European fusion program is based on the Roadmap to the realization of fusion energy. EUROfusion funds the Research Units in accordance with their participation to the mission-oriented Work Packages outlined in the Consortium Work Plan [1].

In general the program has two aims: Preparing for ITER experiments and developing concepts for the fusion power demonstration plant DEMO.

ITER
The objectives of the EUROfusion ITER Physics Program for ITER lie in the development of plasma regimes of operation for ITER and in investigating solutions to manage the plasma's heat exhaust. The second issue is connected with concepts for the divertor, which is the area of the reactor wall that experiences the highest heat and particle fluxes. ITER Physics also studies divertor configurations that could reduce this heat loads.

DEMO
Laying the foundation for a Demonstration Fusion Power Reactor (DEMO) to follow ITER by 2050 is the objective of the EUROfusion Plant Physics and Technology Work Program. The central requirements for DEMO lie in its capability to generate several 100 Megawatt of net electricity to the grid and to operate with a closed fuel-cycle (i.e. to produce and burn tritium in a closed cycle). A number of outstanding technology and physics integration issues must be resolved before a DEMO plant concept selection is made. Each of them has very strong interdependencies. One is the selection of the concept for the breeding blanket. Blankets are the internal components of the reactor wall that absorb the energy from the fusion reaction, ensure the tritium breeding process and shield the components outside the reaction chamber from the fast fusion neutrons. The choice of cooling fluid flowing through the blanket is closely connected to the selection of the Balance of Plant. The latter denotes the sum of all systems that transform the fusion energy into electricity – mainly cooling fluid, turbine and generator. Another matter is the selection of the divertor concept and its layout configuration. The design of the first-wall (i.e. the innermost lining of the reactor wall) and its integration into the blanket is a further issue, since it must take into account that the first-wall might see higher heat loads than assumed in previous studies. Furthermore, there is the selection of the minimum pulse duration of DEMO and of the corresponding mix of plasma heating

23

systems (i.e. heating and current-drive systems). DEMO must be designed in a way that all maintenance work can be carried out remotely via manipulators and therefore reliable and fast maintenance schemes must be selected. The impact of the various system design options on the overall plant reliability and availability are analyzed in an integrated approach. The development of DEMO requires many technological advances and innovations in several areas. One example is structural materials that withstand both extreme heat loads and the bombardment with neutrons of unprecedented energy. Another issue is the heat load – not only on the divertor, but also on areas of the reactor wall.

1.2 Motivation

It is widely known that the world economy runs on fossil fuel. However, the world resources of oil, coal and gas are diminishing. If no action is taken, an energy crisis is imminent in the next couple of centuries, maybe decades. Apart from the inevitable fact that we will run out of fuel, the burning coal, oil and gas also has an impact on the environment. The signs of global warming due to carbon dioxide and the accompanying climate change become increasingly more alarming.

Nevertheless, mankind will not give up the present standard of living, so the energy consumption is not expected to be reduced, it will rather be increased. Sources of energy, other than fossils, are therefore needed. Those that are presently available, however, are of very low energy density (solar, wind and bio-energy) or produce long term radioactive waste (nuclear fission). Thermonuclear fusion holds the promise of an abundant supply of energy, without affecting the climate and with minimal short-term radioactive waste.

Nuclear fusion is the reaction in which two or more nuclei combine together in order to form a new element with higher atomic number (more protons in the nucleus). The energy released in fusion is related to $E = mc^2$ (Einstein's famous energy-mass equation). On Earth, the most likely fusion reaction is Deuterium–Tritium reaction. Deuterium and Tritium are both isotopes of Hydrogen.

$$D + T \rightarrow He + n + 17.6 \, Mev \tag{1.1}$$

In this reaction two Hydrogen isotopes, Deuterium and Tritium, fuse resulting in a Helium nucleus and a neutron. The produced energy is divided over the fusion products: the neutron receives kinetic energy of 14.1 MeV, the helium nucleus (also called α-particle) has energy of 3.5 MeV. Deuterium is largely available in the oceans of the Earth. Tritium is not freely available, but can be produced by a nuclear reaction of Lithium – also widely available – and an energetic neutron. The 'waste' of this fusion reaction is Helium: a non-toxic, non-radioactive gas.

In order to achieve fusion on the Earth, some serious matters should be taken into account. First of all, the nuclei of Deuterium and Tritium do not fuse spontaneously. Since they both have a positive charge, the repelling Coulomb force prevents their fusion. A sufficiently high kinetic energy of the nuclei is needed to overcome the Coulomb force, see **Fig. 1.1**. This high kinetic energy is achieved in a gas with temperature T of about 100 million degrees centigrade. At this level of temperature gases are ionized. We do no longer call them gas, but "*plasma*". It is common to express temperatures in a plasma with eV, where 1 eV=12000°C.

25
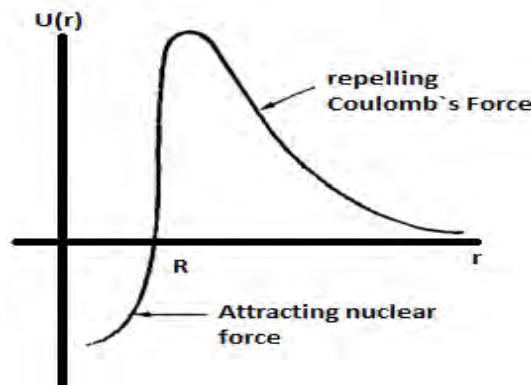
Fig. 1.1 A sufficiently high kinetic energy of the nuclei is needed to overcome the Coulomb force

Unfortunately, a high temperature is not all that is needed to achieve the fusion of nuclei. In order to have enough collisions between the highly energetic nuclei, the density, n, of the particles should be also high enough. A third important parameter is the energy loss. If fusion plasma loses its energy to the outside world faster than it can gain energy from fusion reactions and/or from external heating, then the process will die out. The rate at which plasma loses its energy is given by $1/\tau_E$, where τ_E is the energy confinement time. A fusion reaction will be self-sustained if the product of the above three parameters - temperature T, density n and confinement time τ_E is sufficiently high. For the Deuterium – Tritium fusion reaction the following relationship has been proposed:

$$n\,T\tau_E > 5 \times 10^{21}\,keVs\,/\,m^3 \tag{1.2}$$

The above inequality is the so-called "Lawson criterion". The triple product $nT\tau_E$ is a figure-of-merit for a fusion reactor: the higher it is the better.

To produce energy from fusion, scientists must control the temperature, density and lifespan of the plasma fuel. Since all deuterium/tritium fueled fusion takes place at 150 million degrees Celsius, the two variables that can be controlled to produce fusion are plasma density and lifespan. There are three different lines of research that deal with this problem.

At one end of the spectrum is low density, long lifespan fusion, in which the low density produces a relatively small number of energy producing collisions, but the plasma is long lived enough to achieve sufficient interactions to generate energy. Because the plasma is held stable (confined) for these long periods using magnetic fields, this technique is referred to as Magnetic Confinement Fusion (MCF). Some commonly studied configurations for magnetic confinement are the magnetic mirror, the z-pinch, the stellarator and the Tokamak, **Figs. 1.2-1.5**, respectively.

At the other end of the spectrum is very high density plasma with very short lifespans, referred to as Inertial Confinement Fusion (ICF). Using extremely rapid compression to heat a capsule of fuel to fusion temperatures, inertial confinement fusion takes place in a matter of nanoseconds and produces a short lived burst of energy. The National Ignition Facility (NIF) is the world's largest inertial confinement fusion research facility, and uses the world's most powerful laser to compress and heat a fuel capsule.

26

In the mid-ground between these two approaches is Magnetized Target Fusion (MTF). Magnetized target fusion starts with medium density plasma and compresses it to fusion conditions. The compression phase takes place in microseconds (a thousand times slower than in Inertial Confinement Fusion), allowing for more conventional compression methods such as pistons to be employed. General Fusion and Helion Energy are companies that use this approach in order to develop the world's first commercially viable fusion power plant, [2,3].

Finally, the most important accomplishments concerning the above three different lines of research, namely MCF, ICF and MTF, are shown in **Fig. 1.6a-d.**
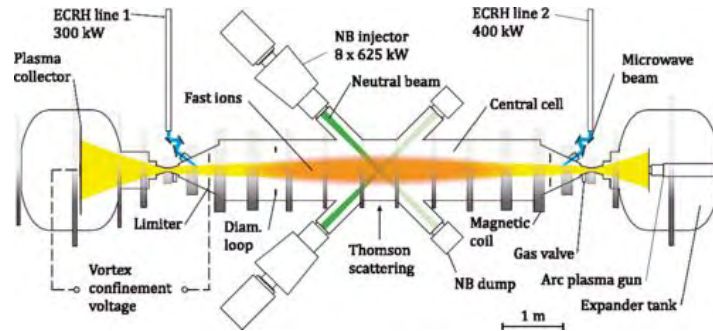
Fig. 1.2 Gas dynamic trap (GDT) magnetic mirror configuration, [4]
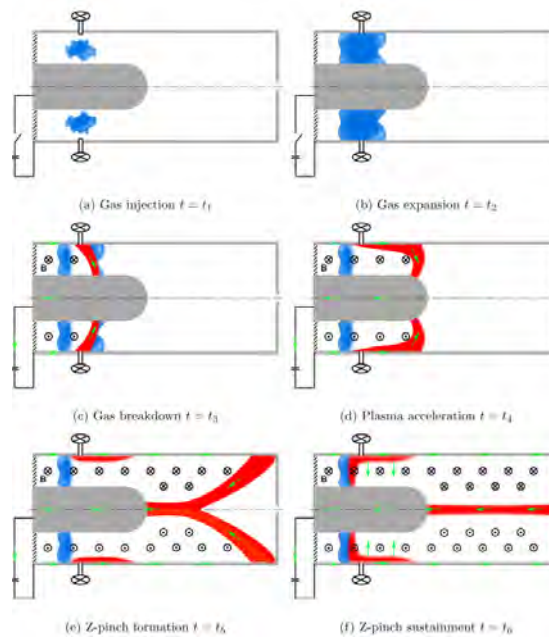
Fig. 1.3 Schematic illustrating the formation of a flow Z-pinch in the ZaP experiment, [5]

27
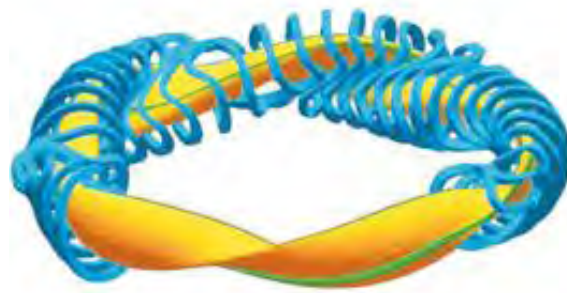
Fig. 1.4 Stellarator configuration, [6]
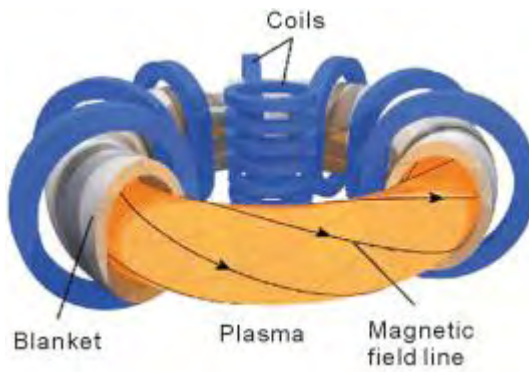
Fig. 1.5 Tokamak configuration, [6]
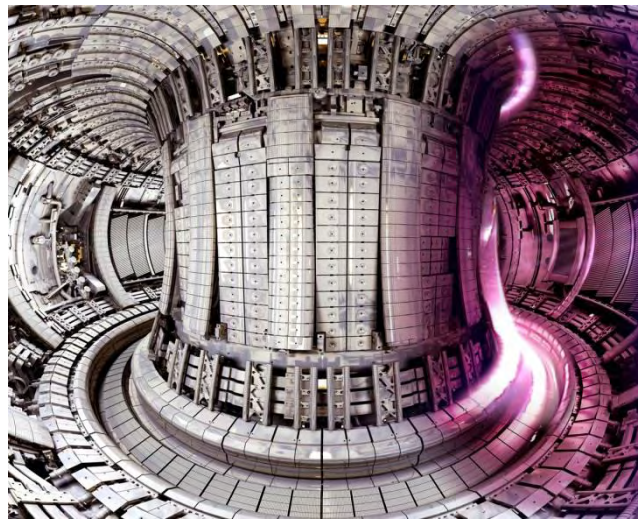
(a)

(b)

(c)
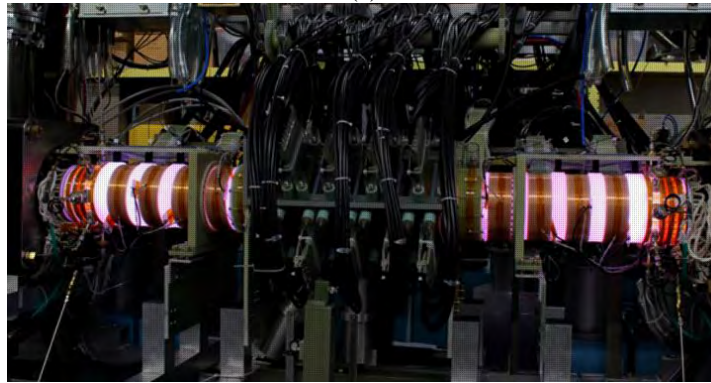
(d)

Fig. 1.6 The most important accomplishments concerning the three different lines of research regarding fusion, namely (a) MCF (JET Tokamak), (b) ICF (National Ignition Facility) and (c, d) MTF (General Fusion and Helion Energy)

1.2.1 Magnetic Confinement: The Tokamak

The Tokamak is the most widely studied magnetic confinement configuration. The term "Tokamak" comes to us from a Russian acronym that stands for "toroidal chamber with magnetic coils". For toroidal plasma confinement, both poloidal and toroidal fields are necessary. The poloidal field is provided by external coils and the plasma current. **Fig. 1.5** shows the basic principles of magnetic confinement in a tokamak.

The movement of a charged particle parallel to the magnetic field is not restricted. Therefore, in order to confine plasma effectively, the field lines should close in themselves and, hence, they form a toroidal geometry. However, just a torus shaped vacuum vessel with a toroidal magnetic field is insufficient to confine the plasma. The curvature of the magnetic field causes electrons and ions to drift to the bottom and top of the torus, respectively, resulting in an electric field. This electric field in its turn leads to an outward drift of all particles and, thus, to a loss of confinement. To neutralize this electric field, particles that drifted to the top of the machine should be brought to the bottom and vice versa. This can be achieved by adding a poloidal component to the magnetic field. In a tokamak configuration the poloidal magnetic field is generated by toroidal plasma current. This plasma current is induced by a transformer, using the plasma as the secondary winding. On top of these poloidal and toroidal field components radial and vertical components are added to the magnetic field by external positioning and shaping coils.

29

1.3 Literature review on the present status of liquid metal research for a fusion reactor

The highest loaded element of a tokamak fusion reactor is its divertor. While the neutron load in the divertor zone is lower than on the first blanket wall, its specific thermal loads are many times higher; their values incorporate flows of high-energy particles carried out of the plasma zone. Thus, high power magnetically confined fusion devices have very high heat and particle loads on the walls that face their plasmas. Handling this heat is a big challenge, in present and future devices, e.g., DEMO. Based on available data from fusion reactors that are in operation, e.g. JET, divertor walls made of tungsten can withstand heat loads up to 20 MW/m^2. Beyond this level the plasma-wall interaction that is generated by such events is seen to cause problems such as erosion, thermal stresses, thermal fatigue and plasma contamination which may irreversibly impair the operation of the reactor.

Designs using realistic materials capable of tolerating such high stationary and especially pulsed heat flows without mechanical damage and sputtering under the influence of particle flows during an extended period of time do not exist [7]. In order to circumvent the above problems liquid metals are considered as alternative plasma facing components (PFCs) [8-10].

The self-cooling and self-annealing properties of flowing liquids increase their life cycle as they interact with the scrape-off-layer of the fusion reactor. The suggested solutions include the following concepts:

- Organization of liquid-metal films quickly flowing along a cooled substrate
- Creation of a "screen" by a liquid-metal flow
- Creation of drops for a liquid-metal screen
- Creation of a screen of dropping solid balls
- Placement of rotating cylinders in the divertor
- Capillary Porous System (CPS)

These ideas seem simple and convincing since they are based on well-known principles of divertor target plate cooling. Nevertheless, it turns out to be difficult to implement them due to the necessity to combine, in one device, a number of new technical approaches that have not been demonstrated separately. Like solid PFCs, the support structure in a liquid surface PFC will be damaged by neutrons, while proper attention to tritium retention, removal and handling is a requirement for any fusion system. Furthermore, it requires the use of diverse constructional materials, various heat-carriers and coolers and a combination of static and dynamic conditions involving instabilities in the working zone. Besides, the flow pattern of liquid metals employed for protection of the divertor region is characterized by the formation of a free surface that is subjected to the electromagnetic field and heat load generated by the plasma. As a consequence, a basic problem persists. Liquid metal magneto-hydrodynamics (MHD) severely constrains solutions that use flowing liquid metals. The related issues have in large part driven the directions for R&D with liquid surface PFCs. Table 1.1 lists confinement devices using liquid surfaces. Moreover, International Symposia on Lithium Applications in Fusion have extensive information on Li R&D [11-14]. Jaworski [15,16] and Nygren and Tabarés [17] have provided reviews of liquid surfaces with an emphasis on Li, as have Lyublinski et al. [18] but with a focus on capillary pore systems. In addition, Coenen

30

summarized considerations for several liquid metals for power exhaust systems in future fusion devices [19]. A more recent paper by Jaworski et al. [20] focused on issues related to flowing Li divertor targets and their integration into NSTX-U.

Table 1.1
Confinement devices using liquid surfaces, [17]

Device	Type	Location
NSTX-U	spherical tokamak	United States
NSTX	spherical tokamak	United States
LTX	tokamak	United States
CDXU	tokamak	United States
DIII-D	tokamak	United States
T-11	spherical tokamak	Russia
T-10	spherical tokamak	Russia
T3-M	spherical tokamak	Russia
TJ-II	stellerator	Spain
RFX-mod	tokamak	Italy
FTU	tokamak	Italy
EAST	tokamak	China
HT-7	tokamak	China
ISSTOK	reverse field pinch	Portugal
KTM	tokamak	Kazakhstan
Aditya	tokamak	India

The basic areas of research on liquid surfaces performed in confinement devices presented in Table 1.1 are briefly described below.

- LTX, the only device with a full liquid Li wall, has extremely encouraging results on confinement [21].
- HT-7 deployed 2 flowing Li modules developed by US researchers plus other ways to expose liquid Li to plasmas. Free Li surfaces produced high Li emission and many shots were conjectured to be disrupted from J×B forces dislodging Li [22].
- NSTX operated with the Liquid Li Divertor (LLD) and coated it using two previously developed LITER Li evaporators. The upgraded NSTX-U is starting operation in 2015–16 [23].
- CDXU is the 1st tokamak with a large area of liquid Li which used heated SS trays as a floor limiter filled from an injector nozzle. Earlier experiments had a mesh-covered rail limiter fed with Li by a tube [24].
- T-3 and T-11 used liquid Ga early in the Russian program. Researchers used flowing Ga limiters, attempted a flowing sheet of Ga, and successful tests in T-3 M compared the impurity influx of a Ga droplet limiter with that from a graphite limiter [25].
- ISTTOK, with a free surface jet of Ga, showed trapping of H and saturation of the effect, but also hydrocarbons and hydroxides in the near surface region [26].
- T-11M and T-10 operated with CPS-LLLs (liquid Li limiters), extracted H and D and Li with cryogenic targets without venting chamber, and collected ~60 mg Li in 200 regular shots. T-15 plans [27].
- FTU had improved plasma performance with a rail type CPS-LLL built in a Russian collaboration with ENEA-Frascati [28].
- HT-7 operation with modular CPS-LLL, developed by Russian researchers, improved the retention of Li on its surface [29].

- TJ-II utilized a CPS-LLL with positive or negative bias and had devoted experiments on recycling, and also exposed Sn-Li [30].
- KTM has an uncooled module. Tests on a CPS module with Na-K confirmed reliable operation over temperature range of 20–200 °C [31].
- Li pellets and Li spray in DIII-D resulted in enhanced confinement correlated with recycling. Motion of liquid Li was observed using the DIII-D DiMES probe [32].
- Researchers at EAST used Li injection for ELM control and various methods to expose liquid Li to the plasma [33].
- Researchers at TJ-II studied the combined effects of Li evaporated onto walls and boronization. Lithitization enabled routine operation using 2 neutral beams, clear transitions to H-mode and doubled confinement times [30].
- Experiments in TJ-II and in ISSTOK also exposed SnLi [34].
- The extensive Russian program on liquid surfaces has included analysis of Li droplet deformation, lab experiments with Ga waterfalls, testing of droplet flow and a flowing Ga sheet, and measuring the sputtering of Ga. R&D in Latvia tested the suppression of splashing in a 1T magnetic field. Li dust injected in T-10 [35].

1.3.1 Critical issues for liquid metals PFCs

The goal is to address the following question: What is the potential of liquid surfaces? The approach is to identify critical issues that need to be solved. To do this, several further questions are posed below, and the answers used to deduce key issues and how the present status of R&D permits an assessment.

Can these provide viable solutions for PFCs for a fusion reactor, or at least for a fusion component test facility? The path forward for Li PFCs may differ from that for other metals or a molten salt. Also, a fusion component test facility must have a high duty factor but could have lower temperatures for the structure than a reactor.

What must a liquid surface PFCs do? Fusion reactor PFCs receive power from the plasma, transfer heat to a coolant that connects to the power conversion system, maintain structural integrity and minimize tritium retention. The plasma configuration and feedback into the plasma from the PFCs must permit sustained confinement and adequate power production in the core plasma. Concepts with full liquid walls (and divertor) have been developed. Systems with a mix of liquid and solid surfaces are also possible.

Surface stability and MHD

The surface of any liquid PFC must remain stable when exposed to the plasma and must accommodate or recover rapidly from conditions that could destabilize the surface, e.g., gross motion that would compromise its function or ejection of droplets. Electrical currents in a PFC can arise from currents in the scrape-off-layer, eddy currents induced by plasma disruptions, or thermionic emission when the surface temperature is high enough. These currents and the Lorentz force from the toroidal field can produce body forces that can be destabilizing.

Rayleigh-Taylor instabilities, which arise when a body force directs a dense material into a less dense material, can promote the ejection of droplets, as can Kelvin Helmholtz instabilities, Jaworski et al. [20]. Reference [41] explains Kelvin Helmholtz instabilities in the ejection of droplets from melted layers of tungsten in tests in the plasma gun QSPA-T. Other papers describe experiments on surface motion of liquids in ASDEX-U [37] and ISSTOK. In particular, Gomes and coworkers at ISSTOK performed extensive

32

studies of Ga jets [26,38,39] with various nozzle sizes and flow rates in preparation for tests in ISSTOK with a Ga jet and a graphite limiter. They noted the minimum time to equilibrate flow increased with the nozzle size and that stability was lost for nozzles with diameter larger than 2.5mm. **Fig. 1.7** is given below, in order to illustrate an image of the phenomena existing in ISSTOK. More specifically, **Fig. 1.7** depicts a sequence of frames showing the evolution of the gallium droplets position when both negative and positive shifts are present [26].
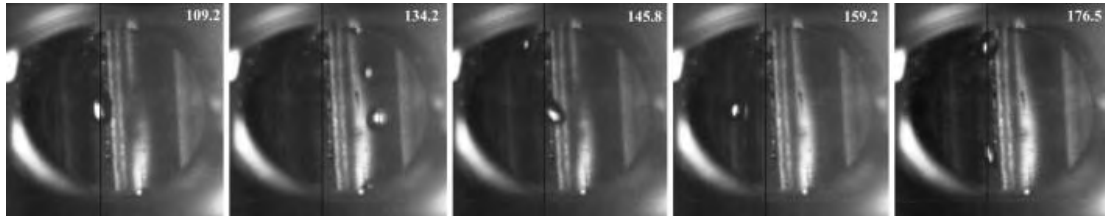
Fig. 1.7 Frames sequence from a movie showing the dynamic behavior of gallium droplets due to the influence of an ISTTOK discharge, [26]

In a nutshell, open films are subject to interfacial and shear instabilities at the speed and thickness required, namely few cms, to exhaust large heat fluxes at DEMO relevant conditions. Besides, liquid metal drops and jets have size on the order of mms which results in their deflection as they interact with the surrounding plasma. Finally, the thickness of the liquid metal film resting on top of the CPS wafer is anticipated to be on the order of μms at near vacuum conditions. Generally speaking, the smaller the thicknesses of the liquid metal arrangement the smaller effect of MHD instabilities are expected.

1.3.2 Protection of tokamak plasma facing components by a Capillary Porous System

The examples above demonstrated the complexity that arises from MHD concerns even in nominally static liquid metal systems. Such concerns in their long history of R&D on liquid metal PFCs led Russian researchers to develop and prefer the CPS as the path forward for liquid surface PFCs.

The CPS concept is based on the use of evaporation cooling for eliminating high thermal loads. Evaporation-condensation devices with liquid metals as the heat carrier are known to be the most effective means of power/energy removal in high temperature facilities.

If the design of the target substrate is done properly, such a way of eliminating thermal loads can provide very good performance, which achieves hundreds of MW/m^2 [40]. To supply the evaporation surface with liquid metal, a porous construction of the target plate with a capillary-pore "pumping" system for the liquid metal is used. The characteristics of the capillary pore system (changing porosity, permeation anisotropy, working surface geometry, etc.) are maintained in broad ranges by using appropriate manufacturing technologies.

The design provides sufficient working pressure in the supply system without applying external pressure by using only capillary force pressure. This system is self-sustaining and self-regulating because the pressure distribution of the liquid-metal coolant in the capillary-pore structure reacts to local changes of the thermal load distribution on its surface.

33

The use of such a technological approach satisfies all of the critical requirements that designers might have when selecting materials and ITER divertor design and construction approaches.

The CPS seems to be the most mature path for liquid surface PFCs and the result of extensive prior and ongoing R&D [41-43]. Excerpts are paraphrased here to acknowledge the continuing contributions from the Russian program.

- Surface tension suppressed splashing of Li splashing, and regenerated the surface during the long experimental campaign [44].
- Erosion of liquid Li from the PFC is a strong function of Li temperature with a rate nearly the same as ion beam sputtering of liquid Li [44].
- Li non-coronal radiation cools the edge plasma, can protect the PFC structure from high power loads in quasi-steady state and from disruptions [45].
- Hydrogen isotopes implanted in liquid Li by the plasma can be recovered at temperatures of 320–500 $^{\circ}$C with the range of Tritium being 400–500 $^{\circ}$C [25].

Lyublinski, Vertkov, Mirnov, Evtikhin and other scientists have summarized the ongoing program. For example, the reference [44] has useful discussions of the reaction of Li with various gases and capillary forces and deployments of Li CPS applications. The more recent reference [17] includes a set of questions and related criteria by which the progress and readiness of liquid surface PFCs are judged.

In the development of liquid surface PFCs, new ideas are emerging and some concepts are being deployed in early trials. The CPS development is more mature, with continuing development and many deployments targeted at resolving specific issues. Studies in plasma confinement devices began with a Li CPS limiter experiments on T-11M in 1998 with the goals of a) testing of how well the CPS stabilized the liquid Li stabilization and b) investigating the mechanisms of Li influx into the plasma chamber. While much of the recent CPS applications are with Li, examples with Sn are also included below.

The CPS is a liquid delivery system with an architecture engineered to stabilize liquid surfaces on PFCs. The capillary forces in a CPS depend on the wetting properties of the liquid and size of the pores in the host structure. These must be matched for the chosen liquid. Capillarity is expected to provide the necessary driving force to replenish the depleted liquid metal/plasma interface, as a result of evaporation, by drawing liquid from a reservoir. Tabarés [46] noted that the pore size for flow in the supply passages is not always the same as that for retaining the liquid on the surface of the PFC, which further complicates modelling of the CPS arrangement.

In 2005–2006, CPS limiters were deployed in the Italian tokamak FTU at Frascati and in the Russian T-10 tokamak [47]. **Fig. 1.8** and **Fig. 1.9** illustrate upgraded versions of the FTU CPS. The original CPS liquid Li limiter (LLL) in FTU successfully delivered Li to host mesh at the plasma-wetted surface (**Fig. 1.10**) even to the point of depleting the Li in the reservoir at the bottom of the module. The LLL was initially vacuum-canned. Its thin SS seal was peeled away under vacuum in the port with the LLL in its retracted position.
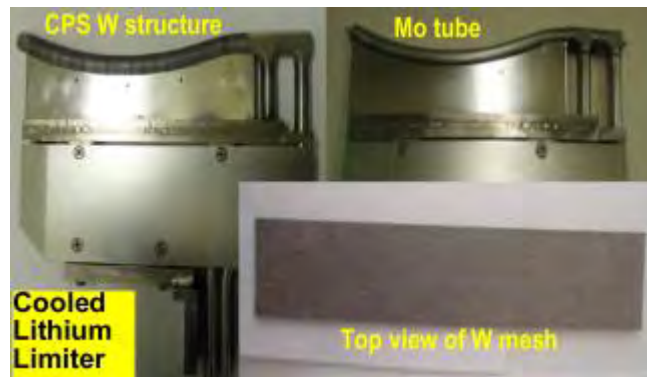
Fig. 1.8 CPS system deployed in the upgraded liquid Li limiter in FTU, [17]

Fig. 1.9 View of complete assembled LLL before installation in FTU, [17]
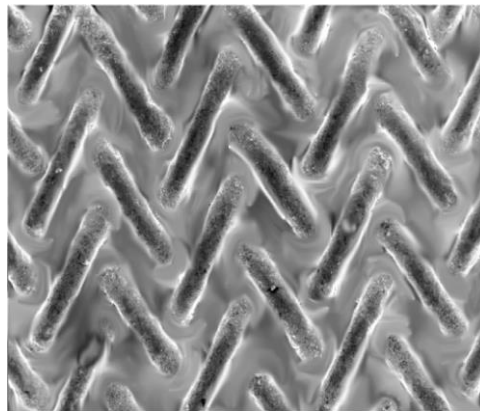
Fig. 1.10 SS mesh wetted by Li as in CPS for first LLL in the Frascati tokamak, [17]

Lyublinski et al. [18] indicated the possibility of PFC protection from the high power load related to cooling of the tokamak boundary plasma by radiation of non-fully stripped lithium ions, an effect supported by experimental results. This approach demonstrated in scheme of closed loops of Li circulation in the tokamak vacuum chamber and realized in a series of design of tokamak in-vessel elements. **Fig. 1.11** depicts a view of targets irradiated in MK-200UG with a) V alloy, b) CPS without Li and c) CPS with Li.

35
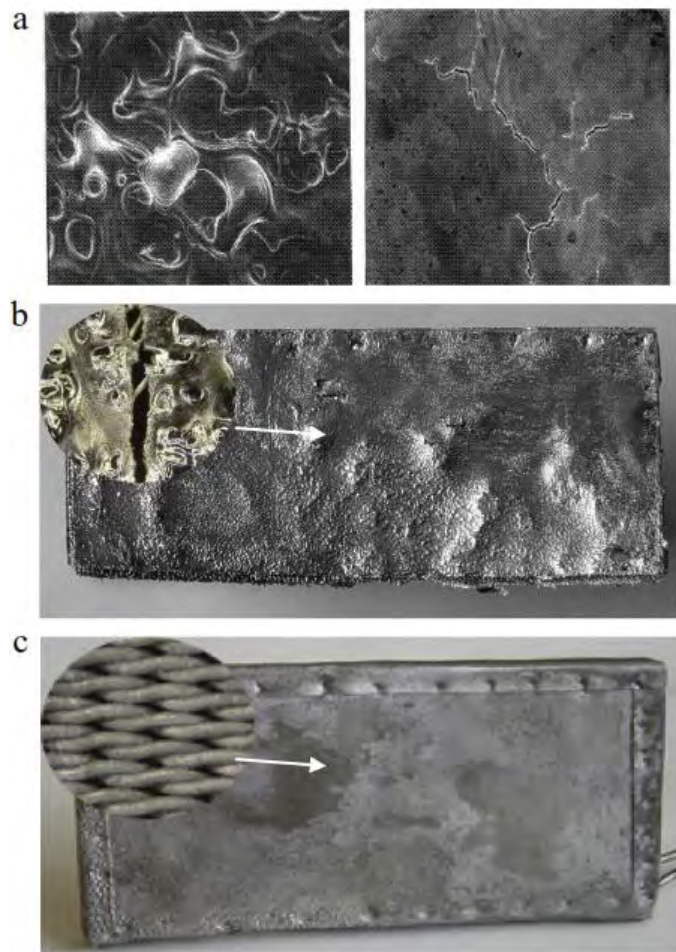
Fig. 1.11 View of targets irradiated in MK-200UG: (a) V alloy after 1 plasma pulse, (b) CPS without Li after 1 plasma pulse, (c) CPS with Li at 250 °C after 17 plasma pulses, [18]

Power exhaust capabilities of CPS

High power density is a design goal for fusion reactors that implies a smaller fusion core and lower capital cost, but also that more power goes into PFCs with a smaller area. Power handling is a challenge.

The highest heat and particle loads flow along magnetic field lines into the divertor. There, flux expansion and the inclined target spread the heat load, and some power in the charged particles converts to radiation. Ions (and electrons) approach the divertor surface at small angles, so protruding edges have unacceptably high heat loads. The presence of hot spots, e.g., protruding diver or tiles, with much higher local heating is a common and well- recognized issue that is exacerbated with higher power density.

Heat fluxes to the first walls are typically lower than the divertor, but we now understand that significant convected power reaches some locations on the first walls. This brings two important changes for the first walls. The first is higher power and particle loads. Second, the hot spot issue well known in divertors now applies also the first walls. Solid close-fitting walls must now have tight requirements for alignment and shaping, a requirement that was not recognized in past design studies [17].

Evaporation and relocating the heat, as with a flowing stream or droplet curtain, are ways liquid surfaces can transfer locally from a heated area. In most cases, and certainly for

36

PFCs with a slow moving liquid surface, the PFC must conduct heat through the liquid and its host structure, and through a portion of the underlying support structure to the primary coolant. The surface temperature depends on the coolant temperature and the temperature gradients in the materials along this path. In this conduction dominated scheme, the upper temperature limit is controlled by the allowable heat flux to the PFC. The thermal conductance in the layer with the host structure and liquid itself is a non-trivial analysis. The recent paper by Coenen [19] has a discussion of the heat removal challenge for liquid surface PFCs.

In the case of a Li PFC, with its relatively high evaporation rate at temperatures of interest for PFCs and without a process that stems the influx of Li, the limits for the surface temperature appear to be rather low. For example, early edge modeling by Rognlien and Rensink [48] to find limits for a Li wall using UEDGE and a simple expression for Li evaporation found very low values and computational issues. Later, with further study, base limits of ~400 °C and ~450 °C for low and high recycling were obtained and ~490 °C in the divertor with better screening. The hope is that vapor shielding may increase the allowable limit for Li. Rates for Sn and Ga are much higher.

Non-coronal discharge and vapor shielding are ways the plasma edge, under some circumstances, can dissipate and transfer power from local areas otherwise subject to overheating. Unless evaporation rates are high, as in those associated with vapor shielding, evaporation itself provides relatively little cooling compared to the incoming power from the plasma [17].

Non-coronal radiation
Historically, the long standing research program in Russia provided the largest body of early experimental work on liquid surfaces for fusion applications and included the introduction of Li into both the T-11M and T-10 tokamaks. In T-11, researchers observed non-coronal radiation in a prolonged circulation of Li ions between the plasma and wall that dissipated almost 80% of the total ohmic heating power to the wall by Li UV radiation [25].

Evaporative cooling, conduction to substructure, and physical relocation in fast-flowing systems, including droplets, are all processes that remove heat from where it was deposited. Evaporation and ionization are important in determining the limits for Sn or Ga as moderate-Z plasma impurities. And the main issue is how to maintain operation with a tolerable amount in the plasma edge.

For liquid Li PFCs, non-coronal radiation (and vapor shielding) in the plasma edge can improve plasma performance and enhance heat transfer. The objective in exploiting Li non-coronal radiation (Li^+ or Li^{2+} not Li^{3+}) is to cool the boundary plasma and protect the PFC during quasi-steady state and disruption events. Here the issue is whether robust operational regimes are possible to exploit these processes.

Fig. 1.12 shows an example by Mirnov and collaborators [25,45] proposing sets of limiters that separately emit and collect Li. Li non-coronal radiation cools the plasma edge and protects the PFC itself from high transient power loads. The objective is continuous circulation of Li^+ and Li^{++} between the plasma and PFC that produces much enhanced power dissipation through non-coronal radiation.

37

More specifically, the cooled horizontal lithium rod touches the plasma column. The plasma contact area of the limiter (hot spot) is the main source of the Li atom influx (Li emitter) into plasma. Sputtering and evaporated Li atoms are ionized and excited by electron impact and are diffused as ions (Li^+ or Li^{2+} not Li^{3+}) into the SOL and hot plasma column. Some parts of the outward ion flux can go back to the cold ends of the Li rod and collect there (Li collector). The capillary forces return this amount of lithium to the hot spot again. As a result the Li ions travelling in a SOL can recycle. If the travelling (or life) time τ of lithium ions is lower compared with their transient time to stationary ionized coronal balance, the total lithium radiation can significantly surpass the coronal limit and play a role as the main coolant of the plasma SOL. In this model the main radiated power flux goes to the broad area of the tokamak vessel surface (first wall) and spreads the limiter heat load. Secondary limiters should work as additional collectors of lithium atoms and as a secondary emitter, which can multiply the lithium non-coronal radiation due to a decrease in lithium confinement time τ. In the particular case of one Li-limiter (Li emitter) the vessel wall plays the role of the lithium and hydrogen flux collector (first wall lithization).
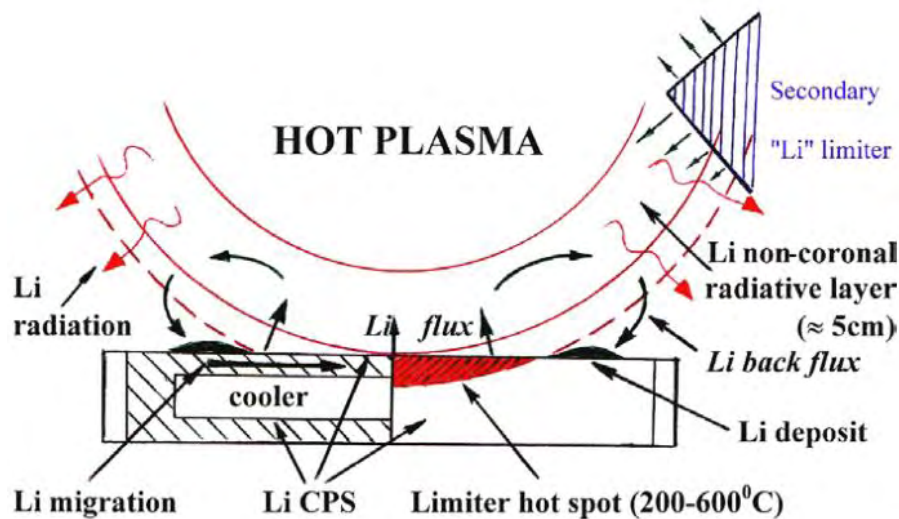
Fig. 1.12 A principal scheme of lithium-limiter interaction with a tokamak plasma, [44]

Vapor shielding
Vapor shielding is a general term not specific to Li. Modelers of high power disruptions on solid surfaces (e.g., W and Be in ITER) described vapor shielding over melt layers as the initial evaporation producing a dense cloud of neutrals that interact with the incoming plasma and reduced the erosion of the surface [49].

The formation of Li vapor-clouds has some rich underlying physics in its PSI. Researchers at FTU noted a highly radiating Li cloud over the CPS liquid Li limiter during its operation in 2006-2007.

Finally, in a recent experimental investigation, utilized in DIFFER [50], a steady-state high-flux H or He plasma beam was balanced against the pressure of a Sn vapor cloud for the first time, resulting in a self-regulated heat flux intensity near the liquid surface. The plasma heat flux impinging on the target was found to be mitigated, as heat was partially dissipated by volumetric processes in the vapor cloud rather than wholly by surface effects.

1.3.3 Lithium CPS

The work for the ITER reactor showed that conventional design solutions of divertor and divertor plates for plasma burning practically in steady state in a tokamak of such a scale, meet with serious difficulties. At the same time, high Z materials were rejected in classical tokamaks because of plasma contamination by dust resulting from limiter erosion in MHD-unstable discharge conditions. There is a principal possibility to move lower in the low Z range, namely, to develop a lithium divertor where dust and contamination problems would be solved naturally.

It is known that the most efficient means of heat transfer in high temperature machines for energy conversion are evaporation–condensation elements with liquid metal as a coolant. This method of heat removal provides the highest performance with an appropriate choice of the working fluid; for lithium it is hundreds of MWm^{-2} at temperatures below the boiling point. The second efficient mechanism to decrease local heat loads is lithium radiation. While puffing of (heavy) gases is envisaged in the gas target concept, in a lithium divertor such a target is formed naturally by appropriate temperature control. Thus, energy is redistributed over a larger area by radiation, and the heat flux to the divertor plate is decreased. Finally, power removal from the divertor is carried out by thermal conductivity and convective effects to cooling loops and further to energy conversion system without overheating.

Lithium makes the proposed divertor concept highly efficient and it has a number of principally new features. The concept is feasible for the following reasons, as described in [45]:

- Lithium has a low Z that determines its minimal effect on the main plasma in comparison with any other materials.
- High latent heat of lithium evaporation, radiation and ionization of lithium vapour lead to redistribution of the important part of incoming energy, thus decreasing power load density on the divertor.
- Lithium fits well the reactor design with self-cooled lithium–lithium blanket; service systems could be used both for the blanket and the divertor; tritium extraction technology can be the same for both components; the same structure material can be used in those systems - low activated vanadium alloys that are well compatible with lithium at temperatures below 700˚C.
- Helium and other noble gases do not interact with lithium in ordinary conditions.
- For low melting metals, lithium has the best physical and thermal properties for application in a liquid metal reactor.

On the other hand, the use of liquid lithium causes some other problems as presented in [42]:

- Mechanical stability of liquid lithium films.
- Ion sputtering and evaporation (thermal emission) of lithium.
- Accumulation of lithium in plasma column.
- Lithium deposition on the surface of vacuum chamber.

Research and development on plasma surface interactions and liquid surface plasma facing components has included liquid gallium (Ga), tin (Sn), lithium (Li) and Sn-Li. The use of liquid tin as both a first wall PFC and in the divertor looks promising so far from

39

an erosion/redeposition and plasma contamination standpoint. The primary advantage of liquid Sn over other liquid metals is the tremendous drop in evaporative flux and the subsequent increase in the evaporation-limited.

40

Chapter 2: Basic aspects of wetting phenomena

In this chapter, a brief description is given concerning the theory of the action of surface forces, i.e. forces needed to account for phenomena occurring near surfaces, very thin layers, corners, borders, contact lines, etc. All forces do originate at the microscopic level, but the phenomenological, macroscopic manifestations of those forces are accentuated. In particular, the role of the so-called disjoining pressure is emphasized, which is considered to be the manifestation of the surface forces. The disjoining pressure acts in the vicinity of the three-phase contact line, and its action becomes dominant as a liquid profile approaches a solid substrate.

2.1 Wetting and Young's equation

Droplets of different liquids deposited on identical solid substrates behave differently. For example, the mercury layer immediately forms a droplet on a glass surface, which is a spherical cap with the contact angle bigger than 90° (Nonwetting case: **Fig. 2.1**). However, it is easy to make an oil layer on the same glass surface; for this purpose an oil droplet can be deposited on the same glass substrate, and it will spread out completely. In this case, the contact angle decreases with time down to a zero value (Complete wetting case: **Fig. 2.2**). Finally, a water droplet deposited on the same glass substrate spreads out only partially down to some contact angle, θ, which is in between 0 and 90° (Partial wetting case: **Fig. 2.3**). Thus, an aqueous droplet on a glass surface behaves in a way that is intermediate between the behavior of the mercury and oil. In broader terms, complete wetting, partial wetting, and nonwetting behavior are determined by the nature of both the liquid and the solid substrate.

Fig. 2.1 Nonwetting case: contact angle is bigger than 90°
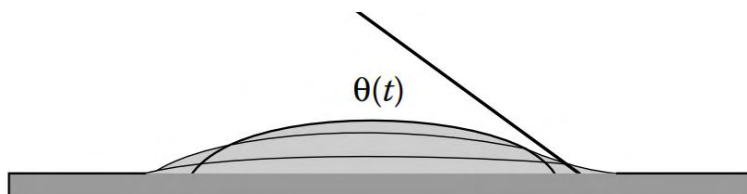
Fig. 2.2 Complete wetting case: the contact angle decreases with time down to a zero value

41
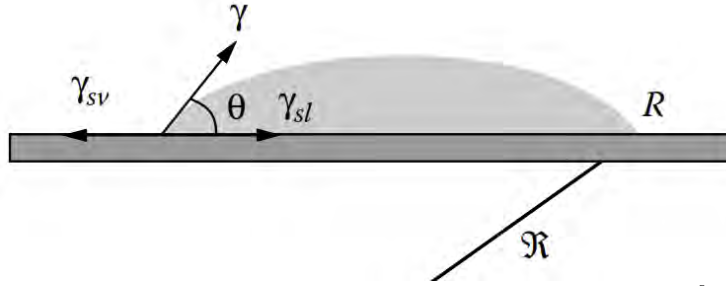
Fig. 2.3 Partial wetting case: contact angle is smaller than 90°

Liquid Li partially wets the solid substrate as will be discussed later in the PhD Thesis. As a consequence, let us consider the picture presented in **Fig. 2.3**. In the processes of wetting three phases (air, liquid and solid) meet along a line, which is referred to as a three-phase contact line. Consideration of forces in the tangential direction at the three-phase contact line results in the well-known Young's equation, Eq. 2.1, which connects three interfacial tensions, γ_{sl}, γ_{sv} and γ with the value of the equilibrium contact angle, θ, where γ_{sl}, γ_{sv} and γ stand for solid–liquid, solid–vapor, and liquid–vapor interfacial tensions, respectively:

$$\cos\theta = (\gamma_{sv} - \gamma_{sl}) / \gamma \tag{2.1}$$

According to **Fig. 2.2**, the complete wetting case corresponds to the case when all forces cannot be compensated in the tangential direction at any contact angle, that is, if $\gamma_{sv} > \gamma_{sl} + \gamma$. Partial wetting case, according to Eq. 1.1, corresponds to $0 < \cos\theta < 1$. That is, Eq. 2.1 reduces complete wettability, partial wettability, and nonwettability cases to the determination of the three aforementioned interfacial tensions.

At equilibrium, the following three equilibrium considerations should be held:

1. Liquid in the droplet must be in equilibrium with its own vapor.
2. Liquid in the droplet must be in equilibrium with the solid.
3. Vapor must be in equilibrium with the solid substrate.

The first requirement in the list above results in the equality of chemical potentials of the liquid molecules in vapor and inside the droplet. This results that the droplets can be at equilibrium only with oversaturated vapor.

As far as the second requirement is concerned, it is unavoidable as the liquid molecule adsorption on the solid substrate and the presence of liquid molecules on the surface changes the initial surface tension. This means that the liquid molecules from the vapor must be adsorbed on the solid substrate outside the liquid droplet under consideration. The latter consideration results in the formation of an adsorption liquid film on the surface as can be depicted in **Fig. 2.4a.**

Let us consider the third requirement. In **Fig. 2.4a**, an equilibrium liquid droplet is presented in contact with an equilibrium-adsorbed liquid film on the solid surface. However, the situation presented in **Fig. 2.4a** is not possible since such sharp transition from the liquid droplet to the liquid film is impossible. On the line shown by the arrow, the capillary pressure will be infinite. Hence, it should be a smooth transition from the flat equilibrium liquid film on the solid surfaces to the spherical droplet, as shown in **Fig.**

42

2.4b, where this smooth transition is shown. The arrow in **Fig. 2.4b** shows the point to the right where the liquid profile is concave and to the left where the profile is convex.
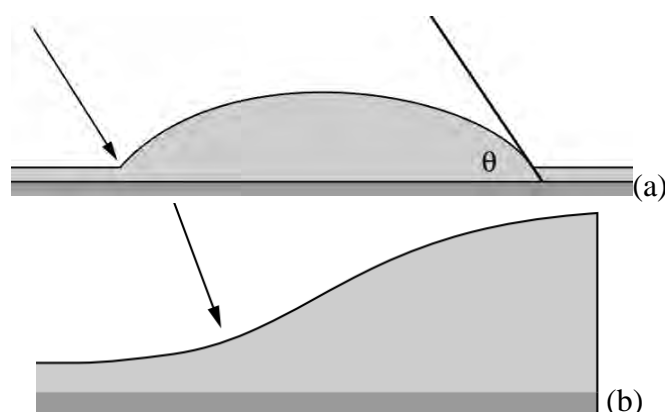
Fig. 2.4 (a) Cross section of an equilibrium liquid droplet (at oversaturation) in contact with an equilibrium-adsorbed liquid film on the solid substrate and (b) Transition zone from the flat equilibrium liquid film on a solid surface to the liquid droplet

In the case of partial wetting, as have already been seen, liquid droplets cannot be in equilibrium with a bare solid surface. They should always be at equilibrium with an adsorption layer of the liquid molecules on the solid substrate in front of the droplet on the bare solid surface. If the liquid is volatile, then this layer is created by means of evaporation and adsorption. However, if the liquid is nonvolatile, the same layer should be created by means of flow from the droplet edge onto the solid substrate. As a result, at equilibrium the solid substrate is covered by an equilibrium liquid layer of thickness, h. The thickness of the equilibrium liquid film, h, is determined by the potential of action of some special forces, referred to as surface forces. The characteristic time scale of this process is hours, because it is determined by the flow in the thinnest part in the vicinity of the apparent three-phase contact line, where the viscose resistance is very high.

43

2.2 Surface forces and disjoining pressure

It looks like the profile presented in **Fig. 2.4b** cannot be in equilibrium because capillary pressure should change the sign inside the transition zone, and it is in contradiction with the requirement of the constancy of the capillary pressure everywhere inside the droplet. Some additional forces are missing. The mentioned problem was under consideration by a number of scientists for more than a century. Their efforts resulted in considerable reconsideration of the nature of wetting phenomena and the introduction of surface phenomena, which are determined by the special forces acting in thin liquid films or layers in the vicinity of the apparent three-phase contact line. They determine the stability and behavior of colloidal suspensions and emulsions. The theory which was developed is widely referred to as the DLVO theory [51] after the names of the four scientists: Derjaguin, Landau, Vervey, and Overbeek.

It has been established that the range of action of surface forces is usually of the order of 0.1 μm [51]. As Middleman [52] and, in more detail, Starov et al. [53] analyzed, in the vicinity of a three-phase contact line, the thickness of the liquid film becomes very thin tending to zero. This thickness means that close to the three-phase contact line, surface forces come into play and their influence cannot be ignored. These forces can depend on the thickness, h, in a very peculiar way. A manifestation of the action of surface forces is the disjoining pressure [53]. Note that this term is a bit misleading, because the mentioned force can be both disjoining (repulsion between surfaces) and conjoining (attraction between surfaces).

Let us consider the liquid–air interface of **Fig. 2.5**. It is obvious that the physical properties of the very first layer on the interface are substantially different from the properties of the liquid (in bulk) far from the interface. It is understandable that the physical properties do not change by jumping from the very first layer on the interface to the subsequent layers, but the change proceeds in a continuous way. This continuous change results in the formation of a special layer, which is referred to as the boundary layer, where all properties differ from corresponding bulk properties. Such boundary layers exist in proximity to any interface: solid–liquid, solid–air, or liquid–air. In the vicinity of the apparent three-phase contact line, these boundary layers overlap. The overlapping of boundary layers is the physical phenomenon that results in existence of surface forces. The surface force per unit area has a dimension of pressure and is referred to as disjoining pressure, as we have already mentioned in the preceding section. Let the thickness of the boundary layers be δ. In the vicinity of the three-phase contact line, the thickness of a droplet, h, is small enough, that is, h ~ δ, and hence boundary layers overlap, **Fig. 2.5**, which results in the creation of disjoining pressure. The above mentioned characteristic scale, δ, determines the characteristic thickness where the disjoining pressure acts. In **Fig. 2.5** region 1 represents the bulk liquid and region 2 the boundary layer in the vicinity liquid–air and liquid–solid interfaces where, in both cases, boundary layers do not overlap. In region 3 the boundary layers overlap while region 4 represents a flat thin equilibrium film. The latter two are the regions where disjoining pressure acts. Thus, the main conclusion is that the pressure in thin layers close to the three-phase contact line is different from the pressure in the bulk liquid, and it depends on the thickness of the layer, h, and also varies with the thickness, h.

44
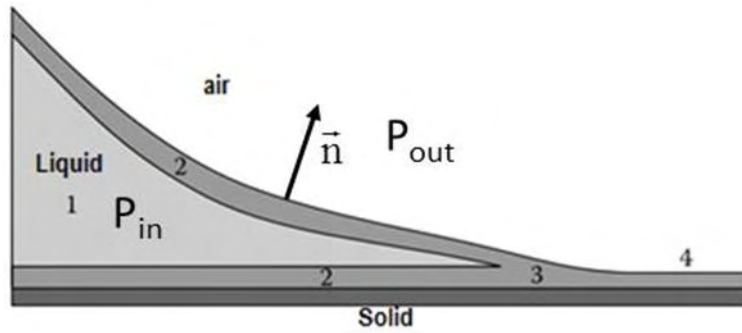
Fig. 2.5 The liquid profile in the vicinity of the apparent three-phase contact line

Fig. 2.5 will aid our definition of terms relevant to the forces acting on and within ultrathin films. When a planar liquid film intervenes between a solid and a vapor, there is a free energy per unit of interfacial surface area, the magnitude of which is a sum of contributions from the solid-liquid surface tension, γ_{sl}, and the liquid-vapor surface tension, γ. We may write this in the form:

$$F = \gamma_{sl} + \gamma \tag{2.2}$$

Since the energies involved are those of the interfaces, the free energy F does not depend upon the film thickness itself. This is a macroscopic view. It treats the boundaries of the liquid film as mathematical interfaces. In fact, as it has already been mentioned these boundaries separate physical interphases within which the liquid molecules exhibit variations in density and orientation as one moves from each interface into the liquid phase. If the film thickness h is small enough, these interphases overlap in the sense that there can be molecular interactions between the molecules in these interphases.

2.2.1 Molecular Component
Calculation of the molecular contribution to disjoining pressure, Π, has been approached in two ways; from the approximation of interactions as a pairwise additive, and from a field theory of many-body interactions in condensed matter [53].

In ultra-thin films, F can be a function of the film thickness, and we can define a contribution to the free energy due to these molecular interactions by adding a term to Eq. 2.2:

$$F = \gamma_{sl} + \gamma + W(h) \tag{2.3}$$

The form taken by the function W depends upon the nature of the liquid. The simpler and, historically, earlier approach followed a theory based on summing individual London–van der Waals interactions between molecules pair-by-pair, undertaken by Hamaker [51]. One of the commonest representations of the function W is:

$$W(h) = \frac{A}{12\pi h^2} \tag{2.4}$$

The constant A is the so-called Hamaker constant, and it depends upon the properties of the three phases shown in **Fig. 2.5**. The constant A can be either positive indicating a purely repulsive potential or negative, thus, indicating a purely attractive potential. A

45

detailed discussion of the various types of molecular interactions of interest is given by Teletzke et al. [54].

The corresponding disjoining pressure, Π, can be calculated from:

$$\Pi(h) = -\frac{dW(h)}{dh} = \frac{A}{6\pi h^3} \tag{2.5}$$

The potential W is the free energy of a film of thickness h relative to that of the bulk liquid on that surface, that is, relative to that of a very thick film such that $\Pi \rightarrow 0$. For films that satisfy such an expression, and for A > 0, Π increases as the film thickness grows small. This corresponds to an increase in the free energy, and so very thin films (i.e., of nearly atomic dimensions) of this liquid are energetically disfavored. Thus, van der Waals forces could support a finite film thickness under conditions that classical continuum physics would not permit.

2.2.2 Other components of the disjoining pressure

The overlapping of the boundary layers results in the existence of surface forces originated not only from the intermolecular interactions but from other reasons as well.

The electrostatic component of the disjoining pressure can be explained as follows. Let us examine two charged surfaces (not necessarily of the same nature) as illustrated in **Fig. 2.6**. The surfaces are assumed to have equal charges or opposite charges, i.e., there are electrical double layers near each of them. The sign of the charge of the diffusive part of each electrical double layer is opposite to the sign of the charge of the corresponding surface. If the width of clearance between surfaces is h >> R_d, where R_d stands for the Debye length, the electrical double layers of surfaces do not overlap, **Fig. 2.6a**, and there is no electrostatic interaction of surfaces. However, if the thickness of the clearance, h, is comparable with the thickness of the electrical double layer, then electrical double layers overlap, **Fig. 2.6b**, and this results in an interaction between the surfaces. In **Fig. 2.6** ζ_1 and ζ_2 represent the electrical potentials of the charged surfaces.

If the surfaces are equally charged, their diffusive layers are equally charged as well, i.e., the repulsion appears as a result of their overlapping (the electrostatic component of the disjoining pressure, Π_e, is positive in this case). If the surfaces have opposite charges, an attraction would ensue as a result of the overlapping of opposite charges (The electrostatic component of the disjoining pressure, Π_e, is negative in this case). There are a number of approximate expressions for the electrostatic component of the disjoining pressure [53] which are beyond the scope of this Thesis.

46
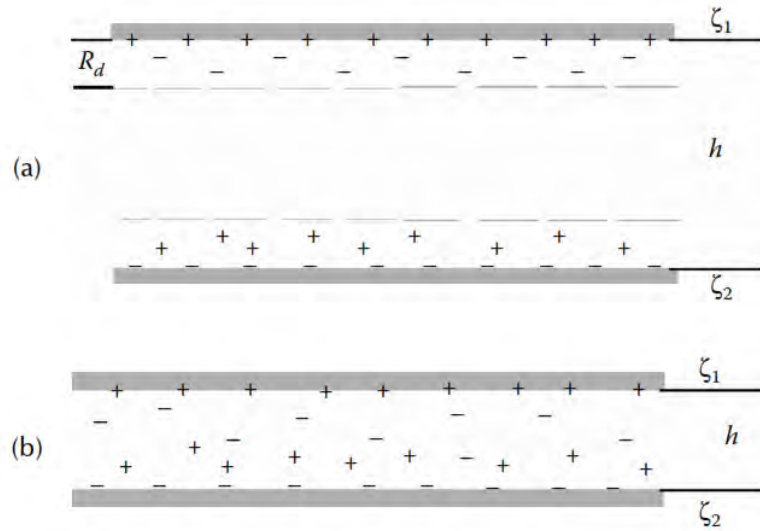
Fig. 2.6 (a) The electrical double layers of surfaces do not overlap (no electrostatic interaction of surfaces) and (b) The electrical double layers of surfaces overlap (electrostatic interaction of surfaces)

As a reminder, the layer, where the concentration of cations and anions differ from their bulk values, is referred to as a diffusive part of the electrical double layer. The characteristic thickness of the diffusive part of electrical double layer is the Debye length, R_d. The characteristic value of the Debye length is

$$R_d = \frac{3 \cdot 10^{-8}}{\sqrt{C}} \, cm \tag{2.6}$$

where C is the electrolyte concentration.

The theory for the calculation of the disjoining pressure based on the two indicated components, i.e., molecular and electrostatic is referred to as the DLVO theory. According to the DLVO theory, the total disjoining pressure is the sum of the two components. The DLVO theory made possible the explanation of a range of experimental data on the stability of colloidal suspensions/emulsions as well as the static and the kinetics of wetting. However, it has been understood later that only these two components are insufficient for explaining the phenomena in thin liquid films, layers and in colloidal dispersions. There is a requirement of a third important component of disjoining pressure, which becomes equally important in aqueous electrolyte solutions.

This component of the disjoining pressure is caused by the orientation of water molecules in a vicinity of aqueous solution–solid interface or aqueous solution–air interface. If two interfaces with hydration layers are close to each other, then at a close separation, comparable with the thickness of the hydration layer, these surfaces "feel each other," that is, hydration layers overlap, **Fig. 2.7**. This overlapping results either in attraction or repulsion of these two surfaces. This is the structural component of the disjoining pressure for which, until now, there is no firm theoretical background [53]. There is only a semi-empirical expression which gives the dependence of the structural component of disjoining pressure on the thickness of the liquid film:

$$\Pi_s(h) = K \cdot e^{-\lambda h} \tag{2.7}$$

47

where K and λ are constants. There is a clear physical meaning of the parameter $1/\lambda$, which is the correlation length of water molecules in aqueous solutions. This parameter further gives $1/\lambda \sim 10$–15 Å, which is the characteristic thickness of the hydration layer. However, we are still far from a complete understanding of the pre-exponential factor K, which can be extracted on the current stage only from experimental measurements of the disjoining pressure.

Currently, it is assumed, as referred in [53], that the disjoining pressure of thin aqueous films is equal to the sum of the three components:

$$\Pi(h) = \Pi_m(h) + \Pi_e(h) + \Pi_s(h) \qquad (2.8)$$

where Π_m, Π_e and Π_s represent the molecular, the electrostatic and the structural components of the disjoining pressure, respectively.
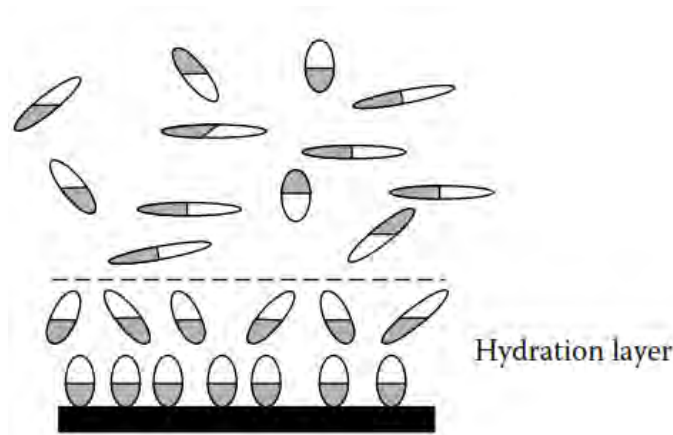
Fig. 2.7 Formation of a hydration layer of water dipoles in the vicinity of a negatively charged interface. The darker part of water dipoles is positively charged, whereas the lighter part is negatively charged, [53]

Apart from DLVO theory and the more general form described via Eq. 2.8, other forms of the micro-scale liquid-solid interaction potential have been also proposed such as the modified embedded-atom potential [55] and N-body potential [56].

2.2.3 Disjoining pressure terms used in the current PhD dissertation
For the purpose of the PhD dissertation only the aforementioned intermolecular interactions and the forces originated from overlapping of the electrical double layers were assembled in a disjoining pressure term. Two different simplified kinds of potentials were investigated, namely, a purely repulsive potential and a long range attractive short range repulsive potential.

Purely repulsive potential
As far as the purely repulsive potential is concerned, it is described via Eq. 2.9:

$$W = \frac{A}{12\pi\delta^2} \qquad (2.9)$$

Besides, only positive values of the Hamaker constant were selected. As a consequence, only repulsion between the liquid and solid interfaces exists, if the thickness of the boundary layers is less than a critical value.

48

Long range attractive short range repulsive potential

The idea is to use a Lennard–Jones type potential as a simple way to approximate strong repulsion at short distances between the liquid and the solid phases, and attraction at intermediate distances [57-62]. The action of the potential is taken into account only along the interface and its range is small compared to both droplet radius and the scale of solid structures.

Thus, micro-scale liquid-solid interactions result in a disjoining pressure for the purpose of stabilizing an intermediate thin layer between the liquid and solid phases. The aforementioned potential is given by the following equation:

$$W = W_{,0}\left[\left(\frac{\delta_A}{\delta}\right)^4 - 2\left(\frac{\delta_A}{\delta}\right)^2\right]$$

(2.10)

Eq. 2.10 provides a standard form of such an interaction potential [57,58] with W_0 signifying the wetting parameter, which is directly related with the solid wettability (an increase of W_0 indicates stronger liquid-solid interaction) and δ_A denoting a characteristic length scale for which the energy is minimized and the interaction force vanishes. Constants 4 and 2, were selected so that the disjoining pressure Π is positive at distances $\delta < \delta_A$, indicating repulsion, and negative at distances δ from the substrate that are larger than the characteristic scale δ_A, indicating attraction. The constants 4 and 2 are typical selections that can be modified based on the nature of the interacting materials. For relatively small δ, Eq. 2.10 models the overlapping of the electrical double layers while it models the van der Waals interactions for relatively large δ. The interaction potential W is not affected by displacements parallel to the substrate and becomes negligibly small at distances that are significantly larger than δ_A.

2.3 Augmented Young-Laplace equation

The usual Young-Laplace equation, which relates the pressure difference to the shape of the interface, is given by:

$$\Delta p = P_{in} - P_{out} = \gamma 2 k_m = \gamma \nabla_s \cdot \mathbf{n} = \gamma \left(\frac{1}{R_1} + \frac{1}{R_2} \right) \tag{2.11}$$

where Δp is the pressure gradient across the fluid-gas interface, γ is the surface tension, $\mathbf{n}$ is the unit normal vector pointing out of the surface, k_m is the mean curvature, in the manner shown in **Fig. 2.5**, while R_1 and R_2 signify the principal radii of curvature.

In the absence of an external field force, the normal force balance, which is described by Eq. 2.11, is augmented with microscale interactions between the solid and the liquid phases using a disjoining pressure term, Π:

$$P_{in} - P_{out} + \Pi = (\gamma + W_0) \left(\frac{1}{R_1} + \frac{1}{R_2} \right), \qquad \Pi \equiv -\frac{\partial W}{\partial n} \tag{2.12}$$

where the disjoining pressure terms, which were used in the present study, have already been mentioned in subsection 2.2.3. It should be stressed that the disjoining pressure acts so that it minimizes energy due to interaction between the liquid and substrate.

50

2.4 Wetting properties of liquid lithium on several fusion relevant materials

When implementing a Capillary Porous System, it should be guaranteed that the CPS is actually wetted by the lithium. The experiments, conducted in Illinois by Filfis et al. [63], investigated the wetting behavior of liquid lithium on several fusion relevant surfaces, namely stainless steel, Tungsten, Molybdenum, TZM (99.4% Mo, 0.5% Ti, 0.08% Zr), and Tantalum.

Lithium droplets were injected via a lithium injector onto the material to be tested. The lithium injector consisted of a reservoir, tube and nozzle. To inject lithium, lithium is placed in the reservoir, the chamber is pumped to vacuum, the injector is heated past the melting point of the lithium and a pressure of Argon is applied to the backside of the lithium reservoir, forcing it down the tube and out the nozzle. The material to be investigated is placed on a moveable stainless steel stage, actuated by a stainless steel rod welded to the stage which passes through an Ultra-Torr vacuum feedthrough. The temperature of the stage is variable and can be adjusted via a plate heater situated below the stage. A photo and schematic of the experimental setup can be seen in **Figs. 2.8a** and **2.8b**, respectively. The procedure utilized was to place a drop, record images of the droplet, and heat the sample while taking still frames at various temperatures. Though the oxidation rate is suppressed by the vacuum, it is still significant at the temperatures investigated. To combat this, at set intervals, the stage was moved and a new droplet was placed to ensure that the surface of the lithium would be fresh. A diagram of this process is shown in **Figs 2.9**. The still frames were then analyzed to determine the contact angle. This was done via a program which employed image processing. Thus, when a droplet is placed, the contact angle is measured optically and registered in a plot such as this illustrated in **Fig. 2.10**. The surface is considered wetted when the contact angle is below 90°. As can be gleaned from the latter figure there is a distinct drop in the contact angle, or increase in substrate wettability, with rising temperature. This effect warrants closer attention to the possibility for Marangoni convection to arise at more realistic conditions of operation of the CPS, [63].

(a)

51

(b)
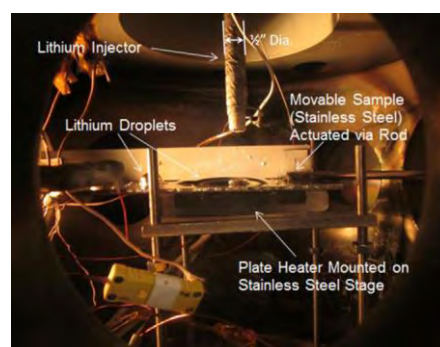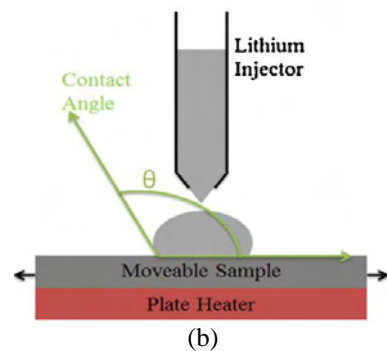
Fig. 2.8 (a) Photo and (b) schematic of experimental setup, [63]
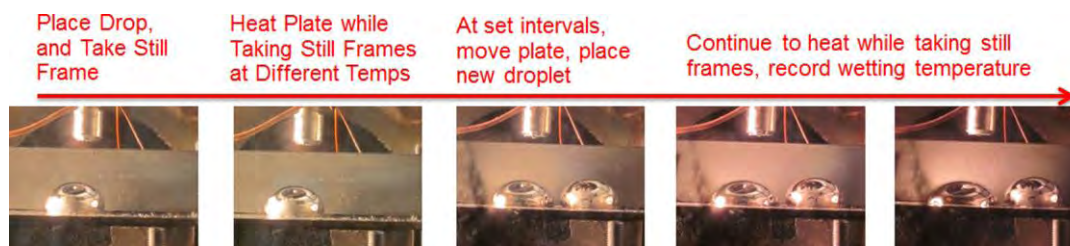
Fig. 2.9 Experimental procedure, [63]
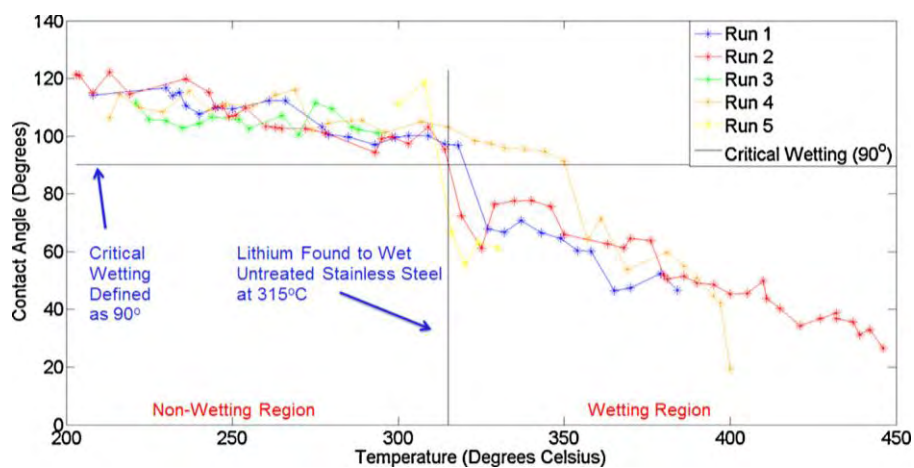
Fig. 2.10 Contact angle of lithium on stainless steel, [63]

Chapter 3: Deflection of a liquid metal jet/drop in a tokamak environment

In this chapter, the steady flow of a liquid metal jet is modelled inside an electromagnetic field in the presence of inertia and capillary forces. Due to the jet break-up as a capillary instability, also the trajectory of the ensuing droplets is modelled in the presence of Lorentz forces. The aforementioned proof of principle studies were performed in reference to experimental observations of jet and drop, deflection because of jxB effects in the ISTTOK tokamak.

3.1 Introduction

As analyzed in detail in the first chapter, in large size tokamaks plasma facing components (PFC) are going to be submitted to high power loads that could even reach the GW/m^2 range during off-normal events in the divertor region. The free surface plasma facing components, which have initially been proposed by Christofilos [8], offer the potential to solve the lifetime issues limiting current solid surface designs by eliminating the problems of erosion and thermal stresses accompanying solid surfaces.

The concept of employing a jet or a drop curtain was among the first to be investigated in order to assist power exhaust from fusion reactors. The drop motion was employed as a means to minimize ponderomotive forces arising due to spatial and time variations of the electric field. Moreover, experimental studies focusing on the magnetic field induction effect [64] showed that even a mild intensity magnetic field could suppress spraying of the liquid metal flow. A representative drop curtain configuration is that of T3-M which was tested with a gallium alloy [65], with encouraging preliminary results in terms of plasma contamination. However, especially when a liquid metal sheet was employed in a plasma environment, the reactor's chamber walls were sprayed by small drops.

The interaction of free flying, fully formed liquid gallium jets with the plasma was studied in ISTTOK tokamak [26,38,39,66], in Portugal. These experiments indicated that gallium not only has high heat removal capacity, but it has negligible effect on plasma operation as well. Beyond a certain length, the jet decomposes into droplets due to Rayleigh instability [67,68]. Once plasma was turned on jet break-up was seen to be postponed over a longer distance, possibly as a result of magnetic braking and, more importantly, the emerging drops were deflected from their original trajectory as a result of their interaction with the surrounding plasma. The deflection increased with increasing magnetic field intensity and drops were observed to hit the collector walls. Several interpretations of this effect were considered in relevance to (a) the mechanical stress on the injector due to chamber compression, which was ruled out, (b) the shift due to magnetic induction and the 3-D magnetic field gradient along the jet length which was also ruled out and (c) the plasma kinetic pressure change along the jet width which was also negligible. Consequently, the interaction between electric currents generated along the advancing jet, in response to electric potential gradients within different plasma regions, and the toroidal magnetic field, identified as jxB effect in the literature, seems to

be the most plausible explanation for the observed deflection of both the jet and drop considerations.

Finally, the results obtained in this study corroborated the belief that employment of liquid metal drops/jets cannot be regarded as an optimal alternative plasma facing component mainly due to their strong deflection as they interact with the surrounding plasma, see also [115].

3.2 Brief description of the liquid metal loop experimental setup and operating conditions in ISTTOK

ISTTOK is a small size tokamak (major radius R = 0.46 m and minor radius a = 0.085 m), with typical plasma parameters: toroidal magnetic field B_t = 0.45 T, electron temperature at the center $T_e(0)$ = 150 eV, center chord-average electron density $n_e(0)$ = $5 \times 10^{18} m^{-3}$, plasma current $I_p \sim$ 6 kA and loop voltage $V_p \sim$ 3 V. The ohmic power deposition in the plasma is within the 9-18 kW range. This feature can be taken as a benefit, since it allows a controlled power deposition in jets and subsequently controlled gallium evaporation. **Fig. 3.1** presents a schematic of the liquid metal loop that has been installed in ISTTOK to perform the injection of liquid gallium jets at the plasma edge. The design of the setup had to obey to some restrictions, due to gallium specific physical properties and compatibility with tokamak operation which were described in [38].

The most critical issue for tokamak operation is to avoid currents in the jet that would lead to perturbation owing to Lorentz forces. The entire injector part of the setup was designed to float at the plasma potential, while the isolation from tokamak vessel and other grounds is ensured by ceramic isolators located at suitable places. Due to its high density, gallium flows have typically high Weber number (We = $\rho u^2 d/\gamma$, where ρ is the fluid density, u the flow velocity, d a characteristic length and γ is the surface tension). One of the consequences of this effect is the reflection of gallium droplets scattered from the bottom of the collector. This effect can be seen from movies like the one depicted in **Figs. 3.2** and **3.3**.

Since the jet crosses plasma regions with different electric potentials and gallium is a good electrical conductor, a net current will be generated along the jet with the plasma acting as an electron source. The interaction of this current with the toroidal magnetic field provides a force along the radial direction that is believed to explain the observed shift [38,115].
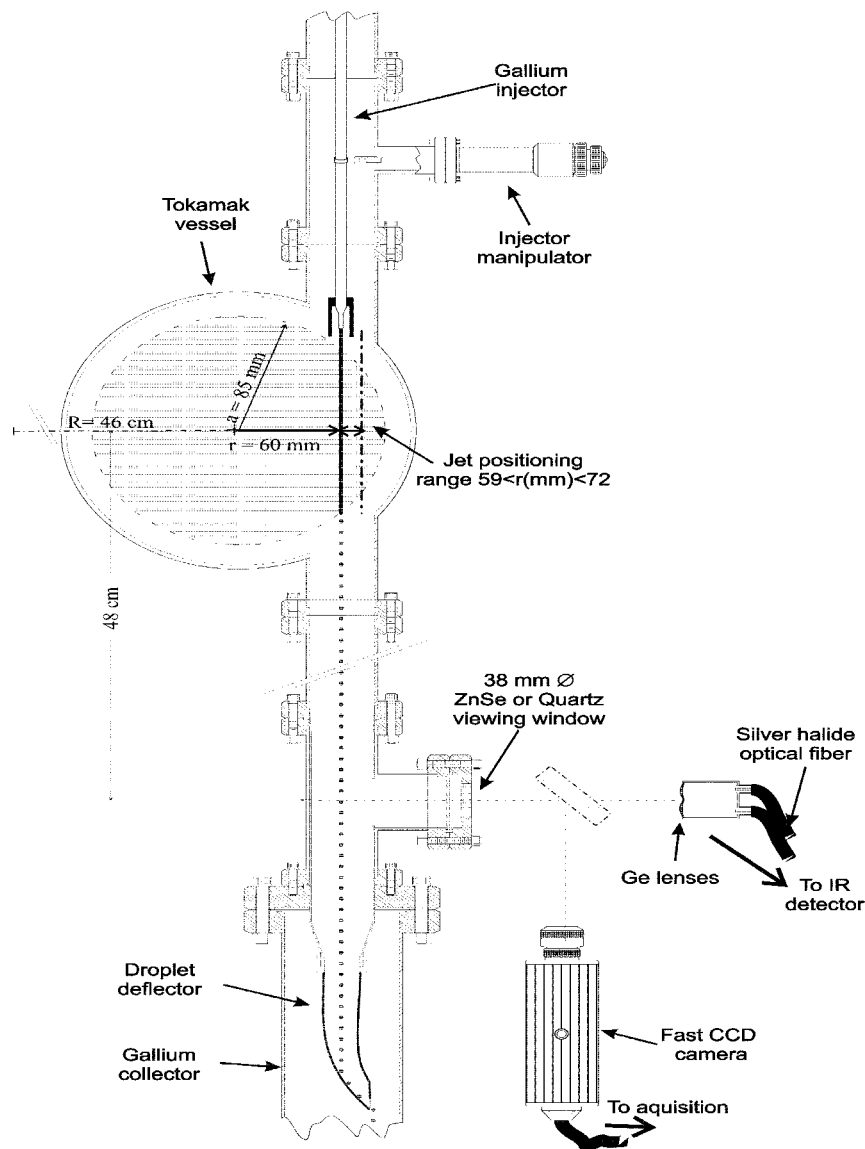
Fig 3.1 Cross-section of the experimental setup in the vicinity of the plasma–jet interaction region [38]
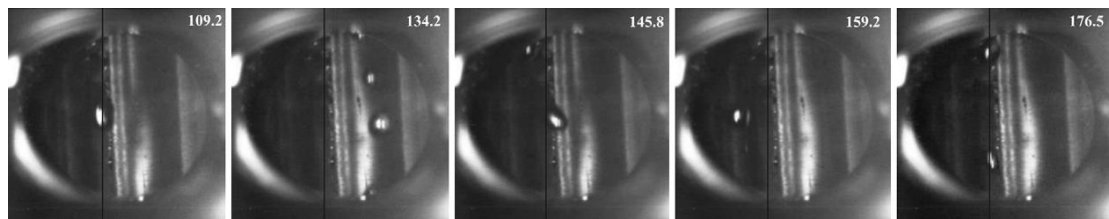
Fig 3.2 Frames sequence from a movie showing the dynamic behavior of gallium droplets due to the influence of an ISTTOK discharge, [39]

56
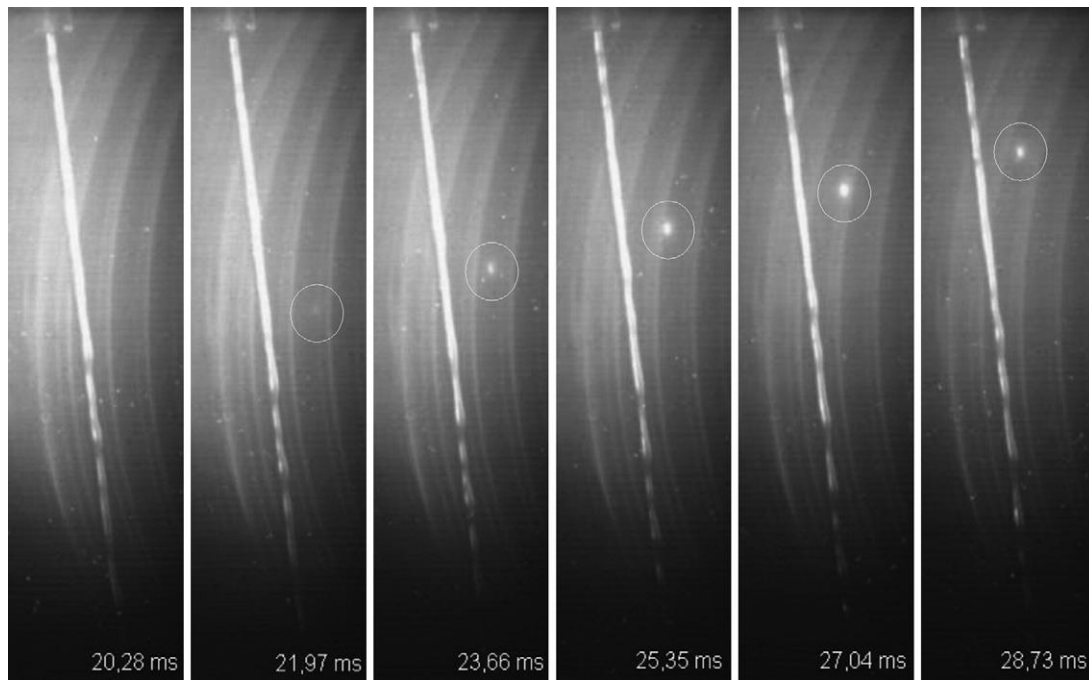
Fig 3.3 Gallium droplets appearing during plasma-liquid metal interaction, [36]

Several nozzle sizes (1.45, 1.80, 2.09 and 2.30 mm diameter) have been tested to determine the best choice for ISTTOK application. These have been characterized by measuring the jet break-up length parameter, flow rate curves and jet flow velocity. **Fig. 3.4** shows a picture of a typical jet, produced in this experiment for the 2.30 mm nozzle. Besides in **Fig. 3.5** it is possible to observe the break-up length (L), as a function of the jet diameter, measured using a fast frame camera, for all the tested nozzles. The observed increase in break-up-length is almost linear with jet diameter. The stability of a viscous jet in vacuum has been theoretically investigated by Rayleigh [67] and, later, by Weber [69].
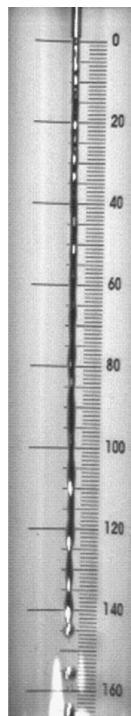
Fig 3.4 Picture of the jet produced using the 2.3 mm nozzle, [38]

57
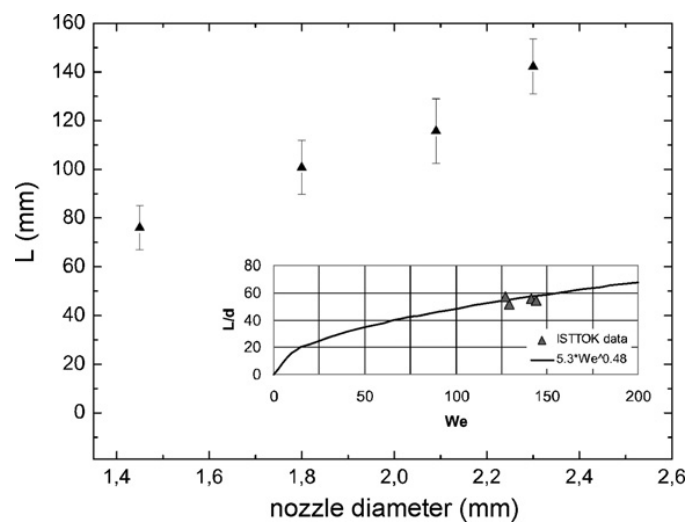
Fig 3.5 Break-up length (L) for several nozzles sizes and also L/d as a function of Weber number, [38]

3.3 Prediction of jet propagation

Initially, an investigation, concerning the prediction of the trajectory of a jet travelling inside an electromagnetic field, was conducted in order to capture and, possibly, quantify the effect of the observed deflection due to jxB effects in ISTTOK experiments.

3.3.1 Modelling and mathematical formulation

This study assumes a cylindrical liquid metal jet that is moving at speed of $\mathbf{u_0} = -u_0\mathbf{e_z}$ entering a region, $z < 0$, where a uniform magnetic field, $\mathbf{B_0} = B_0\mathbf{e_x}$, exists along with an externally imposed electric potential gradient, $\nabla\varphi_p = d\varphi_p / dz\mathbf{e_z} = -a\mathbf{e_z}$, where $u_0 > 0$, $B_0 > 0$, $a > 0$ and subscript "p" stands for plasma i.e. the surrounding medium, as illustrated in **Fig. 3.6**.
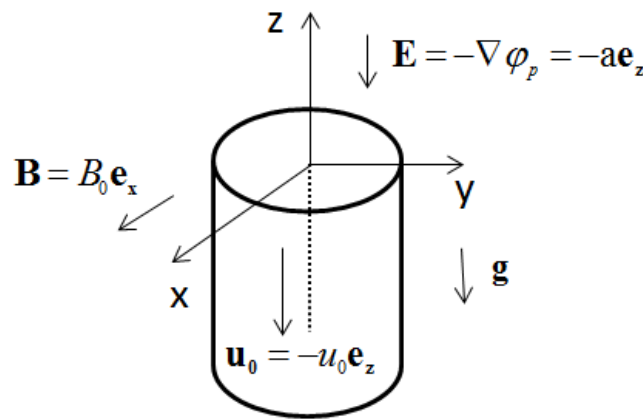
Fig 3.6 Schematic of cylindrical liquid metal jet

The jet cross-section is taken to be circular as a first approximation. Due to the small size of the jet, the magnetic Reynolds is quite small and consequently we can neglect magnetic induction.

Once the jet enters a region, where fluctuations of the electric potential are present due to the surrounding plasma, the electromagnetic forces induce displacement in the horizontal plane and the electric stresses developed on the interface result in deforming the jet.

Before the tackling of the aforementioned flow problem, the electric potential in the jet should be established. To a first approximation, both the jet and the surrounding medium can be treated as perfect dielectrics, i.e. no bulk or surface electric charges. As a consequence, the following conditions hold on their interface:

$$\varphi = \varphi_p, \quad \in \frac{\partial \phi}{\partial n} = \in_p \frac{\partial \varphi_p}{\partial n} \tag{3.1}$$

with $\in$ and φ representing the electric permittivity of Ga and the electric potential, respectively. For a sufficiently thin jet the flow inside it can be assumed to remain unidirectional and electric potential variations can be neglected in the direction normal to the interface, $d\phi / dn \ll d\phi / ds$, with s signifying the arc length along the jet trajectory and **n** the unit normal vector pointing out of the surface. Thus, electric potential

59

variations along the jet passively follow variations in the surrounding medium based on its trajectory, with $\mathbf{e}_s$ its unit vector:

$$\nabla \phi = \frac{\partial \phi}{\partial s}\mathbf{e}_s = \frac{\partial \phi_p}{\partial s}\mathbf{e}_s = -a\frac{dz}{ds}\left(\frac{dy}{ds}\mathbf{e}_y + \frac{dz}{ds}\mathbf{e}_z\right) \qquad (3.2)$$

As it has already been mentioned, the jet cross-section is assumed to remain circular with its center of mass inscribing a trajectory within the yz plane with z(s), y(s) constituting its parametric representation as can be illustrated in **Fig. 3.7a**.
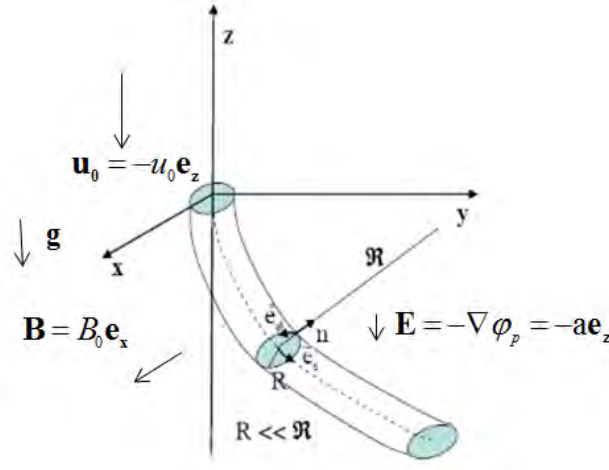
(a)
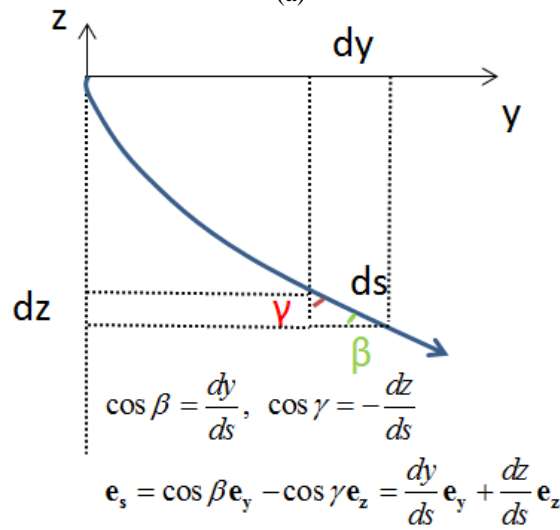
(b)

Fig 3.7 Schematic diagram of: (a) Liquid metal jet trajectory and (b) Trajectory of the center of mass of jet

The currents induced within the liquid Gallium are in the following form:

$$\mathbf{j} = \sigma\left(-\nabla\phi + \mathbf{u}\times\mathbf{B}\right) \qquad (3.3)$$

As a consequence, the resulting Lorentz force is of the form:

60

$$\mathbf{F}_L = \mathbf{j} \times \mathbf{B} = \sigma a B_0 \frac{dz}{ds}\left(-\frac{dy}{ds}\mathbf{e_z} + \frac{dz}{ds}\mathbf{e_y}\right) - \sigma u B_0^2 \mathbf{e_s} \tag{3.4}$$

In the above analysis, $\mathbf{u} \cdot \mathbf{e_x} = 0$ at all times. In other words, the trajectory of the jet center of mass lies entirely within yz plane at the base state. Besides, **Fig. 3.7b** helps understanding Eq. 3.4 better.

The second term in the Eq. 3.4 stands for the jet deceleration due to the part of the Lorentz force that arises because of the induced electric currents in the jet, whereas the first term corresponds to the part of the Lorentz force that arises due to the interaction between the external magnetic and electric fields. Obviously, the latter term is responsible for the deflection of the jet. Thus, based on the constant volumetric flow rate Q and assuming a circular cross section of radius R, mass and momentum conservation within the jet read for unidirectional flow:

$$\nabla \cdot \mathbf{u} = 0 \rightarrow Q = \iint_A \mathbf{u} \cdot \mathbf{e_s} dA = u\pi R^2 \tag{3.5}$$

$$\rho\frac{du}{dt} = \rho u \frac{\partial u}{\partial s} = -\frac{\partial p}{\partial s} + \rho g \cdot \mathbf{e_s} + \mathbf{F_L} \cdot \mathbf{e_s} = -\frac{\partial p}{\partial s} + \rho g \cdot \mathbf{e_s} + \mathbf{F_L} \cdot \mathbf{e_s} \tag{3.6}$$

where $\mathbf{F_L}$ represents the Lorentz forces estimated via Eq. 3.4.

When the radius of curvature of the trajectory is much larger than the jet radius pressure variations within the jet cross-section can be neglected and pressure in the jet is determined by the following interfacial stress balance:

$$\left[-\Delta p\underline{\underline{I}} + \left(\underline{\underline{\tau}}_e - \underline{\underline{\tau}}_e^p\right)\right] \cdot n + 2\gamma H_c n = 0 \quad \text{at} \quad r = r_s(s,n,\varphi) \tag{3.7}$$

where the viscous stresses have been neglected. In the above equations σ, γ and ρ represent the electrical conductivity, the surface tension and the density of Ga, respectively, H_c the mean curvature, Δp the pressure difference, $\underline{\underline{I}}$ the unit tensor. Finally, $\underline{\underline{\tau}}_e$, $\underline{\underline{\tau}}_e^p$ are the electric stress tensors of Ga and plasma, respectively:

$$\underline{\underline{\tau}}_e^p = \in_p\left(E_iE_j - \frac{1}{2}\delta_{ij}E_iE_j\right), \quad \underline{\underline{\tau}}_e = \in_e\left(E_iE_j - \frac{1}{2}\delta_{ij}E_iE_j\right) \tag{3.8}$$

$$n \cdot \underline{\underline{\tau}} \cdot n = \in_p n \cdot \left(\nabla\varphi\nabla\varphi^T - \underline{\underline{I}}\frac{1}{2}\nabla\varphi \cdot \nabla\varphi\right) \cdot n = \in_p\left[\left(\frac{\partial\varphi}{\partial n}\right)^2 - \frac{1}{2}\left(\left(\frac{\partial\varphi}{\partial n}\right)^2 + \left(\frac{\partial\varphi}{\partial s}\right)^2 + \left(\frac{\partial\varphi}{\partial\varphi}\right)^2\right)\right] \tag{3.9}$$

Averaging around the periphery of the jet cross-section and accounting for capillary and electric stresses, electric potential variations along the tangential, φ, and normal, n, direction cancel out and the pressure drop across the interface reads:

61

$$p - p_p = 2\gamma\left(\frac{1}{R} + \frac{1}{\Re}\right) + \left(\epsilon_p - \epsilon\right)\frac{\frac{1}{2}\int_0^{2\pi}\left[\left(\frac{\partial\varphi}{\partial n}\right)^2 - \frac{1}{2}\left(\left(\frac{\partial\varphi}{\partial n}\right)^2 + \left(\frac{\partial\varphi}{\partial s}\right)^2 + \left(\frac{\partial\varphi}{\partial\varphi}\right)^2\right)\right]Rd\theta}{2\pi R}$$

$$p - p_p \approx 2\gamma\frac{1}{R} + \frac{\left(\epsilon_p - \epsilon\right)}{2}\left(\frac{d\phi}{ds}\right)^2$$

(3.10)

Combining equations 3.5-3.7 with the velocity decomposition along the y and z directions:

$$\mathbf{u} = \dot{z}\mathbf{e}_z + \dot{y}\mathbf{e}_y \rightarrow u = \sqrt{\dot{y}^2 + \dot{z}^2}$$

$$u = \frac{ds}{dt}, \quad \dot{y} = \frac{dy}{dt}, \quad \dot{z} = \frac{dz}{dt}$$

(3.11)

provides the time evolution of the jet radius, R, pressure, p, and y, z coordinates of its trajectory. Upon introducing dimensionless quantities, using the jet length, L, and initial jet radius, R_0, as characteristic length scales, and the balance between the Lorentz force and inertia for the characteristic velocity $\hat{u}$

$$\bar{y}, \bar{z} \equiv y, z/L, \quad \bar{R} \equiv R/R_0, \quad \bar{u} \equiv u/\sqrt{\frac{\sigma a B_0 L}{\rho}} \equiv u/\hat{u}$$

$$\bar{t} \equiv t/\left(L/\hat{u}\right) = t/\frac{L\sqrt{\rho}}{\sqrt{\sigma a B_0 L}}, \quad \bar{p} \equiv p/\left[\sigma a B_0 L\right], \quad \vartheta \equiv u_0/\hat{u}$$

(3.12)

the dimensionless formulation for unidirectional jet motion can be derived. Thus, dropping bars for simplicity:

$$u\dot{u} = -Bo\dot{z} - Fmu^2 - \frac{1}{We}R\dot{u} - Bo_{el}\dot{z}\frac{\ddot{z}u - \dot{z}\dot{u}}{u^3}$$

(3.13)

$$\ddot{z} = -Bo - \frac{\dot{z}\dot{y}}{u^2} - Fm\dot{z} - \frac{1}{We}\frac{R\dot{u}}{\dot{z}} - Bo_{el}\frac{\ddot{z}u - \dot{z}\dot{u}}{u^3}$$

(3.14)

$$\ddot{y} = \frac{\dot{z}^2}{u^2} - Fm\dot{y} - \frac{1}{We}\frac{R\dot{u}}{\dot{y}} - Bo_{el}\frac{\dot{z}}{\dot{y}}\frac{\ddot{z}u - \dot{z}\dot{u}}{u^3}$$

(3.15)

$$R = \sqrt{\frac{\vartheta}{u}}$$

(3.16)

with equations 3.13-3.15 corresponding to the s, z, y momentum equations and Eq. 3.16 to continuity. The first term on the right hand side of equation 3.15 represents the Lorentz force component responsible for jet deflection perpendicular to its original trajectory, provided it has acquired a certain longitudinal velocity. The dimensionless variables that arise in the above formulation and determine the jet trajectory are:

$$Bo \equiv \frac{gL}{\hat{u}^2}, \quad Fm \equiv \frac{\sigma B_0^2 L}{\rho\hat{u}}, \quad We^{-1} \equiv \frac{\gamma\pi R_0}{Q\rho\hat{u}}$$

$$Bo_{el} \equiv \frac{a^2\left(\epsilon_p - \epsilon\right)}{\rho\hat{u}^2}, \quad \vartheta \equiv \frac{u_0}{\hat{u}}$$

(3.17)

62

The above dimensionless numbers provide the relative strength of the different forces affecting the jet development and can be estimated from values that are available in the literature and from the geometry of the particular experimental setup. More specifically, Bo relates gravitational to inertial forces, Fm magnetic to inertial forces, We inertial to surface tension forces and Bo_{el} electric stresses to inertia.

3.3.2 Results

According to the ISTTOK experiment, B_0=0.4 T, R_0=2.3 mm, L=13 cm, u_0= 2.5 m/s, whereas Gallium properties are set to ρ=6.1 g/cm^3, σ=4.0x10^6 Ohm^{-1} m^{-1}. Besides, the surface tension, γ, of Ga is approximately equal to 0.661 N/m for a temperature of 100 ^{o}C. The value L=13 cm was selected as characteristic for jet length since it was observed in [38] that a gallium jet with radius and speed as those above prescribed, breaks-up to drops at a distance of 13 cm from the nozzle when plasma activity is off. Moreover, the electric permittivity of plasma and gallium are estimated to, $\in_p$=590 and $\in$=16.2, respectively. Finally, two cases were considered with a=0.13V/m and 1100V/m.

Based on the time integration of the model equations (3.13-3.16) the jet trajectory may exhibit a significant shift and is progressively accelerated along the y direction due to the action of the electric potential gradient part of the Lorentz force, $-\sigma\nabla\phi\times\mathbf{B}$. Clearly, the terms of Eqs. 3.14 and 3.15 are mainly responsible for the relative motion in the z and y directions, respectively, and the resulting jet deflection. The latter intensifies as the electric potential gradient increases. The deflection of the jet trajectory is illustrated in **Fig. 3.8a** and **3.8b**, when the parameter a is set to 0.13 and 1100 V/m respectively, for a jet that is initially aligned with the negative z axis and travels at a velocity u_0=2.5m/s, along the z direction.

When plasma is absent no deflection is observed since there are no disturbances of the external electric potential that can generate currents within the jet. When the magnetic field is only present the length required for capillary break-up to take place increases due to the retardation of the flow induced by the Lorentz force. These effects were verified in the experiments presented in [38,39] and conform with Weber's theory for capillary jet break-up [70].

The jet trajectory was calculated based on the above model for a flight time of 30 ms for two different values of electric potential gradient. Thus, it was seen that jet deflection commences earlier as the magnetic field intensity increases, as illustrated in **Figs. 3.8**.

(a)

(b)
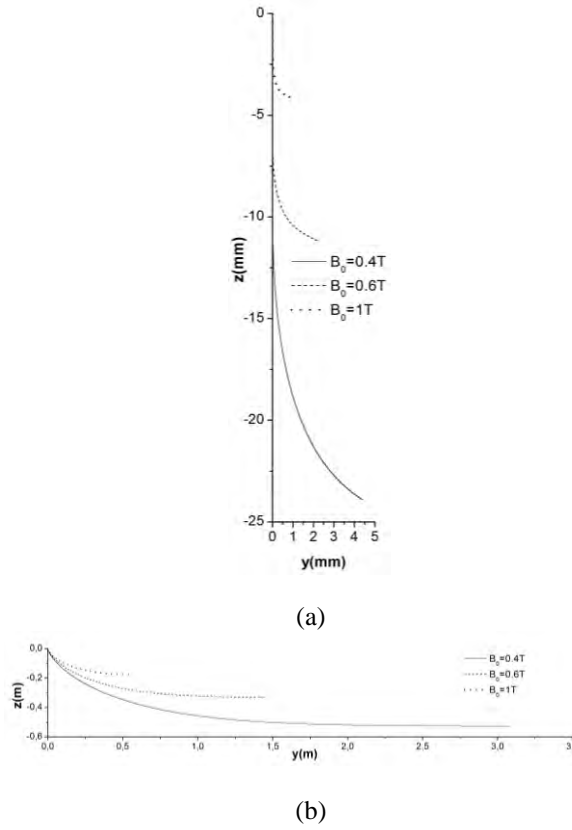
Fig. 3.8 Trajectories for a jet that is initially aligned with the negative z axis, for a range of magnetic field intensities while the electric potential gradient set to (a) 0.13 V/m and (b) 1100 V/m.

This is a result of the intensification of the Lorentz force that causes deflection mainly in the y direction, $\sim \sigma a B_0$. In addition, the amount of deflection increases as the electric potential gradient increases, as can be gleaned by the comparison between **Figs 3.8**a and **3.8b**.

The importance of electric stresses is indicated by the magnitude Bo_{el}. As the electric potential gradient, a, increases Bo_{el} increases as well and affects pressure drop in the jet via the interfacial force balance. As can be inferred by examining Eq. 3.18 and illustrated in **Fig 3.9b**, a=1100 V/m, the electric stresses generate a pressure gradient in the jet that accelerates it while at the same time suppressing its radius due to incompressibility. This is a result of the gradual subsidence of the z-component of the jet velocity in favor of the deflected y component:

$$p - p_p = \frac{1}{We}\frac{1}{R} + \frac{Bo_{el}}{2}\frac{\dot{z}^2}{u^2} \xrightarrow{\ Bo_{el} >> 1\ } \frac{dp}{dz} >> 1 \tag{3.18}$$

However, as the jet velocity builds up in both directions, the part of the Lorentz force that retards the jet motion dominates, $\sim \sigma u B_0^2$, thereby decelerating the jet to the point of almost arresting its motion. Consequently, the jet speed starts decreasing and this reflects in the gradual increase of the radius. This is a rather extreme case of a very large gradient, a=1100 V/m, that generates unrealistic deflections and jet speeds on the order of meters, **Fig. 3.8b**, and hundreds of meters per second, **Fig. 3.9b**, respectively.

64

When a more realistic value of the electric potential gradient is used, a=0.13 V/m, the electric stresses at the interface are not as important. A certain small amount of jet deflection is captured, **Fig. 3.8a**, whereas magnetic damping dominates, Fm=7, right from the outset of the jet motion. As a result, the jet speed decreases in the simulations throughout the jet motion, **Fig. 3.10**, and this effect is intensified as the magnetic field intensity increases.

At the same time, the jet radius inflates in order to accommodate mass balance, **Fig. 3.9a**. The extent of deflection is realistically small, ~5 mm for a jet length of 25 mm. However, the jet development length remains relatively small in comparison with the 7.5 cm of jet length that were reported in the experimental measurements presented in [38,39]. This discrepancy can be attributed to the unidirectional nature of the flow arrangement studied here.

(a)

(b)
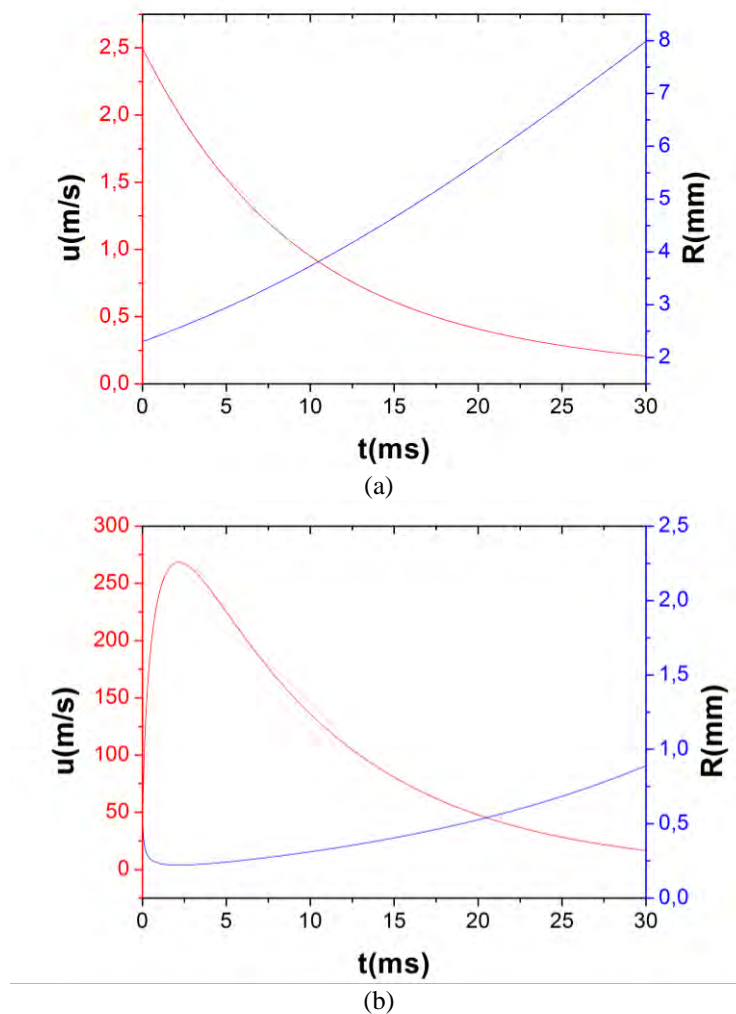
Fig. 3.9 Evolution of jet velocity and radius when B_0=0.42 T and (a) a=0.13 V/m and (b) a=1100 V/m

65
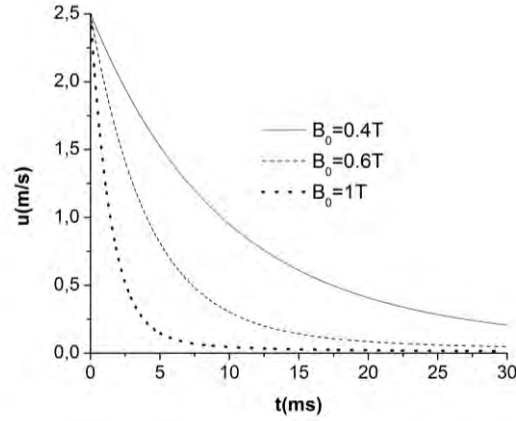
Fig. 3.10 Evolution of the jet velocity as a function of the magnetic field intensity for the first 30 ms;
a=0.13 V/m

As the jet radius increases in order to accommodate continuity, since the jet decelerates due to magnetic damping, a point is reached where, due to capillary action, shape undulations will appear at the jet/plasma interface. This has been observed in the ISTTOK experiments [38,39]. In this context, it should be pointed out that, based on Weber's theory the jet break-up length scales like $L/R_0 \sim (We^{1/2})^{0..85}$ in the laminar regime[70]. Consequently, since the jet radius and speed vary in such a way as to satisfy mass conservation, jet inflation results in shortening the break-up length thus accelerating drop formation. Once the jet interface starts deforming, growth of its radius is arrested along with the process of deceleration. This probably explains the fact that in our simulations the jet does not reach a comparable length with the experiments after a flight time of 30 ms. Therefore, in order to accurately recover the jet break-up length shape oscillations of the jet have to be accounted for. Nevertheless, the above presented model serves as a first principle illustration of the mechanism behind the observed jet deflection, as a result of the interaction between the magnetic and electric fields, i.e. the jxB effect, that the jet encounters as it interacts with plasma.

66

3.4 Prediction of drop propagation

As was discussed above, it is certain that beyond a certain length, depending on the jet speed, drop formation will take place. Thus, as an alternative flow arrangement the motion of a drop is examined in a similar environment as that described above for the case of a jet.

3.4.1 Modelling and mathematical formulation

In this consideration we are interested in studying the trajectory of a droplet regarded as spherical all the time. The droplet enters a region, similar to the previous one, $z < 0$, at a speed of $\mathbf{u_0} = -u_0\mathbf{e_z}$, where a uniform magnetic field $\mathbf{B_0} = B_0\mathbf{e_x}$ exists along with an externally imposed electric potential gradient, $\nabla \varphi_p = d\varphi_p / dz\mathbf{e_z} = -a\mathbf{e_z}$, where $u_0 > 0$, $B_0 > 0$, $a > 0$ and subscript "p" stands for plasma i.e. the surrounding medium, as illustrated in **Fig. 3.11**.
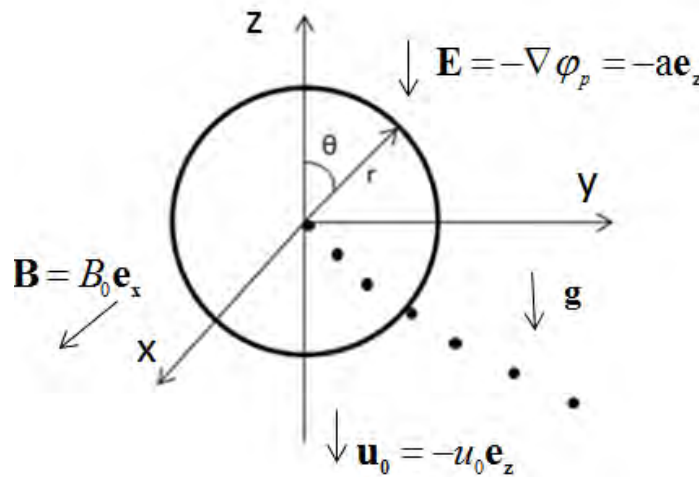
Fig. 3.11 Schematic of the droplet trajectory. The thick circle depicts the drop outline and the small dark circles the trajectory of its center of mass

Once a droplet enters the area where fluctuations of the electric potential are present due to the surrounding plasma, the Lorentz force induces displacement in the horizontal plane. In order to obtain the magnitude of this force a calculation of the electric potential distribution inside the drop and the surrounding medium is needed, taking them both as perfect dielectrics, to a first approximation, assuming a spherical drop in one dimensional irrotational motion. We solve the Laplacian in both media using spherical coordinates, with the interfacial conditions provided in Eq. 3.1 and the far field condition:

$$\text{r} \rightarrow \infty: \quad \phi_{\text{p}} \approx -ar\cos\theta \tag{3.19}$$

This is a standard problem in electrodynamics [72]. The derivation of the mathematical form concerning the electrical potential inside and outside the drop is presented in Appendix A. Thus, according to equations A.10 and A.11:

$$\varphi = -\frac{3a}{\in / \in_p + 2} r\cos\theta \tag{3.20}$$

67

$$\varphi_{out} = -\mathrm{a}r\cos\theta + \frac{\in/\in_p -1}{\in/\in_p +2}\frac{\mathrm{a}R^3\cos\theta}{r^2} \tag{3.21}$$

Based on the above distribution and due to spherical symmetry the electric stresses cancel out at the drop interface leaving gravity, inertia and the Lorentz force as the main factors of the drop motion. Moreover, the inertia is $\dfrac{4}{3}\pi R^3 \rho \ddot{\mathbf{r}}$ and gravity is $-\dfrac{4}{3}\pi R^3 \rho g \mathbf{e_z}$.

The Lorentz force is:

$$\mathbf{F}_L = \mathbf{j}\times\mathbf{B} = \sigma\left(-\nabla\varphi + \mathbf{u}\times\mathbf{B}\right)\times\mathbf{B} =$$
$$\underbrace{-\sigma\nabla\varphi\times\mathbf{B}}_{F_{L,1}} + \underbrace{\sigma\left(\mathbf{u}\times\mathbf{B}\right)\times\mathbf{B}}_{F_{L,2}} \tag{3.22}$$

$$\mathbf{F}_{L,1} = -\sigma\nabla\varphi\times\mathbf{B} = -\sigma\left(\frac{\partial\varphi}{\partial r}\mathbf{e_r} + \frac{1}{r}\frac{\partial\varphi}{\partial\theta}\mathbf{e}_\theta\right)\times B_0\mathbf{e}_x =$$
$$-\sigma\left\{\frac{\partial\varphi}{\partial r}\left(\sin\theta\cos\varphi\mathbf{e}_x + \sin\theta\sin\varphi\mathbf{e}_y + \cos\theta\mathbf{e}_z\right)\right.$$
$$\left.+\frac{1}{r}\frac{\partial\varphi}{\partial\theta}\left(\cos\theta\cos\varphi\mathbf{e}_x + \cos\theta\sin\varphi\mathbf{e}_y - \sin\theta\mathbf{e}_z\right)\right\}\times B_0\mathbf{e}_x = \tag{3.23}$$
$$= -\sigma B_0\left\{\left(\frac{\partial\varphi}{\partial r}\cos\theta - \frac{1}{r}\frac{\partial\varphi}{\partial\theta}\sin\theta\right)\mathbf{e}_y - \left(\frac{\partial\varphi}{\partial r}\sin\theta\sin\varphi + \frac{1}{r}\frac{\partial\varphi}{\partial\theta}\cos\theta\sin\varphi\right)\mathbf{e}_z\right\}$$

and

$$\mathbf{F}_{L,2} = \sigma u_0 B_0^2\left(\mathbf{e_s}\times\mathbf{e_x}\right)\times\mathbf{e_x} =$$
$$= \sigma u_0 B_0^2\left[\left(\frac{dy}{ds}\mathbf{e}_y + \frac{dz}{ds}\mathbf{e}_z\right)\times\mathbf{e_x}\right]\times\mathbf{e_x} =$$
$$= -\sigma u_0 B_0^2\left(\frac{dy}{ds}\mathbf{e}_y + \frac{dz}{ds}\mathbf{e}_z\right) = \tag{3.24}$$
$$= -\sigma B_0^2\left(\dot{y}\mathbf{e}_y + \dot{z}\mathbf{e}_z\right)$$

In order to find the total Lorentz force that is eventually applied, an integration of the electromagnetic forces around the droplet should be done on each component:

$$\mathbf{F}_{L,1} = -\sigma B_0 \left\{ \int_0^R \int_0^\pi \int_0^{2\pi} \left[\left(-\frac{3a}{2+\varepsilon/\varepsilon_p}\cos^2\theta - \frac{3a}{2+\varepsilon/\varepsilon_p}\sin^2\theta \right) r^2 \sin\theta \, dr \, d\theta \, d\varphi \, \mathbf{e}_y \right] \right.$$

$$\left. - \int_0^R \int_0^\pi \int_0^{2\pi} \left[\left(-\frac{3a}{2+\varepsilon/\varepsilon_p}\cos\theta\sin\theta\sin\varphi + \frac{3a}{2+\varepsilon/\varepsilon_p}\cos\theta\sin\theta\sin\varphi \right) r^2 \sin\theta \, dr \, d\theta \, d\varphi \, \mathbf{e}_z \right] \right\} =$$

$$= \frac{3a}{2+\varepsilon/\varepsilon_p}\sigma B_0 \int_0^R \int_0^\pi \int_0^{2\pi} \left(\cos^2\theta + \sin^2\theta \right) r^2 \sin\theta \, dr \, d\theta \, d\varphi \, \mathbf{e}_y = \tag{3.25}$$

$$= \frac{3a}{2+\varepsilon/\varepsilon_p}\sigma B_0 \frac{4\pi R^3}{3}\mathbf{e}_y$$

Similarly,

$$\mathbf{F}_{L,2} = -\sigma B_0^{\,2}\left(\dot{y}\mathbf{e}_y + \dot{z}\mathbf{e}_z \right)\frac{4\pi R^3}{3} \tag{3.26}$$

Thus, by adding Eqs.(3.25, 3.26),

$$\mathbf{F}_L = \mathbf{F}_{L,1} + \mathbf{F}_{L,2} = \frac{4\pi R^3}{3}\left[\left(\sigma B_0 \frac{3a}{2+\varepsilon/\varepsilon_p} - \sigma B_0^{\,2}\dot{y} \right)\mathbf{e}_y - \sigma B_0^{\,2}\dot{z}\mathbf{e}_z \right] \tag{3.27}$$

The first term represents the force due to interaction between the external electromagnetic fields that is responsible for the drop deflection, whereas the last two terms represent the force that retards the drop motion as a result of the induced electric currents inside it.

Assuming that

$$\mathbf{r} = x\mathbf{e}_x + y\mathbf{e}_y + z\mathbf{e}_z \tag{3.28}$$

the force balances in y and z directions, respectively read as:

$$\frac{4\pi R^3}{3}\left[-\rho\ddot{y} - \sigma B_0^{\,2}\dot{y} + \sigma B_0 \frac{3a}{2+\varepsilon/\varepsilon_p} \right] = 0 \Rightarrow \tag{3.29}$$

$$\Rightarrow \ddot{y} = -\frac{\sigma B_0^{\,2}}{\rho}\dot{y} + \frac{\sigma B_0}{\rho}\frac{3a}{2+\varepsilon/\varepsilon_p}$$

$$\frac{4\pi R^3}{3}\left[-\rho\ddot{z} - \rho g - \sigma B_0^{\,2}\dot{z} \right] = 0 \Rightarrow$$

$$\Rightarrow \ddot{z} = -\frac{\sigma B_0^{\,2}}{\rho}\dot{z} - g \tag{3.30}$$

Upon introducing the dimensionless length scale via the drop radius R and time scale via the balance between the deflective part of the Lorentz force and inertia:

69

$$t_0 = \sqrt{\frac{R\rho\left(2 + \varepsilon/\varepsilon_p\right)}{3a\sigma B_0}}$$ (3.31)

$$\tilde{u} = R/t_0$$

and dropping the bars for simplicity the equations describing the drop trajectory on the y,z plane are derived:

$$\frac{R}{t_0^2}\ddot{y} = -\frac{R}{t_0}\frac{\sigma B_0^2}{\rho}\dot{y} + \frac{R}{t_0^2} \Rightarrow$$

$$\Rightarrow \ddot{y} = -Fm\dot{y} + 1$$ (3.32)

$$\frac{R}{t_0^2}\ddot{z} = -\frac{R}{t_0}\frac{\sigma B_0^2}{\rho}\dot{z} - g \Rightarrow$$

$$\Rightarrow \ddot{z} = -Fm\dot{z} - Bo$$ (3.33)

where the two dimensionless numbers:

$$Fm = \frac{\sigma B_0^2}{\rho}t_0, \ Bo = \frac{gt_0^2}{R} = \frac{gR}{u^2}$$ (3.34)

provide the relative strength of electromagnetic to inertial forces and the gravitational to inertial forces, respectively.

The part of the Lorentz force that arises as a result of the interaction between the external electric and magnetic fields appears as unity in the above dimensionless formulation, because it is through the balance between this force and inertia that we make things dimensionless. It is this term that is responsible for drop deflection.

The electric potential gradient, a, is set to 0.13 V/m in the present study. The latter variable may vary significantly inside the reactor chamber. Here we use an indicative value in an effort to capture the experimentally obtained drop deflection as close as possible, based on this qualitative model. In particular, parameter a was determined so that the deflection of 10 mm that was observed after a flight time of 30 ms for the droplets emerging after jet break-up in the presence of a magnetic field with intensity B_0=0.42 T [38,39], is recovered. In order to examine the effect of electric potential variations also the value of a=1100 V/m was used in the parametric study that follows.

3.4.2 Results
The droplet trajectory can be found analytically by integrating the nonhomogeneous differential equations 3.32 and 3.33:

$$\ddot{y} + Fm\dot{y} = 1 \quad \overset{\dot{y}(0)=0}{\Rightarrow}$$

$$\dot{y}(t) = -\frac{e^{-Fm \cdot t}}{Fm} + \frac{1}{Fm} \quad \overset{y(0)=0}{\Rightarrow} \tag{3.35}$$

$$y(t) = \frac{e^{-Fm \cdot t}}{Fm^2} + \frac{t}{Fm} - \frac{1}{Fm^2} \tag{3.36}$$

$$\ddot{z} + Fm\dot{z} = -Bo \quad \overset{\dot{z}(0)=-1}{\Rightarrow}$$

$$\dot{z}(t) = \frac{Bo - Fm}{Fm} e^{-Fm \cdot t} - \frac{Bo}{Fm} \quad \overset{z(0)=0}{\Rightarrow} \tag{3.37}$$

$$z(t) = \frac{Fm - Bo}{Fm^2} e^{-Fm \cdot t} - \frac{Bo}{Fm} t + \frac{Bo - Fm}{Fm^2} \tag{3.38}$$

Thus, the parametric form of the aforementioned trajectory can be described via the system of Eqs. 3.36 and 3.38.

Since, in this investigation, gallium is considered to be dielectric, when the droplet travels through regions with different electrical potentials, because of the existence of plasma, an electric field with variable strength will be generated in the drop. This field in conjunction with the magnetic field, which corresponds to the toroidal one in the ISTTOK experiments, is expected to generate drop deflection, in the manner discussed above for the jet consideration. Based on the analytical solution of the model equations (Eqs 3.36 and 3.38.) and the parameter values when a=0.13 V/m and B_0=0.42 T, Fm=0.76 and Bo=0.18, the deflection is more intense as the magnetic field increases, as can be depicted in **Fig 3.12**. In fact, it is more severe in comparison with the one predicted, and observed in experiments [38,39], in the case of jet motion. This is a result of the dominating action of the gradient of the electric potential which, owing to the small drop size in comparison with the length of the jet, generates a force that acts solely along the y direction. This action is intensified as the magnitude of the magnetic field increases, **Fig. 3.12**. It should also be stressed that the experimentally observed [38,39] drop deflection of 10 mm after a flight time of 30 ms subject to a field intensity of 0.42 T, is recovered in the simulations, as expected, since the gradient, a, was selected to match that value.
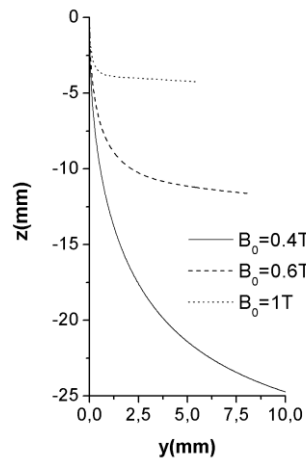
Fig. 3.12 Gallium droplet trajectories during the first 30 ms, for a droplet that its center of mass is initially aligned with the negative z axis; a=0.13 V/m

71

The important effect of the magnetic field intensity is also illustrated via the magnetic damping on the drop velocity over the same time interval, as shown in **Fig. 3.13** below; Fm=0.8. Eventually, the droplet motion is almost arrested due to the retarding effect of the magnetic field, which dominates owing to the relatively small value of the electric potential gradient, and its trajectory is shifted entirely towards the y axis.
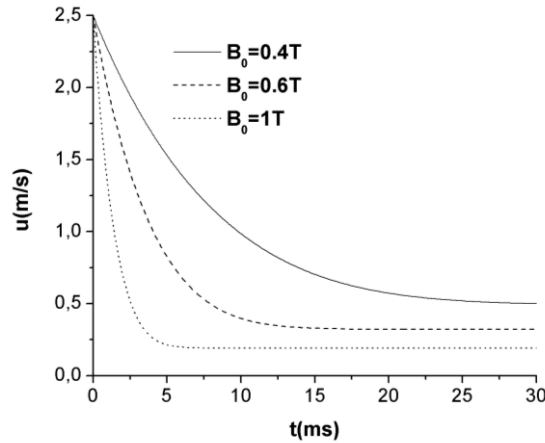
Fig. 3.13 Evolution of the gallium droplet velocity during the first 30 ms; a=0.13 V/m

As can be gleaned from **Figs. 3.8a** and **3.12** deflection is much stronger on the same time scale for the case of a drop, when B_0=0.4 T and a=0.13 V/M. Similarly, based on **Figs 3.10** and **3.13**, the drop acquires a much larger velocity than the jet over the same time scale. The significant difference in deflection and speed perhaps explains events of drop spraying in the walls of fusion reactors when liquid metal limiters in the form of a jet-drop curtain are employed.

It should also be pointed out that during the experiments the radius of the droplet will not be constant at all times but it must be determined by a stability analysis of both the jet and the emerging droplets. Finally, if the shape of the droplet is not spherical, electric stresses must then be taken into account since they might affect the acceleration of the gallium droplet. It is known from the literature of free surfaces [73] that accelerating drops generate shape modes in the direction of the interface facing away from that of the acceleration. Subsequently, they may generate the translational mode via nonlinear interaction of pulsating shape modes. The latter effect has been well documented for pulsating bubbles [74]. It may then be possible, based on the dynamic response of specific shape modes [75], to dynamically excite drops, perhaps by vibrating the nozzle that introduces the liquid metal with the proper frequency, which will follow the desired trajectory.

Concluding, it was seen by a proof of principle study that when a jet moves inside an electromagnetic field deflection arises due to the $\mathbf{j} \times \mathbf{B} \sim -\sigma \nabla \phi \times \mathbf{B}_0$ interaction between the external electric potential gradients and the magnetic field. As a result the jet accelerates and eventually decays into drops. The latter, due to their small size and spherical shape, experience a stronger deflection. Jet and drop stability to shape oscillations, subject to jxB effects and electric stresses, is essential in capturing realistic dynamics of the jet/drop motion. The above picture conforms, within the proper order of magnitude, with the findings at ISSTOK [26,38,39]. Improved modeling of the jet/drop motion is required in order to obtain a quantitative comparison.

72

Chapter 4: Capillary Porous System (CPS): Modelling and mathematical formulation

In this chapter, the step-by-step effort is described concerning the analysis of the operation of the CPS as plasma facing component. In particular, the modelling as well as its mathematical formulation of CPS is analyzed for both the preparation and static configuration phases. The latter phase arises after liquid metal depletion has taken place due to a large external heat flux, and the replenishment of the evaporated liquid metal film at the CPS/plasma interface has completed as a result of capillary activity within the porous matrix. The current study focuses principally on the static arrangement of the liquid metal resting onto the CPS top surface. More specifically, the effects of the reservoir overpressure, electric stresses and, the more relevant to fusion applications, jxB effects are investigated on the static film arrangement. Moreover, since, according to the experiments, the film thickness reduces down to micron or even submicron sizes, the nature of the micro-scale liquid-solid interactions is taken into account. In addition, the capillary fluid motion within a single pore is investigated providing the framework for studying the interplay between the different forces that act towards pushing liquid lithium out of the porous matrix or resist its motion. Finally, a first-principles study is performed pertaining to the power exhaust capabilities of the CPS configuration.

4.1 Introduction

As detailed in the Chapter 1, CPS is a capillary pumping system engineered to stabilize a protective liquid metal film against electromagnetic and thermal forces as well as drop ejection which is a key issue concerning the reliability of a free surface plasma facing component.

Thus, in order to allow for stable operation, the liquid metal should be confined within a mesh or porous structure as already demonstrated in devices such as T11, T10 [76], FTU [77] and NSTX [78]. The CPS and its potential application under tokamak relevant conditions as well as its heat-exhaust capabilities with respective liquid metal choices has been the subject of extensive experimental research during the last two decades. In addition, experiments related to material compatibility [50] and wetting [63] as well as plasma impact [19] have been performed. Up to now, Lithium seems to make the proposed concept highly efficient. However, due to some problems accompanied Lithium, described in 1.3.3, also the use of Ga, Sn and Sn-Li has been investigated. **Table 4.1** lists their properties and also those ones for solid tungsten (W), often used in DEMO designs.

Table 4.1

Properties of fusion liquid metals and W, [17]

Symbol (units)	Li	Sn	Ga	W
Atomic no. Z	3	50	31	74
Atomic weight	6.94	118.7	69.72	183.84
Density, ρ (g/cm^3)	0.512	6.99	6.095	17.6
Melting point, T_m (^{o}C)	180.5	231.9	29.8	3695
Heat of melting, H_{melt} (J/g)	0.021	0.83	0.39	6.49
Boiling point, T_b (^{o}C)	1347	2270	2403	5828
Latent heat of vaporization, H_{vap} (J/g)	1.02	35.15	17.86	1429
Dynamic viscosity, η (10^{-3} Pa-s) at T_m	0.25	1.85	0.95	
Surface tension, σ (N/m) at T_m	0.4	0.55	0.69	
Thermal conductivity, k (W/mm-K) at T_m	0.045	0.030	0.051	0.072
Heat capacity, C_p (J/g-K)	4.30	0.250	0.380	0.140
Volumetric heat capacity, ρ C_p (MJ/m^3-K)	2.30	1.83	2.25	2.70
Ionization energy, 1st (10^6 J/g)	3.61	84.1	40.4	141.6
Ionization energy, 2nd (10^6 J/g)	50.6	167.6	138.0	312.5
Ionization energy, 3rd (10^6 J/g)	82.0	349.3	206.6	

Thus far, CPS has not been the subject of extensive modelling activity partly due to the complex flow arrangement of the limiter containing the liquid metal. Available studies [40,79,80] focus on the importance of the capillary forces to supply a mass flow rate of lithium through the CPS system via a balance between pressure drop and resistance to flow [80], while qualitatively emphasizing the relative merits of the arrangement [79,81]. Modelling of the power exhaust capabilities of such a system requires knowledge of the flow arrangement, if at all present.

For a better understanding of the process and before presenting the CPS modelling, some images of an example of a tokamak with a CPS installed in it, namely the FTU tokamak, are depicted. First of all, the whole configuration, located in Frascati, is shown, **Fig. 4.1**. During the FTU operation, a radiative cloud, limiting the power load on the surface of liquid lithium limiter, was also observed, **Fig. 4.2**. More specifically, when the heat load is increased, a radiative cloud of lithium is formed all around the limiter produced by enhanced evaporation due to the increase of surface temperature. This self-protecting mechanism is considered to be useful for solving the problem of heat removal in a future reactor and, at the same time, to give a limit to lithium production by evaporation [47]. Finally, in **Fig. 4.3** an image is given shown the liquid lithium limiter taken after the last experimental campaign.

74
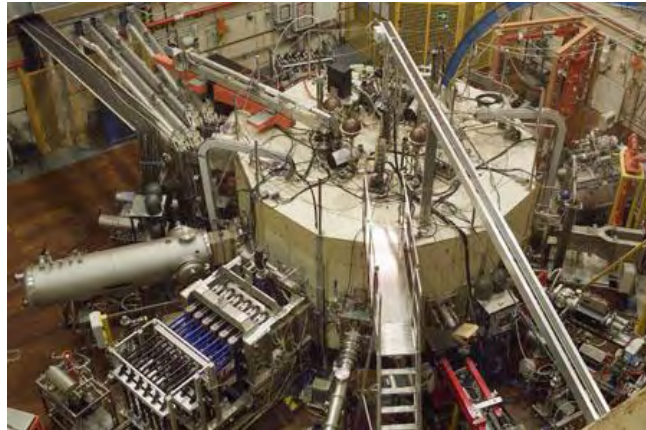
Fig. 4.1 Top view of FTU, [82]
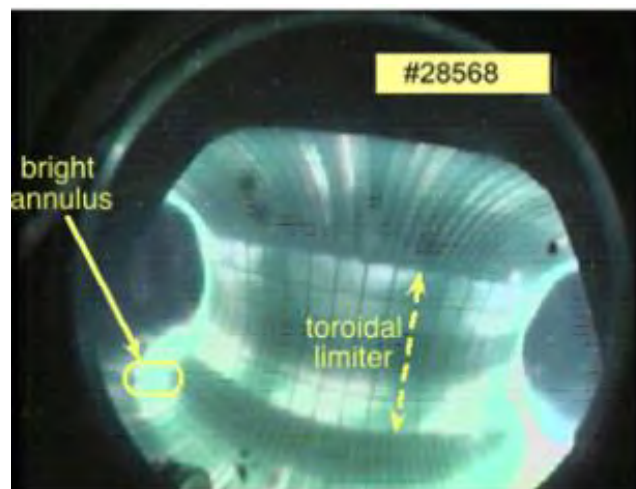
Fig. 4.2 Image taken in FTU: Evidence of a radiative cloud, [47]

I
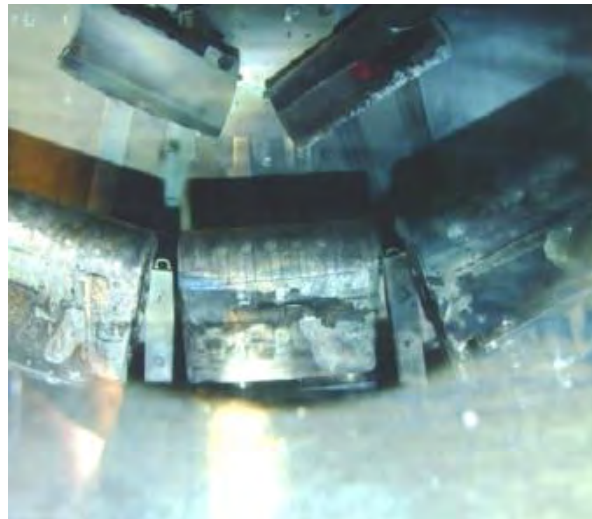
Fig. 4.3 Image of the three units after exposition on FTU at more than hundred discharges, [47]

75

4.2 Outline of the envisioned CPS operation

This section deals with the step-by-step effort in order to understand the CPS configuration as plasma facing component. As a consequence, it focuses on the qualitative analysis of the different concepts underpinning operation of the CPS configuration.

4.2.1 Preparation Phase

Firstly, the CPS configuration during the preparation phase, in the absence of thermal and Lorentz forces, is investigated. In the preparation phase lithium, or some other material such as those presented in **Table 4.1**, is in solid state which, for simplicity, is represented in the form of cylindrical rods with density ρ_s, placed within the porous wafer as shown in **Fig. 4.4**. The wafer is in contact with the surrounding medium via the top surface that is initially covered (green layer in **Fig. 4.4**). Initially, it is assumed that there is no additional reservoir of lithium for simplicity, $h_r=0$. If there was additional reservoir of lithium, it would also liquefy, thus, offering additional mass that would end up at the top of the wafer. The porous matrix thickness h_0 is taken to be on the order of 1 mm. Moreover, to a first order, the volume of the wafer is considered not to change significantly in the process of heating and expansion of the liquid metal. Upon heating, the lithium liquefies at density $\rho_l < \rho_s$, with the subscripts "l" and "s" standing for the liquid and the solid state, respectively. Consequently, the top cover breaks by the expanding liquid and liquid metal covers the top surface forming a protective coating. In the schematic provided below, **Fig. 4.5**, the thickness of the liquid metal film is drawn out of scale. In qualitative **Figs. 4.4** and **4.5** red colour represents the solid state of Lithium while the blue one its liquid phase.
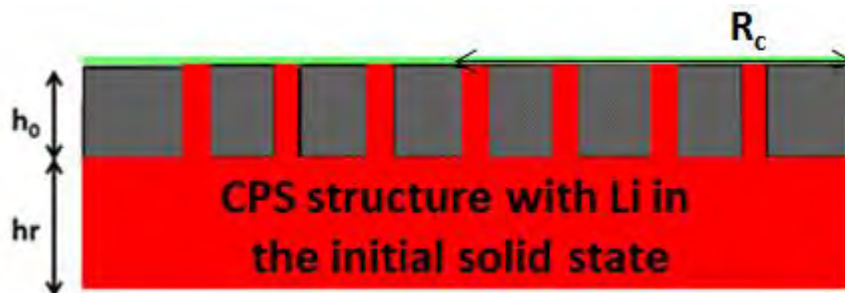
Fig. 4.4 Schematic arrangement of CPS in the preparation phase before heating and melting of lithium takes place
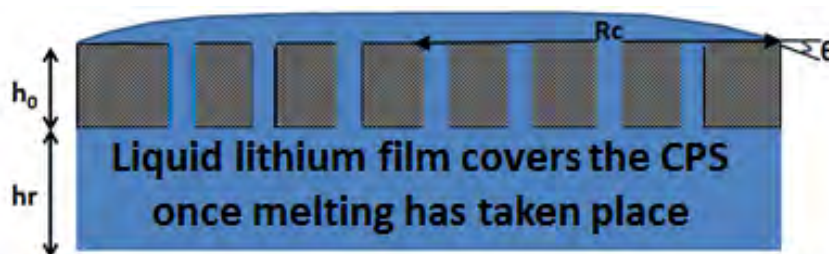
Fig. 4.5 Schematic of the liquid lithium film that covers the CPS once melting has taken place; the thickness of the liquid metal film is sketched out of scale

4.2.2 Depletion and replenishment

A more relevant to plasma operation situation is described below. In particular, a qualitative description is provided of the depletion process of liquid metal covering the

76

CPS, due to an external heat flux, followed by the replenishment process that is dominated by capillary activity. The final static arrangement is difficult to be achieved and more difficult to be maintained at high enough heat fluxes. Nevertheless an attempt was made in the present Thesis to obtain the basic characteristics of such a static configuration.

Heat transfer considerations

Once the machine is "turned on", an external heat pulse depletes the ultra-thin film existing on top of the porous matrix due to the evaporation process. Depending on the intensity and duration of the oncoming heat load, part of the liquid metal located within the porous structure also evaporates as illustrated in **Fig. 4.6**. Finally, capillary driven replenishment of the liquid metal film will take place, **Fig. 4.7**, by pumping the liquid metal from the reservoir. In this fashion, the CPS concept can provide sufficient working pressure in the supply system without applying external pressure, by means of the capillary pressure. This system is self-sustaining and self-regulating as mentioned in Chapter 1.

Once the liquid metal layer on the top of the wafer evaporates, a different operating regime emerges, i.e. transpiration cooling. The oncoming heat flux will be balanced by (a) evaporation of Li captured within the pores, (b) heat conduction within the porous matrix but also (c) by convective heat transfer due to the preheating of liquid lithium, from the reservoir temperature up to the temperature of the interface, that is drawn out of the reservoir by capillary forces once the top of the CPS is depleted of liquid metal. In view of the above, convective heat transfer is not to be excluded from a comprehensive analysis of CPS.
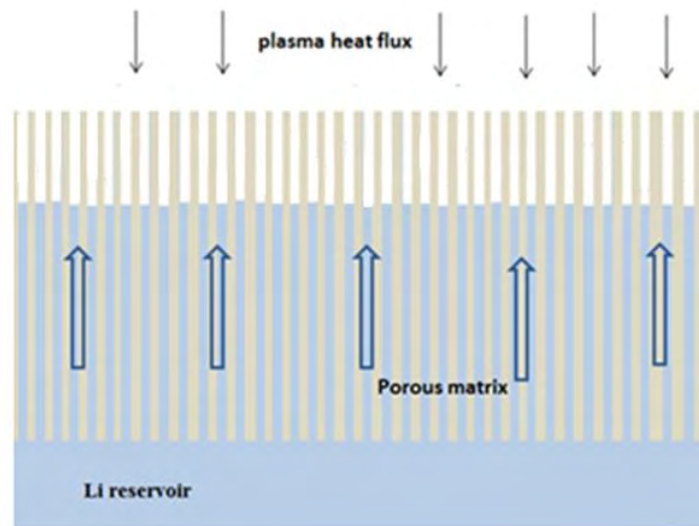
Fig. 4.6 Schematic of the depletion and replenishment process of the liquid metal film during plasma operation

77
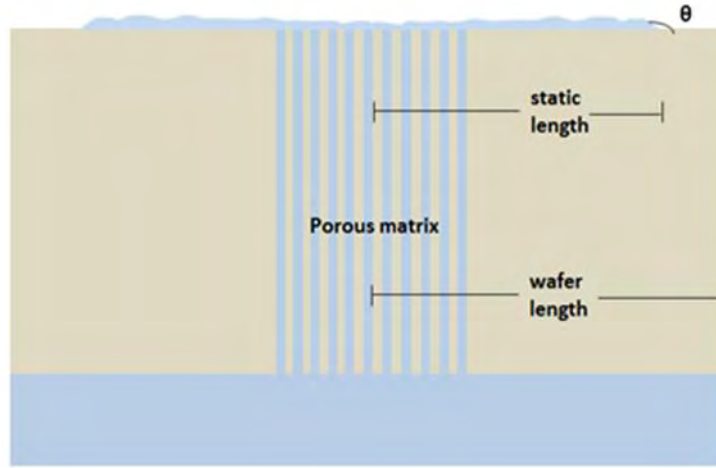
Fig. 4.7 Reestablishment of static arrangement via capillary driven motion, after depletion

Capillary fluid motion within a pore

As a first attempt to provide an upper bound of the convective effects within the CPS matrix, the flow within a cylindrical pore is also examined. This simplified geometry, shown in **Fig. 4.8**, overestimates the permeability of the CPS, but provides the framework for studying the interplay between the different forces that act towards pushing liquid lithium out of the porous matrix or resist its motion. As a first approximation, the pore is considered to be isothermal and evaporation effects are neglected. Emphasis is placed in studying the potential of the CPS system to act as a capillary pump against gravity and viscosity.

The static configuration is sought for fixed height, h, of the liquid metal column. The volumetric flow rate of liquid lithium is obtained, along with the meniscus shape at the interface, for known interfacial tension and contact angle, known pressure drop and material properties. The hydrodynamic problem is examined in the context of axisymmetry in order to obtain an understanding of the operation principle of the capillary pump.
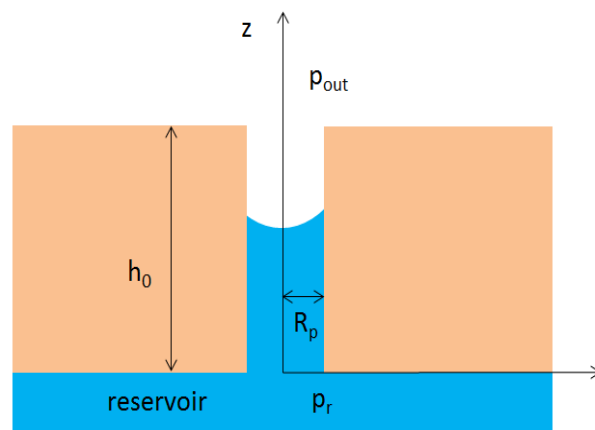
Fig. 4.8 Schematic arrangement of the flow arrangement within a single pore via capillary action

In a more general situation the window of CPS proper operation is determined by the following inequality:

$$P_c \geq \Delta P_L + \Delta P_G + \Delta P_F + \Delta P_{MHD} \tag{4.1}$$

78

where P_c represents the CPS capillary pressure, ΔP_L the hydraulic pressure drop in CPS, ΔP_G the hydrostatic pressure drop, ΔP_F the pressure drop on the evaporating surface due to liquid-vapor phase transition, ΔP_{MHD} the pressure drop due to the MHD effect on flowing Li in a magnetic field. P_c values for reasonable pore sizes can reach the values of 0.2 - 0.3 MPa and exceeds the sum of pressure drops estimated as 10 kPa for the tokamak with a magnetic field of about 6 T, [18]. Finally, ΔP_{MHD} can push liquid lithium out of the porous matrix or resist its motion depending on the direction of the externally applied magnetic field.

4.2.3 Static arrangement of the CPS after depletion and replenishment

Once the liquid metal reaches the pore`s "mouth", driven mainly due to capillary action, it is anticipated to coat the top surface of the CPS matrix forming a static ultra-thin film. It is of major interest to investigate the static arrangement of the protective liquid metal layer and identify the important forces that participate in the equilibrium.

The static film thickness established after depletion has taken place is a more relevant situation to plasma operation. This is a different process from the one that takes place during the preparation phase and will be drastically affected by the overpressure between the reservoir and the surrounding medium, as explained below.

Keeping in mind that when the reservoir is in contact with the surrounding medium the respective pressures are more or less equal [83,84] and consequently capillary activity acts on its own in order to replenish the liquid metal. The kind of force helping the liquid layer adhere onto the porous matrix is very important in establishing the static equilibrium but also in stabilizing the film against jxB effects and drop ejection.

Effect of reservoir overpressure

In this fashion, the static arrangement of CPS is studied as a function of the overpressure, P_r-P_{out}, between the reservoir and the surrounding medium and the physical properties of the employed liquid metal. The flow arrangement resembles the experimental study performed in DIFFER by Rindt [83,84]. In particular, it is similar to the "vented oil lamp" concept, as mentioned in [83] and illustrated in **Fig 4.9**, which works like an oil lamp. Briefly, the liquid lithium rests in a reservoir of arbitrary shape and is transported to the surface through a channel. As a result of the vent, the pressure of the gas in the reservoir is equal to the outside pressure. As the meniscus of liquid metal in the reservoir descents, different cases of reservoir overpressures take place reflecting the height difference between the top and bottom menisci. The scope of the present study was not to model the process occurring in DIFFER. However, the latter experimental set-up was useful in developing the modeling concepts employed herein and is mentioned because it is a similar instrumental in visualizing the flow arrangement examined.

79
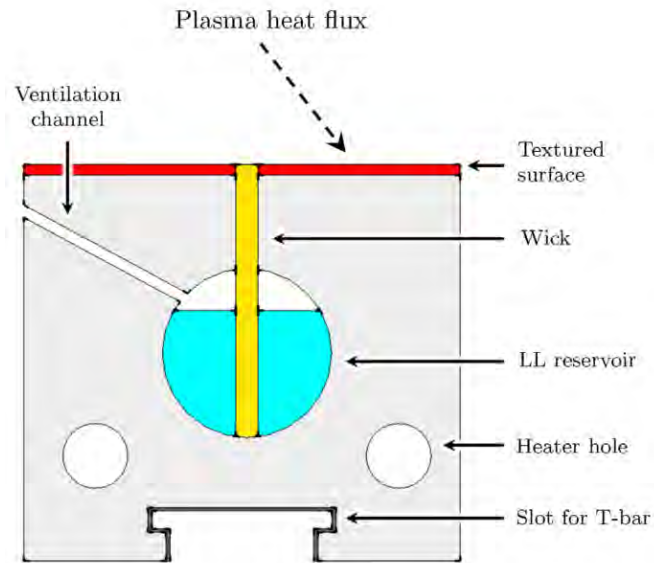
Fig. 4.9 Schematic of the "vented oil lamp" concept design. A wick provides lithium from the reservoir to the textured surface, which faces the plasma. Space for heaters is provided so the lithium can be liquified beforehand. A T-shaped slot is available for fastening. The slot is electrically and thermally insulated on the inside, [84]

In the present investigation a more simplified model was used, as will be elaborated in the modelling section below. The porous system is considered to be a circular disk of small thickness h_0, on the order of 1 mm. In addition, it is in contact with a reservoir that provides the liquid metal via a thin wick. Static arrangements are obtained with partial or full coverage of the top surface of the porous structure, depending on the reservoir overpressure, **Fig. 4.10a** and **b**, respectively.

Effect of an externally applied electric field
As a first step to assess the impact of field forces on the liquid metal layer that covers the porous system, the effect of an external electric field is taken into account that is aligned with the axis of symmetry of the porous wafer in the far field, **Fig. 4.10c**. The evolution of the shape of the interface is of interest as the intensity of the electric field increases, aiming at identifying conditions for which electric stresses overwhelm adhesion forces and conical angle formation is obtained [85].

(a)

(b)

(c)
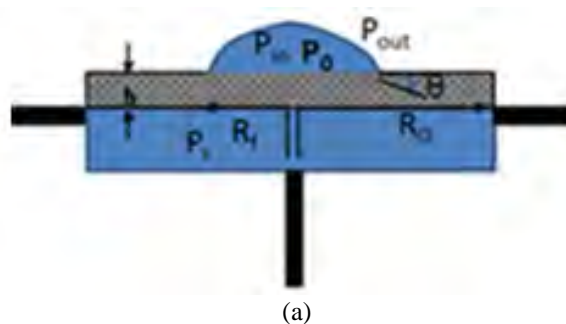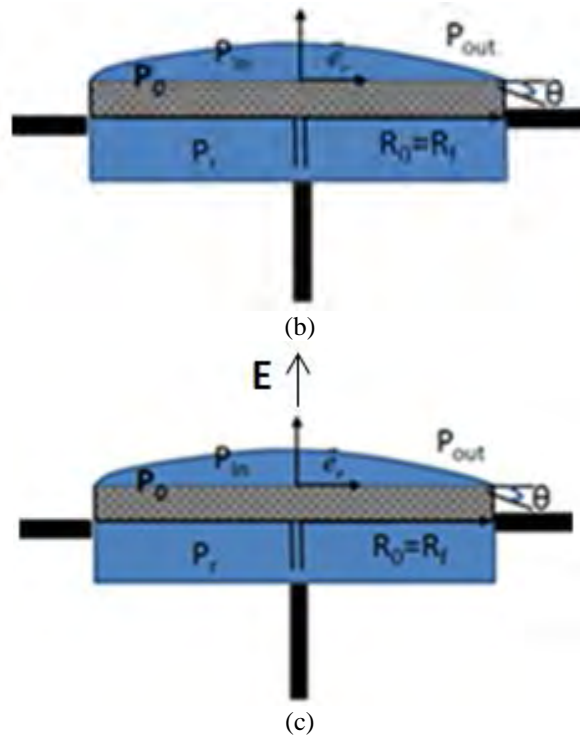
Fig. 4.10 Schematic of the present studied geometry and the anticipated static configurations for (a) partial and (b) full coverage of the top surface depending on the reservoir overpressure and (c) anticipated static configuration in the presence of an external electric field

Effect of Lorentz forces

The impact of the more relevant Lorentz forces was also investigated in the present study. The so-called "jxB effects" are anticipated to generate an additional effective overpressure leading to similar or even more deformed static configurations, depending on the magnitude of the magnetic field and the electric currents that enter the liquid metal layer. Thus, an externally applied constant magnetic field is added, **B**. In general, the liquid metal is anticipated to occupy the region within the pore, **Fig. 4.11a**, and, depending on the intensity of the Lorentz force, extend over a certain portion of the substrate, **Fig. 4.11b**. As a first approximation, the precursor layer and the surface forces, which were discussed in Chapter 1, are neglected. However, as will be detailed below, the latter are implicitly taken into account by fixing the contact angle rather than the contact point when the liquid metal exits from the pore and forms a thin "drop" on top of the CPS matrix.

(a)
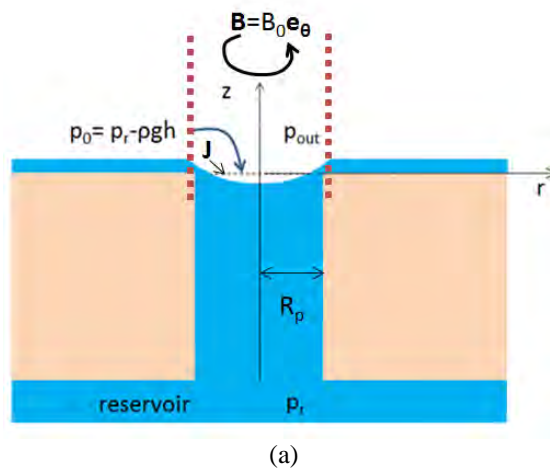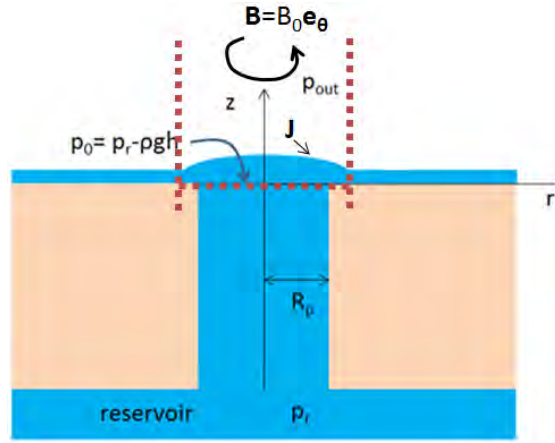
(b)

Fig. 4.11 Schematic of the anticipated static configurations for the liquid metal (a) trapped in the pore and (b) extended over the pore

Effect of the topography of the porous substrate

At near vacuum conditions, the film thickness reduces down to micron or even submicron sizes. In this regime, the interfaces overlap and, as a consequence, the nature of micro-scale interactions between the liquid metal film and the solid substrate cannot be ignored and needs to be considered. To this end, different forms of the interaction potential have to be tested in order to accommodate different types of surface forces. This kind of interactions has already been discussed in Chapter 2 which deals with wetting phenomena.

Hence, the envisioned static configuration is characterized by an almost uniform coverage of the CPS outer surface, **Fig. 4.12**, with the reservoir overpressure being slightly negative or positive. In the first consideration, i.e. when the overpressure is slightly negative, small indentations are expected near the pore region, while small swellings are anticipated for the second case as can be shown in **Figs. 4.13a** and **4.13b**, respectively. Such effects have been registered in experimental observations [86]. In this investigation, the distance between the pores is considered to be much greater than the pore radius. As a consequence, the static arrangement of the liquid metal can be studied in the vicinity of a single pore, **Fig. 4.14.**
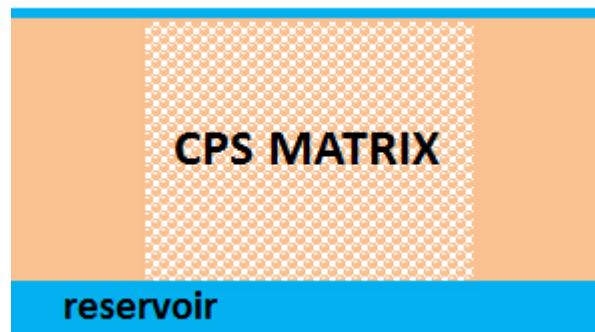
Fig. 4.12 Anticipated schematic arrangement of the CPS static configuration with an almost uniform coverage of the CPS outer surface

82

(a)

(b)
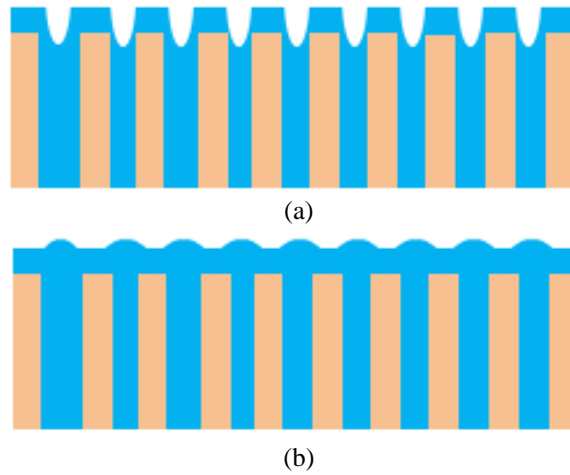
Fig. 4.13 Blow up of the region near the pores` "mouth" for (a) slightly negative or (b) slightly positive reservoir overpressures

(a)

(b)
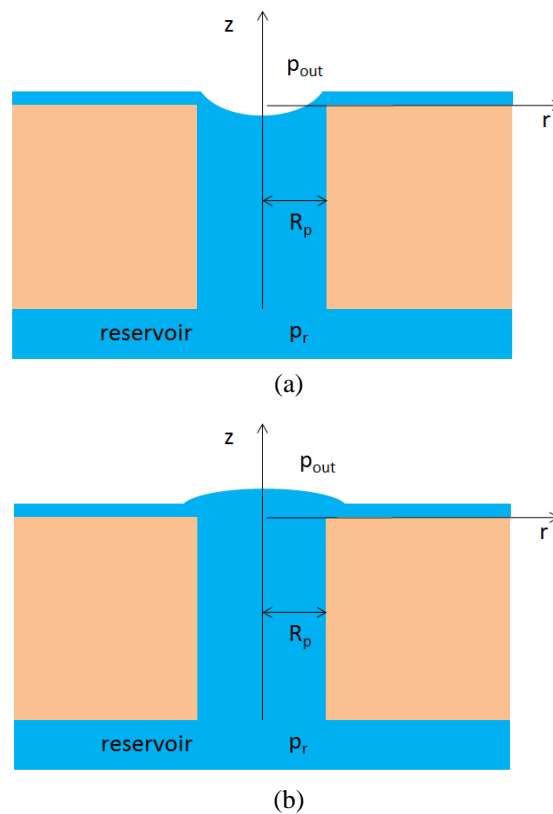
Fig. 4.14 Static arrangement of the liquid metal in the vicinity of a single pore for (a) slightly negative and (b) slightly positive reservoir overpressures

4.3 Modelling and mathematical formulation of the Replenishment Process

This section deals with the modelling as well as the mathematical formulation of the study of the flow in a single pore as a first attempt to provide an upper bound of the convective effects within the CPS matrix.

Liquids in general provided that they wet the material, of which the capillary is made, will be spontaneously and rapidly drawn into small-diameter tubes upon contact of one end of the open tube with the liquid. The driving force for this phenomenon is the surface tension, and the term "capillarity" as a synonym for surface tension effects was born of this observation, [70].

"Wicking" is the term that is used in literature for the spontaneous penetration of a liquid into a capillary under the action of surface tension. The simplest model of wicking is based upon flow into a long straight capillary, as depicted in **Fig. 4.15a**. The meniscus of the liquid-gas interface is a section of a sphere of radius R_s which is related to the capillary radius R_p and the contact angle, θ_d, as shown in **Fig. 4.15b**. A number of models of the wicking process are available in literature such as [87-90].

| (a) | (b) |
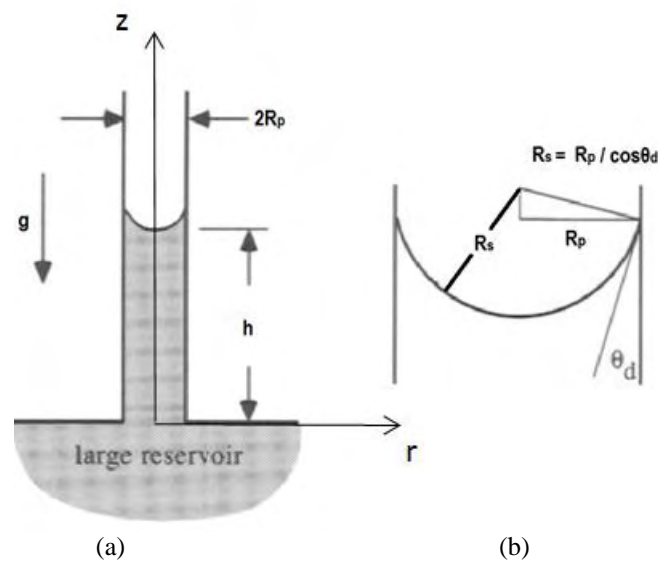
Fig 4.15 (a) Schematic of wicking into a single capillary and (b) The meniscus of the liquid-gas interface

The driving force for wicking is the capillary pressure P_c, which, for a small diameter capillary, is well approximated by using the Young-Laplace equation, namely the normal stress balance that holds on the liquid-gas interface. Assuming, as mentioned above, that the meniscus is a section of a spherical surface that intersects the capillary at a finite contact angle θ_d:

$$P_c = -\frac{2\gamma}{R_p}\cos\theta_d \tag{4.2}$$

where γ is the surface tension of the liquid. Note the sign on the pressure. The pressure is reduced by the (negative) curvature of this meniscus as one passes from the ambient medium just above the meniscus into the liquid. The dynamic contact angle θ_d may be

84

different from the equilibrium contact angle θ_c. Joos et al. [90] presented an experimental relationship between the dynamic contact angle and the equilibrium one. Besides, it is known that the dynamic contact angle depends upon the rate of flow of the liquid through the capillary, [90]. An elaborated literature review concerning capillary penetration dynamics can be found in [70].

Assuming that the capillary is vertical, as in **Fig. 4.15a,** and that the flow is opposed by gravity, the net pressure driving force is given by:

$$\Delta P = -\frac{2\gamma}{R_p}\cos\theta_d + \rho g h \tag{4.3}$$

Returning to the problem under investigation, a steady delivery of liquid metal via the porous matrix is investigated in this section. The pore is considered to be a long straight cylindrical capillary and in contact with a reservoir that provides the liquid metal, as shown in **Fig. 4.15a**. In this fashion, no external field forces are taken into account besides gravity. As mentioned above, this first principle analysis overestimates the permeability of the CPS. Nevertheless, it provides the framework for studying the interplay between the different forces that act towards pushing liquid lithium out of the porous matrix or resist its motion. Besides, it provides the replenishment speed on top of the porous structure which is considered to be in contact with plasma.

The pore is considered to be isothermal and evaporation effects are neglected. Emphasis is placed in studying the potential of the CPS system to act as a capillary pump against gravity and viscosity. A steady state configuration is sought for fixed height of the liquid metal column. The volumetric flow rate of liquid lithium is obtained along with the meniscus shape at the interface, for known interfacial tension, γ, and equilibrium contact angle, θ_c, known pressure drop and material properties. Hence, the hydrodynamic problem is examined in the context of axisymmetry in order to obtain an understanding of the operation principle of the capillary pump.

To this end the momentum equation is solved by neglecting the transient terms, assuming a quasi-steady pattern with the dynamics of the rising fluid passively following the time evolution of the meniscus:

$$\rho\left(\mathbf{u}\nabla\right)\mathbf{u} = -\nabla P + \rho\mathbf{g} + \mu\nabla\cdot\underline{\underline{\tau_v}} \tag{4.4}$$

along with continuity equation:

$$\frac{1}{r}\frac{\partial}{\partial r}\left(ru_r\right) + \frac{\partial u_z}{\partial z} = 0 \tag{4.5}$$

the kinematic condition stating that the normal velocity of the interface is the same as the normal fluid velocity evaluated at the interface:

$$\frac{\partial f}{\partial t}\frac{1}{\sqrt{1+z_r^2}} = \vec{u}\cdot\vec{n} = \frac{u_z - u_r\frac{\partial f}{\partial r}}{\sqrt{1+z_r^2}} \Rightarrow \frac{\partial f}{\partial t} + u_r\frac{\partial f}{\partial r} = u_z \tag{4.6}$$

85

and the normal stress balance on the liquid-gas interface:

$$P_{in}\underline{\underline{I}} - \mu\underline{\underline{\tau_v}} - P_{out}\underline{\underline{I}} = \gamma\nabla_s \cdot \mathbf{n} \tag{4.7}$$

In the above system of **Eqs.4.4-4.7**, ρ, μ and γ denote the fluid density, the dynamic viscosity and the surface tension of liquid lithium. Moreover, **u** is the vector of fluid velocity with u_r, u_z being its radial and axial components. Besides **g** represents the vector of gravity acceleration, f stands for the axial distance between the bottom of the capillary and the liquid-gas interface and $\underline{\underline{\tau_v}}$ the viscous stress tensor. This mathematical formulation incorporates the cylindrical coordinates due to the cylindrical geometry of the capillary. Thus, r and z denote the radial and axial coordinates, respectively. Note that $\frac{\partial}{\partial\varphi} = 0$ due to the axial symmetry around z axis. Thus, the flow arrangement is unchanged if rotated around z axis.

The dimensionless quantities are introduced:

$$\tilde{r} = \frac{r}{R_p}, \; \tilde{z} = \frac{z}{R_p}, \; \tilde{P} = \frac{P}{\gamma/R_p}, \tag{4.8a}$$
$$\tag{4.8b}$$

$$\hat{u} = \frac{\gamma R_p}{\mu h_0} \tag{4.8c}$$

$$\text{or } \hat{u} = \sqrt{\frac{\gamma}{\rho R_p}}$$

Eqs. 4.8b,c regarding $\hat{u}$ are derived via a force balance between surface tension forces and viscous or inertial forces, respectively. Besides, $\hat{u}$ derived via Eq. 4.8b is used when no inertial effects are taken into account while Eq. 4.8c when inertia forces dominate. The use of this discrimination is related to the dominant forces acting to the liquid metal capillary rise and is going to be discussed in detail in subsection 6.3.

Dropping bars for simplicity, the governing system of equations reads:

$$We(\mathbf{u}\nabla)\mathbf{u} = -\nabla(P + Bond \cdot z) + Ca\nabla \cdot \underline{\underline{\tau_v}} \tag{4.9}$$

along with continuity equation:

$$\frac{1}{r}\frac{\partial}{\partial r}(ru_r) + \frac{\partial u_z}{\partial z} = 0 \tag{4.10}$$

and kinematic condition:

$$\frac{\partial f}{\partial t} + u_r\frac{\partial f}{\partial r} = u_z \tag{4.11}$$

86

and the normal stress balance on the liquid-gas interface:

$$P_{in}\underline{\underline{I}} - Ca\underline{\underline{\tau}}_v - P_{out}\underline{\underline{I}} = \nabla_s \cdot \mathbf{n} \tag{4.12}$$

where $We = \dfrac{\rho\hat{u}^2 R_p}{\gamma}, Ca = \dfrac{\mu\hat{u}}{\gamma}, Bond = \dfrac{\rho g R_p^2}{\gamma}$ are the Webber, Capillary and Bond numbers representing the relative strength of inertial, viscous and gravitational forces to surface tension forces, respectively.

Multiplying both legs of Eq. 4.12 by $\mathbf{n}$ and using the following geometrical relationship in order to decrease the order of differentiation:

$$2H\mathbf{n} = \frac{\partial \mathbf{t}}{\partial s} - \frac{\mathbf{n}}{R_2} = -(\nabla_s \cdot \mathbf{n})\mathbf{n} \tag{4.13}$$

Eq. 4.12 results in:

$$\left(P_{in}\underline{\underline{I}} - Ca\underline{\underline{\tau}}_v - P_{out}\underline{\underline{I}} \right)\mathbf{n} = -\left(\frac{\partial \mathbf{t}}{\partial s} - \frac{\mathbf{n}}{R_2} \right) \tag{4.14}$$

where:

$$\mathbf{n} = \frac{-f_r\mathbf{e_r} + \mathbf{e_z}}{\sqrt{1+f_r^2}}, \ \mathbf{t} = \frac{\mathbf{e_r} + f_r\mathbf{e_z}}{\sqrt{1+f_r^2}}, \ R_2 = \frac{r\sqrt{1+f_r^2}}{-f_r} \tag{4.15}$$

which have been derived in Appendix B.

The pressure in the reservoir is set to P_r while symmetry conditions prevail at the axis of symmetry:

$$u_r(r=0,z) = 0, \quad \partial u_z/\partial r(r=0,z) = 0 \tag{4.16}$$

Finally the transverse velocity is set to zero at the pore entrance, $u_r(z=0,r) = 0$, whereas at the pore wall a slip length, ℓ, is allowed near the meniscus tip in order to accommodate the rise velocity of the liquid metal:

$$u_r(r=1,z;t) = 0, \quad u_z(r=1,z;t) = \frac{\partial f}{\partial t}(r=1;t)e^{-\frac{1-x}{\varepsilon}}, \quad \varepsilon = \frac{\ell}{R_p} \tag{4.17}$$

The above relationship ensures that the no-slip condition pertaining to the axial velocity at the wall is reinstated after a very small slip length ℓ. Variable x is introduced in order to fix the size of the mesh in the r, x plane within 0 and 1, as will be discussed in Chapter 5.

4.4 Static arrangement of the CPS: Modelling and mathematical formulation

This section deals with the modelling and the mathematical formulation of the static arrangement of the liquid metal in the context of CPS configuration. Each study, pertaining to the effects of reservoir overpressure, external field forces and topography of the porous substrate is modelled in a different subsection for a better understanding.

4.4.1 Effect of reservoir overpressure

First of all, the static arrangement of CPS is investigated as a function of the pressure difference between the reservoir and the surrounding medium and the physical properties of the employed liquid metal. In this study, a porous system is considered, shaped as a circular disk of small thickness, h_0, on the order of 1 mm. It is in contact with a reservoir that provides the liquid metal via a thin wick. Furthermore, isothermal conditions are considered and a liquid metal layer is assumed to have been established on top of the CPS, while the entire configuration has reached an axisymmetric static arrangement. As a first approximation, the CPS top surface is assumed to be flat. Nevertheless, in real experiments the topography of the top of the porous wafer is going to play an important role in the accomplishment of the static arrangement, as will be discussed later.

In the present study, the possibility is investigated for a static arrangement to be established with the liquid metal covering the top of the porous wafer. Moreover, the prediction of the thickness of the film which is formed on top of the porous structure, at static equilibrium, as well as the extent of its coverage, constitutes the scope of this analysis.

Fig. 4.16 illustrates the anticipated static arrangement as well as the interplay of the different forces acting on the liquid metal "drop". The surface tension forces, in the vicinity of the three phase contact line, tend to "pin" the liquid metal onto the solid substrate and, thus, stabilize it against pressure forces. In this context, the prevailing static arrangement will be a function of reservoir overpressure. In particular, for very large overpressures, or small liquid metal "drops", gravity is out of the picture. However, as the size of the "drop" increases, gravity becomes significant.
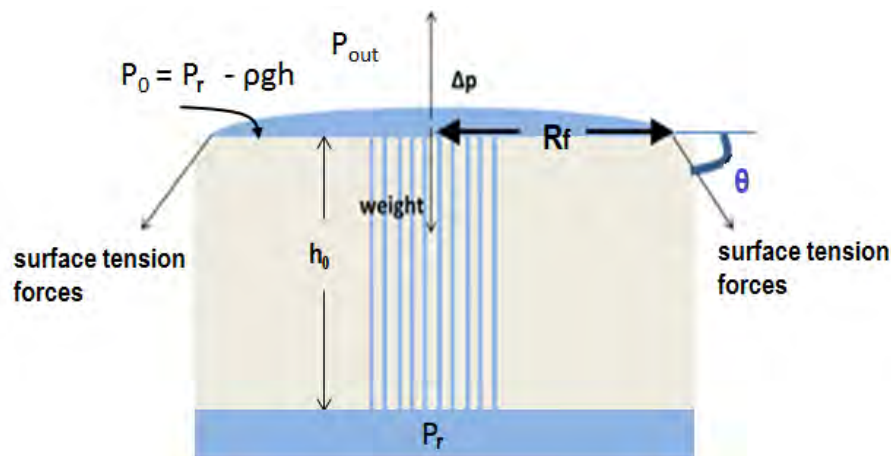
Fig. 4.16 Schematic of the anticipated static arrangement and depiction of the governing forces

As depicted in **Fig. 4.16**, the porous layer is assumed to be saturated with liquid metal before the liquid metal "drop" spreads to reach static equilibrium. This assumption is

88

corroborated by previous studies accounting for the spreading dynamics of a liquid drop on a saturated porous substrate [91] where the spreading process is shown to take place in a fashion similar to spreading on a dry solid. Moreover, for a thin enough porous substrate, the saturation process of the substrate takes place much faster than drop spreading, owing to the much larger capillary pressure inside a partly filled porous matrix in comparison with the drop; $\gamma / R_p \gg \gamma / R_f$; since $R_p \ll R_f$ with γ, R_p, R_f denoting the surface tension of the liquid metal, the pore radius and the radial extent of the liquid film, respectively. As a consequence, it can be safely assumed that static equilibrium will be achieved over a saturated substrate. Once the static arrangement is achieved, the pore size and the number of the pores do not affect the shape of the liquid metal layer, provided the thickness remains larger than a characteristic length δ_A determining the range of the interaction potential with the porous substrate.

The normal stress balance holds on the interface between the liquid metal and the surrounding medium at equilibrium:

$$\mathbf{n}\left(P_{in} - P_{out} \right)\underline{\underline{I}} + \mathbf{n}2H_c\gamma = 0 \tag{4.18}$$

where $\mathbf{n}$ is the normal unit vector of the interface in cylindrical coordinates obtained in Appendix B:

$$\mathbf{n} = \frac{\mathbf{e_z} - z_r\mathbf{e_r}}{\sqrt{1 + z_r^2}} \tag{4.19}$$

H_c signifies the mean curvature and $\underline{\underline{I}}$ the unit tensor. Finally, P_{out} represents the pressure at the surrounding medium and

$$P_{in} = P_0 - \rho g z, \; P_0 = P_r - \rho g h_0 \tag{4.20}$$

with P_r standing for the reservoir pressure and P_0 the pressure at top of the porous wafer, as shown in **Fig. 4.16**, whereas ρ signifies the fluid density of the liquid metal and g is the gravitational acceleration.

The governing boundary conditions concerning the shape of the interface $z = z(r)$ for cylindrical coordinates read:

$$r = 0: \; z_r = 0 \tag{4.21}$$
$$r = R_f: \; z = 0 \tag{4.22}$$

As long as the liquid metal "drop" partially covers the top of the porous substrate the contact angle is fixed to 30°, an angle in the range of those presented in [63]. As a consequence, partial wetting has been considered between the liquid metal and the substrate. This contact angle is set at the three phase contact line which has the form of circle in the present case due to axisymmetry. However, when the liquid metal covers the entire top surface a fixed contact point is imposed at $r = R_c$, with R_c denoting the CPS radius, rather than a fixed contact angle.

89

The normal stress balance, Eq. 4.18, and the corresponding boundary conditions, Eqs. 4.21 and 4.22, constitute the problem formulation. The z coordinate of the interface and the radial position of the contact point, R_f, are the unknowns of the problem that are obtained as a function of the imposed overpressure. Once the liquid metal covers the entire top surface of the wafer a fixed contact point condition is imposed and the z coordinate of the interface is the only unknown of the problem.

4.4.2 Effect of an externally applied electric field

As a first approach to assess the impact of field forces on the liquid metal layer covering the porous system, the effect of an external electric field is also considered that is aligned with the axis of symmetry of the porous wafer in the far field, **Fig. 4.10c**:

$$\mathbf{E} = -\nabla\Phi, \quad \mathbf{E}(\vec{r} \rightarrow \infty) = \mathrm{E}_0\mathbf{e_z} \tag{4.23}$$

with Φ denoting the electric potential. The evolution of the shape of the interface is of interest as the intensity of the electric field increases, aiming at identifying conditions for which electric stresses overwhelm adhesion forces and conical angle formation is obtained, [85,92].

The liquid metal is treated as a very electrically conducting material in comparison with the external medium, in which case the electric potential is constant inside it and we set $\in \equiv \in_{out} / \in_{in} << 1$, with $\in_{in}, \in_{out}$, representing the electric permittivity of the liquid metal and surrounding medium, respectively.

The normal stress balance on the interface between the liquid metal layer and the surrounding medium which holds at equilibrium, Eq. 4.18, is augmented with the electric stresses term, $\underline{\underline{\tau}}_{el}$:

$$\mathbf{n}\left[\left(P_{in} - P_{out} \right)\underline{\underline{I}} + \left(\underline{\underline{\tau}}_{el}^{out} - \underline{\underline{\tau}}_{el}^{in} \right) \right] + \mathbf{n}2H_c\gamma = 0 \tag{4.24}$$

where the terms "in" and "out" stand for the liquid metal and the surrounding medium, respectively.

The electric stresses can be expressed via the following relationship:

$$\underline{\underline{\tau}}_{el}^{i} = \in_i (\nabla\Phi_i\nabla\Phi_i - \frac{1}{2}\nabla\Phi_i \cdot \nabla\Phi_i \cdot \underline{\underline{I}})\mathbf{n} =$$
$$= \in_i \frac{1}{2}\left(\frac{\partial\Phi_i}{\partial n} \right)^2 \mathbf{n} - \in_i \frac{1}{2}\left(\frac{\partial\Phi_i}{\partial s} \right)^2 \mathbf{n} + \in_i \frac{\partial\Phi_i}{\partial s}\frac{\partial\Phi_i}{\partial n}\mathbf{t} \tag{4.25}$$

with the index "i" representing the "in" and "out" cases mentioned above. When an external electric field is applied, taking the "drop" to be very thin, i.e. z / R_f << 1:

$$\frac{\partial\Phi}{\partial n} \approx \frac{d\Phi}{dz} = E_0, \quad \frac{\partial\Phi}{\partial s} \approx \frac{d\Phi}{dz}\frac{dz}{ds} \tag{4.26}$$

90

The above assumption loses validity in the vicinity of the "drop" equator where the normal potential gradient, $\partial\Phi/\partial n$, is much smaller than its value at the pole, E_o. For comparable film thickness and length the boundary element method may be used to calculate the electric potential inside and outside the film [92-94] more accurately.

Upon the subtraction $\underline{\underline{\tau}}_{el}^{out} - \underline{\underline{\tau}}_{el}^{in}$ the tangential component becomes zero. Finally, in agreement with previous studies [85,92], the electric stresses term reads as:

$$\mathbf{n}\underline{\underline{\tau}}_{el} = \mathbf{n} \cdot \left(\underline{\underline{\tau}}_{el}^{out} - \underline{\underline{\tau}}_{el}^{in} \right) = \mathbf{n} \frac{1}{8\pi} E_n^2 \approx \mathbf{n} \frac{1}{8\pi} \frac{E_0^2}{1 + z_r^2} \tag{4.27}$$

Once the static arrangement is obtained, then the mass of the liquid metal that is pinned onto the substrate, m, is estimated via:

$$m = 2\pi\rho \int_0^{R_f} z(r) r \, dr \tag{4.28}$$

Then, the effect of the electric field on the static configuration is captured by setting the contact point at r = R_f while leaving the contact angle as an unknown. The latter is calculated in the post-processing phase of the numerical solution. In this fashion, the pressure difference is treated as an unknown and is obtained as part of the solution, for a given mass m of the adhered drop.

As mentioned before, via this investigation, a first attempt is made to capture the effect of external electromagnetic field forces on the liquid metal layer and, possibly, obtain plausible conjectures regarding its stability once plasma activity is "turned on" [95].

4.4.3 Effect of Lorentz forces

As mentioned in Chapter 1, the surface of any liquid metal PFC must remain stable when exposed to the plasma. Electrical currents in a PFC can arise from currents in the scrape-off-layer, eddy currents induced by plasma disruptions, or thermionic emission when the surface temperature is high enough.

Thus, in a tokamak environment, Lorentz forces arise due to the interaction of the currents entering into the liquid metal layer, with the magnetic field, which are referred as "jxB effects" in the literature. The CPS configuration aims to stabilize the liquid metal film, resting on top of the wafer, against these body forces mainly due to the surface tension forces mentioned before and illustrated in **Fig. 4.16.** CPS static film thickness is very small, on the order of μm`s, thus, decreasing the effects of electromagnetic forces in favor of film stability.

In order to incorporate the jxB effects in the formulation, an externally applied constant magnetic field is added in the azimuthal direction, $\mathbf{B}=B_0\mathbf{e_\theta}$, along with currents which "hit" on the liquid-plasma interface, as can be illustrated in **Fig. 4.17**. The magnetic field was added in the azimuthal direction as a first effort to capture and understand the mechanism via which even more deformed static configurations can be obtained leading to destabilization of the static liquid metal film or even drop ejection. Finally, at near

91

vacuum conditions the pressure in the reservoir is anticipated to be approximately equal to the pressure in the surrounding medium, thus, $P_r = P_{out}$.
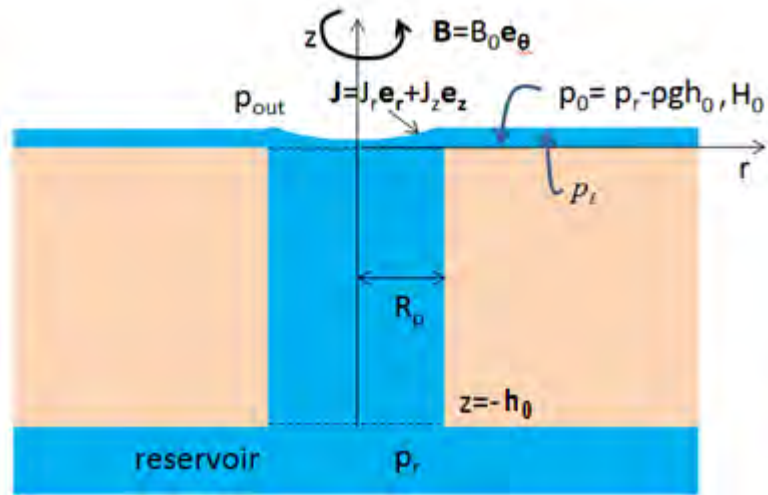
Fig. 4.17 Schematic of the studied geometry and the resulting anticipated static configuration in the presence of an externally applied magnetic field

According to Maxwell there are no magnetic monopoles. Consequently, and assuming also that the constant magnetic field is in the azimuthal direction:

$$\nabla \cdot \mathbf{B} = 0 \Rightarrow \nabla \cdot \left(B_0 \mathbf{e_\theta} \right) = \frac{1}{r} \frac{\partial B_0}{\partial \theta} = 0 \tag{4.29}$$

However, the curl of the vector field **B** is nonzero:

$$\nabla \times \mathbf{B} = \frac{1}{r} \frac{\partial}{\partial r} \left(r B_0 \right) \mathbf{e_z} = \frac{B_0}{r} \mathbf{e_z} \neq 0 \tag{4.30}$$

This may pose problems in the formulation by introducing fictitious currents. In order to circumvent this issue, following the analysis of Gao and Morley [96-97] the magnetic field can be decomposed into an applied and an induced magnetic field $\mathbf{B_0}$ and $\mathbf{B_i}$, respectively:

$$\mathbf{B} = \mathbf{B_0} + \mathbf{B}_i \tag{4.31}$$

Using the Ampere`s Law in order to determine the electric current we get:

$$\mathbf{J} = \frac{\nabla \times \mathbf{B}_i}{\mu_m} = \nabla \times \mathbf{H} \tag{4.32}$$

where **H** serves as a stream function for the emerging electric current, so that we can avoid any spurious currents associated with a rotational applied magnetic field. Moreover, μ_m stands for the magnetic permeability of the liquid metal.

The Lorentz force then reads:

92

$$\mathbf{F_L} = \mathbf{J} \times \mathbf{B} = (\nabla \times \mathbf{H}) \times \mathbf{B}_0 \tag{4.33}$$

Both **H** and **B₀** are considered to lie along $\mathbf{e_\theta}$. Then, $\mathbf{H} = H\mathbf{e_\theta}$ and

$$\mathbf{F_L} = (\nabla \times \mathbf{H}) \times \mathbf{B}_0 = \left(-\frac{\partial H}{\partial z}\mathbf{e_r} + \frac{1}{r}\frac{\partial(rH)}{\partial r}\mathbf{e_z} \right) \times B_0\mathbf{e}_\theta \Rightarrow$$

$$\mathbf{F_L} = -\frac{\partial \mathrm{H}}{\partial z}B_0\mathbf{e_z} - \frac{B_0}{r}\frac{\partial(rH)}{\partial r}\mathbf{e_r} \tag{4.34}$$

The above form of the Lorentz forces can be viewed as a manifestation of the Maxwell stresses [98] decomposed in the magnetic pressure and rotational parts. Equating the electric currents provided by Ampere`s and Ohm`s Law:

$$\mathbf{J} = \nabla \times \mathbf{H} = \sigma(\mathbf{u} \times \mathbf{B}) \Rightarrow$$
$$\Rightarrow \nabla \times (\nabla \times \mathbf{H}) = \sigma\nabla \times (\mathbf{u} \times \mathbf{B}) \Rightarrow$$
$$\Rightarrow \frac{\nabla\left(\overset{=0}{\nabla \cdot \mathbf{H}}\right)}{\sigma} - \frac{\nabla^2\mathbf{H}}{\sigma} = \mathbf{u}\left(\overset{=0}{\nabla \cdot \mathbf{B}}\right) - \mathbf{B}\left(\overset{=0}{\nabla \cdot \mathbf{u}}\right) + (\mathbf{B}\nabla)\mathbf{u} - (\mathbf{u}\nabla)\mathbf{B} \Rightarrow \tag{4.35}$$
$$\Rightarrow \frac{\nabla^2\mathbf{H}}{\sigma} = (\mathbf{u}\nabla)\mathbf{B} - (\mathbf{B}\nabla)\mathbf{u}$$

where σ is a material-dependent parameter called electrical conductivity.

For static equilibrium u=0. As a consequence:

$$\nabla^2\mathbf{H} = 0 \Rightarrow \left\{ \frac{\partial}{\partial r}\left[\frac{1}{r}\frac{\partial(rH)}{\partial r} \right] + \frac{\partial^2 H}{\partial z^2} \right\}\mathbf{e_\theta} = 0 \Rightarrow$$
$$\Rightarrow \frac{\partial^2 H}{\partial r^2} + \frac{1}{r}\frac{\partial H}{\partial r} + \frac{\partial^2 H}{\partial z^2} = \frac{H}{r^2} \Rightarrow \tag{4.36}$$
$$\Rightarrow \nabla^2 H = \frac{H}{r^2}$$

When there is motion:

$$\frac{\nabla^2\mathbf{H}}{\sigma} = (\nabla^2 H - \frac{H}{r^2})\frac{\mathbf{e_\theta}}{\sigma} =$$
$$= u_r\frac{\partial}{\partial r}\left[(B_0 + \mu_m H)\mathbf{e_\theta}\right] + u_z\frac{\partial}{\partial z}\left[(B_0 + \mu_m H)\mathbf{e_\theta}\right] - \frac{B_0 + \mu_m H}{r}\frac{\partial}{\partial\theta}\left[u_r\mathbf{e_r} + u_z\mathbf{e_z}\right] \Rightarrow$$
$$\Rightarrow (\nabla^2 H - \frac{H}{r^2})\frac{\mathbf{e_\theta}}{\sigma} = u_r\frac{\partial(B_0 + \mu_m H)}{\partial r}\mathbf{e_\theta} + u_z\frac{\partial(B_0 + \mu_m H)}{\partial z}\mathbf{e_\theta} - \frac{B_0 + \mu_m H}{r}u_r\mathbf{e_\theta} \Rightarrow \tag{4.37}$$
$$\Rightarrow \frac{1}{\sigma}(\nabla^2 H - \frac{H}{r^2}) = u_r\frac{\partial(\mu_m H)}{\partial r} + u_z\frac{\partial(\mu_m H)}{\partial z} - \frac{B_0 + \mu_m H}{r}u_r$$

93

However, if $B_0 \gg \mu_m H$ then:

$$\frac{1}{\sigma}(\nabla^2 H - \frac{H}{r^2}) = -\frac{B_0}{r} u_r \qquad (4.38)$$

Lithium is a paramagnetic material. Paramagnetic materials are slightly attracted by a magnetic field and the material does not retain the magnetic properties when the external field is removed. Finally, they have a small, positive susceptibility to magnetic field ($\chi_{m,Li}$=1.4 $\cdot 10^{-5}$). Thus, $\mu_m = \mu_0 (\chi_{m,Li} +1)$= 4.000056$\pi \cdot 10^{-7}$ N/A^2, where μ_m, μ_0 are the magnetic permeabilities of liquid lithium and free space, respectively. In view of the above very small value of the magnetic permeability of lithium, the assumption of small magnetic induction is validated for a magnetic field intensity, B_0, on the order of several Tesla.

Returning to the flow arrangement that is the subject of this consideration, as a first approach the rotational part of the magnetic stress is neglected so that emphasis can be placed on the effect of Lorentz forces on the static arrangement. It should be stressed, however, that this static arrangement is not strictly valid as it suffers from the drawback that it does not account for the recirculation triggered by the rotational part of the Lorentz force. Clearly, as the external electric current increases the importance of convective effects and the resulting rotational motion increases and has to be taken into consideration. Nevertheless, it is anticipated that the location of the interface predicted in this fashion will not be significantly different from the one obtained by incorporating the equations of motion within the pore in the model. In fact, for relatively small electric current intensities the emerging rotational motion will be very weak to affect the final result which will be determined by the magnetic pressure component of the Maxwell stresses.

In this context, the interfacial normal stress balance reads:

$$P_\ell - P_{out} = \gamma \nabla_s \cdot \mathbf{n} \qquad (4.39)$$

where P_ℓ is the pressure on the liquid-gas interface and P_{out} the external pressure, as can be shown in **Fig. 4.17**.

In the bulk of the liquid metal a Poisson-type equation holds, Eq. 4.36, while the Navier-Stokes equations augmented with the Lorentz Forces, estimated in Eq. 4.34 are:

$$0 = -\nabla P + \rho\mathbf{g} + \underbrace{\left[-B_0 \frac{\partial H}{\partial z}\mathbf{e_z} - \frac{B_0}{r}\frac{\partial (rH)}{\partial r}\mathbf{e_r}\right]}_{\mathbf{F_L}} \Rightarrow$$

$$\Rightarrow 0 = -\nabla(P + \rho gz) - \nabla(B_0 H) - \frac{B_0 H}{r}\mathbf{e_r} \Rightarrow \qquad (4.40)$$

$$\Rightarrow \nabla(P + \rho gz + B_0 H) = -\frac{B_0 H}{r}\mathbf{e_r}$$

94

Hence, upon neglecting the rotational part of the Lorentz force we obtain in the z direction:

$$\frac{\partial}{\partial z}\left(P + \rho g z + B_0 \mathrm{H}\right) = 0 \Rightarrow P_\ell + \rho g z + B_0 \mathrm{H}_{\text{int}} = P_{z=0} + B_0 \mathrm{H}_{z=0} \Rightarrow$$

$$\Rightarrow P_\ell = P_{z=0} - \rho g z + B_0 \left(\mathrm{H}_{z=0} - \mathrm{H}_{\text{int}}\right) \tag{4.41}$$

where $P_{z=0}$ represents the pressure on z = 0 plane and $\mathrm{H}_{z=0}$ and H_{int} denote the value of H on z=0 plane and on the liquid-gas interface, respectively.

Eventually, the normal stress balance at the interface reads:

$$P_{z=0} - \rho g z + B_0 \left(\mathrm{H}_{z=0} - \mathrm{H}_{\text{int}}\right) - P_{out} = \gamma \nabla_s \cdot \mathbf{n} \tag{4.42}$$

where $B_0 \left(\mathrm{H}_{z=0} - \mathrm{H}_{\text{int}}\right)$ is an extra pressure related to Lorentz forces.

Davidson [98] gives one other aspect of Lorentz forces via Maxwell stresses representation. In his analysis he expresses Lorentz forces as:

$$\mathbf{F_L} = \mathbf{J} \times \mathbf{B} = \left(\mathbf{B} \cdot \nabla\right)\left(\mathbf{B}/\mu_m\right) - \nabla\left(\mathbf{B}^2/2\mu_m\right) \tag{4.43}$$

The second term on the right of Eq. 4.43 acts on the fluid in exactly the same way as the pressure force. If the magnetic field is irrotational, it makes no contribution to the vorticity equation. In flows without a free surface its role is simply to augment the fluid pressure. Its absence from the vorticity equation implies that it cannot influence the flow field. For this reason, $\mathbf{B}^2/2\mu_m$ is called the magnetic pressure and in many, if not most, problems it is of no dynamical significance.

Considering the first term on the right of Eq. 4.33 the ith component of this force is:

$$\left(\mathbf{B} \cdot \nabla\right)\left(\mathbf{B}_i/\mu_m\right) = \frac{\partial}{\partial x_j}\left(\frac{B_i B_j}{\mu_m}\right) \tag{4.44}$$

where there is an implied summation over the index j. From this, according to Davidson, it can be shown that the effect of the body force in Eq. 4.44 is exactly equivalent to a distributed set of fictitious stresses, $B_i B_j / \mu_m$, acting on the surface of fluid elements. One approach is simply to compare Eq. 4.44 with the viscous forces, $\partial \tau_{ij}/\partial x_j$ in momentum balance equation. Davidson deduces that Lorentz forces can be replaced by an imaginary set of stresses:

$$\tau_{ij} = \left(\frac{B_i B_j}{\mu_m}\right) - \left(\frac{\mathbf{B}^2}{2\mu_m}\right)\delta_{ij} \tag{4.45a}$$

where $\delta_{i,j}$ denotes that if i = j then $\delta_{i,j}$ = 1 while if i $\neq$ j then $\delta_{i,j}$ = 0. These stresses, describing by Eq. 4.44, are called the Maxwell stresses and their utility lies in the fact that

95

we can represent the integrated effect of a distributed body force via stresses exerted on the surface of fluid elements.

A more general form of Maxwell stress tensor, in S.I. units, including also electric stresses, is given by:

$$\tau_{ij} = \left(E_i E_j - \frac{1}{2}\delta_{ij}E^2 \right) + \left(B_i B_j - \frac{1}{2}\delta_{ij}B^2 \right) \tag{4.45b}$$

However, when the Maxwell stresses include a rotational part, as in our case, Eq. 4.34, the resulting Lorentz force may drive a recirculating flow preventing static configuration to be established. As a matter of fact, this recirculating flow can act in favor of power exhaust in the divertor region via the convection heat transfer mechanism.

Returning to the static problem under investigation, as mentioned above, the liquid metal layer is anticipated to occupy the region within the pore and, depending on the intensity of the external magnetic field, B_0, and the electric currents entering the liquid metal layer from the surrounding plasma, extend over a certain portion of the substrate, as depicted in **Fig. 4.11**. In both considerations, i.e. static configuration for the liquid metal (a) being trapped within the pore and (b) extended over the pore, the system of equations to be solved are formed by the Poison-type Eq. 4.36 and the normal stress balance equation, Eq. 4.42, along with the boundary conditions which are going to be discussed below.

(a) Static configuration for the liquid metal trapped in the pore
In this context, the axisymmetric static arrangement of the liquid metal being "trapped" within the pore, **Fig. 4.11a**, is investigated imposing a fixed contact point at the pore`s edge. The cylindrical coordinates are used in order to conform with the geometry of the problem. The line, surface and volume elements, the del operator as well as the derivation of the unit vectors and curvatures concerning cylindrical coordinates are elaborated in Appendix B.

The boundary conditions concerning the current density J are summarized below. As a first approximation, insulated walls are considered:

$$r = R_p, \quad -h_0 \le z \le 0 : J_r = 0 \tag{4.46a}$$

Also, due to symmetry at r = 0:

$$r = 0 : J_r = 0 \tag{4.46b}$$

Finally, on the interface z = z(r) a known current density exists:

$$\mathbf{J} = J_r \mathbf{e_r} + J_z \mathbf{e_z} \tag{4.46c}$$

At z = -h_0 J can be calculated based on the conservation of the electric current:

$$\int_{\text{int}} \mathbf{J} \cdot \mathbf{n}\, dA = \int_{z=-h_0} \mathbf{J} \cdot \mathbf{n}\, dA \Rightarrow J = \frac{2\int_0^{R_p} (J_z - J_r z_r)\, r dr \Big|_{Int}}{R_p^2} \tag{4.46d}$$

96

Assuming a very large pore length compared to its radius, at z = - h$_0$:

$$H = H(\text{r}),\ J_r = 0$$

$$J_z = \frac{1}{r}\frac{\partial(rH)}{\partial r} \overset{J_z = J}{\Rightarrow}$$

$$\Rightarrow rJ = \frac{\partial(rH)}{\partial r} \Rightarrow \frac{r^2 J}{2} + c \overset{c=0}{=} rH \Rightarrow$$

$$\Rightarrow H = \frac{rJ}{2} \tag{4.47a}$$

Hence, at r = R$_p$ and -h$_0 \leq z \leq 0$ we have that:

$$H = \frac{R_p J}{2} \tag{4.47b}$$

while at *r = 0*:

$$H = 0 \tag{4.47c}$$

Finally, a Robin-type boundary condition holds on the interface:

$$\frac{\partial H}{\partial n} = \nabla H \cdot \mathbf{n} = \frac{-\dfrac{\partial H}{\partial r}z_r + \dfrac{\partial H}{\partial z}}{\sqrt{1+z_r^2}} = \frac{-\left(J_z - \dfrac{H}{r}\right)z_r - J_r}{\sqrt{1+z_r^2}} \tag{4.47d}$$

The boundary conditions described by Eqs. 4.47a-4.47d along with the depiction of the fixed contact point discussed above are illustrated in **Fig. 4.18**. As was above mentioned this simplified study is a first attempt to obtain the effect of the Lorentz forces on the liquid metal/plasma interface.
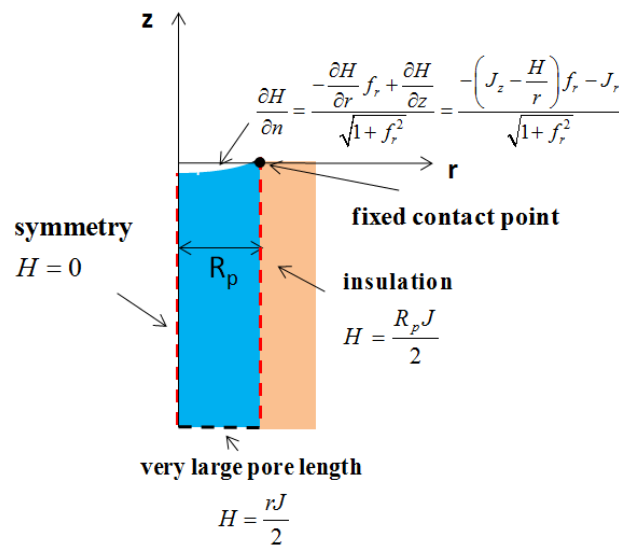
Fig. 4.18 Schematic of the studied geometry with the liquid metal being trapped in the pore along with the boundary conditions pertaining to H

(b) Static configuration for the liquid metal covering the pore
Secondly, the axisymmetric static arrangement of the liquid metal extended over the pore, **Fig. 4.11b**, is investigated imposing a fixed contact angle rather than a fixed contact point. As a matter of fact, the value of this contact angle is prescribed by the interaction potential between the liquid metal and the solid substrate as will be discussed in detail in the results section. Hence, the micro-scale surface forces are implicitly taken into account by fixing the contact angle. The spherical coordinates are used due to the geometry of the problem. The line, surface and volume elements, the del operator as well as the derivation of the unit vectors and curvatures concerning the spherical coordinate system are described in Appendix C.

The studied geometry along with the boundary conditions pertaining to H are illustrated in **Fig. 4.19**.
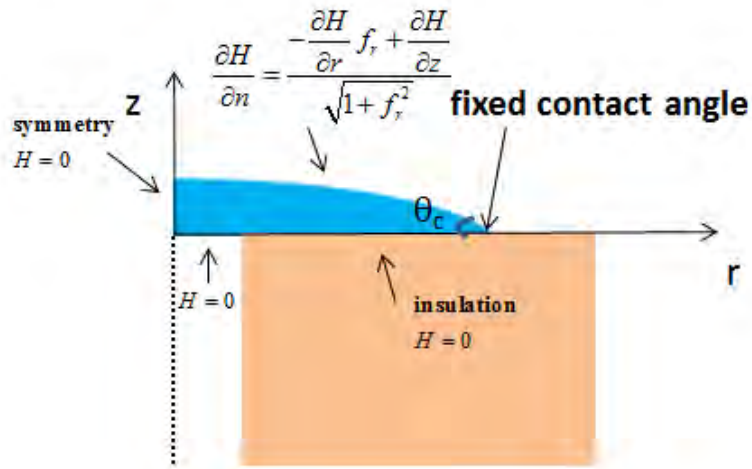
Fig. 4.19 Schematic of the studied geometry with the liquid metal extended over the pore along with the boundary conditions pertaining to H

4.4.4 Effect of the topography of the porous substrate
In this study, we do not assume the classic partial wetting case, i.e. liquid lithium with a dry substrate beyond the contact point, as presented in Chapter 2. The classic partial wetting case cannot be assumed, because it is not possible to obtain such a static solution at near vacuum conditions ($P_r \approx P_{out.}$) for a CPS thickness of 1mm, a pore size on the order of 30 μm and a contact angle $\theta = 30^{\circ}$. Such a static configuration would require an unrealistically tall liquid metal column of, roughly, $h = 2\gamma \cos\theta / (\rho g R_p) \approx 4.5m$ that would not be useful, in terms of stability, in protecting the CPS structure and the divertor below.

As mentioned above, the envisioned static configuration is characterized by full coverage of the CPS outer surface whether the pressure difference $\Delta P = P_0 - P_{out}$ is slightly positive or slightly negative. The latter case pertains to the situation after replenishment has taken place but without considering the Lorentz forces. In this regime, coatings rather than films should be considered covering the entire CPS wafer and, thus, micro-scale liquid-solid interactions, known as surface forces, need to be accounted for as analyzed in Chapter 2. In particular, in terms of finding a proper interaction potential fitting with the current study, firstly a purely repulsive potential was incorporated, which was found not

98

to be compatible with the current investigation, and secondly a long range attractive short range repulsive potential.

A manifestation of the action of surface forces is the disjoining pressure, Π [53,54,57]. Although this term is a bit misleading, since the surface force can be either disjoining (repulsion between surfaces) or conjoining (attraction between surfaces), it is used for historical reasons.

Purely repulsive potential
The aforementioned purely repulsive potential, based on summing individual London–van der Waals interactions between molecules pair-by-pair, is described via:

$$W(\delta) = \frac{A}{12\pi\delta^2} \qquad (4.48)$$

The constant A is the so-called Hamaker constant and it depends upon the properties of the three phases. The constant A can be positive indicating a purely repulsive potential, incorporated in this study, or negative, thus, indicating a purely attractive potential.

The corresponding disjoining pressure, Π, can be calculated from:

$$\Pi(\delta) = -\frac{dW(\delta)}{d\delta} = \frac{A}{6\pi\delta^3} \qquad (4.49)$$

For films satisfying such an expression, and for A > 0, Π increases as the film thickness grows small. Thus, van der Waals forces could support a finite film thickness under conditions that classical continuum physics would not permit.

The interaction potential along with the corresponding disjoining pressure as a function of the film thichness, for the case of a perfectly flat solid surface, are illustrated in **Fig. 4.20** for a typical Hammaker constant value, $A = 10^{-18}$ Nm :
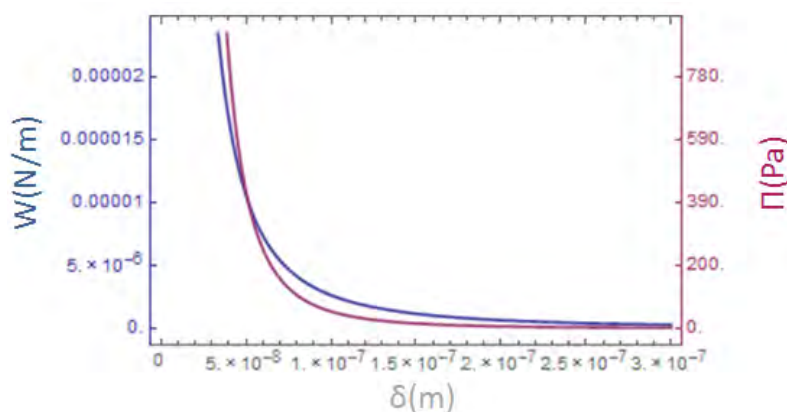
Fig 4.20 Case of purely repulsive potential: Interaction potential, W, and the corresponding disjoining pressure, Π, as a function of the film thickness for $A=10^{-18}$ Nm

Long range attractive short range repulsive potential
A Lennard–Jones type potential, as a simple way to approximate strong repulsion at short distances between the liquid and the solid phases, and attraction at intermediate distances, is considered in this subsection. This consideration seems to give more realistic results

99

comparing to the previous one. However, certainly better forms of the potential of the liquid-solid interactions may be incorporated based on the available literature.

Hence, this kind of micro-scale liquid-solid interactions results in a disjoining pressure for the purpose of stabilizing a thin liquid metal layer upon the porous wafer. This interaction potential is described via:

$$W = W_{.0}\left[\left(\frac{\delta_A}{\delta}\right)^4 - 2\left(\frac{\delta_A}{\delta}\right)^2\right] \tag{4.50}$$

with W_0 signifying the wetting parameter, which is directly related with the solid wettability (an increase of W_0 indicates stronger liquid-solid interaction) and δ_A representing a characteristic length scale for which the energy is minimized and the interaction force vanishes. Constants 4 and 2, were selected so that the disjoining pressure Π is positive at distances $\delta < \delta_A$, indicating repulsion, and negative at distances δ from the substrate that are larger than the characteristic scale δ_A, indicating attraction. The constants 4 and 2 are typical selections that can be modified based on the nature of the interacting materials. The interaction potential W becomes insignificant at distances that are significantly larger than δ_A.

The corresponding disjoining pressure, Π, can be calculated from:

$$\Pi(\delta) = -\frac{dW(\delta)}{d\delta} = \frac{4W_{.0}}{\delta_A}\left[\left(\frac{\delta_A}{\delta}\right)^5 - \left(\frac{\delta_A}{\delta}\right)^3\right] \tag{4.51}$$

The interaction potential of this kind along with the corresponding disjoining pressure as a function of the film thichness, for the case of a perfectly flat solid surface, are illustrated in **Fig. 4.21** for $W_0 = 0.05$ N/m and $\delta_A = 50$ nm.
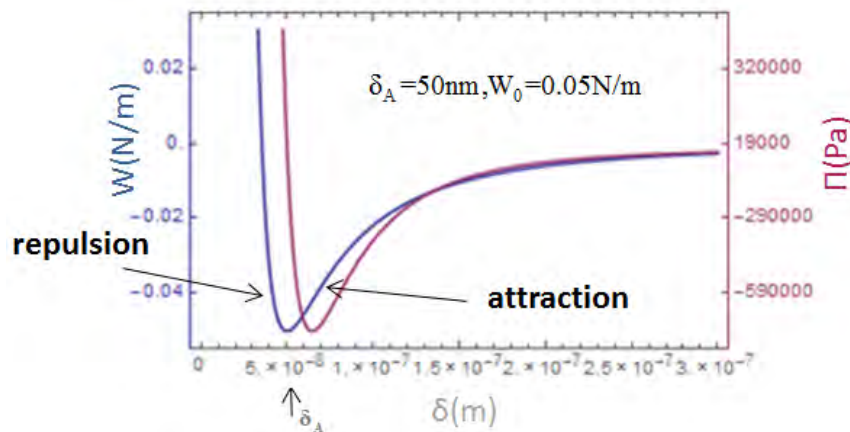
Fig 4.21 Case of long range attractive short range repulsive potential: Interaction potential, W, and the corresponding disjoining pressure, Π, as a function of the film thickness for $W_0 = 0.05$ N/m and $\delta_A = 50$ nm

In the case of a perfectly flat solid surface, the distance δ is defined as the vertical distance of the liquid surface from the solid boundary, see also the configuration depicted in **Fig 2.5**. For non-flat, rough, solid surfaces, the definition of distance, δ, requires special consideration. Here, δ represents the Euclidean distance between the liquid-plasma interface and the solid substrate. As mentioned in Chapter 2, this quantity can also

be obtained via the solution of the Eikonal equation, as proposed by studies such as [60,62].

The disjoining pressure term in both cases investigated in this study (purely repulsive potential and a long range attractive short range repulsive potential) was calculated via Eq. 4.52:

$$\Pi = -\frac{\partial W}{\partial \mathbf{n}} = -\frac{\partial W}{\partial \delta}\frac{\partial \delta}{\partial \mathbf{n}} = -\frac{\partial W}{\partial \delta}\nabla \delta \cdot \mathbf{n} \tag{4.52}$$

where $\mathbf{n}$ represents the normal unit vector pointing out of the liquid-gas interface and away from the solid substrate, see also **Fig 2.5**, in such a way that $\partial \delta / \partial \mathrm{n} = 1$ for a flat substrate. As deduced in Appendix B, for cylindrical coordinates and Eulerian representation for the liquid-gas interface the normal vector assumes the form:

$$\mathbf{n} = \frac{-z_r \mathbf{e_r} + \mathbf{e_z}}{\sqrt{1 + z_r^2}} \tag{4.53}$$

Hence, in the absence of an external field forces, the surface forces enter the normal force balance on the interface in the form of a disjoining pressure Π:

$$P_0 - \rho g z + \Pi - P_{out} = -(\gamma + W_0)2H_c \tag{4.54}$$

Note that if the case of Lorentz forces is to be considered, the left hand side of Eq. 4.54 can be augmented with the magnetic pressure term, $B_0\left(\mathrm{H}_{z=0} - \mathrm{H}_{int}\right)$. Moreover, if the case of electric stresses is to be taken into account the left hand side of Eq. 4.54 can be augmented with the electric stresses term, $\dfrac{1}{8\pi}\dfrac{E_0^2}{1 + z_r^2}$.

Using Lagrangian rather than Eulerian representation for the liquid-gas interface the normal unit vector reads:

$$\mathbf{n} = \frac{-z_\xi \mathbf{e_r} + r_\xi \mathbf{e_z}}{S_\xi}, \; S_\xi = \sqrt{r_\xi^2 + z_\xi^2} \tag{4.55}$$

Furthermore, H_c in Eq. 4.54 is the mean curvature which is, according to Appendix B, defined by:

$$-2H_c = \nabla_s \cdot \mathbf{n} = \frac{-z_\xi}{rS_\xi} - \frac{r_\xi z_{\xi,\xi} - r_{\xi,\xi} z_\xi}{S_\xi^3} \tag{4.56}$$

The system of the governing equations of the problem comprises the Eq. 4.54 along with the condition for generating an equidistant mesh along the interface. The boundary conditions imposed in this problem are going to be elaborated in subsection 5.4.5.

Chapter 5: Numerical Analysis

In this chapter, a brief description is given concerning the numerical methodology that was employed in order to solve selected problems related to the CPS static and dynamic configuration as modelled in Chapter 4. In particular, the Finite Element Methodology is used for the purpose of discretizing the governing nonlinear differential equations, while the resulting set of algebraic equations is solved via the Newton-Raphson method until convergence. Simple or arc-length continuation is utilized depending on the existence or not of a limit point in the emerging solution family. Finally, benchmark calculations are conducted in order to investigate the validity of the above numerical models.

5.1 Finite Element Methodology

The Finite Element Method is a technique in which a given domain is represented as a collection of simple domains, called finite elements, so that it is possible to systematically construct the approximation functions needed in a variational or weighted-residual approximation of the solution of a problem over each element. For a typical problem, according to Reddy [99], the basic steps involved in the finite element analysis of a problem are the following ones:

1. Discretization of the given domain into a collection of preselected finite elements.
    a. Construct the finite element mesh of preselected elements.
    b. Number the nodes and elements.
    c. Generate the geometric properties (e.g., coordinates and cross-sectional areas) needed for the problem.
2. Derivation of element equations for all typical elements in the mesh.
    a. Construct the variational formulation of the given differential equation over the typical element.
    b. Assume that a typical dependent variable u is of the form $u = \sum_i u_i \psi_i$

       and substitute it into Step 2a to obtain element equations in the form $\left[K^e \right] \left(u^e \right) = \left(F^e \right)$
    c. Derive or select element interpolation functions ψ_i and compute the element matrices.
3. Assembly of element equations to obtain the equations of the whole problem.
    a. Identify the interelernent continuity conditions among the primary variables by relating element nodes to global nodes. Construct the variational formulation of the given differential equation over the typical element.
    b. Identify the "equilibrium" conditions among the secondary variables.
    c. Assemble element equations using Steps 3a and 3b.
4. Imposition of the boundary conditions of the problem.
    a. Identify the specified global primary degrees of freedom.
    b. Identify the specified global secondary degrees of freedom.
5. Solution of the assembled equations.
6. Post-processing of the results.

5.2 Approximation of the solution - Basis Functions

The approximation solution u^e should fulfill certain requirements in order to be convergent to the actual solution u as the number of elements is increased. These are:

1. The approximate solution should be continuous over the element, and differentiable, as required by the weak form.
2. It should be a complete polynomial, i.e., include all lower-order terms up to the highest order used.
3. It should be an interpolant of the primary variables at the nodes of the finite element.

5.2.1 The Lagrangian quadratic shape functions

A quadratic approximation is of the form:

$$u^e_{h_e} = c^e_1 + c^e_2 x + c^e_3 x^2 \tag{5.1}$$

where h_e stands for the length of the element, e, which requires three nodes. Two of the nodes are identified as the endpoints of the element to define the geometry, and the third node is taken interior to the element. In this study, the midpoint of the element, being equidistant from the end nodes, was selected. In terms of the three nodal values, (u_1, u_2, u_3) we have:

$$u_1 = c_1 + c_2 x_1 + c_3 x_1^2 \tag{5.2}$$
$$u_2 = c_1 + c_2 x_2 + c_3 x_2^2 \tag{5.3}$$
$$u_3 = c_1 + c_2 x_3 + c_3 x_3^2 \tag{5.4}$$

Solving the algebraic system of Eqs. 5.2-5.4 c_1, c_2, c_3 can be found. Hence, $u^e_{h_e}$ can be written as:

$$u^e_{h_e} = \sum_{i=1}^{3} u_i b_i \tag{5.5}$$

where:

$$b_1\left(x\right) = \frac{x - x_2}{x_1 - x_2} \frac{x - x_3}{x_1 - x_3}$$

$$b_2\left(x\right) = \frac{x - x_1}{x_2 - x_1} \frac{x - x_3}{x_2 - x_3} \tag{5.6}$$

$$b_3\left(x\right) = \frac{x - x_1}{x_3 - x_1} \frac{x - x_2}{x_3 - x_2}$$

The reference element can be converted from the global to the local coordinate system, as depicted in Fig. 5.1, using the formula:

104

$$\xi = \frac{2x - (x_a + x_b)}{\underbrace{x_b - x_a}_{h_e}} \Rightarrow$$

$$\Rightarrow x = \frac{\xi h_e}{2} + \frac{x_a + x_b}{2}$$

(5.7)
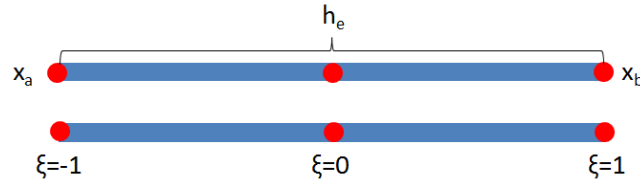
Fig. 5.1 Typical 3-node finite element and its conversion from the global to the local coordinate system

Thus, the Lagrangian quadratic shape functions in terms of ξ ($0 < \xi < 1$) are:

$$b_1(\xi) = \frac{\xi(\xi - 1)}{2}$$
$$b_2(\xi) = 1 - \xi^2$$
$$b_3(\xi) = \frac{\xi(\xi + 1)}{2}$$

(5.8)

and can be illustrated in **Fig. 5.2**:
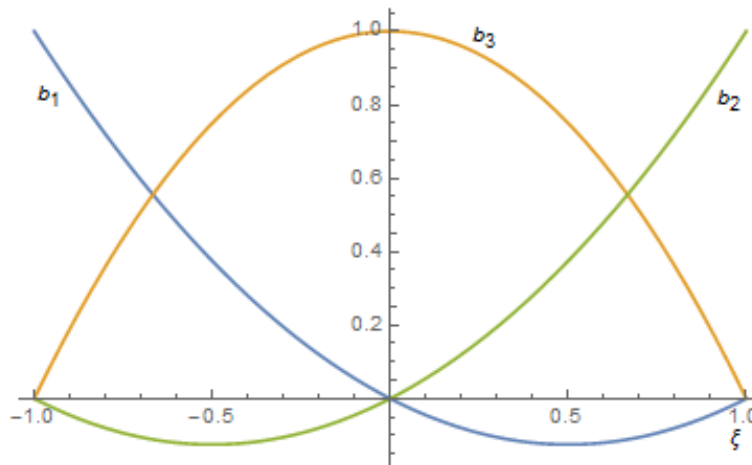
Fig. 5.2 The Lagrangian quadratic shape functions

5.2.2 The 4-node rectangular element and bilinear basis functions

In this study rectangular elements are used for the discretization of the domain. The bilinear basis functions can easily be derived by multiplying the linear basis functions, depicted in **Fig. 5.3** for one direction, in local ξ- and η- directions ($0 < \xi < 1$, $0 < \eta < 1$):

$$\psi_1(\xi) = \frac{1 - \xi}{2}, \psi_2(\xi) = \frac{1 + \xi}{2}$$

$$\psi_1(\eta) = \frac{1 - \eta}{2}, \psi_2(\eta) = \frac{1 + \eta}{2}$$

(5.9)

105
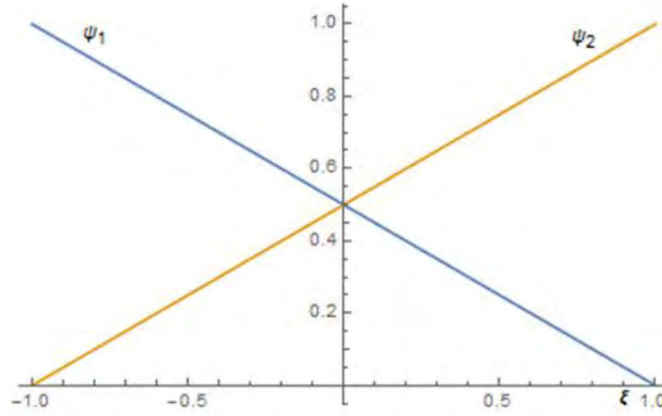
Fig. 5.3 The Lagrangian linear shape functions

Hence, $u_{h_e}^e$ can be written as:

$$u_{h_e}^e = \sum_{i=1}^{4} u_i \Psi_i \qquad (5.10)$$

where Ψ_i represent the bilinear basis functions :

$$\Psi_1(\xi,\eta) = \psi_1(\xi) \cdot \psi_1(\eta) = \frac{(1-\xi)(1-\eta)}{4}$$

$$\Psi_2(\xi,\eta) = \psi_2(\xi) \cdot \psi_1(\eta) = \frac{(1+\xi)(1-\eta)}{4}$$

$$\Psi_3(\xi,\eta) = \psi_1(\xi) \cdot \psi_2(\eta) = \frac{(1-\xi)(1+\eta)}{4} \qquad (5.11)$$

$$\Psi_4(\xi,\eta) = \psi_2(\xi) \cdot \psi_2(\eta) = \frac{(1+\xi)(1+\eta)}{4}$$

The 4-node rectangular element and its conversion from the global to the local coordinate system are illustrated in **Fig. 5.4.**
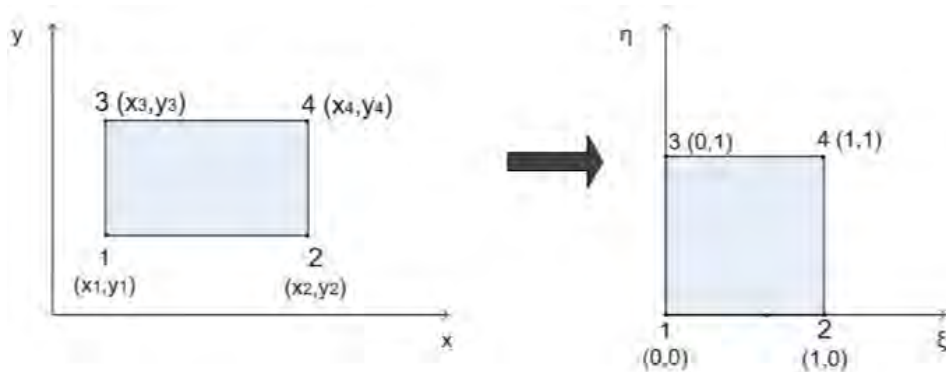
Fig. 5.4 The 4-node rectangular element and its conversion from the global (right) to the local (left) coordinate system

106

5.2.3 The 9-node rectangular element and biquadratic basis functions

Similarly, the biquadratic basis functions can easily be derived by multiplying the 1D quadratic basis functions (Eqs. 5.8) in local ξ- and η- directions ($0 < \xi < 1$, $0 < \eta < 1$):

$$B_1(\xi,\eta) = b_1(\xi) \cdot b_1(\eta) = \frac{(\xi^2 - \xi)(\eta^2 - \eta)}{4}$$

$$B_2(\xi,\eta) = b_3(\xi) \cdot b_1(\eta) = \frac{(\xi^2 + \xi)(\eta^2 - \eta)}{4}$$

$$B_3(\xi,\eta) = b_1(\xi) \cdot b_3(\eta) = \frac{(\xi^2 - \xi)(\eta^2 + \eta)}{4}$$

$$B_4(\xi,\eta) = b_3(\xi) \cdot b_3(\eta) = \frac{(\xi^2 + \xi)(\eta^2 + \eta)}{4}$$

$$B_5(\xi,\eta) = b_2(\xi) \cdot b_1(\eta) = \frac{(1 - \xi^2)(\eta^2 - \eta)}{2}$$

$$B_6(\xi,\eta) = b_1(\xi) \cdot b_2(\eta) = \frac{(\xi^2 - \xi)(1 - \eta^2)}{2} \qquad (5.12)$$

$$B_7(\xi,\eta) = b_2(\xi) \cdot b_2(\eta) = (1 - \xi^2)(1 - \eta^2)$$

$$B_8(\xi,\eta) = b_3(\xi) \cdot b_2(\eta) = \frac{(\xi^2 + \xi)(1 - \eta^2)}{2}$$

$$B_9(\xi,\eta) = b_2(\xi) \cdot b_3(\eta) = \frac{(1 - \xi^2)(\eta^2 + \eta)}{2}$$

Hence, $u_{h_e}^e$ can be written as:

$$u_{h_e}^e = \sum_{i=1}^{9} u_i B_i \qquad (5.13)$$

The 9-node rectangular element and its conversion from the global to the local coordinate system are illustrated in **Fig. 5.5**.
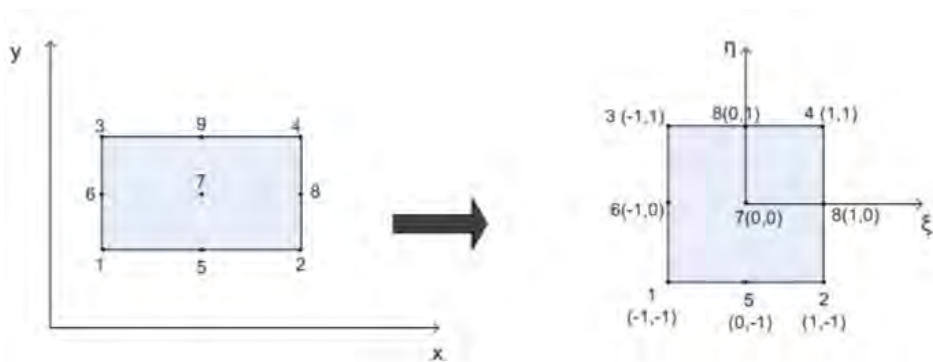
Fig. 5.5 The 9-node rectangular element and its conversion from the global (right) to the local (left) coordinate system

5.2.4 Spline representation

The b-cubic splines are used for the investigation concerning the effect of the porous topography on the static arrangement. This kind of basis functions are cubic curves which guarantee continuity of the function and its first and second derivatives [100,101]. For the interpolation of a function, which is known in N+1 nodes, two extra fictitious nodes are demanded outside the domain. As a consequence, if we use N elements, we have N+3 unknown coefficients, u_{cj}, which is also the total number of the nodes. Thus, we have to calculate all these coefficients of the variable corresponding to the nodes of the computational mesh. A basic difference between the b splines and the usual Lagrangian basis functions is that in the former case, the unknowns are not the actual nodal values of the function they represent. The b-cubic splines basis functions have the following form:

$$\Phi_i(\xi_j) = \frac{1}{h^3} \begin{cases} (\xi - \xi_{i-2})^3, & \xi \in [\xi_{i-2}, \xi_{i-1}] \\ h^3 + 3h^2(\xi - \xi_{i-1}) + 3h(\xi - \xi_{i-1})^2 - 3(\xi - \xi_{i-1})^3, & \xi \in [\xi_{i-1}, \xi_i] \\ h^3 + 3h^2(\xi_{i+1} - \xi) + 3h(\xi_{i+1} - \xi)^2 - 3(\xi_{i+1} - \xi)^3, & \xi \in [\xi_i, \xi_{i+1}] \\ (\xi_{i+2} - \xi)^3, & \xi \in [\xi_{i+1}, \xi_{i+2}] \\ 0, & \xi \notin [\xi_{i-2}, \xi_{i+2}] \end{cases} \tag{5.14}$$

with h representing the element thickness. As can be illustrated in **Fig. 5.6a** a spline polynomial is a non-zero function on the inside of four continuous elements and therefore the Kronecker delta identity is not satisfied. More specifically:

$$\Phi_i(\xi_j) = \begin{cases} 1, & j = 1 \\ 1/4, & j = i \pm 1 \\ 0, & j = i \pm 2 \end{cases} \tag{5.15}$$

Finally, the value of a variable at ξ_i can be computed via:

$$u(\xi) = \sum_{j=1}^{N+3} u_{cj} \Phi_j(\xi) \tag{5.16}$$

(a)

108

(b)
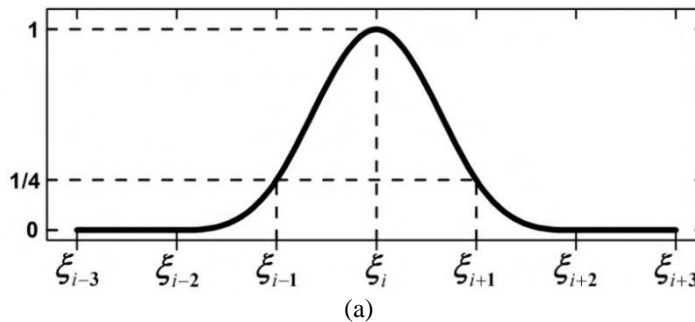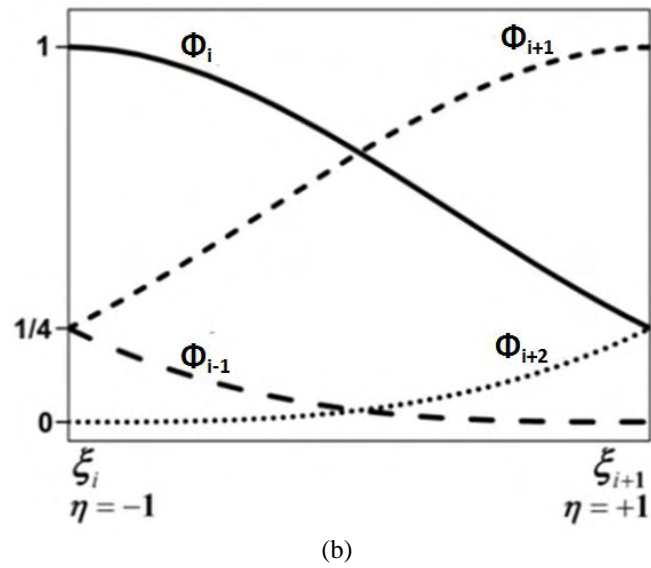
Fig. 5.6 (a) Schematic representation of b spline and (b) Spline representation into one element

5.3 Replenishment of the CPS: Weak form and Newton-Raphson method

As mentioned in Chapter 4, the replenishment process of the CPS following depletion of the liquid metal layer due to an intense external heat load, can be studied by considering the flow of a liquid metal in a single cylindrical pore. A variable $x \equiv z / f(r)$ is introduced in order to fix the size of the mesh in the z direction within 0 and 1. In this fashion, the shape of the interface, z=f(r), is introduced in the problem formulation that now becomes more complicated, but the process of following the dynamic evolution in the shape of the interface is facilitated [102,103], **Fig. 5.7**.

(a)

(b)
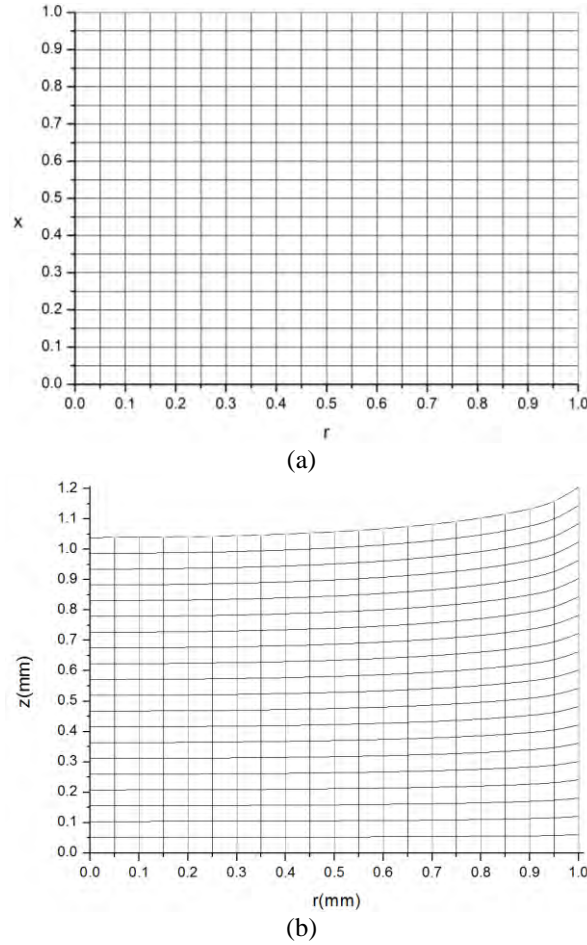
Fig. 5.7 (a) Computational mesh and (b) real mesh, at the same time instant

The axial and radial velocities, u_x, u_r, respectively and pressure field P along with the shape of the interface f constitute the unknown parameters of the problem as a function of the cylindrical coordinates (r, x = z / h) and time t. The finite element representation is employed for the discretization of the unknowns:

$$\left(u_x, u_r\right) = \sum_{i=1}^{nnx \cdot nnr} \left(u_{xi}, u_{ri}\right) B_i, \; P = \sum_{i=1}^{(n_{xel}+1)\cdot(n_{rel}+1)} P_i \Psi_i, \; f = \sum_{i=1}^{nnr} f_i b_i \tag{5.17}$$

with the biquadratic, B_i, bilinear, Ψ_i and quadratic b_i basis functions used for the velocity, pressure field and the shape of the interface, respectively, in the standard staggered mesh approach. Besides, n_{xel} and n_{rel} are the number of elements used in x and r directions of

110

the computational mesh, **Fig. 5.7a**, and nnr and nnx are the total number of the nodes used in the horizontal and axial direction, respectively.

In this fashion, the weak form and the corresponding residuals of the momentum equation are obtained:

$$
R_{ki} = \iiint\limits_V B_i \cdot \mathbf{e_k} \cdot \left[-We \cdot \mathbf{u}\nabla\mathbf{u} - \nabla(P + Bond \cdot z) + Ca \cdot \nabla \underline{\underline{\tau_v}} \right] dV =
$$

$$
= \iiint\limits_V \left[-We \cdot \mathbf{u}\nabla\mathbf{u} \cdot B_i \cdot \mathbf{e_k} + (P + Bond \cdot z) \cdot \nabla(B_i \cdot \mathbf{e_k}) - Ca \cdot \underline{\underline{\tau_v}} : \nabla(B_i \cdot \mathbf{e_k}) \right] dV
$$

$$
+ \oiint\limits_A \left[-B_i \cdot \mathbf{e_k}(P + Bond \cdot z) + Ca \cdot B_i \cdot \underline{\underline{\tau_v}} \cdot \mathbf{e_k} \right] \cdot \mathbf{n} dA \tag{5.18a}
$$

with k=1, 2 standing for the z and r components of momentum. $\nabla(B_i \cdot \mathbf{e_k})$ and $\tau_v : \nabla(B_i \cdot \mathbf{e_k})$ are calculated in Appendix D.

The second term of Eq. 5.18a, namely the boundary integral term for the liquid-gas interface, can be estimated via the following calculations where the dynamic boundary condition is incorporated:

$$
\oiint\limits_A \left[-B_i \cdot \mathbf{e_k}(P + Bond \cdot h) + Ca \cdot B_i \cdot \underline{\underline{\tau_v}} \cdot \mathbf{e_k} \right] \cdot \mathbf{n} dA =
$$

$$
= -\oiint\limits_A B_i \cdot \mathbf{e_k}\left(P - Ca \cdot \underline{\underline{\tau_v}}\right) \cdot \mathbf{n} dA - \oiint\limits_A B_i \cdot \mathbf{e_k} \cdot Bond \cdot h \cdot \mathbf{n} dA =
$$

$$
= \oiint\limits_A B_i \cdot \mathbf{e_k}\left(\frac{\partial \mathbf{t}}{\partial s} - \frac{\mathbf{n}}{R_2}\right) \cdot dA - \oiint\limits_A B_i \cdot \mathbf{e_k} P_{out} \cdot \mathbf{n} dA - \oiint\limits_A B_i \cdot \mathbf{e_k} \cdot Bond \cdot h \cdot \mathbf{n} dA \tag{5.18b}
$$

Taking into account that $dA = r\mathrm{d}s\mathrm{d}\varphi = r\sqrt{1 + f_r^2}\,\mathrm{d}r\mathrm{d}\varphi$, and after the elimination of dφ:

$$
\int\limits_s \left(B_i \cdot \mathbf{e_k} r \frac{\partial \mathbf{t}}{\partial s} - B_i \cdot \mathbf{e_k} r \frac{\mathbf{n}}{R_2} \right) ds - \int\limits_0^1 B_i \cdot \mathbf{e_k} \cdot (Bond \cdot h + P_{out}) \cdot \mathbf{n} r\sqrt{1 + f_r^2}\, dr =
$$

$$
= \int\limits_s \frac{\partial(B_i \cdot \mathbf{e_k} \cdot r \cdot \mathbf{t})}{\partial s} ds - \int\limits_0^1 \mathbf{t} \frac{\partial(B_i \cdot \mathbf{e_k} \cdot r)}{\partial r} dr - \int\limits_0^1 B_i \cdot \mathbf{e_k} \cdot r \cdot \frac{\mathbf{n}}{R_2}\sqrt{1 + f_r^2}\, dr
$$

$$
- \int\limits_0^1 B_i \cdot \mathbf{e_k} \cdot (Bond \cdot h + P_{out}) \cdot \mathbf{n} r\sqrt{1 + f_r^2}\, dr =
$$

$$
= \mathbf{e_k} \cdot (\cos\theta_c \mathbf{e_r} + \sin\theta_c \mathbf{e_z})\big|_{r=1} - \int\limits_0^1 \frac{\mathbf{e_r} + f_r \mathbf{e_z}}{\sqrt{1 + f_r^2}}\left(B_i \cdot \mathbf{e_k} + \frac{\partial B_i}{\partial r} \cdot \mathbf{e_k} \cdot r \right) dr
$$

$$
- \int\limits_0^1 B_i \cdot \mathbf{e_k} \frac{f_r^2 \mathbf{e_r} - f_r \mathbf{e_z}}{\sqrt{1 + f_r^2}} dr - \int\limits_0^1 B_i \cdot \mathbf{e_k} \cdot (Bond \cdot h + P_{out}) \cdot \mathbf{n} r\sqrt{1 + f_r^2}\, dr \tag{5.18c}
$$

The weak form of the z and r components of momentum balance are recovered:

111

$$\sin\theta_c\big|_{r=1} - \int_0^1 \frac{f_r}{\sqrt{1+f_r^2}}\left(B_i + \frac{\partial B_i}{\partial r}\cdot r\right)dr$$

$$+\int_0^1 B_i\cdot\frac{f_r}{\sqrt{1+f_r^2}}dr - \int_0^1 B_i\cdot\left(Bond\cdot h + P_{out}\right)\cdot r\,dr =$$

$$= \sin\theta_c\big|_{r=1} - \int_0^1 \frac{f_r}{\sqrt{1+f_r^2}}\frac{\partial B_i}{\partial r}\cdot r\,dr - \int_0^1 B_i\cdot\left(Bond\cdot h + P_{out}\right)\cdot r\,dr$$

(5.18d)

$$\cos\theta_c\big|_{r=1} - \int_0^1 \frac{1}{\sqrt{1+f_r^2}}\left(B_i + \frac{\partial B_i}{\partial r}\cdot r\right)dr$$

(5.18e)

$$-\int_0^1 \frac{B_i f_r^2}{\sqrt{1+f_r^2}}dr + \int_0^1 B_i f_r\cdot\left(Bond\cdot h + P_{out}\right)\cdot r\,dr$$

Furthermore, the weak forms of the continuity equation and the kinematic condition are:

$$R_{3i} = \iint_{A^e}\Psi_i\left(\frac{u_x}{r} + \frac{\partial u_x}{\partial z} + \frac{\partial u_r}{\partial r}\right)r\,dr\,dz$$

(5.19)

$$R_{4i} = \int_{\Gamma^e} b_i\left[\frac{f^{n+1}-f^n}{\Delta t} - u_x^{n+1} + u_r^{n+1}\frac{\partial f^{n+1}}{\partial r}\right]dS$$

(5.20)

The latter is discretized in time using a fully implicit scheme.

In addition, as mentioned in subsection 4.3, symmetry conditions are imposed at the axis of symmetry $u_r(r=0,z)=0$, $\partial u_z/\partial r(r=0,z)=0$, while the transverse velocity is set to zero at the pore entrance $u_r(z=0,r)=0$, whereas at the pore wall we impose $u_r=0$ with a slip length allowed near the meniscus tip in order to accommodate the rise velocity of the liquid metal $u_z(r=1,z;t)=\frac{\partial f}{\partial t}(r=1;t)e^{-\frac{1-x}{\varepsilon}}$, $\varepsilon=\frac{\ell}{R_0}$. This relationship ensures that the no-slip condition pertaining to the axial velocity at the wall is reinstated after a very small slip length ℓ.

Finally, the known pressure P_r in the reservoir is incorporated in the z component of Eq. 5.18b. In particular, the external pressure P_{out} in 5.18b is really $\Delta P=P_{out}-P_r$ so that the major forces driving the motion of the meniscus explicitly appear in the boundary term of the weak form of the z-momentum balance.

The Jacobian matrix of the coordinate's transformation reads:

$$|J| = \begin{vmatrix}\dfrac{\partial r}{\partial r} & \dfrac{\partial r}{\partial x}\\[2mm] \dfrac{\partial z}{\partial r} & \dfrac{\partial z}{\partial x}\end{vmatrix} = \begin{vmatrix}1 & 0\\ xf_r(r) & f(r)\end{vmatrix} = f(r)$$

(5.21)

112

Thus using,

$$\nabla = \frac{\partial}{\partial r}\bigg|_z \mathbf{e_r} + \frac{\partial}{\partial z}\bigg|_r \mathbf{e_z} = \left(\frac{\partial}{\partial r} - \frac{x\mathbf{f_r}}{f}\frac{\partial}{\partial x}\right)\mathbf{e_r} + \frac{1}{f}\frac{\partial}{\partial x}\mathbf{e_z} \qquad (5.22)$$

and Eq. 5.17, 5.21, Eqs. 5.18-5.20 and the boundary conditions are transformed into r, x coordinate system.

The final system of equations to be solved has the following form:

$$\vec{R}(\vec{x}) = 0 \qquad (5.23)$$

where $\vec{x}$ represents the unknown vector and $\vec{R}(\vec{x})$ the residual vector. Seeking for solutions of the Eqs. 5.18-5.20 the Newton-Raphson method is used and Eq. 5.23 can be written in the form:

$$[A] \cdot \delta \vec{x} = -\vec{R} \qquad (5.24)$$

where [A] stands for the Jacobian matrix that contains the derivatives of all the residuals with respect to each unknown vector $\vec{x}$ and $\delta\vec{x} = \vec{x}_{new} - \vec{x}_{old}$ is the correction of the unknown vector, $\vec{x}$, during each iteration. The new potential solution is updated via:

$$x_{new} = x_{old} + \delta\vec{x} \qquad (5.25)$$

and the whole process is iterated until convergence.

If n_{xel} and n_{rel} are the number of elements used in x and r directions of the computational mesh, respectively, depicted in **Fig. 5.7a**, then the total nodes in these directions are:

$$nnx = 2n_{xel} + 1, \ nnr = 2n_{rel} + 1 \qquad (5.26)$$

Thus, the total nodes are:

$$n_{total} = nnx \cdot nnr \qquad (5.27)$$

As a consequence, the total number of equations required for both the axial and radial velocity, u_x and u_r respectively, is $2 \cdot n_{total}$ while for the pressure field, P, $(n_{xel} + 1) \cdot (n_{rel} + 1)$ equations are needed. Finally, we used nnr equations for the shape of the interface, f. Hence, if we define $n_{band} = 2 \cdot n_{ntotal} + (n_{xel} + 1) \cdot (n_{rel} + 1)$, the total number of equations is:

$$neq_{total} = n_{band} + nnr \qquad (5.28)$$

The aforementioned system of equations produces a set of nonlinear equations with the Jacobian matrix, A, being in the form of an arrowhead matrix, [104]. An arrow matrix has

113

nonzero elements only in a narrow band centered on the main diagonal and in the last few columns and rows. Hence, A matrix can be divided into four sub-matrices:

1. A banded Jacobian matrix (J) of dimension $n_{band} \times n_{band}$ with derivative entries of the residuals relating to momentum balances (in both directions) and continuity equation with respect to u_{xi}, u_{ri} and P_i,
2. A matrix in the form of a column (COL) of dimension $n_{band} \times nnr$ with derivative entries of the residuals relating to momentum balances (in both directions) and continuity equation with respect to f_i,
3. A matrix in the form of a row (ROW) of dimension $nnr \times n_{band}$ with derivative entries of the residual relating to the kinematic condition with respect to u_{xi}, u_{ri} and P and
4. A matrix in the square arrowhead at the bottom right (HEAD) of dimension $nnr \times nnr$ with derivative entries of the residual relating to the kinematic condition with respect to f_i.

A schematic illustration of the arrowhead matrix used in this study can be shown in **Fig. 5.8**:

$$A= \quad \begin{array}{|c|c|} \hline J \ (n_{band} \times n_{band}) & COL \ (n_{band} \times nnr) \\ \hline ROW \ (nnr \times n_{band}) & HEAD \ (nnr \times nnr) \\ \hline \end{array}$$
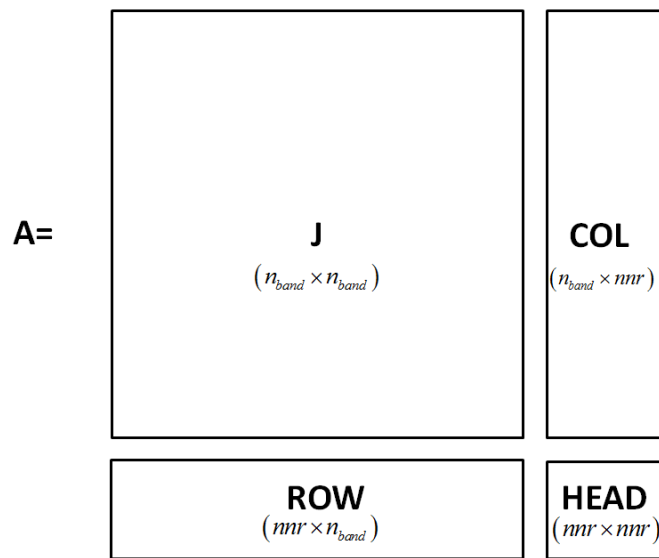
Fig. 5.8 Schematic illustration of the arrowhead matrix

After storing the equations in the above form, A matrix is inversed by a standard routine, written for arrow matrices. Consequently, the unknown vector is calculated via the Newton-Rapson, as discussed above.

Concerning this problem, a previously converged solution is used as initial guess for a new solution corresponding to a new value of the control parameter. Thus, simple continuation is performed since the solutions are smooth and without limit points.

114

5.4 Static arrangement of the CPS: Weak forms

5.4.1 Effect of reservoir overpressure

The normal stress balance on the liquid-gas interface described via:

$$\mathbf{n}\left(P_{in} - P_{out}\right)\underline{\underline{I}} + \mathbf{n}2H_c\gamma = 0 \tag{5.29a}$$

$$P_{in} = P_r - \rho g h_0 - \rho g z \tag{5.29b}$$

is discretized using the finite element methodology, with the unknown z coordinate of the liquid metal layer interface with the surrounding medium described via a number of quadratic Lagrangian basis functions b_i:

$$z = \sum_{i=1}^{n_{total}} z_i b_i \tag{5.30}$$

where z_i represent the axial position of the nodes. The total interfacial nodes, with n_{el} denoting the total number of elements, are:

$$n_{total} = 2 \cdot n_{el} + 1 \tag{5.31}$$

Multiplying Eq. 5.29a by the quadratic basis functions while employing Eq. 5.30, the weak form is obtained:

$$\iint_A b_i \Big[\mathbf{n}\big(P_{in} - P_{out}\big) + \mathbf{n}2H_c\gamma \Big] dA = 0 \Rightarrow$$

$$\Rightarrow \iint_A b_i \big(P_{in} - P_{out}\big)\frac{-z_r\mathbf{e_r} + \mathbf{e_z}}{\sqrt{1+z_r^2}} \, r ds d\varphi + \iint_A \gamma b_i \left[\frac{\partial \mathbf{t}}{\partial s} - \frac{\mathbf{n}}{R_2} \right] r ds d\varphi = 0 \Rightarrow$$

$$\Rightarrow \int_0^{R_f} b_i r dr \big(P_{in} - P_{out}\big)\left(2\pi\mathbf{e_z} - z_r \int_0^{2\pi} \mathbf{e_r} d\varphi \right) + \int_0^{2\pi} \gamma d\varphi \left(b_i r \mathbf{t}\big|_{s(r=0)}^{s(r=R_f)} - \int_s \mathbf{t}\frac{\partial(b_i r)}{\partial s} ds \right)$$

$$-\iint_A \gamma b_i \frac{\mathbf{n}}{R_2} r ds d\varphi = 0 \Rightarrow$$

$$\Rightarrow 2\pi\mathbf{e_z} \int_0^{R_f} b_i \big(P_{in} - P_{out}\big) r dr + \int_0^{2\pi} \gamma d\varphi b_i r \mathbf{t}\big|_{s(r=R_f)} - \int_0^{2\pi}\int_s \left(\gamma \mathbf{t}\frac{\partial(b_i r)}{\partial s} + \frac{\gamma b_i r \mathbf{n}}{R_2} \right) d\varphi ds = 0 \Rightarrow$$

$$\Rightarrow 2\pi\mathbf{e_z} \int_0^{R_f} b_i \big(P_{in} - P_{out}\big) r dr - 2\pi\mathbf{e_z}\gamma\sin\theta_c \delta_{i,n_{total}} R_f$$

$$-2\pi\mathbf{e_z} \int_0^{R_f} \gamma\sqrt{1+z_r^2}\left[\frac{z_r}{\sqrt{1+z_r^2}}\frac{\partial(b_i r)}{\partial r}\frac{1}{\sqrt{1+z_r^2}} + \frac{b_i r}{R_2\sqrt{1+z_r^2}} \right] dr = 0 \Rightarrow \quad (5.32)$$

$$\Rightarrow \int_0^{R_f} b_i \big(P_{in} - P_{out}\big) r dr - \int_0^{R_f} \gamma\left[\frac{z_r}{\sqrt{1+z_r^2}}\frac{\partial(b_i r)}{\partial r} + \frac{b_i \cancel{r}(-z_r)}{\cancel{r}\sqrt{1+z_r^2}} \right] dr - \gamma R_f \sin\theta_c\delta_{i,n_{total}} = 0 \Rightarrow$$

$$\Rightarrow \int_0^{R_f} b_i \big(P_r - \rho g h_0 - \rho g z - P_{out}\big) r dr - \int_0^{R_f} \gamma\frac{z_r r}{\sqrt{1+z_r^2}}\frac{\partial b_i}{\partial r} dr - \gamma R_f \sin\theta_c\delta_{i,n_{total}} = 0$$

In the above calculations it has been taken into account that:

$$2H_c\mathbf{n} = \frac{\partial \mathbf{t}}{\partial s} - \frac{\mathbf{n}}{R_2}, \quad \mathbf{n} = \frac{\mathbf{e_z} - z_r\mathbf{e_r}}{\sqrt{1+z_r^2}}, \quad \mathbf{t} = \frac{z_r\mathbf{e_z} + \mathbf{e_r}}{\sqrt{1+z_r^2}}$$

$$\mathbf{t}\big|_{r=R_f} = \cos(\theta - \pi/2)\mathbf{e_z} + \sin(\theta - \pi/2)\mathbf{e_r}, \quad \int_0^{2\pi} \mathbf{e_r} d\varphi = 0 \quad (5.33)$$

$$ds = \sqrt{1+z_r^2} \, dr, \quad \frac{1}{R_2} = \frac{-z_r}{r\sqrt{1+z_r^2}}, \quad \delta_{i,n_{total}} = \begin{matrix} 1 \text{ for the } n_{total} \text{ node} \\ 0 \text{ elsewhere} \end{matrix}$$

Eq. 5.32 is made dimensionless by using the radial position of the liquid metal, R_f as a characteristic length scale. Thus, upon dividing both legs of Eq. 5.32 by $\gamma \cdot R_f$:

$$R_i = Bond_p\left(\frac{R_f}{h_0}\right)\int_0^1 b_i r dr - Bond\left(\frac{R_f}{h_0}\right)^2 \int_0^1 b_i r z dr - \int_0^1 \frac{z_r r}{\sqrt{1+z_r^2}}\frac{\partial b_i}{\partial r} dr - \sin\theta_c\delta_{i,n_{total}} \quad (5.34)$$

where:

$$Bond_p = \frac{P_r - \rho g h_0 - P_{out}}{\gamma / h_0}, \quad Bond = \frac{\rho g h_0}{\gamma / h_0} \quad (5.35)$$

116

are the dimensionless numbers relating the relative strength of pressure and gravitational forces to surface tension forces, respectively. Furthermore, we impose $z_r\big|_{r=0} = 0$, z(r=1) = 0, while the contact angle is implicitly fixed via the last term of Eq. 5.34. It should be stressed that θ_c is the angle of the liquid metal drop that rests on the CPS surface and is equal to the negative of the angle between the tangent vector and the r axis at the contact point.

The resulting set of nonlinear algebraic equations is solved in an iterative fashion via the Newton-Raphson method until convergence, as described in the previous subsection. Each iteration involves an inversion of a banded matrix. The banded Jacobian matrix (J) has dimension $n_{total} \times n_{total}$ with derivative entries of the residuals relating to Eq. 5.34 with respect to z_i and R_f/h_0 for fixed reservoir over or under pressure, $\Delta P = P_r - P_{out}$. Finally, simple continuation is used as in the previous study.

5.4.2 Preparation phase: Estimation of the static film arrangement
As mentioned in Chapter 4, in the preparation phase lithium is in a solid state with density ρ_s, placed within the porous wafer. Upon heating the lithium it liquefies at density $\rho_l < \rho_s$, the top cover breaks by the expanding liquid and the liquid metal covers the top surface forming a protective coating, **Fig. 4.5**.

Performing a simple mass balance on lithium, relating its initial solid state to its final liquid state, it turns out that, for a given porosity, α, and CPS radius, R_c, the total mass is:

$$
\begin{aligned}
M &= \left(\alpha h_0 + h_r\right)\pi R_c^2 \rho_s = \left(\alpha h_0 + h_r\right)\pi R_c^2 \rho_l + M_{film} \Rightarrow \\
\Rightarrow M_{film} &= \left(\alpha h_0 + h_r\right)\pi R_c^2 \left(\rho_s - \rho_l\right) \Rightarrow \\
\Rightarrow V_{film} &= \left(\alpha h_0 + h_r\right)\pi R_c^2 \left(\rho_s - \rho_l\right) / \rho_l
\end{aligned}
\tag{5.36}
$$

where h_0 and h_r denote the thickness of the porous wafer and that of the reservoir, respectively. If no additional reservoir of lithium is considered $h_r = 0$. Besides, M_{film} and V_{film} represent the mass and the volume of the liquid metal film that rests on top of the porous substrate upon heating the CPS. The final static arrangement is a result of the pressure driven flow due to density change of heated lithium. Adhesive forces are needed in order to pin the film onto the substrate and are implicitly incorporated in the model by fixing the contact point.

The static calculations pertaining to this study need to satisfy the normal stress balance on the liquid-gas interface, Eq. 5.29a. In this investigation, the contact point is fixed, $R_f = R_c$, rather than the contact angle and the pressure on the porous top surface $P_0 = P_r - \rho g h_0$ in now an extra unknown parameter. Hence, the resulting residual concerning the interfacial normal stress balance reads:

$$
R_{1i} = \int_0^{R_c} b_i P_0 r dr - \int_0^{R_c} b_i P_{out} r dr - \int_0^{R_c} b_i \rho g z r dr - \int_0^{R_c} \frac{\gamma z_r r}{\sqrt{1 + z_r^2}} \frac{\partial b_i}{\partial r} dr
\tag{5.37}
$$

where the unknown z coordinate of the liquid metal layer interface with the surrounding medium is described via a number of quadratic Lagrangian basis functions, Eq. 5.30.

117

Consequently, Eq. 5.37 is made dimensionless by using the fixed radial position of the liquid metal, R_c as a characteristic length scale and γ/R_c as a characteristic pressure:

$$R_{1i} = \int_0^1 b_i P_0 r dr - P_{out} \int_0^1 b_i r dr - Bond \int_0^1 b_i z r dr - \int_0^1 \frac{z_r r}{\sqrt{1+z_r^2}} \frac{\partial b_i}{\partial r} dr \qquad (5.38)$$

All the variables in the residual R_{1i} are dimensionless and no bars or other symbols are used for simplicity. The boundary term that arises in Eq. 5.34 describing the interfacial shape subject to an imposed reservoir overpressure, does not appear in this case since the contact point is fixed and the contact angle is calculated once the shape of the interface is known. Also, the Bond number here is:

$$Bond = \frac{\rho g R_c}{\gamma / R_c} \qquad (5.39)$$

and relates the relative strength of gravitational to surface tension forces.

Residuals described via Eq. 5.38 are used along with the dimensionless fixed volume of the liquid metal, $\tilde{V}_{film} = \dfrac{M_{film}}{\rho R_c^3} = 2\pi \int_0^1 r z dr$

If n_{el} is the total number of elements, then the total nodes are:

$$n_{total} = n_{band} = 2 \cdot n_{el} + 1 \qquad (5.40)$$

As a consequence, the total number of equations required is:

$$neq_{total} = n_{total} + 1 \qquad (5.41)$$

i.e. n_{total} equations for z and one equation for P_0.

The aforementioned system of equations produces a set of nonlinear equations with the matrix, A, similar to **Fig. 5.8**. Hence, A matrix can be divided into four sub-matrices:

1. A banded Jacobian matrix (J) of dimension $n_{band} \times n_{band}$ with derivative entries of the residuals relating to Eq. 5.38 with respect to z_i,
2. A matrix in the form of a column (COL) of dimension n_{band} with derivative entries of the residuals relating to Eq. 5.38 with respect to P_0,
3. A matrix in the form of a row (ROW) of dimension n_{band} with derivative entries of the residual relating to the fixed volume of the liquid metal with respect to z_i and
4. A matrix in the square arrowhead at the bottom right (HEAD) of dimension 1×1 with derivative entries of the residual relating to the fixed volume of the liquid metal with respect to P_0.

118

After storing the equations in the above form, A matrix is inversed by a standard routine, written for arrow matrices. Consequently, the unknown vector is calculated via the Newton-Rapson, as discussed above.

A previously converged solution is used again, as in the previous study, as initial guess for a new solution corresponding to a new value of the control parameter.

5.4.3 Effect of an externally applied electric field
As mentioned in Chapter 4 in order to assess the impact of field forces on the liquid metal layer covering the porous system, the effect of an external electric field was firstly considered that is aligned with the axis of symmetry of the porous wafer in the far field, **Fig. 4.10c**.

Hence, once the static arrangement is obtained, via the investigation presented in 5.4.1, then the mass of the liquid metal that is pinned onto the substrate, m, is known via:

$$m = 2\pi\rho \int_0^{R_f} z(r) r dr \qquad (5.42)$$

The interfacial normal stress balance which was used in this Chapter, Eq. 5.29a, is augmented with the electrostatic part of the Maxwell stresses [98] $\underline{\underline{\tau}}_{el}$, Eq. 4.27:

$$\mathbf{n}\left[(P_{in} - P_{out})\underline{\underline{I}} + \underline{\underline{\tau}}_{el} \right] + \mathbf{n}2H_c\gamma = 0 \qquad (5.43)$$

In this investigation, the contact point is fixed, $R_f = R_c$, rather than the contact angle and the pressure on the porous top surface $P_0 = P_r - \rho g h_0$ in now an extra unknown parameter. Hence, the resulting residual concerning the interfacial normal stress balance reads:

$$R_{1i} = \int_0^{R_c} b_i P_0 r dr - \int_0^{R_c} b_i P_{out} r dr - \int_0^{R_c} b_i \rho g z r dr - \int_0^{R_c} \frac{\gamma z_r r}{\sqrt{1+z_r^2}} \frac{\partial b_i}{\partial r} dr + \frac{E_0^2}{8\pi} \int_0^{R_c} \frac{r b_i}{1+z_r^2} dr \qquad (5.44)$$

where again the unknown z coordinate of the liquid metal layer interface is described via Eq. 5.30. Consequently, Eq. 5.44 is made dimensionless by using the fixed radial position of the liquid metal, R_c, as a characteristic length scale and γ/R_c as a characteristic pressure:

$$R_{1i} = \int_0^1 b_i P_0 r dr - P_{out}\int_0^1 b_i r dr - Bond\int_0^1 b_i z r dr - \int_0^1 \frac{z_r r}{\sqrt{1+z_r^2}} \frac{\partial b_i}{\partial r} dr + \frac{Bond_{el}}{8\pi} \int_0^{R_c} \frac{r b_i}{1+z_r^2} dr \qquad (5.45)$$

All the variables of the residual R_{1i} are now dimensionless and no bars or other symbols are used for simplicity. The contact angle is not prescribed in this calculation. Rather the contact point is fixed at the edge R_c of the CPS surface, while the contact angle θ_c is recovered in the post processing phase of the calculation as shown below. Thus, the relevant dimensionless numbers here are:

119

$$Bond = \frac{\rho g R_c}{\gamma / R_c}, \; Bond_{el} = \frac{E_0^2}{\gamma / R_c} \qquad\qquad (5.46)$$

relating the gravitational and electric forces to surface tension forces, respectively, and identifying the contact angle of the drop.

The numerical procedure followed here is exactly the same as that discussed in subsection 5.4.2 with the extra term $\dfrac{Bond_{el}}{8\pi} \displaystyle\int_0^{R_c} \dfrac{r\mathrm{b}_i}{1+z_r^2} dr$ added in R_{1i} expressing the electric stresses on the interface. One more difference is that in the preparation phase the volume of the liquid film resting upon the porous substrate is derived analytically via Eq. 5.36, while in this investigation it is calculated numerically from the study pertaining to subsection 5.4.1.

5.4.4 Effect of Lorentz forces
Static configuration for the liquid metal trapped in the pore
In this study, which was modelled in subsection 4.4.3, cylindrical coordinates are used, Appendix B, due to the cylindrical shape of the capillary. Besides, a variable x is introduced in order to fix the size of the mesh in the r, x plane within 0 and 1 similar to the investigation pertaining to the fluid motion within a single pore, which was analyzed in subsection 5.3. The resulting form of the computational mesh can be shown in **Fig. 5.7a**.

The stream function of current, H(r,x), along with the shape of the interface f(r) constitute the unknown parameters of the problem as a function of the cylindrical coordinates (r, x = z / f(r)).

The finite element representation is employed for the discretization of the unknown parameters:

$$H = \sum_{i=1}^{nnx \cdot nnr} H_i B_i, \; f = \sum_{i=1}^{nnr} f_i b_i \qquad\qquad (5.47a)$$

with the biquadratic, B_i, and quadratic, b_i, basis functions used for H and the shape of the interface, f, respectively, in the standard staggered mesh approach. Besides, nnr and nnx are the total number of the nodes used in the horizontal and axial direction, respectively.

Finally, an extra unknown parameter of the problem is the current density, J, existing on the bottom of the pore, which according to Eq. 4.46d is given by:

$$J = \frac{2 \displaystyle\int_0^{R_p} \left(J_z - J_r z_r \right) r dr}{R_p^2} \qquad\qquad (5.47b)$$

In this fashion, the weak form, and the corresponding residuals corresponding to the Poisson-type Eq. 4.36 are obtained:

120

$$\iiint_V B_i \left(\nabla^2 H - \frac{H}{r^2} \right) dV = 0$$

$$-\iiint_V \nabla B_i \cdot \nabla H dV - \iiint_V B_i \frac{H}{r^2} dV + \oiint_A B_i \mathbf{n} \cdot \nabla H dA = 0$$

$$\iiint_V \nabla B_i \cdot \nabla H dV + \iiint_V B_i \frac{H}{r^2} dV - \oiint_A B_i \frac{\partial H}{\partial n} dA = 0 \tag{5.48}$$

$$R_{1i} = \iint \left(\frac{\partial B_i}{\partial r} \frac{\partial H}{\partial r} + \frac{\partial B_i}{\partial z} \frac{\partial H}{\partial z} \right) r dr dz + \iint B_i \frac{H}{r} dr dz - \oint_s B_i \frac{\partial H}{\partial n} r ds$$

Substituting Eqs. 5.21 and 5.22 into Eq. 5.48:

$$R_{1i} = \iint \left(\frac{\partial B_i}{\partial r} - \frac{x f_r}{f} \frac{\partial B_i}{\partial x} \right) \left(\frac{\partial H}{\partial r} - \frac{x f_r}{f} \frac{\partial H}{\partial x} \right) r f dr dx + \iint \frac{1}{f^2} \frac{\partial B_i}{\partial x} \frac{\partial H}{\partial x} r f dr dx$$

$$+ \iint B_i \frac{H}{r} f dr dx - \oint_s B_i \frac{\partial H}{\partial n} r ds \tag{5.49}$$

The final term is going to be written only at the liquid-gas interface. Thus:

$$-\oint_s B_i \frac{\partial H}{\partial n} r ds = -\int_0^{R_p} B_i \frac{\partial H}{\partial n} r \sqrt{1 + f_r^2} dr \tag{5.50}$$

Hence, substituting Eq. 4.47d into 5.50:

$$-\oint_s B_i \frac{\partial H}{\partial n} r ds = -\int_0^{R_p} B_i \frac{-\frac{\partial H}{\partial r} f_r + \frac{\partial H}{\partial z}}{\sqrt{1 + f_r^2}} r \sqrt{1 + f_r^2} dr = \int_0^{R_p} B_i \left[\left(J_z - \frac{H}{r} \right) f_r + J_r \right] r dr \tag{5.51}$$

The normal stress balance on the liquid-gas interface is described via:

$$P_r - \rho g f(\mathrm{r}) + \mathrm{B}_0 \left(\frac{rJ}{2} - H \right) - P_{out} + \gamma 2 H_c = 0 \tag{5.52a}$$

Multiplying by $\mathbf{n}$ each leg of Eq. 5.52a:

$$\mathbf{n} \left[P_r - \rho g f(\mathrm{r}) + \mathrm{B}_0 \left(\frac{rJ}{2} - H \right) - P_{out} \right] + \gamma \left(\frac{\partial \mathbf{t}}{\partial s} - \frac{\mathbf{n}}{R_2} \right) = 0 \tag{5.52b}$$

where the identity from Eq. 4.13 has been used.

The weak form, and the corresponding residuals corresponding to normal stress balance can be obtained similar to the derivation described when Eq. 5.32 was obtained:

$$\iint\limits_A b_i \mathbf{n} \left[P_r - \rho g f(\mathbf{r}) + B_0 \left(\frac{rJ}{2} - H \right) - P_{out} \right] r ds d\varphi + \iint\limits_A b_i \gamma \left(\frac{\partial t}{\partial s} - \frac{\mathbf{n}}{R_2} \right) r ds d\varphi = 0$$

$$R_{2i} = \int_0^{R_p} b_i \left[P_r - \rho g f(\mathbf{r}) + B_0 \left(\frac{rJ}{2} - H \right) - P_{out} \right] r dr - \int_0^{R_p} \gamma \frac{f_r r}{\sqrt{1 + f_r^2}} \frac{\partial b_i}{\partial r} dr \qquad (5.53)$$

Consequently, R_{1i} and R_{2i}, described via Eqs. 5.49 and 5.53, respectively, are made dimensionless by using the pore radius, R_p, γ/R_p, J_r and $J_r \cdot R_p$ as a characteristic length scale, pressure, current density and stream function of current, respectively. Hence:

$$R_{1i} = \iint \left(\frac{\partial B_i}{\partial r} f - x f_r \frac{\partial B_i}{\partial x} \right) \left(\frac{\partial H}{\partial r} - \frac{x f_r}{f} \frac{\partial H}{\partial x} \right) r dr dx + \iint \frac{1}{f} \frac{\partial B_i}{\partial x} \frac{\partial H}{\partial x} r dr dx$$

$$+ \iint B_i \frac{H}{r} f dr dx + \int_0^1 B_i \left(J_z f_r r + J_r r - H f_r \right) dr \qquad (5.54)$$

$$R_{2i} = \left(P_r - P_{out} \right) \int_0^1 b_i r dr - Bond \int_0^1 b_i f r dr + \frac{1}{2} Bond_m \int_0^1 b_i J r^2 dr - Bond_m \int_0^1 b_i H r dr$$

$$- \int_0^1 \frac{f_r r}{\sqrt{1 + f_r^2}} \frac{\partial b_i}{\partial r} dr \qquad (5.55)$$

Also, the dimensionless numbers here are:

$$Bond = \frac{\rho g R_p}{\gamma / R_p}, \; Bond_m = \frac{B_0 J_r R_p}{\gamma / R_p} \qquad (5.56)$$

relating the gravitational and magnetic forces to surface tension forces, respectively.

The third dimensionless residual is given by:

$$R_3 = J - 2 \int_0^1 \left(J_z - f_r \right) r dr \qquad (5.57)$$

Besides, if n_{xel} and n_{rel} are the number of elements used in x and r directions of the computational mesh depicted in **Fig. 5.7a**, then the total nodes in these directions are:

$$nnx = 2 n_{xel} + 1, \; nnr = 2 n_{rel} + 1 \qquad (5.58)$$

Thus, the total nodes are:

$$n_{total} = nnx \cdot nnr \qquad (5.59)$$

As a consequence, the total number of equations required for H is n_{total} while nnr equations are required for the shape of the interface, f and one equation for J. Hence, if we define $n_{band} = n_{total}$ the total number of equations is:

$$neq_{total} = n_{band} + nnr + 1 \qquad\qquad (5.60)$$

The aforementioned system of equations produces a set of nonlinear equations with a matrix, A, similar to **Fig. 5.8**.

After storing the equations in the above form, A matrix is inversed by a standard routine, written for arrow matrices. Consequently, the unknown vector is calculated via the Newton-Rapson, as discussed in subsection 5.3.

A previously converged solution is used as initial guess for a new solution corresponding to a new value of the control parameter.

Static configuration for the liquid metal extended over the pore

In this study, which was modelled in subsection 4.4.3, spherical coordinates are used in order to mathematically formulate the problem of a liquid metal layer fully covering while extending beyond a cylindrical pore, see **Fig 4.19** for a schematic diagram of the arrangement and Appendix C for a short description of vectorial quantities in spherical coordinates. We assume that the induced magnetic field H is negligible within the pore and consequently there is no motion in it, an assumption that is expected to be more or less valid as the liquid metal is pushed out of the pore with increasing magnitude of the electric current density. Consequently, variable $\eta = r/f(\theta)$ is introduced in order to fix the size of the mesh in the η, θ plane within 0 and 1. In this fashion, the shape of the interface, $f(\theta)$, is introduced throughout the problem formulation. Hence, the spine method is used in order to generate the present computational mesh, **Fig. 5.9a** from the real one, **Fig. 5.9b**. The natural boundaries S_1, S_2, S_3 and S_4 of **Fig. 5.9b** have been transformed to the simple computational boundaries depicted in **Fig. 5.9a**.

(a)

(b)
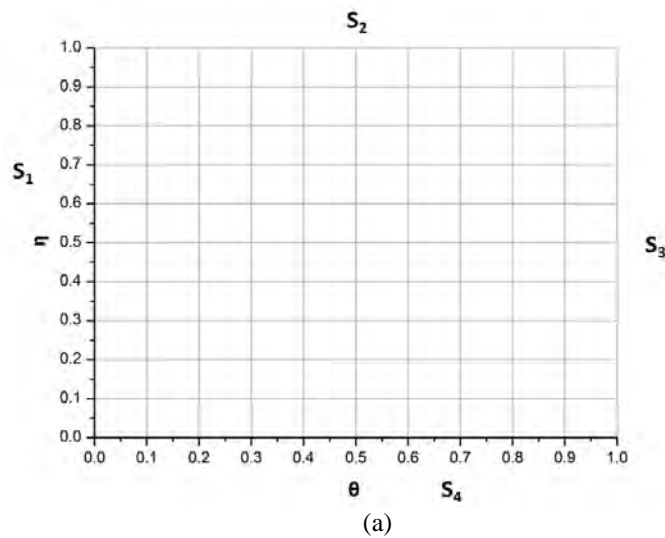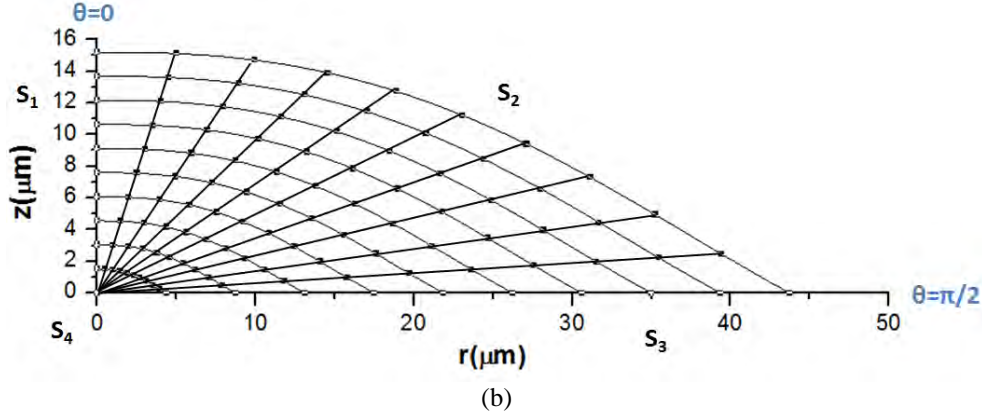
Fig. 5.9 (a) Computational and (b) real mesh

The stream function of current, H, along with the shape of the interface, f, constitute the unknown parameters of the problem as a function of the spherical coordinates (θ, $\eta = r / f(\theta)$). The finite element representation is employed for the discretization of the unknown parameters:

$$H = \sum_{i=1}^{nn\theta \cdot nn\eta} H_i B_i, \; f = \sum_{i=1}^{nn\theta} f_i b_i \tag{5.61}$$

with the biquadratic, B_i, and quadratic, b_i, basis functions used for H and the shape of the interface, f, respectively, in the standard staggered mesh approach. Besides, $nn\theta$ and $nn\eta$ are the total number of the nodes used in the horizontal and vertical direction of the computational mesh, respectively.

In this fashion, the weak form, and the corresponding residuals corresponding to the Poisson-type Eq. 4.36 are obtained:

$$\iiint_V B_i \left(\nabla^2 H - \frac{H}{r^2 \sin^2 \theta} \right) dV = 0$$

$$-\iiint_V \nabla B_i \cdot \nabla H dV - \iiint_V B_i \frac{H}{r^2 \sin^2 \theta} dV + \oiint_A B_i \nabla H \cdot \mathbf{n} dA = 0 \tag{5.62}$$

$$\iint \left(\frac{\partial B_i}{\partial r} \frac{\partial H}{\partial r} + \frac{1}{r^2} \frac{\partial B_i}{\partial \theta} \frac{\partial H}{\partial \theta} + \frac{B_i H}{r^2 \sin^2 \theta} \right) r^2 \sin \theta dr d\theta - \oint_s B_i \frac{\partial H}{\partial n} r \sin \theta ds = 0$$

where H stands for the azimuthal component of H.

The Jacobian matrix of the coordinate's transformation reads:

$$|J| = \begin{vmatrix} \dfrac{\partial \theta}{\partial \theta} & \dfrac{\partial \theta}{\partial \eta} \\ \dfrac{\partial r}{\partial \theta} & \dfrac{\partial r}{\partial \eta} \end{vmatrix} = \begin{vmatrix} 1 & 0 \\ \eta f_\theta(\theta) & f(\theta) \end{vmatrix} = f(\theta) \tag{5.63}$$

Thus using,

124

$$\nabla = \frac{\partial}{\partial\theta}\bigg|_r \mathbf{e_\theta} + \frac{\partial}{\partial r}\bigg|_\theta \mathbf{e_r} = \left(\frac{\partial}{\partial\theta} - \frac{\eta f_\theta}{f}\frac{\partial}{\partial\eta}\right)\mathbf{e_\theta} + \frac{1}{f}\frac{\partial}{\partial\eta}\mathbf{e_r} \tag{5.64}$$

and Eqs. 5.61 and 5.63, Eq. 5.62 is transformed into the (θ, η) coordinate system:

$$\iint\left[\frac{\partial B_i}{\partial\eta}\frac{\partial H}{\partial\eta}\eta^2 f^2 + \left(f\frac{\partial B_i}{\partial\theta} - \eta f_\theta\frac{\partial B_i}{\partial\eta}\right)\left(\frac{\partial H}{\partial\theta} - \frac{\eta f_\theta}{f}\frac{\partial H}{\partial\eta}\right)\right]\sin\theta d\eta d\theta \tag{5.65}$$
$$+\iint\frac{B_i H}{\sin\theta}f d\eta d\theta - \oint_s B_i\frac{\partial H}{\partial n}\eta f\sin\theta ds = 0$$

Moreover,

$$\frac{\partial H}{\partial n} = \nabla H\cdot\mathbf{n} = \left(\frac{\partial H}{\partial r}\mathbf{e_r} + \frac{1}{r}\frac{\partial H}{\partial\theta}\mathbf{e_\theta}\right)\frac{r\mathbf{e_r} - r_\theta\mathbf{e_\theta}}{\sqrt{r^2 + r_\theta^2}} = \frac{r\dfrac{\partial H}{\partial r} - \dfrac{r_\theta}{r}\dfrac{\partial H}{\partial\theta}}{\sqrt{r^2 + r_\theta^2}} \tag{5.66}$$

The final term is going to be written only at the liquid-gas interface, thus, $\eta = 1$. In order to find the Robin-type boundary condition holding on the interface we should firstly estimate $\nabla\times H$. Hence, taking into account that $H = H_\varphi$ and $\dfrac{\partial}{\partial\varphi} = 0$ (axisymmetry):

$$\nabla\times\mathbf{H} = \mathbf{J} = J_r\mathbf{e_r} + J_\theta\mathbf{e_\theta} = \frac{1}{r}\left(\frac{\partial H}{\partial\theta} + H\cot\theta\right)\mathbf{e_r} - \left(\frac{H}{r} + \frac{\partial H}{\partial r}\right)\mathbf{e_\theta} \Rightarrow$$
$$\Rightarrow J_r = \frac{1}{r}\left(\frac{\partial H}{\partial\theta} + H\cot\theta\right),\ J_\theta = -\left(\frac{H}{r} + \frac{\partial H}{\partial r}\right) \tag{5.67}$$

Substituting Eq. 5.67 to Eq. 5.66:

$$\frac{\partial H}{\partial n} = \frac{-H - rJ_\theta - r_\theta J_r + r_\theta\dfrac{H}{r}\cot\theta}{\sqrt{r^2 + r_\theta^2}} = \frac{-H - fJ_\theta - f_\theta J_r + f_\theta\dfrac{H}{f}\cot\theta}{\sqrt{f^2 + f_\theta^2}} \tag{5.68}$$

the boundary integral term of Eq. 5.62 becomes:

$$-\oint_s B_i\frac{\partial H}{\partial n}r\sin\theta ds = \int_0^{\pi/2} B_i\left(Hf + J_\theta f^2 + J_r ff_\theta - H\cot\theta f_\theta\right)\sin\theta d\theta \tag{5.69}$$

Thus, the first residual is:

$$R_{1i} = \iint\left[\frac{\partial B_i}{\partial\eta}\frac{\partial H}{\partial\eta}\eta^2 f^2 + \left(f\frac{\partial B_i}{\partial\theta} - \eta f_\theta\frac{\partial B_i}{\partial\eta}\right)\left(\frac{\partial H}{\partial\theta} - \frac{\eta f_\theta}{f}\frac{\partial H}{\partial\eta}\right)\right]\sin\theta d\eta d\theta$$
$$+\iint\frac{B_i H}{\sin\theta}f d\eta d\theta + \int_0^{\pi/2} B_i\left(Hf + J_\theta f^2 + J_r ff_\theta - H\cot\theta f_\theta\right)\sin\theta d\theta \tag{5.70}$$

125

As far as the normal stress balance on the liquid-gas interface is concerned, it is described via:

$$P_0 - \rho g r \cos\theta + B_0\left(H_{z=0} - H\right) - P_{out} + \gamma 2 H_c = 0 \tag{5.71}$$

Multiplying by **n** each leg of Eq. 5.71:

$$\mathbf{n}\left[P_0 - \rho g r \cos\theta + B_0\left(H_{z=0} - H\right) - P_{out}\right] + \gamma\left(\frac{\partial \mathbf{t}}{\partial s} - \frac{\mathbf{n}}{R_2}\right) = 0 \tag{5.72}$$

where the identity in Eq. 4.13 has been used. Then, multiplying by $\mathbf{e_z}$ each leg of Eq. 5.72 we obtain:

$$\frac{r\cos\theta + r_\theta \sin\theta}{\sqrt{r^2 + r_\theta^2}}\left[P_0 - \rho g r \cos\theta + B_0\left(H_{z=0} - H\right) - P_{out}\right]$$

$$+\gamma \mathbf{e_z} \cdot \frac{\partial \mathbf{t}}{\partial s} - \gamma \frac{r\cos\theta + r_\theta \sin\theta}{\sqrt{r^2 + r_\theta^2}}\frac{1}{R_2} = 0 \tag{5.73}$$

Multiplying Eq. 5.73 by the quadratic basis functions, b_i, while employing Eq. 5.61 the weak form is derived:

$$\iint b_i \frac{r\cos\theta + r_\theta \sin\theta}{\sqrt{r^2 + r_\theta^2}}\left[P_0 - \rho g r \cos\theta + B_0\left(H_{z=0} - H\right) - P_{out}\right] r\sin\theta \, ds \, d\varphi$$

$$+\iint_A b_i \gamma \frac{\partial \mathbf{t}}{\partial s}\mathbf{e_z} r\sin\theta \, ds \, d\varphi - \iint b_i \gamma \frac{r\cos\theta + r_\theta \sin\theta}{\sqrt{r^2 + r_\theta^2}}\frac{1}{R_2} r\sin\theta \, ds \, d\varphi = 0 \Rightarrow$$

$$\Rightarrow \int_0^{\pi/2} b_i\left(r\cos\theta + r_\theta \sin\theta\right)\left[P_0 - \rho g r \cos\theta + B_0\left(H_{z=0} - H\right) - P_{out}\right] r\sin\theta \, d\theta$$

$$+\int_s b_i \gamma \frac{\partial \mathbf{t}}{\partial s}\mathbf{e_z} r\sin\theta \, ds - \int_0^{\pi/2} b_i \gamma \left(r\cos\theta + r_\theta \sin\theta\right)\frac{1}{R_2} r\sin\theta \, d\theta = 0 \Rightarrow$$

$$\Rightarrow \int_0^{\pi/2} b_i\left(r\cos\theta + r_\theta \sin\theta\right)\left[P_0 - \rho g r \cos\theta + B_0\left(H_{z=0} - H\right) - P_{out}\right] r\sin\theta \, d\theta$$

$$+\int_s \gamma\left[b_i \mathbf{t}\cdot\mathbf{e_z} r\sin\theta\right]_{s(r=0)}^{s(r=R_f)} ds - \int_s \gamma \mathbf{t}\frac{\partial}{\partial s}\left(b_i \mathbf{e_z} r\sin\theta\right) ds - \int_0^{\pi/2} b_i \gamma\left(r\cos\theta + r_\theta \sin\theta\right)\frac{1}{R_2} r\sin\theta \, d\theta = 0 \overset{\mathbf{e_z}=\text{constant}}{\Rightarrow}$$

$$\Rightarrow R_{2i} = \int_0^{\pi/2} b_i\left(r\cos\theta + r_\theta \sin\theta\right)\left[P_0 - \rho g r \cos\theta + B_0\left(H_{z=0} - H\right) - P_{out}\right] r\sin\theta \, d\theta$$

$$-\gamma\sin\theta_c R_f \delta_{i,node\theta} - \int_s \gamma \frac{r_\theta \cos\theta - r\sin\theta}{\sqrt{r^2 + r_\theta^2}}\frac{\partial}{\partial\theta}\left(b_i r\sin\theta\right) d\theta - \int_0^{\pi/2} b_i \gamma\left(r\cos\theta + r_\theta \sin\theta\right)\frac{1}{R_2} r\sin\theta \, d\theta \tag{5.74}$$

Consequently, R_{1i} and R_{2i}, described via Eqs. 5.70 and 5.74, respectively, are made dimensionless by using the pore radius, R_p, γ/R_p and $J_r \cdot R_p$ as a characteristic length scale, pressure and stream function of current, respectively while θ is getting dimensionless by dividing by $\pi/2$. Again, no bars or other symbols are used for simplicity:

126

$$R_{1i} = \int_0^1 \int_0^1 \left[\frac{\partial B_i}{\partial \eta} \frac{\partial H}{\partial \eta} \eta^2 f^2 + \left(f \frac{\partial B_i}{\partial \theta} - \eta f_\theta \frac{\partial B_i}{\partial \eta} \right) \left(\frac{\partial H}{\partial \theta} - \frac{\eta f_\theta}{f} \frac{\partial H}{\partial \eta} \right) \right] \sin\theta \, d\eta \, d\theta \tag{5.75}$$

$$+ \int_0^1 \int_0^1 \frac{B_i H}{\sin\theta} f \, d\eta \, d\theta + \int_0^1 B_i \left(Hf + J_\theta f^2 + J_r f f_\theta - H \cot\theta f_\theta \right) \sin\theta \, d\theta$$

$$R_{2i} = \int_0^1 \left[(P_0 - P_{out}) + Bond_m \left(H_{z=0} - H \right) - Bond \, f \cos\theta \right] b_i \left(f \cos\theta + f_\theta \sin\theta \right) f \sin\theta \, d\theta$$

$$- \int_0^1 \frac{f_\theta \cos\theta - f \sin\theta}{S_\theta} \frac{\partial}{\partial\theta} \left(b_i f \sin\theta \right)$$

$$- \int_0^1 b_i \left(f \cos\theta + f_\theta \sin\theta \right) \left(\frac{1}{S_\theta} - \frac{f_\theta \cot\theta}{f S_\theta} \right) f \sin\theta \, d\theta - \sin\theta_c \frac{R_f}{R_p} \delta_{i,node\theta} \tag{5.76}$$

where $S_\theta = \sqrt{r^2 + r_\theta^2}$; the last term in the above equation fixes the contact angle at the edge of the liquid metal drop. Also, the dimensionless numbers here are:

$$Bond = \frac{\rho g R_p}{\gamma / R_p}, \quad Bond_m = \frac{B_0 J_r R_p}{\gamma / R_p} \tag{5.77}$$

relating the gravitational and magnetic forces to surface tension forces, respectively.

The aforementioned system of equations, Eqs. 5.75 and 5.76, produces a set of nonlinear equations with the matrix, A, to be inversed being in the form of an arrowhead matrix, similar to **Fig. 5.8**.

After storing the equations in the above form, A matrix is inversed by a standard routine, written for arrow matrices. Consequently, the unknown vector is calculated via the Newton-Rapson, as discussed in subsection 5.3. Simple continuation is used in order to capture the evolution of the solution in the parameter space defined by the contact angle and the magnetic Bond number.

5.4.5 Effect of the topography of the porous substrate and arc-length continuation

Assuming that $R_p \gg \delta_A$ ($R_P \approx 1000 \, \delta_A$ in the present study), analysis of the topography in the vicinity of a single pore is performed in order to estimate the Euclidean distance between the liquid-gas interface and the solid substrate. In this investigation, which was modelled in subsection 4.4.4, the domain is divided into three main regions, depending on the evaluation of the minimum distance, δ, from a point on the interface and the pore wall, as depicted in **Fig. 5.10**:

region i: $(r \geq R_p, z \geq 0) : \delta = z, \left. \frac{\partial \delta}{\partial z} \right|_r = 1, \left. \frac{\partial \delta}{\partial r} \right|_z = 0 \rightarrow \nabla\delta = \mathbf{e_z}$ \hfill (5.78a)

127

region ii: $(r \le R_p, z \ge 0)$: $\delta = \sqrt{z^2 + (r - R_p)^2}$, $\left.\dfrac{\partial \delta}{\partial z}\right|_r = \dfrac{z}{\sqrt{z^2 + (r - R_p)^2}}$,

$$\left.\frac{\partial \delta}{\partial r}\right|_z = \frac{r - R_p}{\sqrt{z^2 + (r - R_p)^2}} \rightarrow \nabla \delta = \frac{(r - R_p)\mathbf{e_r} + z\mathbf{e_z}}{\sqrt{z^2 + (r - R_p)^2}} \qquad (5.78b)$$

region iii: $(r \le R_p, z \le 0)$: $\delta = R_p - r$, $\left.\dfrac{\partial \delta}{\partial z}\right|_r = 0$, $\left.\dfrac{\partial \delta}{\partial r}\right|_z = -1 \rightarrow \nabla \delta = -\mathbf{e_r}$ $\qquad (5.78c)$
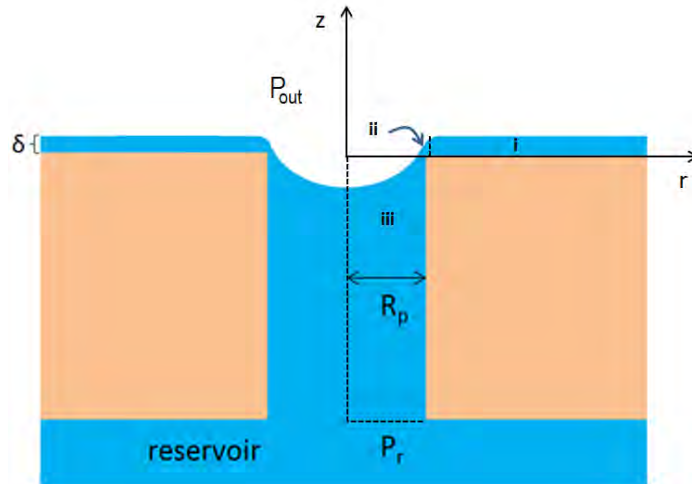
Fig 5.10 Pore geometry along with the division of the main domain into three subregions

In general, according to Eq. 4.52:

$$\Pi = -\frac{\partial W}{\partial \mathbf{n}} = -\frac{\partial W}{\partial \delta}\frac{\partial \delta}{\partial \mathbf{n}} \Rightarrow$$

$$\Rightarrow \Pi = -\frac{\partial W}{\partial \delta}\nabla \delta \cdot \mathbf{n} \qquad (5.79)$$

where $\dfrac{\partial W}{\partial \delta} = \dfrac{A}{6\pi\delta^3}$ or $\dfrac{4W_0}{\delta_A}\left[\left(\dfrac{\delta_A}{\delta}\right)^3 - \left(\dfrac{\delta_A}{\delta}\right)^5\right]$ for the case of a purely repulsive potential or a

long range attractive short range repulsive potential, respectively, described in Chapter 2 and also in subsection 4.4.4.

Using the Lagrangian representetion for the liquid-gas interface, the normal unit vector reads:

$$\mathbf{n} = \frac{-z_\xi \mathbf{e_r} + r_\xi \mathbf{e_z}}{S_\xi}, \text{ where } S_\xi = \sqrt{r_\xi^2 + z_\xi^2} \qquad (5.80)$$

Thus, in region i the disjoining pressure, considering Eq. 5.78a, assumes the form:

128

$$\Pi_i = -\frac{\partial W}{\partial \delta}\frac{r_\xi}{S_\xi} \tag{5.81}$$

and the normal stress balance reads in this region:

$$P_0 - \rho gz - P_{out} - \overbrace{\frac{\partial W}{\partial \delta}\frac{r_\xi}{S_\xi}}^{\Pi_i} =$$

$$= -\left(\gamma + W_0\right)\left(\frac{z_\xi}{rS_\xi} + \frac{r_\xi z_{\xi,\xi} - r_{\xi,\xi} z_\xi}{S_\xi^3}\right) \tag{5.82a}$$

Similarly, in region ii the normal stress balance, considering Eq.5.78b, assumes the form:

$$P_0 - \rho gz - P_{out} - \overbrace{\frac{\partial W}{\partial \delta}\frac{-\left(\mathrm{r}-R_p\right)z_\xi + zr_\xi}{S_\xi\sqrt{z^2 + \left(\mathrm{r}-R_p\right)^2}}}^{\Pi_{ii}} =$$

$$= -\left(\gamma + W_0\right)\left(\frac{z_\xi}{rS_\xi} + \frac{r_\xi z_{\xi,\xi} - r_{\xi,\xi} z_\xi}{S_\xi^3}\right) \tag{5.82b}$$

Finally, in region iii the normal stress balance, considering Eq.5.78c, reads:

$$P_0 - \rho gz - P_{out} - \overbrace{\frac{\partial W}{\partial \delta}\frac{z_\xi}{S_\xi}}^{\Pi_{iii}} =$$

$$= -\left(\gamma + W_0\right)\left(\frac{z_\xi}{rS_\xi} + \frac{r_\xi z_{\xi,\xi} - r_{\xi,\xi} z_\xi}{S_\xi^3}\right) \tag{5.82c}$$

$$-2H_c = 2k_m = \nabla_s \cdot \mathbf{n} = \frac{-z_\xi}{rS_\xi} - \frac{r_\xi z_{\xi,\xi} - r_{\xi,\xi} z_\xi}{S_\xi^3} \tag{5.82d}$$

The system of the governing equations of the problem consists of Eqs. 5.82a-5.82c along with:

$$\frac{dS}{d\xi} = S_{max} \Rightarrow \sqrt{r_\xi^2 + z_\xi^2} - S_{max} = 0 \tag{5.83}$$

and the following boundary conditions:

$$r\left(\xi = 0\right) = 0,\ r\left(\xi = 1\right) = r_{max},\ z_\xi\big|_{\xi=0} = z_\xi\big|_{\xi=1} = 0,\ r_\xi\big|_{\xi=0} = r_\xi\big|_{\xi=1} = S_{max} \tag{5.84}$$

129

Eq. 5.83 essentially fixes the nodes along the interface so that they form an equidistant mesh. The boundary condition $r(\xi = 1) = r_{max}$ constitutes the third residual as will be shown below with S_{max} representing the total length of the generator of the axisymmetric liquid-gas interface; r_{max} is set to a multiple of the pore radius in order to signify a large distance from the axis of symmetry.

Eqs. 5.82-5.84 are discretized using the finite element methodology, with the unknown z and r coordinates described via:

$$(z, r) = \sum_{i=1}^{n_{total} + 2} (z_{ci}, r_{ci}) \Phi_i \tag{5.85}$$

where z_{ci}, r_{ci} are the unknown coefficients of the spline representation and n_{total} is the total number of nodes. The coefficients that correspond to the fictitious nodes outside the domain, i.e. $z_{ci}(1)$, $r_{ci}(1)$ and $z_{ci}(n_{total} + 2)$, $r_{ci}(n_{total} + 2)$ are calculated by the boundary conditions as will be discussed next. Also, b cubic splines, Φ_i, maintain smoothness and continuity of higher order derivatives, as mentioned in subsection 5.2.4.

The total interfacial nodes, with n_{el} denoting the total number of elements, are:

$$n_{total} = n_{el} + 1 \tag{5.86}$$

From now on, only the case of the long range attractive short range repulsive potential is going to be considered for the mathematical formulation. However, the same procedure was followed also for the case of purely repulsive potential. Next, the final equations in their weak form are written for each equation:

$$R_{1i} = \int_0^{R_f} \Phi_i \left(P_0 - \rho g z - P_{out} + \Pi - (\gamma + W_0) 2 k_m \right) r \, dr \tag{5.87}$$

Converting Eq. 5.87 into Lagrangian representation we get:

$$R_{1i} = \int_0^1 \Phi_i \left[P_r - \rho g h_0 - \rho g z - P_{out} - \frac{4 W_{.0}}{\delta_A} \left[\left(\frac{\delta_A}{\delta} \right)^3 - \left(\frac{\delta_A}{\delta} \right)^5 \right] \frac{\partial \delta}{\partial \mathbf{n}} \right] r r_\xi \, d\xi$$
$$+ \int_0^1 \Phi_i (\gamma + W_0) \left(\frac{z_\xi}{r S_\xi} + \frac{r_\xi z_{\xi,\xi} - r_{\xi,\xi} z_\xi}{S_\xi^3} \right) r r_\xi \, d\xi \tag{5.88}$$

Consequently, Eq. 5.88 is made dimensionless by using the pore radius, R_p as a characteristic length scale and γ/R_p as a characteristic pressure:

130

$$R_{1i} = (P_0 - P_{out}) \int_0^1 \Phi_i r r_\xi d\xi - Bond \int_0^1 \Phi_i z r r_\xi d\xi \tag{5.89}$$

$$-\left(\frac{W_{,0}}{\gamma}\right) \int_0^1 \Phi_i \frac{4}{\delta_A} \left[\left(\frac{\delta_A}{\delta}\right)^3 - \left(\frac{\delta_A}{\delta}\right)^5\right] \frac{\partial \delta}{\partial \mathbf{n}} r r_\xi d\xi$$

$$+\left(1 + \frac{W_{,0}}{\gamma}\right) \int_0^1 \Phi_i \left(\frac{z_\xi}{r S_\xi} + \frac{r_\xi z_{\xi,\xi} - r_{\xi,\xi} z_\xi}{S_\xi^3}\right) r r_\xi d\xi$$

All the variables in the residual R_{1i} are dimensionless and no bars or other symbols are used for simplicity. The dimensionless numbers that control the problem are:

$$Bond = \frac{\rho g R_p}{\gamma / R_p}, \quad \frac{W_0}{\gamma} \tag{5.90}$$

relating the relative strength of gravitational and surface forces to surface tension forces. Finally, $\frac{\partial \delta}{\partial \mathbf{n}}$ depends on the sub-region, Eqs. 5.78a-5.78c.

The second and third residuals read as:

$$R_{2i} = \int_0^1 \Phi_i \left(\sqrt{r_\xi^2 + z_\xi^2} - S_{max}\right) d\xi \tag{5.91}$$

$$R_3 = r(\xi = 1) - r_{max} \tag{5.92}$$

If n_{el} is the total number of elements, then the total nodes are:

$$n_{total} + 2 \tag{5.93}$$

with "+2" corresponding to the two fictitious nodes outside the domain. As a consequence, the total number of equations required is:

$$neq_{total} = 2(n_{total} + 2) + 1 \tag{5.94}$$

i.e. $n_{total} + 2$ equations for z(ξ), $n_{total} + 2$ equations for r(ξ) and one equation for S_{max}.

The aforementioned system of equations produces a set of nonlinear equations with the matrix, A, similar to **Fig. 5.8**. Hence, if $n_{band} = 2(n_{total} + 2)$, A matrix can be divided into four sub-matrices:

1. A banded Jacobian matrix (J) of dimension $n_{band} \times n_{band}$, with derivative entries of the residuals R_{1i} and R_{2i} with respect to z_{ci} and r_{ci}. This part of the matrix has non-zero entries in a zone with bandwidth 15,
2. A matrix in the form of a column (COL) of dimension n_{band} with derivative of the residuals R_{1i} and R_{2i} with respect to S_{max},

131

3. A matrix in the form of a row (ROW) of dimension n_{band} with derivative entries of the residual R_3 to z_{ci} and r_{ci} and

4. A matrix in the square arrowhead at the bottom right (HEAD) of dimension 1×1 with derivative entries of the residual R_3 with respect to S_{max}.

Next, for a better understanding of how the boundary conditions are imposed on the fictitious nodes and how the arc length continuation technique is tackled, which is going to be elaborated below, the matrix form of the present problem is given in **Fig. 5.11**:

$$
[A]\rightarrow
\begin{bmatrix}
\begin{bmatrix}
\dfrac{\partial R_{1,i}}{\partial z_{ci}} & \dfrac{\partial R_{1,i}}{\partial r_{ci}} \\[2mm]
\dfrac{\partial R_{2,i}}{\partial z_{ci}} & \dfrac{\partial R_{2,i}}{\partial r_{ci}}
\end{bmatrix} &
\begin{bmatrix}
\dfrac{\partial R_{1,i}}{\partial S_{max}} \\[2mm]
\dfrac{\partial R_{2,i}}{\partial S_{max}}
\end{bmatrix} \\[6mm]
\begin{bmatrix}
\dfrac{\partial R_3}{\partial z_{ci}} & \dfrac{\partial R_3}{\partial r_{ci}}
\end{bmatrix} &
\begin{bmatrix}
\dfrac{\partial R_3}{\partial S_{max}}
\end{bmatrix}
\end{bmatrix}
\cdot
\begin{bmatrix}
z_c \\ r_c \\ \dots \\ \dots \\ S_{max}
\end{bmatrix}
=
\begin{bmatrix}
R_1 \\ R_2 \\ \dots \\ \dots \\ R_3
\end{bmatrix}
$$

[J]   [COL]   [SOL]   [RHS]
[ROW]   [HEAD]

Fig. 5.11 Schematic illustration of the matrix form of the present problem

The matrices [J], [ROW], [COL] and [HEAD] constitute the A matrix to be inversed while [SOL] being the matrix which contains the solutions of the problem, with dimension neq_{total}, and [RHS] containing the aforementioned residuals, with dimension also neq_{total}. The boundary conditions are incorporated in the [RHS] matrix as follows:

$$
\begin{array}{rl}
\text{First fictitious node for z} \rightarrow & z_\xi \\
\text{First fictitious node for r} \rightarrow & r \\
\text{First real node for z} \rightarrow & R_1 \\
\text{First real node for r} \rightarrow & r_\xi - S_{max} \\
& R_1 \\
& R_2 \\
& R_1 \\
& R_2 \\
& . \\
& . \\
& . \\
\text{Last real node for r} \rightarrow & r_\xi - S_{max} \\
\text{Last fictitious node for z} \rightarrow & z_\xi \\
\text{Last fictitious node for r} \rightarrow & r_{\xi,\xi} \\
R_3 \rightarrow & r - r_{final}
\end{array}
\left. \rule{0pt}{7em}\right\} neq_{total}
$$

Fig. 5.12 Schematic illustration of the [RHS] matrix augmented with the boundary conditions

In this problem, solutions are derived for different values of the control parameter, namely $p = P_0 - P_{out}$. Thus, a previously converged solution can be used as initial guess for a new solution corresponding to a new value of the parameter. This idea can be illustrated in the **Fig. 5.13a**. Simple continuation is performed when the solution is smooth and without limit points, as in the previous presented studies. In this case the control parameter, p, changes independently by a step Δp:

$$p^{n+1} = p^n + \Delta p \tag{5.95}$$

However, if the solution has a limit point, **Fig. 5.13b**, a solution in the direction that Δp predicts does not exist, especially near the limit point. As a matter of fact, at the limit point the Jacobian matrix becomes singular and the simulation breaks. As a consequence, the simple continuation is not appropriate to proceed along the solution family. In order to overcome this problem the arc-length continuation was used which is a standard technique for detection of instabilities in shells and drops [105-107]. In this consideration, one more equation is added in the mathematical formulation and the control parameter, p, is now part of the solution. The extra Residual to be taken into account is:

$$R_{4i} = \sum_{i=1}^{n_{total}+2} \left(z_{c,i}^{n+1} - z_{c,i}^n \right)^2 + \sum_{i=1}^{nnode+2} \left(r_{c,i}^{n+1} - r_{c,i}^n \right)^2 + \left(S_{max}^{n+1} - S_{max}^n \right)^2 + \left(p^{n+1} - p^n \right)^2 - \Delta\lambda^2 \tag{5.96}$$

with i standing for the corresponding node of the computational mesh and n denoting the old converged solution for the parameter p^{n+1} and n+1 the current solution. Besides, $\Delta\lambda$ is a constant parameter representing the arc-length of the solution branch. In order to estimate the value of the arc-length $\Delta\lambda$, as a first step simple continuation is performed before the limit point for a relative small value of Δp starting from the solution vector $\vec{x}^0$ and moving to solution vector $\vec{x}^1$ as depicted in **Fig. 5.13c**.
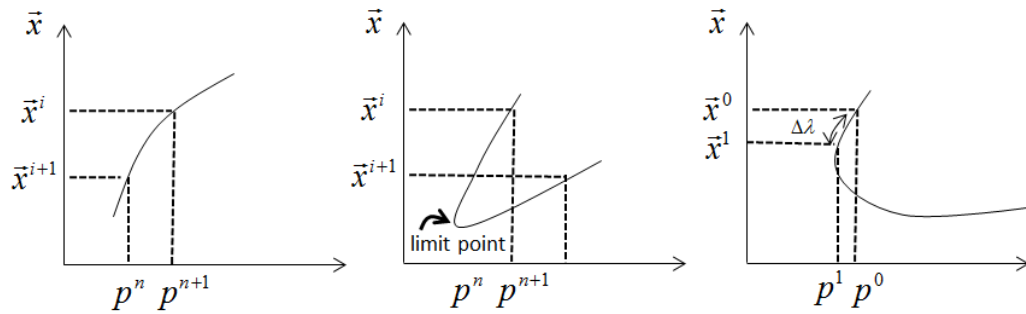
Fig. 5.13 (a) Simple and (b) Arc-length continuation around a limit point and (c) estimation of the arc-length $\Delta\lambda$

Consequently, by adding Eq. 5.96 in A matrix, it has one more row and one more column corresponding to the unknown parameter p. The augmented A matrix has the following form:

Fig. 5.14 Schematic illustration of the matrix form of the present problem including the augmented A matrix

It should be stressed that even if [A] becomes singular, the augmented matrix [A] remains non-singular and therefore the simulation continues around limit point.

After solving the system of equations described in **Fig. 5.14** with the Newton-Rapson method, the initial guess for the next solution is made by solving the following set of equations:

Fig. 5.15 Schematic illustration of the matrix form of the present problem required to be solved for the initial guess of the next solution

Note that $\dfrac{\partial z_{ci}}{\partial \lambda} = \dfrac{\partial r_{ci}}{\partial \lambda} = \dfrac{\partial S_{max}}{\partial \lambda} = 0$ and $\dfrac{\partial R_4}{\partial \lambda} = -2\Delta\lambda$. Subsequently, the initial guess for the next solution is:

$$x_i^{n+1} = x_i^n + \left.\frac{\partial x_i}{\partial \lambda}\right|^n \cdot \Delta\lambda \tag{5.97}$$

and the corresponding parameter is:

$$p_i^{n+1} = p_i^n + \left.\frac{\partial p_i}{\partial \lambda}\right|^n \cdot \Delta\lambda \tag{5.98}$$

134

where for the first continuation, the initial guess of the derivatives is

$$\left.\frac{\partial x_i}{\partial \lambda}\right|^2 = \frac{x_i^1 - x_i^0}{\Delta \lambda}, \quad \left.\frac{\partial p}{\partial \lambda}\right|^2 = \frac{p_i^1 - p_i^0}{\Delta \lambda} \tag{5.99}$$

Finally, the steps in terms of an algorithm are outlined in **Fig. 5.16**.
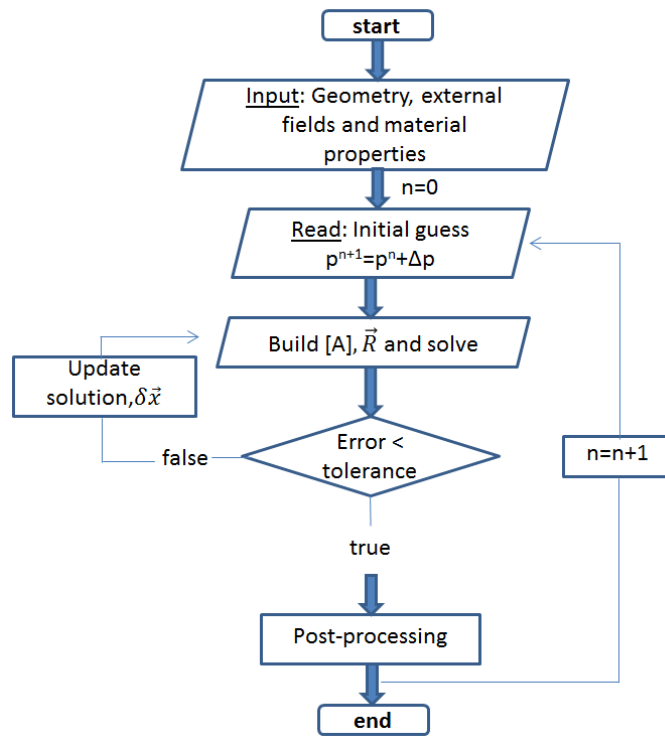
Fig. 5.16 Flow chart of the numerical procedure

135

5.5 Benchmark case studies

In order to validate the numerical model pertaining to the static arrangement of the liquid metal arrangement, a parametric study was conducted on the static arrangement as a function of the reservoir overpressure. For relatively large overpressure in favor of the reservoir, i.e $\Delta P = P_r - P_{out} \approx 500 Pa$ and larger the drop size decreases, the dominant balance is between the pressure drop and the surface tension, $\Delta P = P_0 - P_{out} \approx 2\gamma / R_m$, $P_0 = P_r - \rho g h_0$, and gravity is of minor importance in achieving static equilibrium. In this context an 1 mm thick porous matrix is considered with $h_0 =$ 1mm, $P_0 = P_r$ - 5 Pa, lithium density $\rho \approx 500$ kg/m^3, $\gamma = 0.4$ N/m, g=10 m/s^2, while the contact angle is set to 30° and $\Delta P = 500$ Pa. In **Fig. 5.17** below the drop shape that rests on the CPS surface is calculated numerically by solving the problem formulation provided in section 5.4.1 for fixed contact angle θ=30°. The shape obtained is that of a spherical cap with radius $R_m \sim 2\gamma/\Delta P$, that is pinned onto the substrate with a contact angle of 30° and contact length of $R_m\sin\theta \approx 0.8$ mm and whose center of curvature lies below the CPS surface. As illustrated by **Fig 5.17** shown below the numerically obtained static shape confirms the above prediction, resembling part of the aforementioned circle whose center of curvature lies below the z = 0 line.
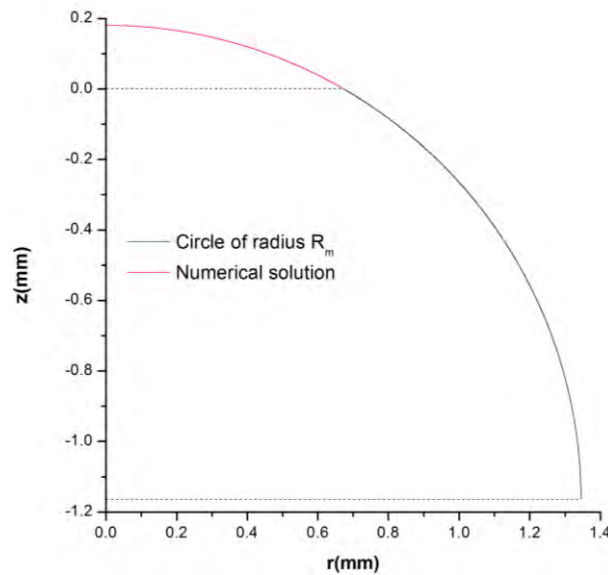
Fig. 5.17 Comparison of the current static numerical model against the circle of radius $R_m = R_{f,numerical}/\sin\theta_c$

In order to validate the model presented in section 5.3 regarding the capillary rise of a liquid within a single cylindrical pore, it was tested for the case of a pore with a radius of 1mm that is gradually filled with water from a reservoir held at atmospheric pressure, solely via capillary forces. The simulation was performed until either a static arrangement within the pore is established or the liquid has risen to the top of pore. More specifically, when Δp=0 Pa, $R_p = 1$mm, $\gamma = 0.073$ N/m, $\rho = 1000$ Kg/m^3 and g = 9.81m/s^2. **Fig. 5.18a** provides a sequence of shapes for the rising water meniscus during the process of capillary rise. As can be gleaned from the final stages of capillary rise, and more clearly in **Fig.5.18b**, the meniscus shape, obtained with and without inertial effects (We = 0 and We ≠ 0, respectively), is in good agreement with the static arrangement of liquid water within a cylindrical pore with a radius of 1 mm obtained independently via solution of the Young Laplace equation at static equilibrium without the viscous terms, i.e. via the above static numerical code. Our numerical results were also tested against the Washburn equation as will be discussed in subsection 6.3.

136

(a)

(b)
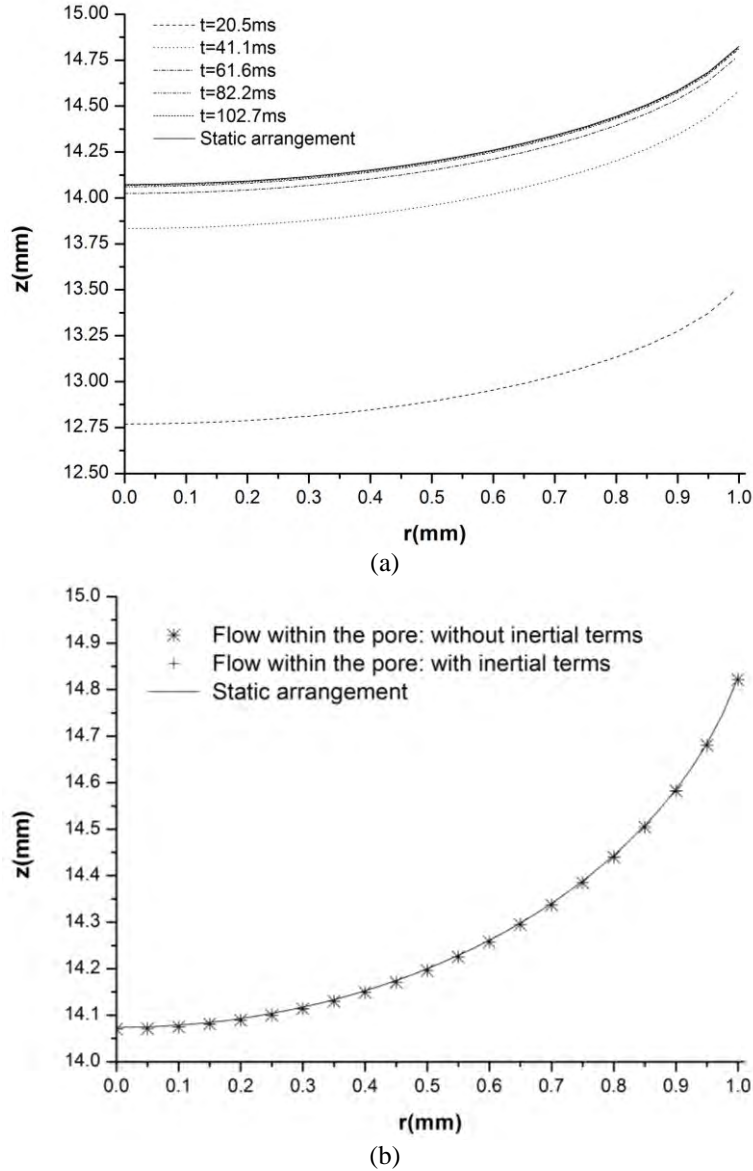
Fig. 5.18 (a) Time evolution of the meniscus shapes during the process of capillary rise and (b) Comparison of the numerical model concerning the capillary flow within a single cylindrical pore (with and without inertial terms) against the static arrangement of liquid water within a pore

As far as the electrostatic model is concerned, comparison of the present numerical approach for the static arrangement of a polymeric droplet that rests on a solid surface with a fixed contact angle $\theta_c = 60^o$, $Bond_{el} = 5.06$ and $Bond = 0.33$, against the boundary element solution obtained by Reznik et al., [92], indicates that our results agree with the maximum and minimum values of z and r, respectively, for the case of negligible electric stress [108], **Fig 5.19**. However, partial agreement is observed, when the case with an external electric field is studied. This is caused by our modelling assumption, that for a very thin film on top of the porous substrate, electrical potential variations at the interface can be estimated via $\dfrac{\partial \Phi}{\partial n} \approx \dfrac{d\Phi}{dz}, \quad \dfrac{\partial \Phi}{\partial s} \approx \dfrac{d\Phi}{dz}\dfrac{dz}{ds}$, where normal derivatives are estimated based on longitudinal variations.

137

Hence, for comparable film thickness and length, the electric potential in the region surrounding the film can be calculated with the boundary element method [106]. Nevertheless, this simplified model gives the qualitatively correct trend of the process which captures the gradual deformation of an initial droplet under the action of the electric stresses. In particular, when a fixed contact point is assumed rather than a fixed contact angle, formation of a conical angle is captured in the pole region at large $Bond_{El}$ indicating possible jetting originated from this region. In **Fig. 5.19** the initial and final static arrangements are portrayed, in the parameter range slightly before the conical angle formation. t stands for the dimensionless time, which was made dimensionless upon dividing the real time by $\mu R_p/\gamma$ that uses as a characteristic time scale, R_p represents the capillary radius while μ and γ are the dynamic viscosity and the surface tension of the working fluid, respectively [92].
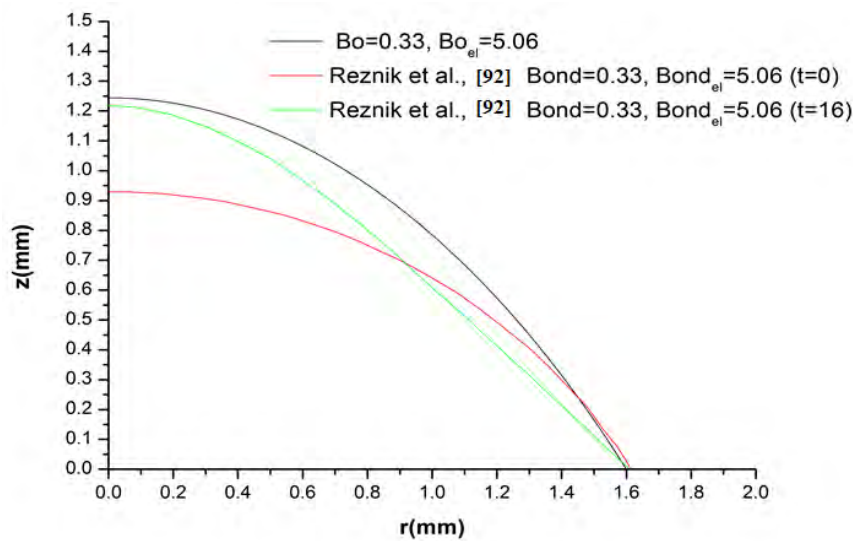
Fig. 5.19 Comparison of the current electrostatic numerical model against the droplet evolution corresponding to contact angle $\theta_c = 60^o$, $Bond_{el} = 5.06$, $Bond = 0.33$ derived by Reznik et al., [92]

Conical angle formation as an effect of the electrostatic part of the Maxwell stress on the static arrangement and the implied impact on the dynamic response of the droplet, will be extended in Chapter 6 to include the magnetic part of the Maxwell stress in an effort to provide a plausible mechanism for drop ejection during operation of the CPS.

The problem formulation, regarding the effects of the Lorentz forces ignores the rotational part of the Maxwell stress for simplicity in these calculations. Thus, for the comparison, the case of the liquid lithium was chosen again with fixed contact point at the pore`s edge. In this context, the computational solution that accounts for magnetic induction H was tested against a simplified analytical solution, which was derived in Appendix E. In particular, the analytical solution for dimensionless H is compared with the computational one, where the interface approaches a line segment at the pore`s mouth for the case of $Bond_m = 1.44 \cdot 10^{-3}$ and $Bond = 1.11 \cdot 10^{-5}$ and H = 0 at the bottom of the pore, at the wall and at the left boundary, see also **Fig. 4.18**. The analytical results are in quite good agreement with the numerical ones, as can be seen in **Fig. 5.20**. The small discrepancies exist because the shape of the aforementioned computationally obtained interface is not a perfect line segment.

138
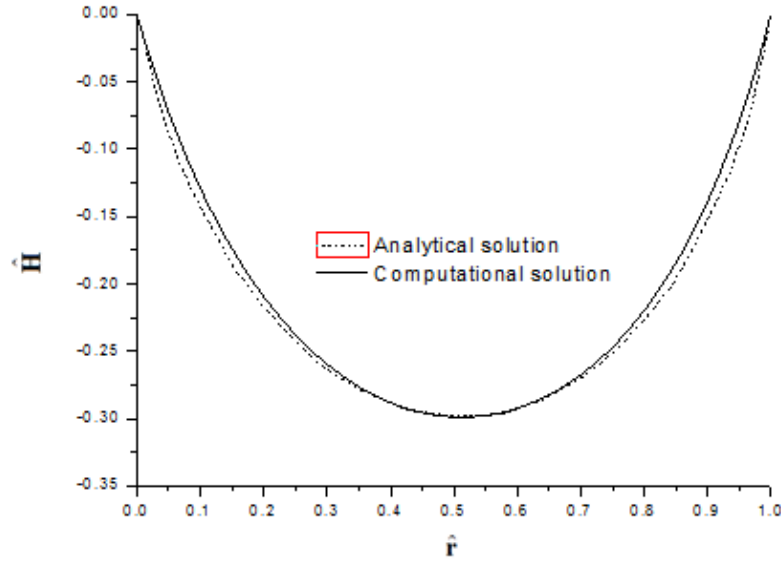
Fig. 5.20 Comparison of dimensionless H derived analytically for a rectangular domain with the computational solution, for $\text{Bond}_m = 1.44 \cdot 10^{-3}$ and $\text{Bond} = 1.1 \cdot 10^{-5}$, when $J_z = 0$

Finally, regarding the static analysis augmented with the interaction potential, for relatively small positive overpressures, the liquid metal was seen not to escape the pore. As ΔP increases it forms a drop that protrudes from the pore and meets the pore at a fixed contact point, i.e. the pore radius R_p, with a macroscopic angle estimated via $\sin\theta = R_p/R_m$, where R_m is the radius of curvature of the drop and is given by the relation $R_m \sim 2\gamma/\Delta P$. For $W_0 = 0.05$ N/m the angle at the contact point is seen to gradually increase as ΔP increases until a limit point arises when $\Delta P \approx 11500$ Pa and $\theta \approx 27^o$. It was shown by an asymptotic analysis of the above regions that, especially when $W_0 \ll \gamma$, the angle at which the transition layer leaves the substrate matches the solution from the pore region and is given by the relation $\cos\theta = 1 - W_0/\gamma$. Thus, for the case considered above, namely when $W_0 = 0.05$ N/m, θ is equal to 29° which is very close to 27° obtained via the numerical analysis. The derivation of the asymptotic solution along with the aforementioned comparison is presented in subsection 6.4.2.

140

Chapter 6: Results

In this chapter, the results are presented related to the simulations of the numerical models described in Chapter 5. First, results pertaining to the preparation phase of the CPS are presented. Then, a first principles heat transfer analysis is presented, introducing the various factors affecting the response of the CPS to an external heat load. Subsequently, numerical results of the study of capillary flow within a single cylindrical pore are presented and discussed in the context of the replenishment problem. Finally, the results of the parametric study on the static arrangement of the CPS are presented, under the influence of the reservoir overpressure, external field forces, namely the electric and Lorentz forces, and the topography of the porous substrate at near vacuum conditions.

6.1 Preparation Phase

The numerical methodology, which was described in subsection 5.4.2, was implemented in order to perform a parametric study on the effect of the additional reservoir of lithium, h_r, on the shape and thickness of the liquid metal layer that coats the porous layer at static equilibrium. Liquid lithium was used as the operating fluid. Molten Li physical properties at 300^oC were used according to [109]. More specifically, the density of liquid and solid lithium is set to $\rho_l = 504.419$ and $\rho_s = 535$ Kg/m^3 while surface tension $\gamma = 0.314$ N/m. Furthermore, the CPS wafer thickness and width are set to $h_0 = 1$mm and $R_c = 10$cm, respectively and $g = 9.81$ m/s^2. Finally, 300 quadratic Lagrangian elements were tested with sufficient accuracy for these calculations.

The eventual static arrangement is a result of the pressure driven flow due to density change of heated lithium. The static film thickness can be approximated as:

$$h_{film} \approx \frac{V_{film}}{\pi R_c^2} = \left(\alpha h_0 + h_r\right)\left(\rho_s - \rho_l\right)/\rho_l \tag{6.1}$$

Thus, when no additional reservoir of lithium exists, i.e. for $h_r = 0$ mm, and for CPS porosity $\alpha = 0.3$ and 0.5 the static film thickness is estimated to be approximately equal to 21.5 μm and 35.8 μm, respectively.

Static calculations fixing the mass of the liquid metal film, via Eq. 5.36, the size of the wafer, $h_0 = 1$mm and the contact point at $r = R_c$, while satisfying the normal force balance confirm this picture as can be gleaned from **Fig. 6.1**.
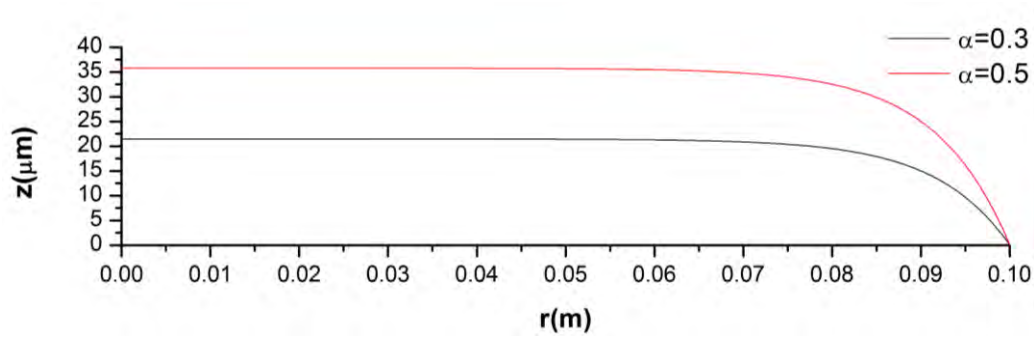
Fig. 6.1 Numerical prediction of the static film arrangement for α = 0.3 and 0.5 with no additional reservoir of lithium existing

On the other hand, if there is additional reservoir of lithium it is also expected to liquefy, thus offering additional mass that would end up at the top of the wafer. For α = 0.5 and for h_r = 1mm, 4mm, 7mm and 10 mm, the static film thicknesses are estimated via Eq. 6.1, to be approximately equal to 107 μm, 322 μm, 537 μm and 751 μm, respectively. Static calculations fixing the mass of the liquid metal film, via Eq. 5.36, the size of the wafer, h_0 = 1mm and the contact point at r = R_c while satisfying the normal force balance, confirm this picture as the reservoir thickness varies, see also **Fig. 6.2**. Based on the above simulations, in the absence of a reservoir a micron size initial film thickness is anticipated, which is a correct order of magnitude estimate based on preliminary experimental observations.
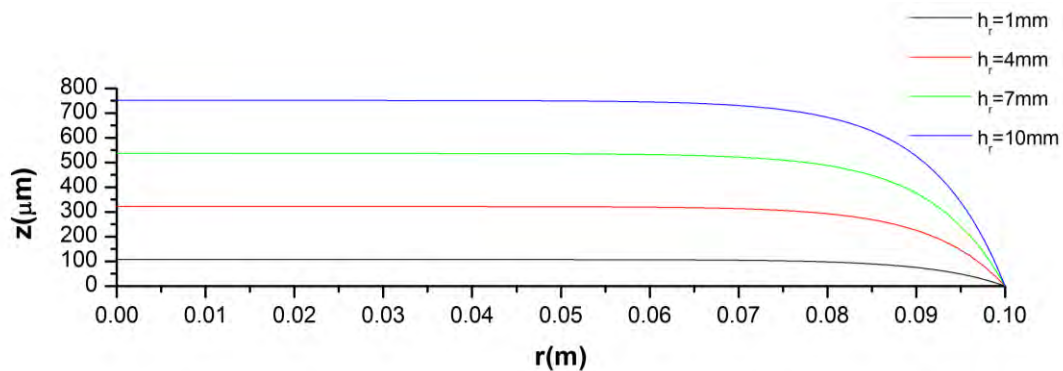
Fig. 6.2 Numerical prediction of the static film thickness arrangement for α = 0.5 and with an additional reservoir of lithium equal to h_r = 1mm, 4mm, 7mm and 10 mm

142

6.2 Depletion and replenishment - Proof of principle study of heat transfer mechanisms in the CPS

6.2.1 Heat exhaust via thermal conduction and evaporation

As emphasized in subsection 4.2.2, the static arrangement is difficult to be achieved and more difficult to be maintained at high enough heat fluxes. Once the machine is "turned on" an external heat pulse is expected to "hit" the CPS configuration. In such a situation, especially for the near vacuum conditions that prevail in the divertor region, a certain amount of the protective lithium layer is expected to evaporate. Provided that the liquid metal film is still intact and covers the CPS surface while no external field forces are considered, the extent of convection is limited and a quasi-static arrangement exists in the CPS. As a first approximation, upon subtracting the amount of heat, $\dot{q}_r$, that is radiated back due to non-coronal radiation shielding, the amount of heat that impinges at the CPS surface is $\dot{q} = \dot{q}_t - \dot{q}_r$, **Fig. 6.3**.
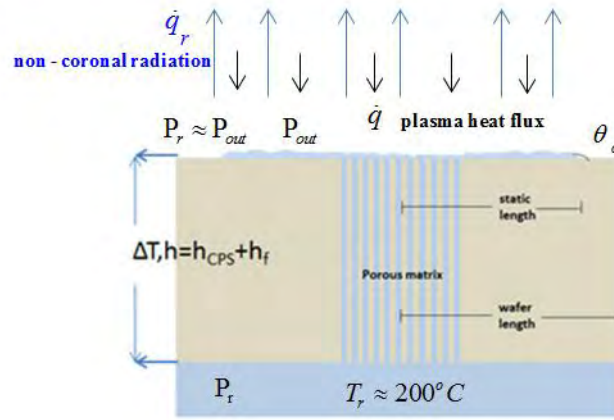
Fig. 6.3 Simplified model of heat transfer problem assuming static arrangement

As a consequence, only conduction (within the CPS mesh and liquid metal film) and evaporation participate in heat exhaust. Thus,

$$\dot{q} = k \frac{T_{out} - T_r}{h} + LW \tag{6.2}$$

where $\dot{q}$ is the oncoming heat flux, k the thermal conductivity, T_r, T_{out} the temperature of liquid lithium within the reservoir and at the outer surface of the wafer, h is the summation of the CPS height, h_{CPS}, and the film thickness formed upon the solid substrate, h_f, L is the lithium latent heat of evaporation and W the rate of evaporation.

We assume that $T_r = 200^{o}C$, $T_{out} = 500^{o}C$, $h_{CPS} = h_f = 1mm$ while k, L are estimated as the average of their values at T_r and T_{out} according to [40]. Equilibrium is assumed with the near vacuum conditions of the surrounding medium, $P_v(500^{o}C) \approx 0.4$ Pa. Thus, considering the oncoming heat flux to be equal to 10 MW/m^2 the rate of evaporation can be found:

$$W = \frac{\dot{q} - k\dfrac{T_{out} - T_r}{h}}{L} = \frac{10{\cdot}10^6 - 48.072\dfrac{500-200}{2{\cdot}10^{-3}}}{22.6{\cdot}10^6} = 0.123\,\frac{kg}{m^2 s} \qquad (6.3)$$

Hence, an oncoming heat flux of 10 MW/m^2 would evaporate the liquid lithium film from the top of the CPS structure at a rate of:

$$\frac{\partial h_f}{\partial t} \approx \frac{W}{\rho} \approx 0.25\,mm/s \qquad (6.4)$$

thus depleting it almost at once. As a consequence, conduction alone cannot exhaust the high enough heat fluxes occurring in real experiments. As mentioned in Chapter 1, JET divertor walls made of tungsten can withstand heat loads up to 20 MW/m^2. Beyond this level the plasma-wall interaction is seen to cause problems such as erosion, thermal stresses, thermal fatigue and plasma contamination which may irreversibly impair the operation of the reactor.

6.2.2 Heat exhaust via transpiration cooling

As stressed in the previous sub-section the liquid metal layer on the top of wafer will soon evaporate leading to a different operating regime, namely the transpiration cooling, **Fig. 6.4**. In this process the oncoming heat flux is going to be balanced by (a) evaporation of Li captured within the pores, (b) heat conduction within the porous matrix but also (c) by convective heat transfer due to the preheating of liquid lithium, from the reservoir temperature up to the temperature of the interface. The latter volumetric flow rate is drawn out of the reservoir by capillary forces once the top of the CPS is depleted of liquid metal.
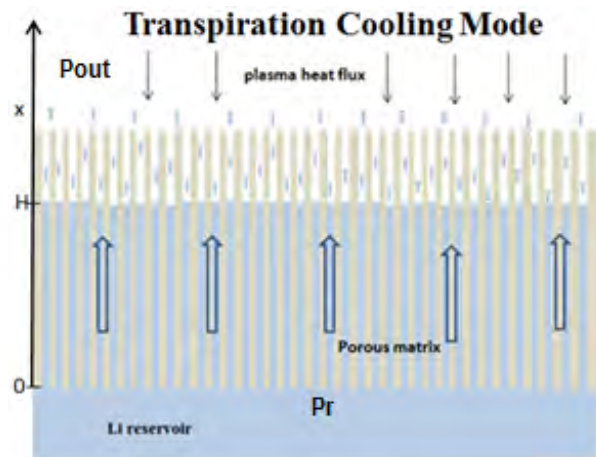
Fig. 6.4 Simplified model of the transpiration cooling mode

Taking the height of the CPS to be much smaller than its width, steady one dimensional heat transfer can be assumed within the CPS structure and a steady heat balance can be established where the above mechanisms balance each other. At the interface with plasma, evaporation takes place while inside the porous matrix conduction and convection co-exist. In this fashion, a steady state can be established producing the necessary liquid metal elevation H within the CPS structure in order to balance the

144

oncoming heat flux $\dot{q}$. Thus, energy balances are used at liquid-plasma interface and across the portion of the CPS which contains the liquid metal. At the liquid plasma interface the oncoming heat flux is equal to the convection/diffusion heat flux from the liquid side of the interface plus the convection heat flux that enters the plasma as a result of evaporation at the interface:

$$\dot{q} + \dot{q}_{in} = \dot{q}_{out} \Rightarrow \dot{q} + \rho C_p uT\big|_{l,x=H} - k\frac{\partial T}{\partial x}\bigg|_{l,x=H} = \rho C_p uT\big|_{g,x=H} \Rightarrow$$

$$\Rightarrow \dot{q} - k\frac{\partial T}{\partial x}\bigg|_{x=H} = \rho C_p uT\big|_{g,x=H} - \rho C_p uT\big|_{l,x=H} \Rightarrow \dot{q} = k\frac{\partial T}{\partial x}\bigg|_{x=H} + L\rho u\big|_{l,x=H} \qquad (6.5)$$

Establishing an energy balance across the portion of the CPS that contains the liquid metal, ranging from the reservoir located at x=0 up to the plasma interface located at x=H, gives:

$$\left[\rho C_p uT - k\frac{\partial T}{\partial x}\right]\bigg|_{x=0} = \left[\rho C_p uT - k\frac{\partial T}{\partial x}\right]\bigg|_{x=H} \overset{\text{Eq. 6.5}}{=}$$

$$= \rho C_p uT\big|_{x=H} - \dot{q} + L\rho u \Rightarrow$$

$$\Rightarrow \dot{q} = L\rho u + \rho C_p u\left(T_H - T_0\right) + k\frac{\partial T}{\partial x}\bigg|_{x=0} \qquad (6.6)$$

It is obvious, via Eq. 6.6, that the main heat transfer mechanisms governing this process are evaporation, convection and conduction, which are represented by the first, second and third term, respectively. As a matter of fact, the conduction and convection terms are known from the analytical solution of the advection-diffusion equation and read as:

$$\dot{q} = L\rho u + \rho C_p u\left(T_H - T_0\right)\left(1 + \frac{1}{e^{\rho C_p uH/k}}\right) \qquad (6.7)$$

where T_0, T_H are the temperatures at x = 0 and x = H, C_p is the specific heat capacity and H the height of the liquid metal column within the mesh. Finally, indices l, g represent the liquid and gas phase of lithium, respectively.

As a first approximation, the seepage velocity, u, of the liquid metal through the CPS is obtained via Darcy's law where capillarity is considered to be the only driving force through the porous matrix:

$$u = \varphi_p \frac{\dfrac{2\gamma}{R_p} - \rho g h_0}{\mu H} k_p \qquad (6.8)$$

145

where φ_p, k_p, h_0, R_p denote the porosity, the permeability, the height and the average pore radius of the porous structure, μ, ρ, γ the dynamic viscosity, the fluid density and the surface tension of lithium and g the gravitational acceleration. We assume $\gamma \approx 0.4$ N/m, $k_p \approx 10^{-11}$ m^2, $\varphi_p \approx 0.3$, $R_p \approx 10\mu$m while k, L, ρ, C_p are estimated as the average of their values at T_r and T_{out} according to [40].

Solving the heat and momentum balances, Eqs. 6.7 and 6.8, respectively, provides the liquid metal thickness required to exhaust an increasing amount of heat flux as a function of the properties of the porous matrix. **Fig. 6.5** shows how the thickness of the film decreases in response to the increasing amount of the external heat flux. In this operation mode, evaporation is the main mechanism of heat exhaust. As can be illustrated in **Fig. 6.6** large heat fluxes can be accommodated at the cost of large evaporation rates. The properties of the porous matrix are essential in delivering the amount of liquid metal that is required for exhausting large amounts of heat flux. Beyond, a certain heat flux, the thickness decreases significantly and the integrity of the reservoir itself is an issue.
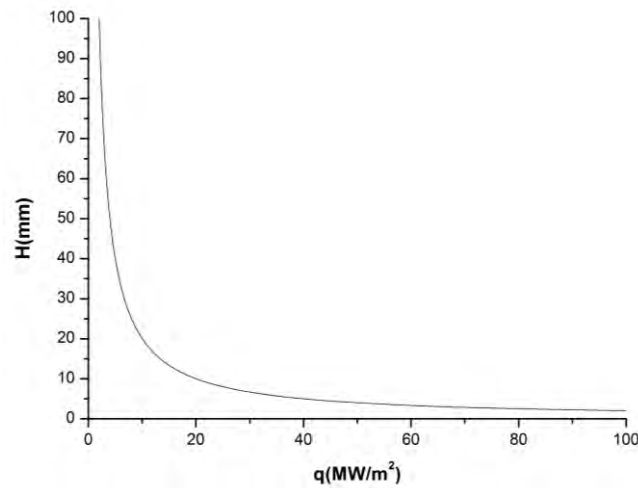
Fig. 6.5 Liquid metal thickness as a function of the external heat flux
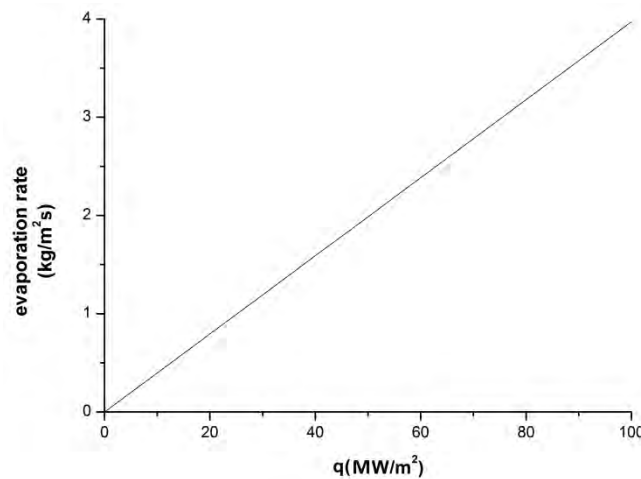
Fig. 6.6 Evaporation rate as a function of the external heat flux

As a result of the above heat balance, and for the anticipated external heat flux levels, very large lithium vapor concentration levels are anticipated in the SOL with possible

146

reactor lithization. Therefore, a threshold in evaporation rate should be established in order to avoid plasma contamination.

According to Van Eden et al., [50], who took into account the case of Sn as a PFC, an approximately steady-state surface temperature was reached after ~0.5s on the liquid surface. Besides, the temperature ramp in the Sn case did not follow a conduction-based cooling curve, where the temperature increases following Newton's law of cooling until the conducted heat equals the received plasma heating. As a result, they concluded that the steady-state temperature of liquid metal reduces significantly, due to vapor shielding and also that other power-loss processes are important.

Hence, as stated in [50], the plasma heat flux is dissipated via a number of processes. Firstly, power is dissipated by vaporization if evaporated neutrals do not return to the surface. Secondly, power is lost by radiation of Sn neutrals and ions in the vapor cloud and mass transport from the plasma as a result of recombination processes. The remaining heat is transferred to the Mo cup (and, subsequently, cooling water) via conduction and convection of the liquid Sn.

6.3 Replenishment of the CPS: Capillary flow of a liquid metal within a single cylindrical pore

As analyzed in detail in subsection 4.3, the flow within a cylindrical pore is examined as a first attempt to provide an upper bound of the convective effects within the CPS matrix. This simplified investigation overestimates the permeability of the CPS but provides the framework for studying the interplay between the different forces that act towards pushing liquid lithium out of the porous matrix or resist its motion. In the present study the hydrodynamic problem is examined in the context of axisymmetry in order to obtain an understanding of the operation principle of the capillary pump.

The numerical methodology, which was described in subsection 5.3, is employed in order to assess how the pore radius affects the seepage velocity of liquid lithium, whose properties derived via [40,109], for a cylindrical pore of $h_0 = 1mm$ in height. These seepage velocities along with the time needed for the liquid metal to exit the pore are going to give an estimation of the liquid metal replenishment speed which is of major importance during plasma operation.

When a capillary is brought into contact with a liquid surface existing within the reservoir, the liquid spontaneously wets the interior part of the capillary. The driving force for this phenomenon in a vertical capillary is given by $\Delta P = 2\gamma / R_p \cos\theta_d - \rho g h$, as mentioned in subsection 5.3, with h denoting the height of the liquid column in the capillary. In this study, the contact angle, θ_d, is considered to be invariable from the beginning and equal to its equilibrium value, $\theta_c = 30^o$, similar to studies such as [87]. The liquid reaches an equilibrium height, h_{eq}, where the capillary pressure equals the hydrostatic pressure. Thus, considering for example a pore radius $R_p = 30\mu m$, the equilibrium height is $h_{eq} = 6.28m \gg h_0$ and therefore the equilibrium arrangement is far from being accomplished. Hence, the seepage velocities are expected to be relatively high giving an overestimation of the replenishment speed, since the rambling geometry of the porous matrix is not taken into account.

If the case of a Newtonian liquid is to be considered and the flow is very slow then according to [52] the average velocity of liquid rising in the capillary can be expressed via Poiseuille's law as:

$$U = \frac{dx}{dt} = \frac{R_p^2 \Delta P}{8\mu x} = \frac{\gamma R_p \cos\theta_d}{4\mu x} - \frac{R_p^2 \rho g}{8\mu} \tag{6.9}$$

Thus, regarding the dynamic contact angle as a constant parameter and independent of velocity, the dynamic equation for capillary rise can be solved analytically with a dimensionless relation:

$$T = -H^2 \left[\frac{X}{H} + \ln\left(1 - \frac{X}{H}\right) \right] \tag{6.10}$$

where the following parameters and variables have been defined:

148

$$T = \frac{t}{t'}, \ t' = \frac{\mu R_p}{4\gamma \cos\theta_d},$$

$$X = \frac{4x}{R_p}, \ H = \frac{4h_{eq}}{R_p}, \ h_{eq} = \frac{2\gamma \cos\theta_d}{\rho g R_p}$$

(6.11)

Eq. 6.10 is often called the WRL equation, which is an acronym standing for Washburn, Rideal and Lucas who derived this equation, [87]. Besides, many authors refer to this simply as the Washburn equation. If gravity is negligible, a simpler relation is obtained according to [52]:

$$X = (2T)^{1/2}$$

(6.12)

Hence, the liquid column height increases continuously with time until the static equilibrium is established. Furthermore, Eqs. 6.10-6.12 have been tested against data on the rate of capillary rise into single capillaries. The data reveal a number of discrepancies relative to this simple model. One problem is that the dynamic contact angle is an unknown function of the rate of rise itself. Another is that the results depend upon whether the capillary has been prewetted with the liquid, or instead is dry prior to the intrusion of the liquid into the capillary, [110].

Our numerical results obtained in this context, indicate that upon decreasing the pore radius the capillary rise velocity, u_s, is seen to decrease linearly owing to the dominating effect of viscous dissipation along the radial direction, **Fig. 6.7**. This scaling qualitatively agrees with the viscous scale employed for making the velocity dimensionless. It corresponds to a balance between the axial pressure drop, generated due to capillary wetting of the interface, and radial momentum diffusion via viscosity:

$$\mu \frac{\partial^2 \hat{u}}{\partial r^2} \sim -\frac{\partial P}{\partial z} \Rightarrow \frac{\mu \hat{u}}{R_p^2} \sim \frac{\gamma / R_p}{h_0} \Rightarrow \hat{u} \sim \frac{\gamma R_p}{\mu h_0}$$

(6.13)

Since the inertial effects are insignificant for the relative small pore radius considered in this study, [52], the numerical results both considering and neglecting inertia are approximately the same with a small difference as the pore radius increases. These discrepancies occur because as R_p increases inertia enters the dominant force balance:

$$\rho \mathbf{u} \nabla \mathbf{u} \sim \nabla p \Rightarrow \frac{\rho \hat{u}^2}{R_p} \sim \frac{\gamma}{R_p^2} \Rightarrow \hat{u} = \sqrt{\frac{\gamma}{\rho R_p}}$$

(6.14)

When the balance between inertia and capillarity dominates, a reduction in the pore radius leads to an increase of the characteristic velocity. Hence, the simulations with inertial effects tend to reduce the seepage velocity as R_p increases in comparison with the simulations assuming purely Stokes flow (We = 0). As a consequence, the time needed for the liquid metal to exit the pore tents to be slightly bigger for the case where the inertial terms are taken into account, **Fig. 6.8**. The importance of transient effects at the pore level seems to play an important role at relatively large pore sizes. Relatively large pore sizes are not employed in the literature of CPS, however this transition from $\hat{u} \sim R_p$

149

to $\hat{u} \sim \dfrac{1}{\sqrt{R_p}}$ qualitative dependence can be used as a design parameter for future concepts.

Furthermore, as illustrated by **Fig. 6.8** the dimensionless time required to reach the pore exit, for fixed height of the capillary, decreases with $R_p^{1/2}$ in agreement with the dimensional form of Eq. 6.12.
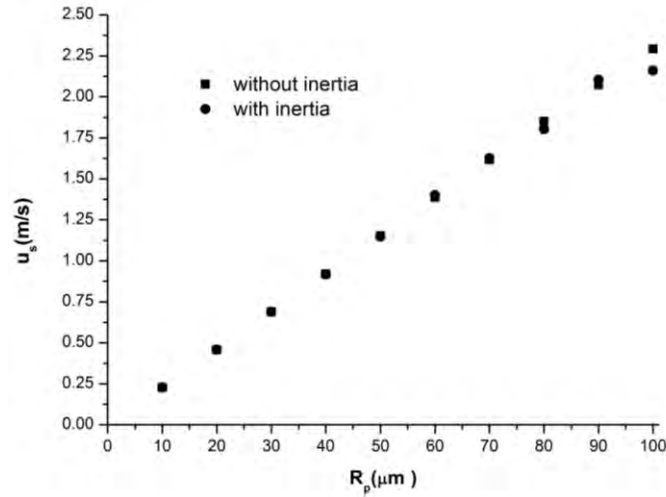
Fig. 6.7 Seepage velocity at the exit of the pore as a function of the pore radius both with and without the inertial terms included
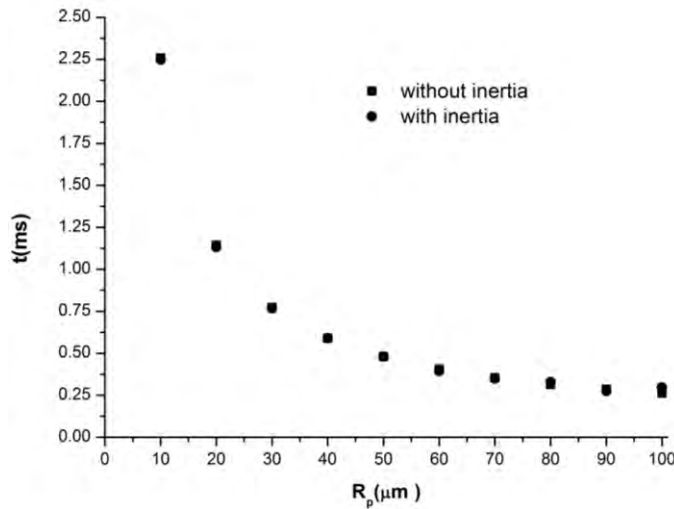
Fig. 6.8 Time needed for the liquid metal to exit the pore as a function of the pore radius both with and without the inertial terms included

Focusing on the case of a pore radius $R_p = 30\mu m$, as a reference study, the dimensional height of the rising liquid metal column at the axis of symmetry, namely z_0 in this investigation, increases like $t^{1/2}$, as illustrated in **Fig. 6.9a**, in agreement with the simplified WRL equation Eq. 6.12, as expected, based on the impact of viscous effects and the small height of the column. As a result, the rise velocity is relatively large at the beginning of the process while being reduced as the height of the column increases, **Fig. 6.9b**. However, as illustrated in **Fig. 6.10**, the numerical values tend to be smaller than the prediction of Eq. 6.12, due to the impact of inertia effects that are accounted for in the numerical simulation. However, the observed deviation was never significant indicating the reliability of the WRL model in estimating the time required to achieve wicking into a capillary in the absence of inertial effects.

150
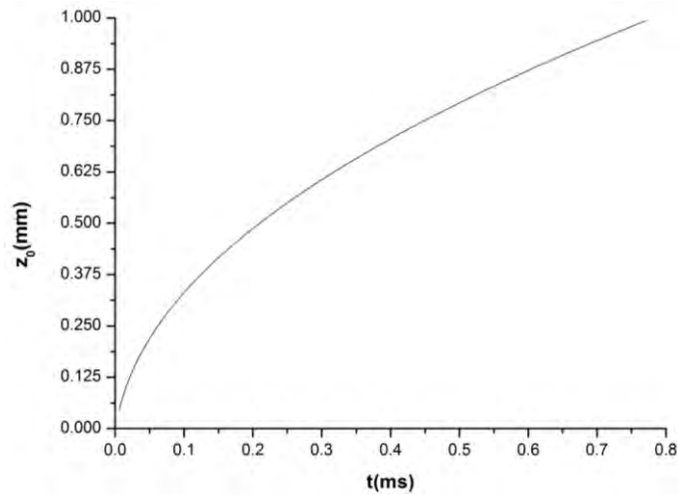
(a)
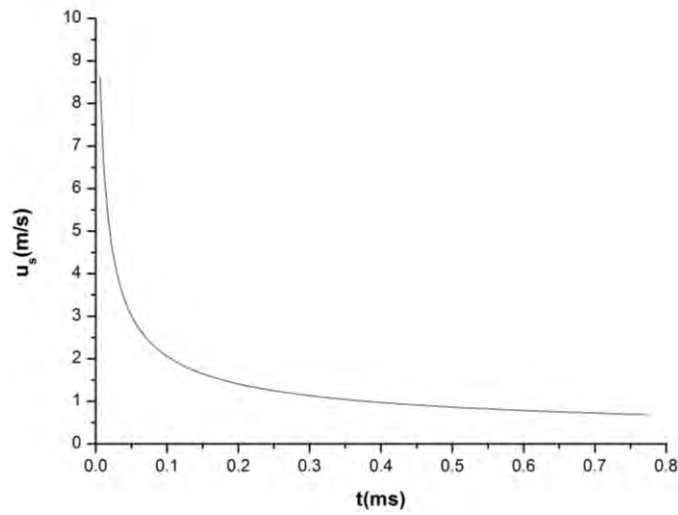
(b)

Fig. 6.9 (a) Height of the liquid metal column and (b) Seepage velocity at the exit of the pore as a function of time for the case of $R_p = 30$ μm
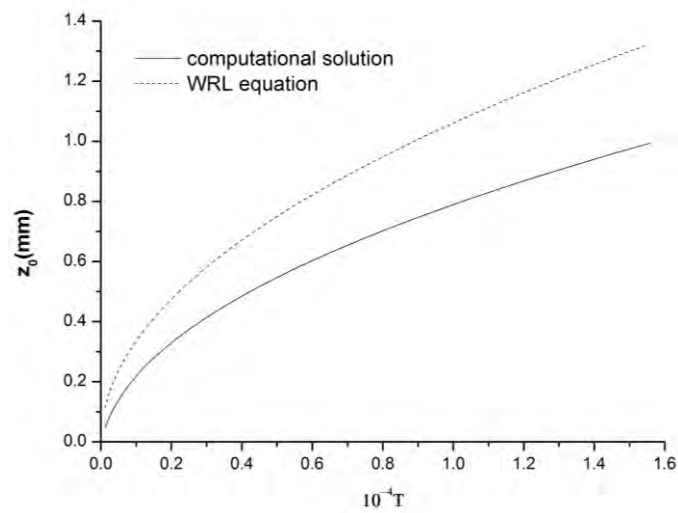
Fig. 6.10 Comparison of the numerical results with the approximate WRL equation (Eq. 6.12) for the case of $R_p = 30$ μm

151

A similar deviation between simulations and experimental observations was captured in the experimental investigation presented in [90]. In the latter study silicone oils of varying viscosities were used and the measurements also consistently lied below the prediction of WRL equation. This tendency was attributed to the fact that the contact angle that arises dynamically will not be constant all the time, in the manner assumed in the simulations and the WRL theory. Rather it is going to change with time depending on the velocity of the liquid column. Joos et al [90] provided an experimentally fitted relationship for the dynamic contact angle in the form of $\cos\theta_{d} = \cos\theta_{c} - 2(1 + \cos\theta_{c})Ca^{1/2}$, where Ca=μu/γ represents the capillary number presented above with the characteristic velocity u being the average velocity of the liquid meniscus rising in the capillary. Based on the above relationship, the dynamic contact angle, θ_{d}, is much larger than the equilibrium contact angle, θ_{c}, at the beginning of the process while being decreased until the static arrangement is reached and the equilibrium contact angle is established. The modified theory fits the experimental rise data better at short times than does the WRL theory due to the smaller rise velocity it predicts as a result of the smaller capillary pressure. Furthermore, experimental relationships for the estimation of the dynamic contact angle have also been introduced by other studies indicating the importance of short range forces in establishing the variation described by empirical formulas, see also the relevant analysis presented in [52].

Finally, entrance and exit effects may be significant in our investigation since the capillary height is very small compare to the equilibrium height. As a matter of fact, most of the viscous friction would lie within the region where the parabolic velocity profile is being developed from the entrance condition and in the pore`s mouth where the liquid exits to cover the top surface. Moreover, Rillaerts and Joos, [110], demonstrated the importance of prewetting of the capillary on the dynamic contact angle. During real CPS operation the porous matrix is going to be pre-wetted since the liquid metal layer is already present and evaporates due to the external heat flux. In the following section 6.4.2, an effort will be made to account for the effect of wetting and adhesion in the final static arrangement of the liquid metal layer covering the pore.

152

6.4 Static arrangement of the CPS

6.4.1 Effect of reservoir overpressure

The numerical methodology, which was analyzed in subsection 5.4.1, was implemented in order to perform a parametric study on the effect of external overpressure on the shape and thickness of the liquid metal layer that coats the porous substrate at static equilibrium. Liquid lithium was used as the operating fluid. The fluid density, ρ, is set equal to $500 kg/m^3$ while its surface tension $\gamma = 0.4 N/m$. The contact angle θ_c is set to 30° and the gravity acceleration $g=10 \ m/s^2$. The geometric configuration envisioned is the one depicted in **Figs. 4.10a,b.** A porous disk of 10 cm radius and 1 mm thickness is assumed. The reservoir overpressures considered in this study are expected to be relatively small and positive, however for the sake of completeness a parametric study is conducted in this section of the static arrangement, by varying the reservoir overpressure, $\Delta P = P_r - P_{out}$, over a wide range of values starting from large positive overpressures until small negative pressure differences. P_{out} signifies the pressure exerted on the liquid metal film by the surrounding plasma in the divertor region and is not expected to be large since almost vacuum conditions prevail in this region. The reservoir pressure is reduced by the hydrostatic pressure $\rho g h_0 \approx 5$ Pa based on the thickness of the porous layer, h_0, plus the additional pressure drop, $\rho g z$, due to the local thickness, z, of the liquid metal layer that rests on top of the porous wafer. For relatively large overpressures the contact angle of the liquid metal drop on the porous matrix is fixed and the contact length emerges as part of the numerical solution. Converged solutions of the drop shape were obtained with a finite element mesh ranging between 500 and 4000 quadratic elements in order to capture abrupt changes in the curvature of the interface.

In this fashion, it was seen that as the reservoir overpressure ($\Delta P = P_r - P_{out}$) increases, $\Delta P > 500$ Pa, the "drop" size decreases. In this regime, gravity is of minor importance and the dominant force balance in achieving static equilibrium is between pressure drop and surface tension, $P_0 - P_{out} \approx 2\gamma / R_m$. R_m is the radius of the circular arc which constitutes the interface between the liquid metal and plasma, **Fig. 6.11,** and decreases with increasing reservoir overpressure. The liquid metal "drop" arrangement that rests on the outer CPS surface is calculated numerically as a function of the reservoir overpressure. Due to axisymmetry and the geometry of the static arrangement, the shape obtained is that of a spherical cap with a contact angle of 30° on the solid substrate that constitutes the porous matrix, and a contact length of $R_f = R_m \sin\theta_c$. The center of curvature of this "drop" that protrudes from the porous matrix lies below the CPS surface, and the position of its center is equal to $R_m \cos\theta_c$ while the contact length is $R_f = R_m \sin\theta_c$. Finally, the thickness of the liquid metal film at the axis of symmetry is $z_0 = R_m - R_m \cos\theta_c = R_m(1-\cos\theta_c)$.
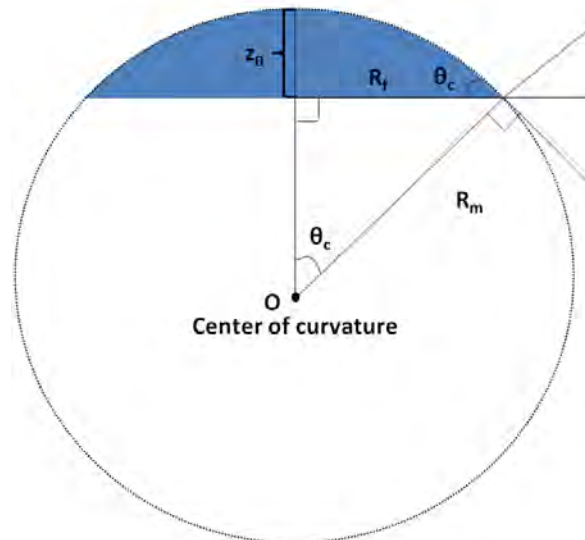
Fig. 6.11 Schematic of the center and radius of curvature, O and R_m, respectively, the radial extent of liquid metal "drop" (depicted by the blue region), R_f and contact angle, θ_c

As illustrated in **Fig. 6.12,** as the overpressure decreases, the "drop" spreads out while more or less retaining its spherical cap shape. **Fig. 6.13** provides a comparison between the numerically obtained contact length and the above prediction based on the assumption of a spherical cap shape, that confirms the validity of the relation $R_{f,apr} \approx R_m \sin\theta_c$ for large overpressures, where $R_{f,apr}$ is the approximate value of contact length. For example, when the case of $\Delta P = 500$ Pa is taken into account $R_{f,apr} = 2\gamma/\Delta P \sin\theta_c = 0.8$mm $\approx R_{f,c}$, with $R_{f,c}$ representing the computational obtained contact length.
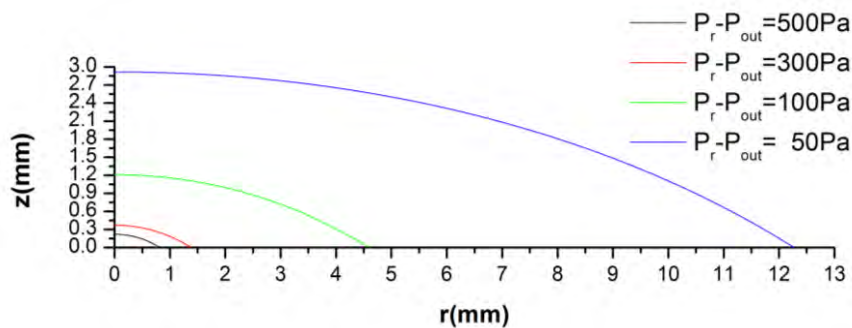
Fig. 6.12 Liquid metal drop shape evolution with decreasing pressure drop
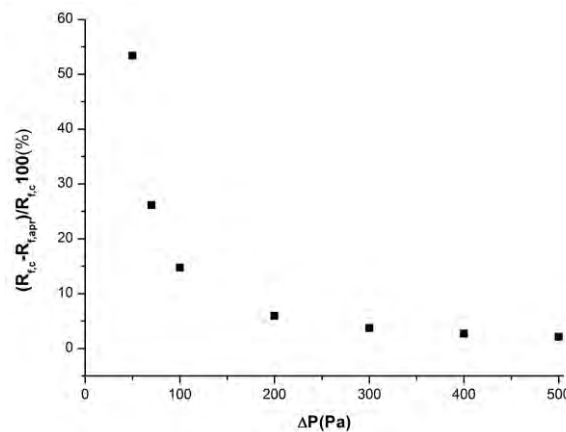
Fig. 6.13 The approximate values estimated via $R_{f,apr} \approx R_m \sin\theta_c$ agree with the computational ones as the pressure drop increases

154

As pressure drop is further decreased, a liquid metal film forms that almost entirely covers a 10 cm long disk when $\Delta P \approx 30$Pa, in which case the spherical cap shape assumption does not hold any more and significant deviations are registered in **Fig. 6.13**. **Fig. 6.14** illustrates the gradual formation of a thin film as the reservoir overpressure decreases. In this regime, the structure of the solution is different since gravity becomes important in the region around the axis of symmetry, while a very thin boundary layer is generated near the contact point. As a result, a very large number of elements is required, on the order of 4000, in order to capture this transition.
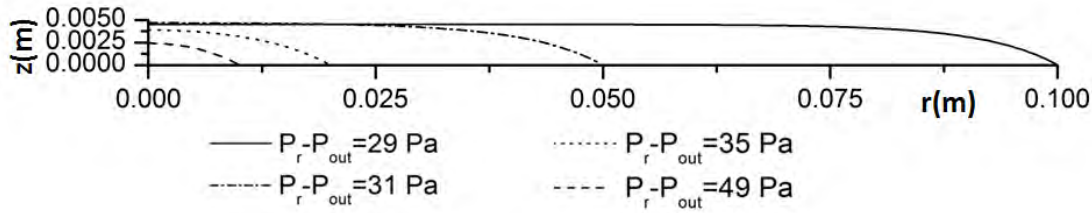
Fig. 6.14 Liquid metal film shape as the overpressure decreases

In fact, upon further decreasing the reservoir overpressure, the contact length increases extremely and exceeds any reasonable wafer length, **Fig. 6.15**. As mentioned above, the importance of gravity increases and forms the dominant force balance along with pressure drop, especially away from the contact point which determines the liquid metal layer thickness in the pole region. For example, when $P_r - P_0 = 28.2$ Pa in the region near the pole the balance between gravity and pressure forces provides the maximum film thickness z_0, see also **Fig. 6.16a**:

$$P_r - P_{out} \approx \rho g \left(h_0 + z_0 \right) \Rightarrow z_0 \approx 4.6mm \tag{6.16}$$

On the contrary, near the contact point it is the surface tension that balances pressure drop. The shape is almost part of a sphere, see also **Fig. 6.16b**. As a consequence, for a given contact angle the critical pressure drop beyond which a solution cannot be obtained can be predicted:

$$P_r - \rho g h_0 - P_{out} = \sigma 2k_m \approx \gamma \left(\frac{\sin \theta_c}{r_c} + \frac{\theta_c - 0}{\Delta s} \right),$$

$$\theta_c = \pi / 6, \ \Delta s \approx \frac{\pi z_0}{12 \left(1 - \cos \theta_c \right)} = 1,95 z_0$$

$$P_0 = P_r - \rho g h_0, \ \Delta P_0 = P_0 - P_{out},$$

$$r_c \approx \frac{1}{\dfrac{2\Delta P_0}{\sigma} - \dfrac{\pi}{3} \dfrac{\rho g}{1,95 \Delta P_0}}, \quad \frac{dr_c}{d\Delta P_0} < 0 \tag{6.17}$$

In the above analysis, the mean curvature at the contact point is decomposed in the azimuthal and polar components with two distinct radii of curvature equal to R_f and $z_0/(1-\cos\theta_c)$, respectively. As ΔP_0 decreases the contact length $r_c = R_f$ increases abruptly until it becomes infinite for a critical pressure drop, $\Delta P_0 \approx 17 \approx P_r - \rho g h_0$, in which case a static

155

solution cannot be obtained when $P_r \approx 22$ Pa since capillarity cannot balance pressure drop anymore due to the large film size.
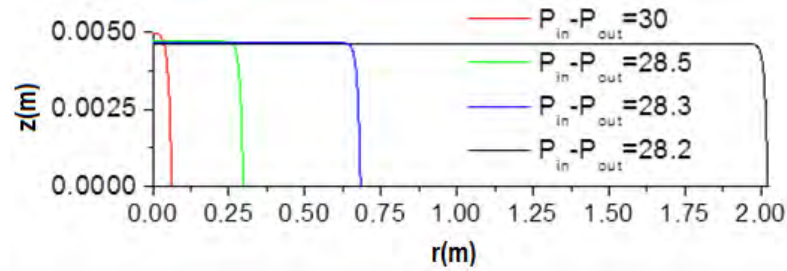
Fig. 6.15 Liquid metal film shape as the overpressure decreases approaching a threshold value
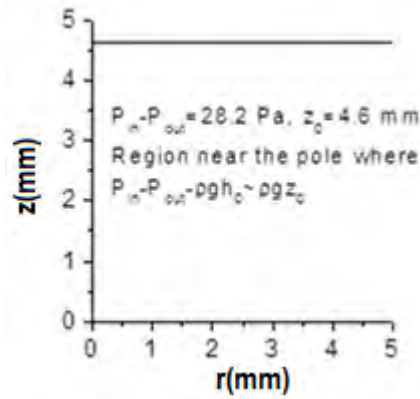
(a)
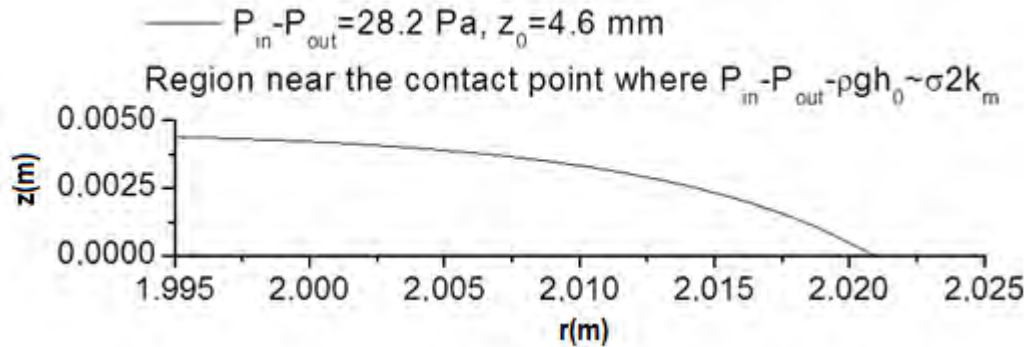
(b)

Fig 6.16 Film shape for a small pressure drop, P_r-P_{out}=28.2 Pa, (a) near the pole and (b) near the contact point

Static simulations conform with this pattern and fail to provide a solution for a reservoir pressure $P_r \approx 28$ Pa, **Fig. 6.16**. The film size in this process exceeds any reasonable wafer length, e.g. ~10 cm, and consequently it ends in a sharp edge, the wafer's edge, in which case we have to impose a fixed contact point rather than a fixed contact angle in order to proceed with the parametric study. In this fashion, a static solution can be obtained for even lower overpressures until ΔP almost vanishes with the film achieving micron-size thickness and near zero contact angles as can be shown in **Fig. 6.17**.
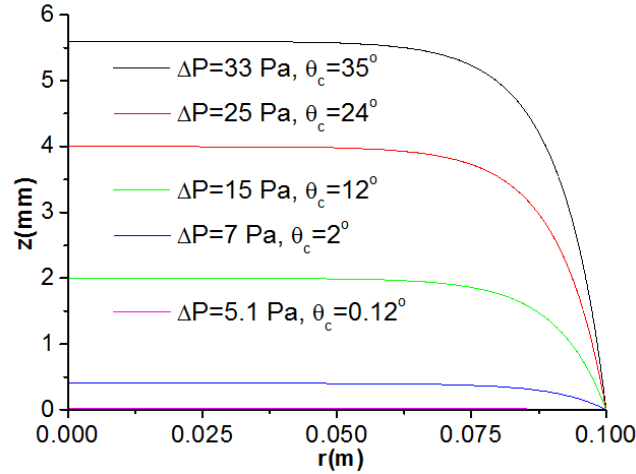
Fig. 6.17 Evolution of film with decreasing overpressure, ΔP=P_r-P_out, and fixed contact point at R=10 cm; when ΔP=5 Pa the pressure drop between the top of the CPS and the plasma is almost zero

In this process gravity gradually gets out of the picture and micron or even sub-micron film thicknesses are obtained. The contact length is fixed at the wafer's length and the contact angle gradually decreases to accommodate the continuous reduction of the film thickness. Furthermore, film formation subject to negative overpressures as well as the effect of the substrate topography, e.g. pore radius, cannot be captured. However such effects have been registered in experimental observations [81,86,111], especially as the pressure drop between the liquid lithium reservoir and the surrounding plasma is expected to be negligible in the actual application of the CPS. Therefore, as the film thickness reduces down to submicron sizes, i.e. for very small positive or negative overpressures, the nature of intermolecular or surface adhesion forces between the liquid metal film and the solid substrate needs to be considered. The numerical results concerning the effect of negative overpressures and also the substrate topography on the static arrangement are presented in the following subsection 6.4.2.

6.4.2 Effect of the topography of the porous substrate
At the end of subsection 6.4.1 it was stressed that at near vacuum conditions, namely considering slightly positive or negative reservoir overpressures, the film thickness reduces down to micron or even submicron sizes. In this regime, the surface forces developed between the liquid metal film and the solid substrate should be considered.

In the following we do not assume the classic partial wetting case**,** of liquid lithium with a dry substrate beyond the contact point, illustrated in **Fig. 2.3**. As emphasized in subsection 6.4.1, it is not possible to obtain such a solution at static equilibrium for $P_r \approx P_{out}$, a CPS thickness of 1mm, a pore size on the order of 30 μm and a contact angle $\theta_c = 30^o$. Such a static configuration would require a liquid metal column of, roughly:

$$h = 2\gamma \cos\theta_c / (\rho g R_p) \approx 4.6m \tag{6.18}$$

A size of liquid metal column of this order would not be useful in protecting the CPS structure and the divertor below since it would be unstable and susceptible to MHD instabilities. The envisioned static configuration is characterized by full coverage of the CPS outer surface whether the pressure difference, $\Delta P = P_0 - P_{out}$, is slightly positive or negative. The latter case pertains to the situation after replenishment has taken place but

157

without taking into account the Lorentz forces. In this fashion, we are dealing with coatings rather than films and micro-scale liquid-solid interactions need to be accounted for. In particular, the cases with a purely repulsive and a long range attractive short range repulsive potential are investigated in order to model the effect of the topography and nature of the porous substrate on the static arrangement of the liquid metal. As pointed out above these surface, or intermolecular, forces enter the normal force balance in the form of a disjoining pressure, Π, which arises by differentiating the aforementioned potentials with respect to the local Euclidean distance between the liquid metal-gas interface and the solid substrate.

Asymptotic analysis of the film shape barely existing the pore
The analysis here, as $R_p \gg \delta_A$, assumes the splitting of the film interface in the inner ($r > R_p$), outer ($r < R_p$) and the transition (among inner and outer regimes) regions as can be depicted in **Fig. 6.18**. In this subsection we are looking for solutions whose thickness is on the order of δ_A in the inner region and $2\gamma/\Delta P$ in the outer region. Gravity is insignificant while the pressure differences are considered to be on the order of $\Delta P = P_0 - P_{out} \sim 1$ in which case an almost flat precursor layer is developed.
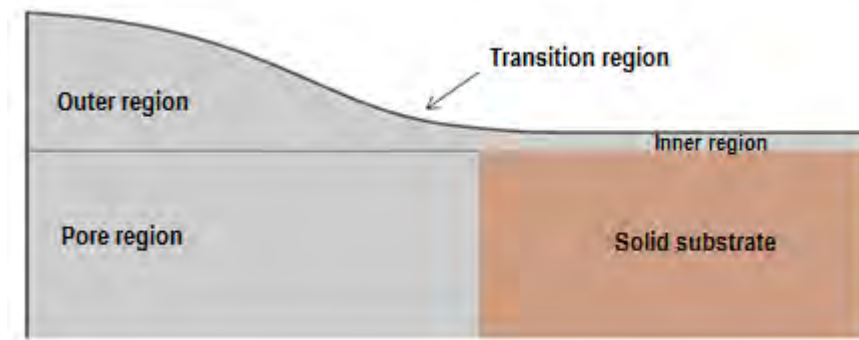
Fig. 6.18 Schematic of the anticipated static configuration with the film barely existing the pore and illustration of the main subregions

In general, the normal stress balance holds on the interface:

$$P_0 - P_{out} + \Pi + (\gamma + W_0)2H_c = 0 \tag{6.19}$$

Taking into account the case of a long range attractive short range repulsive potential, analyzed in the subsection 2.2.3, and also the relationships concerning curvature and normal unit vector derived in Appendix B, Eq. 6.19 results in:

$$P_0 - P_{out} + \frac{4W_0}{\delta_A}\left[\left(\frac{\delta_A}{\delta}\right)^5 - \left(\frac{\delta_A}{\delta}\right)^3\right]\left[\frac{\partial\delta}{\partial z}r_\xi - \frac{\partial\delta}{\partial r}z_\xi\right]\frac{1}{S_\xi}$$
$$+ (\gamma + W_0)\left(\frac{r_\xi z_{\xi,\xi} - r_{\xi,\xi}z_\xi}{S_\xi^3} + \frac{z_\xi}{rS_\xi}\right) = 0, \ S_\xi = \sqrt{r_\xi^2 + z_\xi^2} \tag{6.20}$$

Inner region
In this region the dominant force balance is between pressure forces and intermolecular forces. Besides, regarding the thickness of the inner region, z_I, to be on the order of δ_A, and also $r \sim R_p$, $\delta_A \ll R_p$, $S_\xi \sim R_p$. By defining a new dimensionless parameter $\hat{z}_I = \delta/\delta_A$ the normal stress balance reads at the interface:

158

$$P_0 - P_{out} = \frac{4W_0}{\delta_A}\left[\hat{z}_I^{-3} - \hat{z}_I^{-5}\right] \Rightarrow \frac{\Delta P \delta_A}{4W_0} = \left[\hat{z}_I^{-3} - \hat{z}_I^{-5}\right] \Rightarrow$$

$$\Rightarrow \frac{\Delta P \delta_A}{4W_0} = \left[\frac{\hat{z}_I^2 - 1}{\hat{z}_I^{-5}}\right] \tag{6.21}$$

Assuming $\frac{\Delta P \delta_A}{4W_0} \ll 1$, we set $\hat{z}_I = 1 + \varepsilon$. Thus, Eq. 6.21 results in:

$$\frac{\Delta p}{4W_0/\delta_A} = \frac{(1+\varepsilon)^2 - 1}{(1+\varepsilon)^5} \Rightarrow \frac{\Delta p}{4W_0/\delta_A} = \frac{\cancel{1} + 2\varepsilon - \cancel{1}}{1 + 5\varepsilon}$$

$$\frac{\Delta p}{4W_0/\delta_A} = 2\varepsilon(1 - 5\varepsilon) \Rightarrow \frac{\Delta p}{4W_0/\delta_A} = 2\varepsilon - \overset{\text{very small}}{10\varepsilon^2} \Rightarrow$$

$$\Rightarrow \varepsilon = \frac{\Delta p}{8W_0/\delta_A} \tag{6.22}$$

Thus,

$$\hat{z}_I = 1 + \frac{\Delta p}{8W_0/\delta_A} \tag{6.23}$$

The intermolecular potential W in the inner region results in:

$$W = W_0\left[\left(\frac{\delta_A}{\delta}\right)^4 - 2\left(\frac{\delta_A}{\delta}\right)^2\right]^{\delta/\delta_A \equiv \hat{z}_I} = W_0\left[\hat{z}_I^{-4} - 2\hat{z}_I^{-2}\right] =$$

$$= W_0\left[\left(1 + \frac{\Delta p}{8W_0/\delta_A}\right)^{-4} - 2\left(1 + \frac{\Delta p}{8W_0/\delta_A}\right)^{-2}\right] =$$

$$= W_0\left[1 - 4\frac{\Delta p}{8W_0/\delta_A} - 2\left(1 - 2\frac{\Delta p}{8W_0/\delta_A}\right)\right] = -W_0 \tag{6.24}$$

The above eq. Eq. 6.24 is valid provided that $\frac{\Delta p}{8W_0/\delta_A} = \varepsilon \ll 1$.

Transition region
In this region the dominant force balance is between the surface tension forces and the intermolecular forces. Moreover,

$$z \sim \delta_A,\ r_{tr} = r - R_f,\ r_{tr} \sim \ell \ll R_f,\ \bar{r} = \frac{r}{R_f},\ \hat{r} = \frac{r_{tr}}{\ell},\ \hat{z} = \frac{\delta}{\delta_A},\ \bar{W} = \frac{W}{W_0} = \hat{z}_I^{-4} - 2\hat{z}_I^{-2} \tag{6.25}$$

where ℓ is the length of the transition region and $R_f = R_m \sin\theta_c = (2\gamma/\Delta P)\sin\theta_c$.

159

Consequently, assuming that the transition takes place entirely on top of the substrate rather than the pore:

$$2H_c = \frac{z_\xi}{rS_\xi} + \frac{r_\xi z_{\xi,\xi} - r_{\xi,\xi} z_\xi}{S_\xi^3} = \frac{\delta_A \hat{z}_\xi}{R_f \bar{r} \left(\ell^2 \hat{r}_\xi^2 + \delta_A^2 \hat{z}_\xi^2 \right)^{1/2}} + \frac{\ell \delta_A \hat{r}_\xi \hat{z}_{\xi,\xi} - \ell \delta_A \hat{r}_{\xi,\xi} \hat{z}_\xi}{\left(\ell^2 \hat{r}_\xi^2 + \delta_A^2 \hat{z}_\xi^2 \right)^{3/2}} \tag{6.26}$$

and the normal stress balance reads at the interface:

$$P_0 - P_{out} + \frac{4W_0}{\delta_A} \left[\hat{z}^{-5} - \hat{z}^{-3} \right] \frac{\ell \hat{r}_\xi}{\left(\ell^2 \hat{r}_\xi^2 + \delta_A^2 \hat{z}_\xi^2 \right)^{1/2}} =$$

$$= (\gamma + W) \left(\overbrace{\frac{-\delta_A \hat{z}_\xi}{R_f \bar{r} \left(\ell^2 \hat{r}_\xi^2 + \delta_A^2 \hat{z}_\xi^2 \right)^{1/2}}}^{\delta_A / R_f \ll 1} - \frac{\ell \delta_A \hat{r}_\xi \hat{z}_{\xi,\xi} - \ell \delta_A \hat{r}_{\xi,\xi} \hat{z}_\xi}{\left(\ell^2 \hat{r}_\xi^2 + \delta_A^2 \hat{z}_\xi^2 \right)^{3/2}} \right) \Rightarrow$$

$$\overset{\text{if } \ell = \delta_A}{\Rightarrow} \quad \underbrace{\frac{P_0 - P_{out}}{\gamma / \delta_A}}_{\text{not necessarily small}} + \frac{W_0}{\gamma} 4 \left[\hat{z}^{-5} - \hat{z}^{-3} \right] \frac{\hat{r}_\xi}{\left(\hat{r}_\xi^2 + \hat{z}_\xi^2 \right)^{1/2}} \simeq \left(1 + \frac{W_0}{\gamma} \bar{W} \right) \left(-\frac{\hat{r}_\xi \hat{z}_{\xi,\xi} - \hat{r}_{\xi,\xi} \hat{z}_\xi}{\left(\hat{r}_\xi^2 + \hat{z}_\xi^2 \right)^{3/2}} \right) \tag{6.27}$$

Upon recognizing that:

$$\frac{r_\xi}{\sqrt{\hat{r}_\xi^2 + \hat{z}_\xi^2}} = \cos\theta, \quad -\frac{\hat{r}_\xi \hat{z}_{\xi,\xi} - \hat{r}_{\xi,\xi} \hat{z}_\xi}{\left(\hat{r}_\xi^2 + \hat{z}_\xi^2 \right)^{3/2}} = \frac{d\cos\theta}{d\xi} \frac{1}{\hat{z}_\xi}, \quad \frac{d\bar{W}}{d\hat{z}} = -4 \left(\hat{z}^{-5} - \hat{z}^{-3} \right), \tag{6.28}$$

Eq. 6.27 is recast in the form:

$$\frac{P_0 - P_{out}}{\gamma / \delta_A} - \frac{d\left(1 + \frac{W_0}{\gamma} \bar{W} \right)}{d\hat{z}} \cos\theta - \left[1 + \frac{W_0}{\gamma} \bar{W} \right] \frac{d\cos\theta}{d\xi} \frac{1}{\hat{z}_\xi} = 0 \Rightarrow$$

$$\Rightarrow \hat{z}_\xi \frac{P_0 - P_{out}}{\gamma / \delta_A} - \frac{d}{d\xi} \left[\left(1 + \frac{W_0}{\gamma} \bar{W} \right) \cos\theta \right] = 0 \Rightarrow$$

$$\Rightarrow \frac{P_0 - P_{out}}{\gamma / \delta_A} \hat{z} \Big|_{\hat{z}_{-\infty}}^{\hat{z}_I} = \left(1 + \frac{W_0}{\gamma} \bar{W} \right) \cos\theta \Big|_{\hat{z}_{-\infty}}^{\hat{z}_I} \xrightarrow[\theta_{-\infty} \equiv \theta_c, \theta_{\hat{z}_I} = 0]{\frac{P_0 - P_{out}}{\gamma / \delta_A} \hat{z} \ll 1} \cos\theta_c \approx 1 + \frac{W_0}{\gamma} \bar{W} (\hat{z}_I) \Rightarrow$$

$$\Rightarrow \frac{W_0}{\gamma} \left(2\hat{z}_I^{-2} - \hat{z}_I^{-4} \right) = 1 - \cos\theta_c \tag{6.29}$$

Setting again $\hat{z}_I = 1 + \varepsilon$ Eq. 6.29 results in:

160

$$\frac{W_0}{\gamma}\left(2\left(1-2\varepsilon\right)-1+4\varepsilon\right)=1-\cos\theta_c$$

$$\frac{W_0}{\gamma}=1-\cos\theta_c \tag{6.30}$$

Eq. 6.30 is similar to the equation produced by Starov et al. [112,113] for a partially wetting fluid resting on a substrate where a precursor layer is formed, and predicts the equilibrium contact angle established at the edge of the coating when the limit point occurs in the above calculations.

Outer region

In this region pressure forces balance surface tension forces. Hence, the normal stress balance reads at interface:

$$P_0 - P_{out} = \gamma \nabla_s \cdot \mathbf{n} \tag{6.31}$$

with an almost spherical shape to be formed with radius $R_m \sim \dfrac{2\gamma}{P_0 - P_{out}}$ that meets the transition layer at an angle according to Eq. 6.30. In this fashion, thicker coatings are obtained with thickness $R_m\left(1-\cos\theta_c\right)$, and radial length $R_m \sin\theta_c$. As W_0 approaches γ, the contact angle, θ_c, approaches $\pi/2$. Beyond this value a contact angle $0 < \theta_c < \pi/2$ cannot be obtained. This is a result of the form of the interaction potential employed in the present study. Thus, a more realistic form should be introduced. Furthermore, it is important to verify that the above presented static configurations will persist in the presence of dynamic effects and other field forces such as Lorentz forces. To this end, careful stability analysis is required.

It should also be stressed that the above relation Eq. 6.30 is different from the relation $\dfrac{W_0}{\gamma}=1+\cos\theta_c$ derived for a closed volume of liquid resting on top of an otherwise dry substrate.

The reason for this discrepancy is that for the case of poor wetting, Eq. 6.30 is recovered with the supplementary angle of contact angle in place of the contact angle. Consequently, upon substitution of the above consideration in Eq. 6.30 we recover the well known formula $\dfrac{W_0}{\gamma}=1+\cos\theta_c$. On the contrary, when partial wetting is considered a gas layer underneath the contact region cannot be envisioned, since it would be incompatible with the concept of good wetting. Furthermore, carrying out analysis generates problems with asymptotic matching when $\theta < \pi/2$, [114].

Numerical Results
Case of Pure Repulsion
As a first attempt to capture the effect of surface forces and the topography of the porous substrate on the static arrangement, a repulsive interaction potential in the form of $W(\delta) = \dfrac{A}{12\pi\delta^2}$ was investigated, illustrated in **Fig. 4.20**, corresponding to a liquid metal film that establishes full contact with the solid substrate, see also **Fig. 2.2**. This, corresponds to the case when all forces cannot be compensated in the tangential direction at any contact angle, that is, if $\gamma_{sv} > \gamma_{sl} + \gamma$, where $\gamma_{sv}, \gamma_{sl}, \gamma$ denote the interfacial tensions between the solid, liquid and gas phases. Assuming the case of liquid lithium again and focusing in the vicinity of a single pore since we have considered that the interpore distance is much larger than the pore radius, useful conclusions can be drawn by the numerical model described in subsection 5.4.5. Assuming that $P_r \approx P_{out}$, which corresponds to $P_0 \approx 5$ Pa and therefore $\Delta P = P_0 - P_{out} = -5$ Pa, the general picture for a CPS thickness of 1mm and a pore size on the order of 30 µm is that of an almost uniform coating of size on the order of submicron's over the substrate, with an indentation in the pore region as can be gleaned from **Fig. 6.19**. In addition, as the strength of the repulsion increases, that is to say that as A increases, the liquid metal film thickness increases as well. Similarly, as the external overpressure increases the coating thickness decreases as well, **Fig. 6.20**. For relatively large values of external overpressures the liquid metal-gas interface enters the pore region and the indentation seems to be bigger.
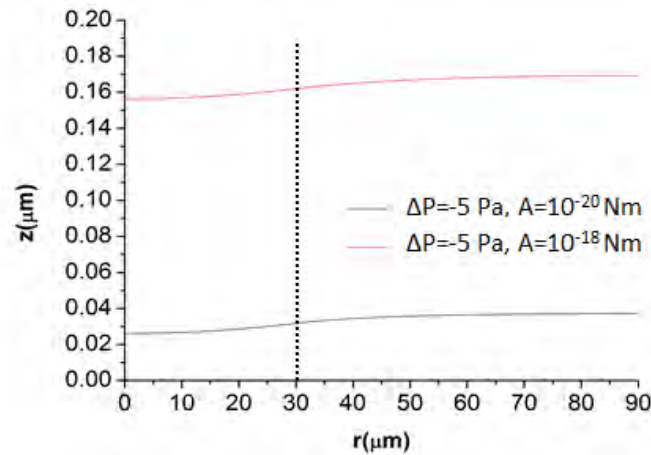
Fig. 6.19 Evolution of the shape of the interface for Hammaker constants A = 10^{-20} and 10^{-18} Nm for fixed external overpressure $\Delta P = P_0 - P_{out} = -5$ Pa and a pore size of 30 µm

162
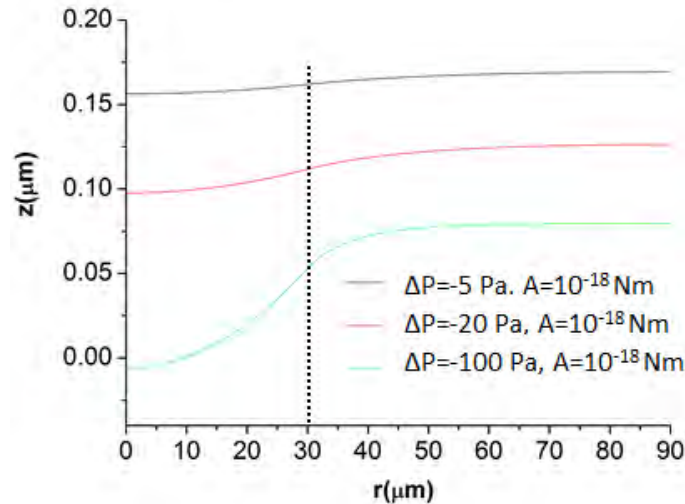
Fig. 6.20 Evolution of the shape of the interface for Hammaker constants A = 10^{-18} Nm for various external overpressure $\Delta P = P_0 - P_{out}$ and a pore size of 30 μm

As far as the investigation of purely repulsive potential is concerned, no static solution is possible for positive reservoir overpressures, $P_0 > P_{out}$ because this kind of interaction potential cannot counterbalance a positive pressure drop across the interface. However, it is anticipated that the presence of Lorentz forces may lead to positive and very large effective reservoir overpressures, in the form of magnetic pressure, especially during off-normal events such as edge-localized modes and disruptions. In such a situation a purely repulsive potential cannot exert a stabilizing attractive force that would pin the film onto the substrate and is considered inappropriate for the real case of CPS static configuration. This type of material and the resulting interaction can only sustain a dynamic coating process with the liquid metal gradually spreading over the substrate. Nevertheless, it gave us beneficial results in order to understand the process of coating over dry or prewetted surfaces.

Case of a long range attractive short range repulsive potential
As was shown in the context of the analysis on the evolution of the film thickness as a function of the external overpressure, when near vacuum conditions prevail the film thickness decreases significantly and the details of the substrate topography and interaction with the liquid film emerge as determining factors for predicting the static configuration. The envisioned static arrangement of the CPS, in the absence of electromagnetic field forces, is shown in **Fig. 6.21** where an undulated interface forms following the topography of the porous structure.

| (a) | (b) | (c) |
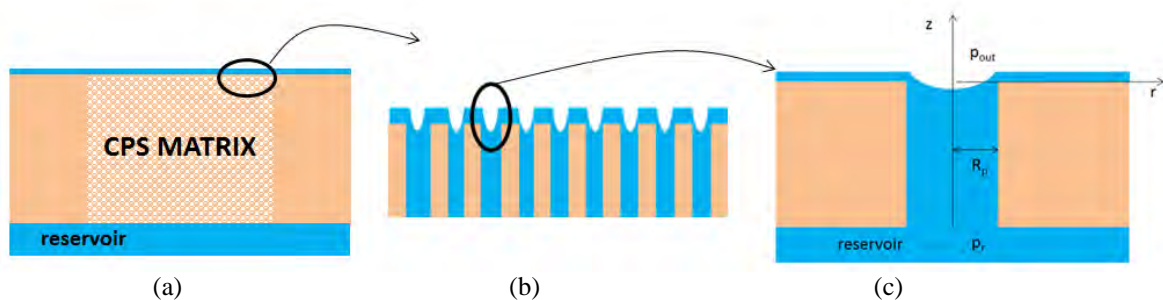
Fig. 6.21 (a) Anticipated schematic arrangement of the CPS static configuration with an almost uniform coverage of the CPS outer surface, Blow up: (b) of the CPS outer surface and (c) in the vicinity of a single pore

163

Assuming that the interpore distance is much larger than the pore radius, the analysis can focus on the static arrangement in the pore level, **Figs. 6.21b,c**. The effect of a long range attractive short range repulsive potential in the form of $W = W_0 \left[\left(\frac{\delta_A}{\delta} \right)^4 - 2 \left(\frac{\delta_A}{\delta} \right)^2 \right]$ that is depicted in **Fig. 4.21** was also investigated, corresponding to a liquid metal film that establishes partial wetting with the solid substrate, **Fig. 2.3**. This, corresponds to the case when $\gamma_{sv} < \gamma_{sl} + \gamma$, where γ_{sv}, γ_{sl}, γ denoting the interfacial tensions between the solid, liquid and gas phases.

The numerical analysis described in subsection 5.4.5 provides the shape of the interface as a function of $\frac{P_0 - P_{out}}{\gamma / R_p}, \frac{W_0}{\gamma}, \frac{\rho g R_p}{\gamma / R_p}, \frac{\delta_A}{R_p}$, namely the dimensionless pressure drop, wetting parameter, gravitational Bond number, and the ratio between the characteristic scale for surface forces and pore radius, the former is the length for which the interaction force changes sign becoming repulsive as the distance between the liquid metal interface and the solid substrate decreases, respectively. In real experiments $P_0 - P_{out}$ is anticipated to be very small since the operation takes place at near vacuum conditions. Besides, gravitational effects are negligible compared to surface tension forces in this context, $\frac{\rho g R_p}{\gamma / R_p} \ll 1$, due to the small pore radius and film thickness. Finally, $W_0 / \gamma \sim 1$ since Li exhibits partial wetting. In the absence of any reliable data an estimation of the interaction potential W_0 can be obtained by employing the formula provided by the analysis of the static configuration of a drop that partially wets a dry substrate, see also the relevant subsection below concerning the asymptotic analysis, in conjunction with the contact angle of 30° reported in the literature for lithium:

$$\frac{W_0}{\gamma} = 1 + \cos \theta_c \xrightarrow[W_0 = \gamma + \gamma_{sv} - \gamma_{sl}]{\theta_c \simeq 30^o} \frac{W_0}{\gamma} \simeq 1.866 \tag{6.32}$$

However, the above value is not entirely appropriate in the context of the present problem where a precursor layer exists that proceeds the adhered drop, as illustrated in **Fig. 2.4** and elaborated in Chapter 2. Hence, a parametric study is conducted in order to assess the effect of pressure drop and adhesion forces on the shape and thickness of the coating layer. We want to establish conditions for an almost uniform coating to be developed.

As a general trend, as W_0 increases the attraction between the liquid metal and the pore increases as well and the pore, without the imposition of an extra overpressure, tends to drag the liquid metal inside it and, thus, a small indentation is noted in the vicinity of pore`s "mouth", as can be shown in **Fig. 6.22**.

164
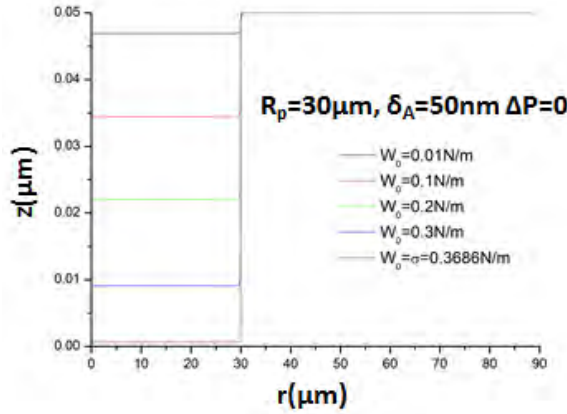
Fig. 6.22 Evolution of the shape of the interface as a function of the interaction potential when $\Delta P = P_0 - P_{out}$ = 0, R_p=30 μm and δ_A=50 nm

The static solution consists of the following regions, with the corresponding dominant balances. It should also be stressed that gravity remains subdominant in this regime owing to the very small film thickness. The region with $r > R_p$ constitutes the "inner region" where the intermolecular forces balance pressure forces, and is characterized by the formation of a precursor layer of almost constant thickness. The region with $r < R_p$ constitutes the "outer region" where the pressure forces balance the surface tension forces. The precursor layer is smoothly matched with the outer region via an intermediate regime, namely the transition region. The latter intermediate regime is characterized by the dominant force balance between intrmolecular forces and surface tension forces and has to appropriately match with both the outer and inner regimes. It was shown by the asymptotic analysis of the above regions, in the subsection above, that the angle at which the transition layer leaves the substrate to match the solution from the outer region is given by the relationship:

$$\cos\theta = 1 - \frac{W_{inner}(\delta)}{\gamma} = 1 - \frac{W_0}{\gamma}\left[2\left(\frac{\delta_A}{\delta}\right)^2 - \left(\frac{\delta_A}{\delta}\right)^4\right]$$

(6.33)

Eq. 6.33 constitutes a relationship that is more pertinent than Eq. 6.32 which corresponds to cases of partial wetting on a dry substrate. Eq. 6.33 applies for the case of liquid lithium resting on a prewet CPS for which a precursor layer is formed on the substrate surface that is prewet during the preparation process. Furthermore, when the liquid metal layer has not escaped the pore, the contact length is expected to be on the order of the pore radius. In this case, either a negative overpressure exists, in which case the outer region of the interface points its concave part towards the surrounding medium, or a small positive overpressure exists with its concave part pointing towards the interior of the pore.

For the case of a weak interaction potential such as the one depicted in **Fig. 6.22** corresponding to $W_0 = 0.01$ N/m, when the liquid metal arrangement is subject to zero overpressure an almost flat film is produced based on the static model presented in section 4.4.4 and the numerical simulations with the methodology outlined in section 5.4.5. Performing a parametric study, by varying the reservoir overpressure, it was seen that for negative and non-zero values of ΔP in the pore region the prevailing force balance in the bulk of the film is between surface tension and pressure forces and this

165

determines the curvature in that region via $2\gamma/\Delta P = R_m$. For a relatively weak interaction potential $W_0 = 0.05$ N/m and $R_p = 30\mu m$, $\delta_A = 150\mu m$ it can be clearly seen that over a wide range of negative and positive overpressures the liquid metal has not escaped the pore, **Figs. 6.23a,b** and **6.24a,b,** and the contact point is nearly fixed at the pore "mouth" at $r = R_p$. **Fig. 6.23b** focuses on the transition region of **Fig. 6.23a**, illustrating the smooth transition from the outer region in the vicinity of the axis of symmetry to the contact region where the film thickness acquires a length determined by the balance between overpressure and the attractive disjoining pressure,

$$P_0 - P_{out} - \rho g\delta = \frac{\partial W}{\partial n} = \frac{4W_0}{\delta_A}\left[\left(\frac{\delta_A}{\delta}\right)^3 - \left(\frac{\delta_A}{\delta}\right)^5\right] \tag{6.34}$$

i.e. the film thickness δ in the contact region remains constant and larger than the characteristic length δ_A.

(a)

(b)
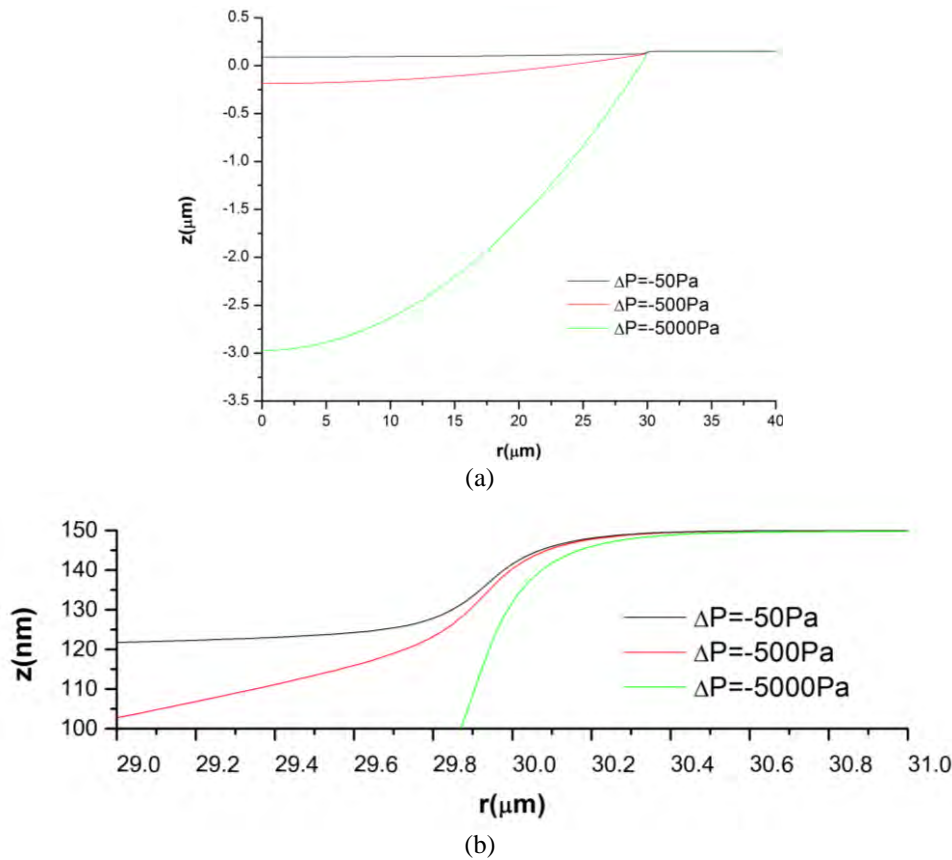
Fig. 6.23 (a) Film shape as a function of relative small overpressures, $\Delta P = P_0 - P_{out}$, for $W_0 = 0.05$ N/m, $R_p = 30$ μm, $\delta_A = 150$ nm and (b) Blow up of the transition and contact regions

As ΔP increases the liquid metal film forms a drop, **Fig. 6.24a,b**, that protrudes from the pore meeting the pore side walls with a macroscopic angle estimated via $\sin\theta = R_p/R_m$. In **Fig. 6.25** that focuses on the transition region merging the drop with the precursor layer in the contact region, the angle at the contact point is seen to gradually increase as ΔP increases until a limit point arises when $\Delta P \approx 11500$ Pa and $\theta \approx 27^o$. It was shown by asymptotic analysis of the above regions that, especially when $W_0 \ll \gamma$, the angle at which the transition layer leaves the substrate to match the solution from the pore region is given by the relation $\cos\theta = 1 - W_0/\gamma$. Thus, for the case considered above, namely when

166

W_0=0.05 N/m, θ is equal to 29°, which is very close to 27° obtained via the numerical analysis. It should also be stressed that the critical overpressure for which the solution family obtained with increasing overpressure exhibits a limit point is the one for which the above angle θ at which the liquid metal drop contacts the substrate is equal to the angle at which the drop shape leaves the pore mouth to match the drop in the bulk of the film. The latter angle is given by the following relationship:

$$\text{Sin}\theta = R_p / R_m = R_p \Delta P / (2\gamma). \tag{6.35}$$

(a)

(b)
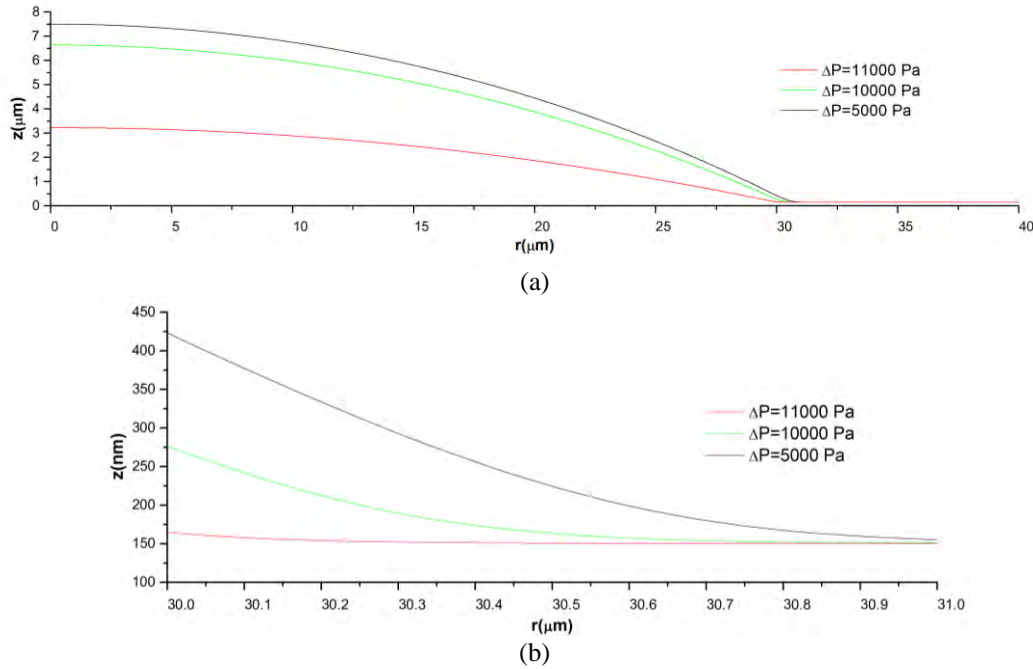
Fig. 6.24 (a) Film shape as a function of relative big overpressures, $\Delta P = P_0 - P_{out}$, for W_0=0.05 N/m, R_p=30 μm, δ_A=150 nm and (b) Blow up of the transition region
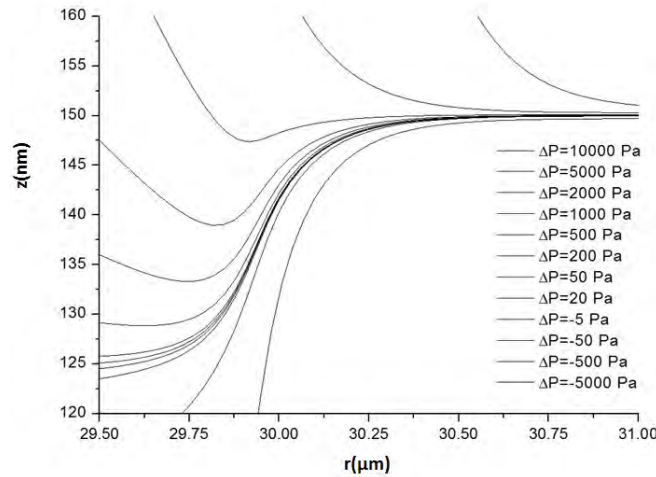
Fig. 6.25 Film shape as a function of overpressures, $\Delta P = P_0 - P_{out}$, for W_0=0.05 N/m, R_p=30 μm, δ_A=150 nm; blow up of the transition region

As was mentioned in the above analysis, no static solution was obtained for larger values of the interaction potential or larger overpressures than the critical one. A similar result has been reached by Starov [112,113] where it was seen that the static arrangement is

167

stable as long as $\dfrac{\partial \Pi}{\partial \delta} < 0$. In the present study the limit point occurs earlier for a value of δ smaller than the one coresponding to maximum Π as the distance from the wall δ varies. In order to provide better understanding an asymptotic analysis was conducted and shown above, on the structure of the static solution when the drop is in contact with a dry solid or with a precursor layer. It describes the structure of the solution right at the point for which, in terms of overpressure, the film starts escaping the pore and the solution branch turns to the classical spherical cap. In fact, this is also very close to the film shape at the limit point which occurs right at the point for which the pore ceases to bear an influence on it. In this fashion Eq. 6.33 was recovered as a necessary condition for the solution in the contact region to match the one in the transition region, in agreement with the analysis presented in [112,113] in a slightly different context. It should also be pointed out that to obtain such a result the form of the interaction potential should be such, i.e. one that prescribes good adhesive properties of the liquid metal, that supports the structure of a coating with a precurson layer covering the substrate. Such a functional relationship is not always available for the studied system of liquid-vapour-substrate and requires additional effort in establishing the type of interaction that adequatrely decsribes the interaction of the specific materials involved in the design of the CPS.

Beyond this critical overpressure, a static solution could not be obtained and the solution family turned to lower values with the film establishing an almost spherical shape with contact length larger than then pore radius and the contact angle fixed at the above critical value. These are shapes that have escaped the pore and cover the entire porous structure. The overall shape is that of a spherical cap and the solution family merges with the one obtained for relatively large overpressures in section 6.4.1. The critical point essentially reveals the change from a fixed contact point to a fixed contact angle behavior of the adhered liquid metal layer as a certain angle is reached. For larger overpressures, a static solution could not be obtained and it is conjectured that a dynamic analysis may provide the response of the CPS in this parameter range, in the same fashion that inclusion of the disjoining pressure provides the dynamic contact angle of a drop spreading over a dry substrate that is fully wet by it. Nevertheless, further research is required in order to verify this conjecture and is left for a suggestion for a future study.

The above type of static response persists until $W_0 \sim \gamma$, see also **Figs. 6.26a,b**, in which case a limit point arises with the contact angle $\theta \sim 45^o$, which is very close to the angle provided via relationship $\sin\theta = R_p/R_m = R_p\Delta P/2\gamma$, when the overpressure approaches the critical value, $\Delta P = \Delta P_{cr}$. Consequently, the numerical calculations fail to provide static solutions for interaction potentials that are quite larger than surface tension. It should be stressed in this point that as the interaction potential increases the level of overpressure required to "force" the liquid metal out the pore increases and this attests to the stabilization that the CPS structure provides against drop ejection and splashing in the presence of Lorentz forces. To first order the effect of Lorentz forces can be incorporated in the static arrangement in the form of a magnetic pressure that effectively increases the apparent reservoir overpressure.

(a)

(b)
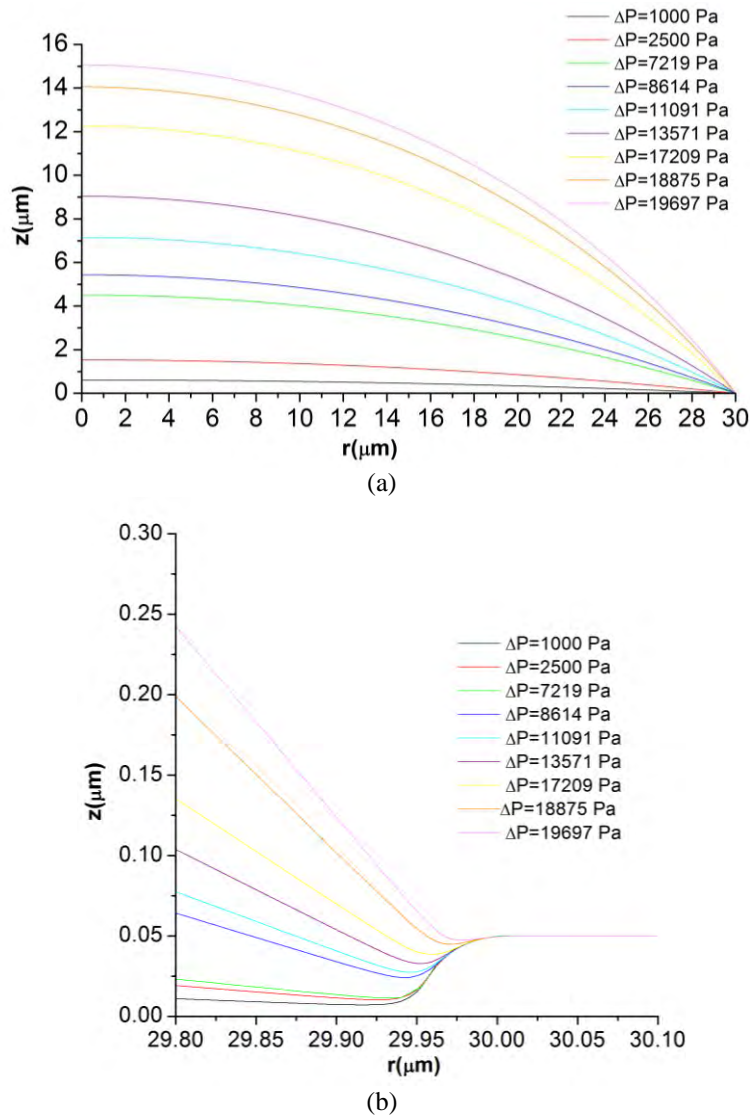
Fig. 6.26 (a) Film shape as a function of overpressures, $\Delta P = P_0 - P_{out}$, for $W_0 \sim \gamma$, $R_p = 30$ μm, $\delta_A = 150$ nm and (b) blow up of the transition region

As stressed above for relatively large values of Δp, the numerical solution exhibits a limit point. In order to continue the solution, the Arc Length Continuation was used instead of Simple Continuation in the manner described in subsection 5.4.5. This kind of continuation revealed the existence of a second branch of solutions, for the same overpressure range as the original branch, characterized by a fixed contact angle. In **Fig. 6.27** a bifurcation diagram is presented for $R_p = 30$ μm and $\delta_A = 50$ nm, where z_0 represents the maximum height of the liquid metal drop at $r = 0$ while $\Delta P = P_0 - P_{out}$. In this graph, the position of the limit point is seen to be displaced to lower values of z_0 and ΔP as W_0 decreases. **Fig. 6.27** also includes graphs depicting the evolution of the shape of the interface around the limit point. As an illustrative example the case of $W_0 = 0.05$ N/m is depicted in **Fig. 6.28.** The numerical solution corresponding to the first branch is represented via the black solid line, while the solution corresponding to the second branch is represented via the purple solid line. Finally, the black dotted line corresponds to the solution at the limit point. As a general trend solutions past the limit point correspond to thicker films with spherical cap shapes identical to those obtained in the standard analysis of a drop that adheres on a solid substrate at fixed contact angle and relatively large pressure difference between the drop interior and the surrounding

169

medium, see also the discussion in section 6.4.1. Furthermore, the drop shape and thickness as a function of overpressure in a bifurcation diagram of this kind is more or less independent of δ_A. Moreover, the position of the limit point has weak dependence of δ_A with a small shift backwards as δ_A increases, see also **Fig. 6.29**. Hence, the fact that **Fig 6.27** was drawn for a different value of δ_A, namely 50nm as opposed to 150 nm that was used in the previous graphs of this subsection, does not play a role in the calculated response pattern. The extended blue line in **Fig. 6.27** corresponds to the case where $W_0 \sim \gamma$ for which no limit point was observed for the range of ΔP values that was investigated. Finally, no static numerical solution was obtained for larger values of the interaction potential.
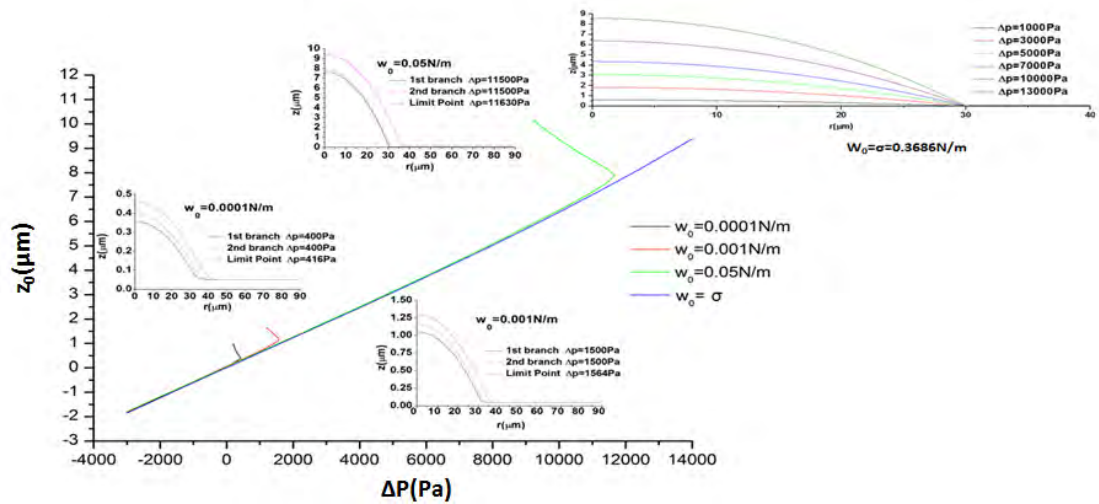
Fig. 6.27 Bifurcation diagram for $R_p=30\mu m$ and $\delta_A=50nm$ and evolution of the shape of the interface around the limit point
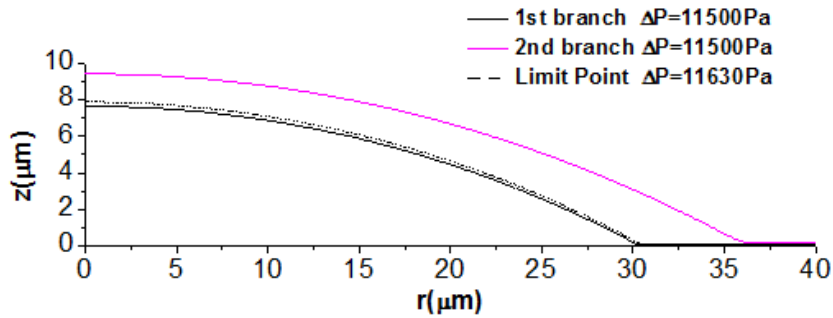
Fig. 6.28 Bifurcation diagram for $W_0 = 0.05$ N/m, $R_p=30\mu m$ and $\delta_A=50nm$ and evolution of the shape of the interface around the limit point

170
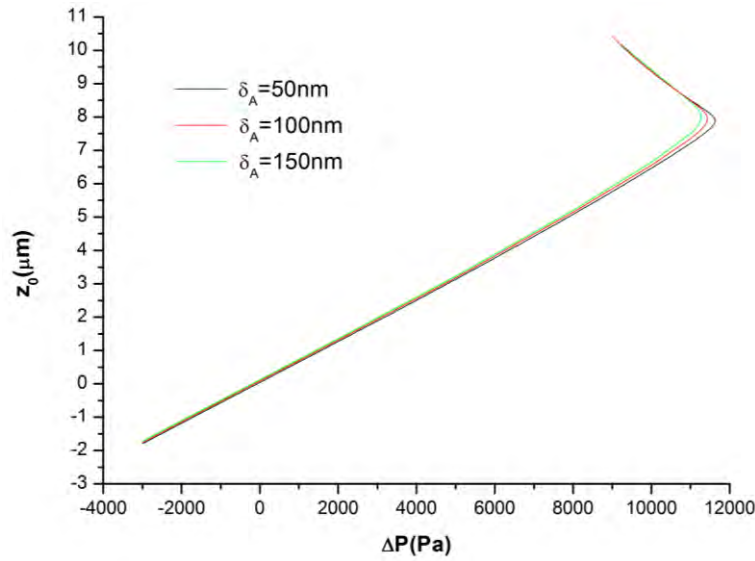
Fig. 6.29 Bifurcation diagram for R_p=30µm and δ_A=50, 100 and 150nm

As mentioned above, the solutions past the limit point correspond to thicker films with longer contact lengths and fixed contact angle. They essentially constitute a continuation of the spherical shapes obtained for relatively large overpressures, shown in subsection 6.4.1, and they are obtained once the pore influence on the static arrangement weakens. It is of interest to study the relative stability of such shapes in order to ascertain the static arrangement that will eventually prevail. Suffice to say at this point that the Jacobian matrix obtained for thicker films contains no unstable eigenvalues, whereas the shapes with pore influence contain an unstable eigenvalue. Perhaps this is associated with the value adopted for the interaction potential $W_0 < \gamma$ and corresponds to a liquid with not very strong adhesion properties on the particular substrate. Dynamic analysis of the above obtained static arrangement, one that couples transient effects and fluid motion with surface and capillary and pressure forces, is necessary to verify its stability.

6.4.3 Effect of an externally applied electric field

Despite the relatively small thickness of the coating film that was obtained in the previous subsection, it may still be subject to instabilities and drop ejection in the presence of large enough electromagnetic forces, the mechanism of which strongly depends on the size of the original layer and its adhesion properties. As a first approximation towards assessing the effect of external field forces on the static arrangement of the liquid metal layer that covers the porous system, an external electric field is introduced that is aligned with the axis of symmetry of the porous wafer, **Fig. 4.10c**, in the far field; $\mathbf{E} = -\nabla\Phi$, $\mathbf{E}(r \to \infty) = E_0 \mathbf{e_z}$, with Φ denoting the electric potential. In order to compare with similar studies from the literature [92] the contact point and the volume of the adhered liquid metal layer is fixed to the values calculated in the absence of an electric field, and the contact angle is calculated as part of the post-processing of the numerical solution.

Upon introduction of electric stresses in the normal stress balance due to the external electric field, the effective internal pressure is affected, thus, rearranging the shape of the drop. This is better illustrated when, $\epsilon_{out}/\epsilon_{in} \ll 1$ in which case a perfectly conducting liquid metal can be assumed. Using the static equilibrium obtained in **Fig. 6.14** with the top of the porous matrix fully covered, i.e. R_f = 10 cm and contact angle θ_c=30°, and

171

gradually increasing the electric field intensity while keeping the mass of the liquid metal within the layer constant, the sequence of the shapes shown in **Fig. 6.30** is captured. As a result of the electric stresses, the pole section of the layer is elongated in the field direction while the contact angle at the equator decreases in order to maintain the same amount of liquid lithium. The liquid metal layer thickness increases away from the contact line and its curvature increases as well. Eventually, a conical angle tends to form at the pole with angle $\theta_c \sim 75^o$ and a solution could not be obtained for stronger electric fields. In this limit capillarity balances the electric stresses in the pole region and this determines the size of the conical angle at the pole. Gravity cannot participate in the dominant balance in the pole region as the intensity of the electric field increases, because it would lead to excessively large axial displacements in this region that would violate the mass balance. As a result, when Bond$_{el}$ increases, beyond a certain point, the layer thickness at the pole is not affected. Rather the curvature increases until a conical angle forms. When the initial size of the lithium layer decreases, e.g. when $R_f = 5$ mm and Bond=0.33, while the contact angle in the absence of electric forces is set to 60°, beyond a certain range of electric field intensities, Bond$_{el} > 500$, the solution does not change significantly except for the curvature in the pole region where eventually a conical angle of $\theta_c \sim 47^o$ is formed, **Fig. 6.31**. The above angle is very close to the angle of 49° predicted by Taylor [85] for conductive cylinders elongated by the action of electric stresses. Overall, it is the interaction between capillarity that pins the drop onto the substrate and electric stresses that determines the coherence and stability of the adhered drop.
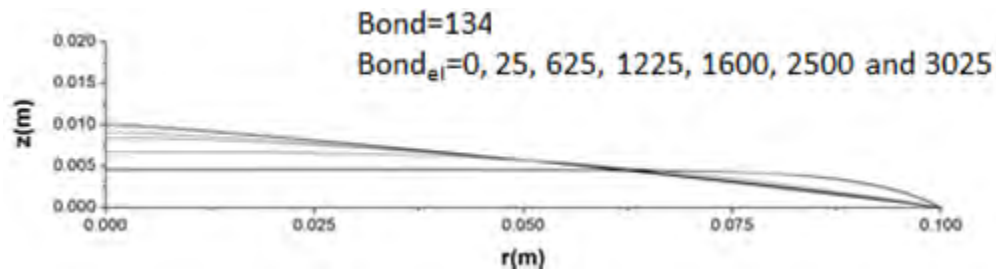

Fig. 6.30 Evolution of the shape of the interface with the porous layer fully covered, with increasing electric field intensity and $\in_{in} / \in_{out} \gg 1$, Bond=134
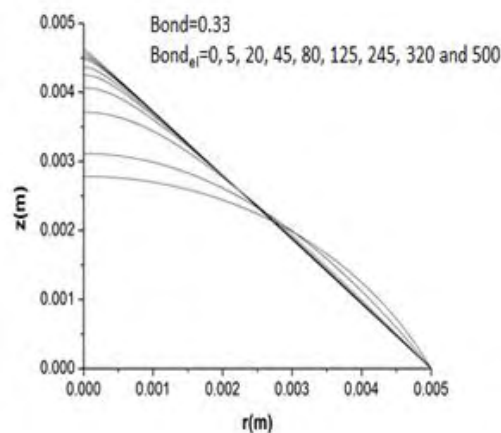
Fig. 6.31 Evolution of the shape of the interface with the liquid metal drop pinned at 5mm, with increasing electric field intensity and $\in_{in} / \in_{out} \gg 1$, Bond=0.33

172

This pattern is verified by more recent studies in the literature [93], where the dynamics of this process was also studied and was seen to alter the value of the eventual conical angle. It was thus predicted that the contact angle that is formed dynamically is smaller than the Taylor angle. Moreover, Reznik et al. [92] stated that depending on the static contact angle and the field intensity, along with the appearance of the dynamic conical angle, jetting is initiated at the pole region. This process is known to generate small droplets once the jet speed reaches a certain threshold. In the same study it was observed that, depending on the static contact angle and the extent of wetting, dislocation of the entire layer may take place instead of jetting. The electric field strength required for such instabilities to arise increases with decreasing thickness of the liquid metal layer. In particular, as the size of the layer increases the intensity of the electric field required for the formation of the conical angle decreases, as suggested by $Bond_{el} = \rho g R_f^2 / \gamma$ since the critical $Bond_{el}$ for conical angle formation is fixed for fixed static contact angle and electric permittivity ratio. Clearly, this places a limit in the thickness of the liquid metal layer that can be placed on a certain substrate, if unwanted instabilities are to be avoided.

The above mechanism of destabilization of a drop that adheres onto a solid substrate, via the onset of electric stresses provides a plausible analogy for the stability of the capillary porous system. In the latter arrangement, however, it is the Lorentz forces (jxB effects) that will be responsible for the destabilization of the CPS, or equivalently the magnetic part of the Maxwell stresses. As a consequence, it is of central importance concerning the feasibility of capillary porous systems in power exhaust of fusion reactors, to ascertain the actual static arrangement of the structure and perform dynamic studies where the more relevant Lorentz forces are incorporated in the analysis, along with the surface forces that act so as to pin the liquid metal layer onto the substrate. The results of this investigation are presented below in the following subsection. The dynamic interaction of these forces will determine the stability window of such an arrangement.

6.4.4 Effect of Lorentz forces
As analyzed in subsection 4.4.3 the film is going to occupy the region within the pore and, depending on the intensity of the Lorentz force and the micro-scale solid-liquid interactions, extend over a certain portion of the substrate.

If the Lorentz force is not very large, then the film remains within the pore and we can focus on the region in the pore, $0 \leq r \leq R_p$, while fixing the contact point to the top of the pore at position, r = R_p and z = 0. Furthermore, in the same regime of relatively weak Lorentz force in comparison with capillarity (i.e. small $Bond_m$), we can neglect the rotational part of the Maxwell stress and concentrate on the effect imposed by the magnetic pressure on the location of the interface between the liquid metal and plasma. In this context, a static arrangement can be obtained where the magnetic pressure plays the role of reservoir overpressure postulated in subsection 6.4.2, where the static arrangement was investigated in the pore level as a function of the strength of the interaction potential relatively to capillarity and pressure forces.

As long as the liquid metal is within the pore, the above mentioned effective overpressure tends to pull liquid Li out of the pore. The analysis in section 4.4.3 showed that this kind of effective pressure is depended on the magnitude of the magnetic field, the electric current that enters the liquid metal layer and the pore radius. As a result the magnetic pressure scales like $P_m = B_0 J_r R_p$. Since no extra overpressure exists, considering vacuum

173

conditions, surface tension balances the magnetic pressure while gravity remains insignificant in this regime. Hence, the whole process is controlled via the dimensionless number $Bond_m = B_0 J_r R_p^2 / \gamma$ which correlates the relative strength of magnetic pressure forces comparing to surface tension forces.

A 2-D finite element mesh consisting of 50 biquadratic rectangular elements in both the horizontal and vertical direction was tested and seen to provide accurate results for the model of static arrangement in the presence of Lorentz forces presented in section 5.4.4. In **Figs. 6.32a,b**, the case of Lithium is studied with its standard physical properties that were used in the present study, while the Bond and $Bond_m$ were set to $1.13 \cdot 10^{-5}$ and 3.96, respectively. As the computational mesh becomes finer, the numerical solution, in terms of the shape of the interface f and the stream function H of the electric current, was seen to converge. In particular, a mesh of 50x50 biquadratic elements was seen to provide a converged and acceptable numerical solution upon comparing it with even finer meshes.

(a)

(b)
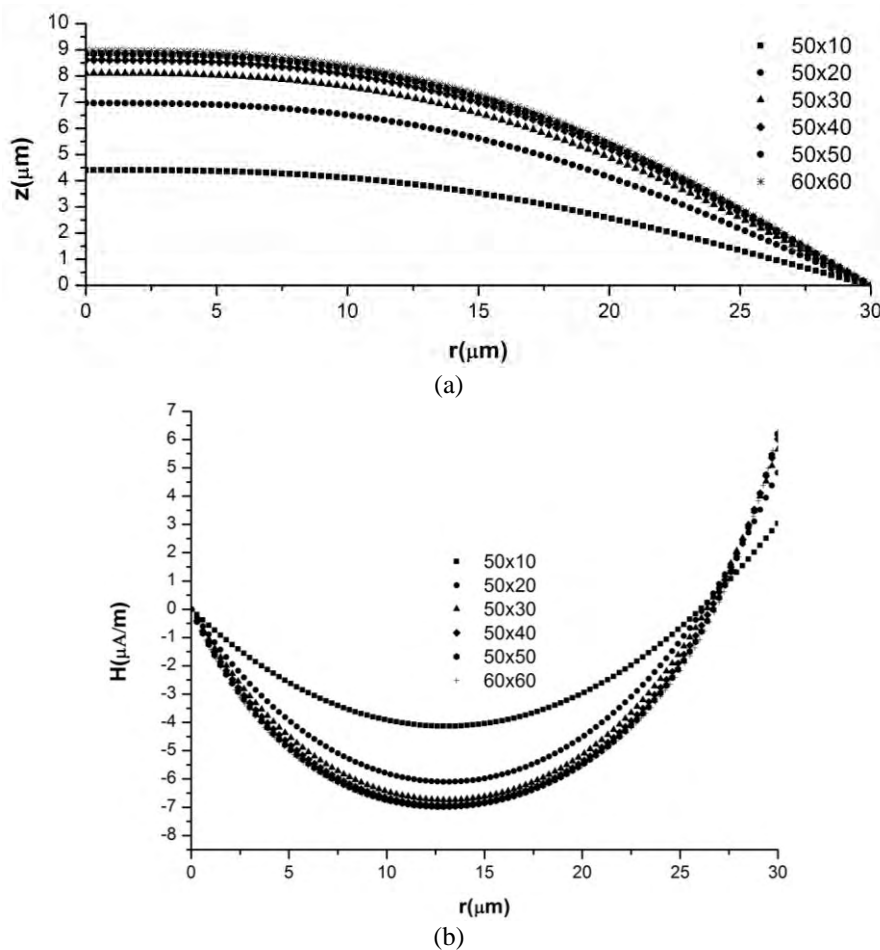
Fig. 6.32 Grid independence study for (a) the shape of the interface with the liquid metal drop pinned at the top of the pore and (b) the stream function of current, H, at the interface when Bond = $1.13 \cdot 10^{-5}$ and $Bond_m$ = 3.96

In this context, fixing the pore radius R_p = 30 μm, surface tension γ = 0.4 N/m, and the external magnetic field B_0 = 0.8T, the shape of the interface as well as the stream function of current, H, at the interface is captured for increasing J_r, or , increasing $Bond_m$, as illustrated in **Figs. 6.33a,b**, respectively.

174

(a)

(b)
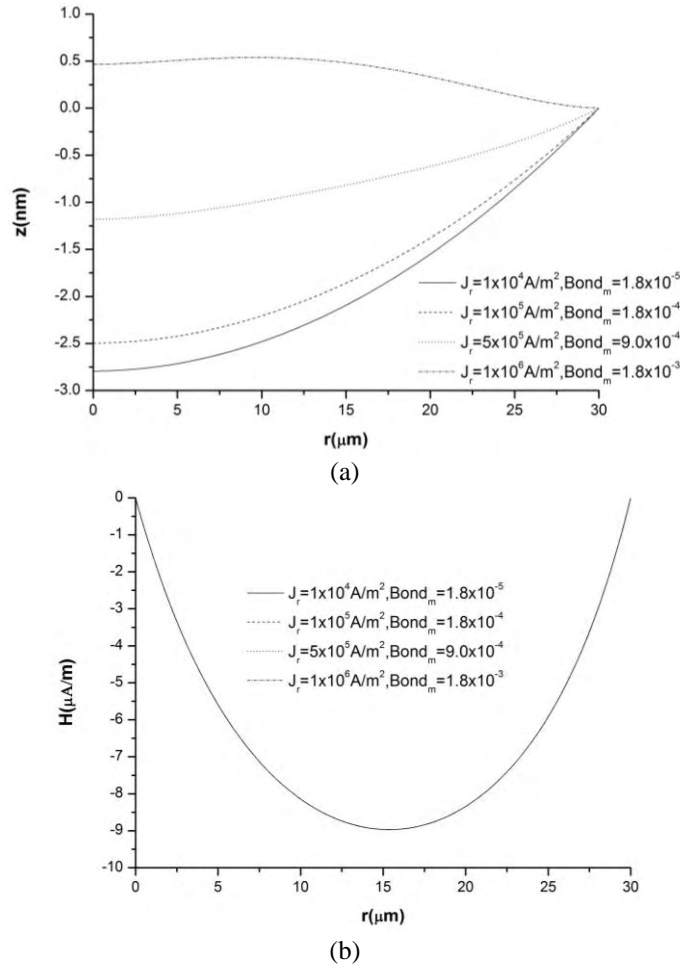
Fig. 6.33 (a) Evolution of the shape of the interface and (b) the stream function of current, H, at the interface with increasing electric current density, thus, increasing $Bond_m$ while R_p = 30 μm, γ = 0.4 N/m, B_0 = 0.8T and Bond = 1.13·10⁻⁵

The angle, θ, at which the interface approaches the wall is increased with increasing electric current density, while the liquid metal interface registers positive excursions from the pore entrance, albeit continuing to be pinned at the pore`s edge. This process evolves until θ reaches a critical value prescribed by the strength of the interaction potential of the liquid metal with the substrate. For relatively weak interactions it is provided by the following relation, $\frac{W_0}{\gamma} = 1 - \cos\theta_c$. The aforementioned relation is derived via an asymptotic analysis which was presented in subsection 6.4.2 concerning the effect of the topography of the porous substrate and the adhesive properties of the liquid metal on the static arrangement. **Fig. 6.34a** illustrates the evolution of the shape of the interface with increasing the electric current density until θ ≈ 29°, which is a critical angle obtained for W_0 ≈ 0.05 N/m and γ = 0.4 N/m. This contact angle is obtained for the critical $Bond_m$ = 3.96 and corresponds to the angle for which the liquid metal starts exiting the pore in the manner explained in section 6.4.2. The corresponding values of stream function H along the interface are shown for increasing $Bond_m$ in **Fig. 6.34b**. $Bond_m$ ranges from 1.8 to 3.96 corresponding to J_r values from 1·10⁹ A/m² to 2.2·10⁹ A/m² for the case of R_p = 30 μm, γ = 0.4 N/m and B_0 = 0.8T that was mentioned above. Since a specific value for the interaction potential is not known, calculations can proceed for larger electric current densities keeping the contact point fixed at the pore entrance. In this fashion, the above trend of expanding interfaces as a result of the magnetic pressure continues.

175
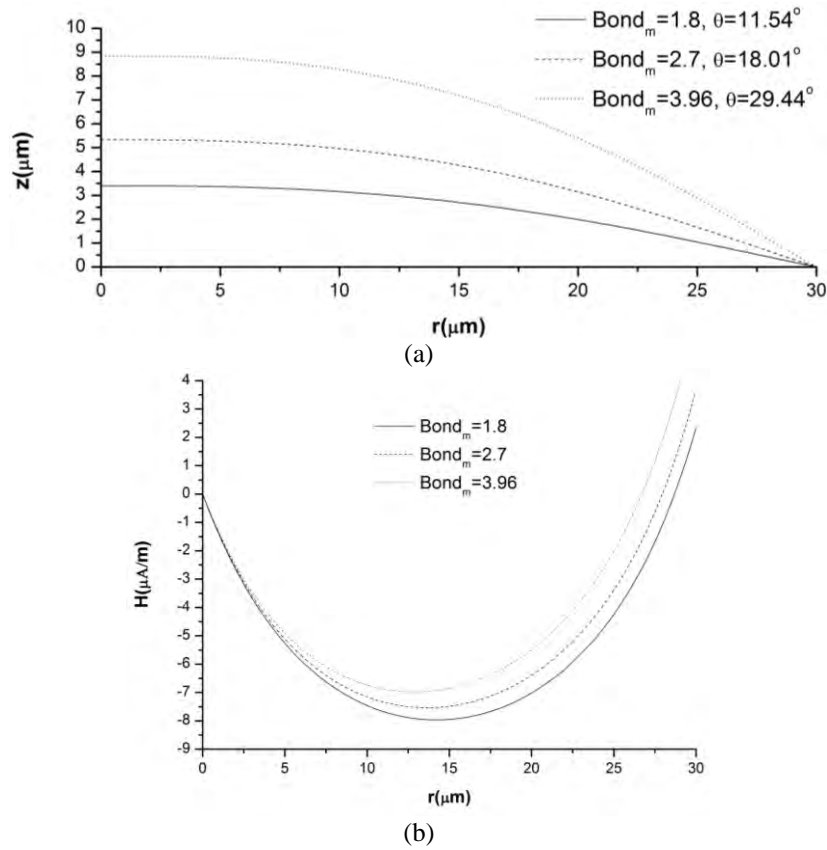
Fig. 6.34 Evolution of (a) the shape of the interface and (b) H along the interface with increasing $Bond_m$ until $\theta \approx 29°$ which is a critical angle obtained for $W_0 \approx 0.05$ N/m and $\gamma = 0.4$ N/m while $Bond = 1.13 \cdot 10^{-5}$

Alternatively, based on the analysis presented in section 6.4.2 for the static arrangement, as a function of overpressure and interaction potential, the contact angle may be fixed to the above critical value via $\frac{W_0}{\gamma} = 1 - \cos\theta_c$. In this case, upon increasing the magnetic Bond number, $Bond_m$, the liquid metal forms a drop with a contact length smaller than the pore radius, $R_c = 2\gamma/P_m < R_p$, which meets the precursor layer with the above macroscopic contact angle θ_c. **Fig. 6.35** illustrates the evolution of the shape of the interface in this process when $W_0 \approx 0.05$ N/m and $\gamma = 0.4$ N/m. Moreover, $Bond_m$ ranges from 1.8 to 9 corresponding to J_r values from $1 \cdot 10^9$ A/m^2 to $5 \cdot 10^9$ A/m^2. **Fig. 6.35** illustrates a process that is similar to the one presented in subsection 6.4.1 pertaining to the effect of the reservoir overpressure. In this investigation, as the $Bond_m$ increases (similar to the reservoir overpressure regarded in 6.4.1), the drop is expected to shrink. The main difference is that in the absence of reservoir overpressure ($P_r \approx P_{out}$) only magnetic pressure, $P_m = B_0 J_r R_p$, exists in order to balance the surface tension forces. Hence, R_f roughly scales like $2\gamma / P_m$ and consequently as P_m increases, the radial contact length decreases. As a result, the drop shrinks and reenters the pore ($R_p < 30\mu m$) and the solutions obtained via the numerical analysis (namely for $Bond_m = 9$ in **Fig. 6.35**) give unrealistic values in view of the existence of the pore. Thus, it can be concluded that no static solution can be obtained by further increasing $Bond_m$ while at the same time fixing the contact angle.
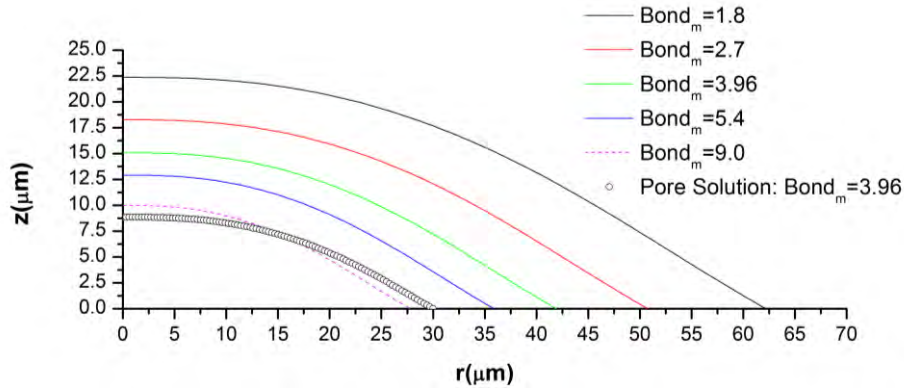
Fig. 6.35 Evolution of (a) the shape of the interface with increasing Bond$_m$ until the radial contact length becomes less than the pore radius

On the other hand, as the electric current density decreases, thus, reducing the magnetic bond number, Bond$_m$, a new solution is found with the liquid metal forming a drop outside the pore for fixed contact angle θ_c. This solution probably emerges after a limit point in the solution branch in the manner spherical cap shapes emerged beyond the limit point towards smaller overpressures in the static analysis without Lorentz forces. In **Fig. 6.35** the case of Bond$_m$ = 3.96 represents the threshold value in Bond$_m$ corresponding to the onset of the limit point leading to larger drops, as the magnetic Bond decreases, that adhere on the substrate with a fixed contact angle.

In **Fig. 6.36** the ratio of the contact length, R_f, over the maximum drop size, z_0, namely $z(r = 0)$, is given as a function of Bond$_m$. The first branch of solutions, derived by fixing the contact point at the pore`s edge and depicted via black squares, corresponds to the pore solution emerging as a result of increasing Bond$_m$ and illustrated in **Figs. 6.33a**, **6.34a**. Moreover, the second branch of solutions, depicted via red squares, corresponds to the alternatively derived liquid metal drop forming outside the pore by fixing the contact angle, θ_c, prescribed by the liquid metal-solid substrate interaction potential, **Fig. 6.35**. As far as the first branch solutions are concerned, the radial length is always fixed and equal to the pore radius, $R_f = R_p$. As a consequence, as Bond$_m$ increases, z_0 also increases and therefore R_f/z_0 decreases, **Fig. 6.36**. On the other hand, regarding the second branch of solutions, based on **Fig. 6.35** z_0 increases by decreasing Bond$_m$, however the contact length R_f decreases as well and it is not constant as before. In particular, in this consideration $R_f = R_m \sin\theta_c$ and $z_0 = R_m \left(1 - \cos\theta_c\right)$, thus,

$$\frac{R_f}{z_0} = \frac{\sin\theta_c}{1 - \cos\theta_c}$$ and so R$_f$/z$_0$ is expected to be constant and a function only of θ_c.

177
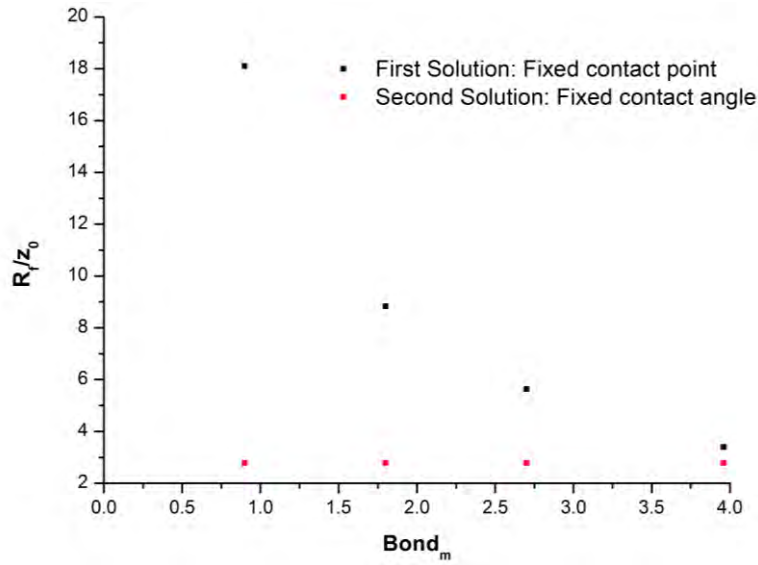
Fig. 6.36 Bifurcation diagram showing the aspect ratio R_f/z_0 as a function of $Bond_m$

Based on the above analysis and for the solution family obtained for fixed contact point, the evolution of contact angle θ at the contact point can be obtained as a function of $Bond_m$ until the critical value $Bond_{m,cr}$ is reached for which the contact angle θ_c is captured, prescribed by a given liquid-solid interaction potential W_0:

$$\sin\theta \approx \frac{R_p P_m}{2\gamma} \approx \frac{B_0 J_r R_p^2}{2\gamma} = \frac{Bond_m}{2} \tag{6.36}$$

For small values of $Bond_m$, a linear dependence is expected between contact angle θ_c and $Bond_m$ and this is validated by the numerical calculations of the contact angle as the solution family with fixed contact point evolves with increasing $Bond_m$ as illustrated in **Fig. 6.37**.
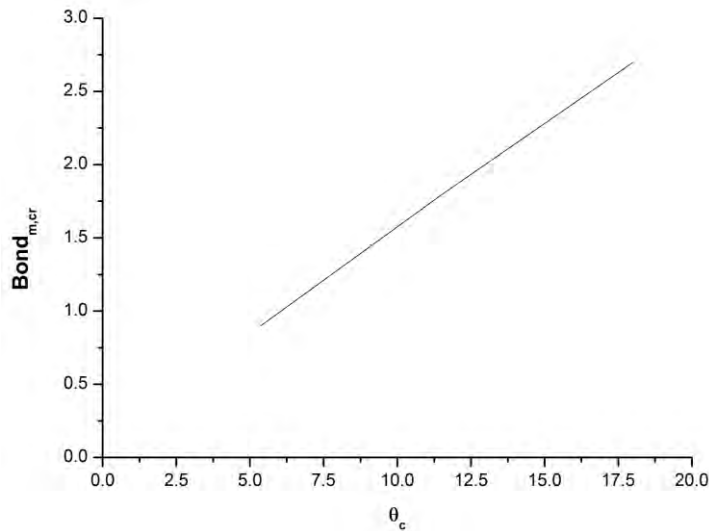
Fig. 6.37 Critical $Bond_m$, $Bond_{m,cr}$, as a function of θ_c

Moreover, the liquid metal which is going to be used as a plasma facing component is going to play a key role in the static arrangement, since different Bond and $Bond_m$ numbers are going to appear. For example, in **Fig. 6.38** the shape of the interface is

178

depicted for $R_p = 30\mu m$, $B_0 = 0.8T$, $J_r = 2.2 \cdot 10^9$ A/m^2 and for the cases of Lithium (Li), Tin (Sn) and Galium (Ga) with the properties of liquid metals derived via **Table 4.1** in Chapter 4. Consequently, for lithium Bond and Bond$_m$ are set to $1.13 \cdot 10^{-5}$ and 3.96, respectively whereas for tin and galium Bond and Bond$_m$ are set to $1.12 \cdot 10^{-4}$, 2.88 and $7.8 \cdot 10^{-5}$, 2.3, respectively. Assuming a fixed contact point solution, Ga exhibits the lower positive excursion out of the pore and smaller contact angle, owing to its larger surface tension among the three materials.
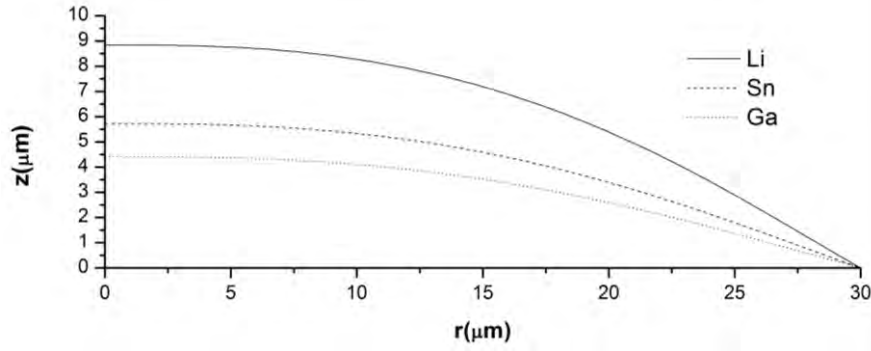
Fig. 6.38 The shape of the interface for $B_0 = 0.8T$, $J_r = 2.2 \cdot 10^9$ A/m^2, $R_p = 30\mu m$ concerning the liquid metals proposed as PFCs, namely Li, Ga and Tin

Based on the above discussion, a first criterion for the stability of the static arrangement of the CPS in the presence of Lorentz forces is obtained. As was discussed in the context of **Fig. 6.35**, once the contact angle of the liquid metal layer is fixed, a static solution cannot be calculated beyond a certain critical magnetic Bond number that depends on the strength of the interaction potential. This critical value increases with increasing interaction potential W_0, or equivalently with increasing contact angle θ_c. Beyond the later critical value, i.e. as the electric current density increases, dynamic considerations should be introduced in the model and this might entail jet formation, break-up of the protective layer and drop ejection. Hence, the dimensionless Bond$_m$ controls the static arrangement and can be used as a key factor for future applications; it can be expressed as the relative strength of Lorentz and adhesion forces as follows:

$$Bond_m = \frac{\text{magnetic pressure forces}}{\text{surface tension forces}} = \frac{B_0 J_r R_p^2}{\gamma} \tag{6.37}$$

Thus, in terms of the CPS reliability as plasma facing component, for a given Bond$_{m,cr}$ bigger plasma currents can be tolerated via decreasing the pore radius. Alternatively, for fixed critical Bond$_m$ number, the pore radius controls the maximum electric current for which a static equilibrium can be established.

179

Chapter 7: Concluding remarks and future directions

In this chapter, the main results from the research concerning the PhD dissertation are summarized. In particular, the current investigation pertaining to the jet/drop deflection in a simplified Tokamak environment managed to give a reasonable explanation of the experimentally observed trajectory shift. As a matter of fact, the numerical results conform, within the proper order of magnitude, to the findings of ISSTOK experiments. Besides, the novel research regarding the CPS static configuration accomplishes, through first-principles studies, to deal with the major phases of the CPS operation. More specifically, it models-explains what happens during the preparation phase, that is to say before the machine is "turned on". Furthermore, a heat balance is performed pertaining to the power exhaust capabilities of the CPS configuration ignoring the non-coronal radiation shielding. Subsequently, this thesis delves into how the replenishment occurs identifying the interplay between the different forces that act towards pushing liquid lithium out of the porous matrix or resist its motion. Besides, the current PhD dissertation studies extensively the static arrangement of the ultra-thin liquid metal film that rests onto the CPS outer surface, as a function of the reservoir overpressure and wetting properties of the working liquid metal on the substrate. Finally, as a first attempt to capture the electromagnetic effects on the static arrangement, an external electric field was applied. Then, the more relevant to fusion applications jxB effects were incorporated and interesting results were conducted that generated new scientific queries that are going to constitute the main proposals for future directions of this PhD dissertation.

7.1 Deflection of a liquid metal jet/drop in a tokamak environment

In this analysis, the effect of Lorentz forces, gravity and pressure drop were accounted for in a unidirectional model that assumes a small jet radius in comparison with the trajectory length. The effect of external electric potential gradients on jet deflection was ascertained in conjunction with the importance of electric stresses in modulating the jet speed and radius. Moreover, the trajectory of the ensuing droplets, by virtue of the jet break-up as a capillary instability, was also modelled in the presence of Lorentz forces as a means to capture and quantify the deflection process reported in the ISTTOK experiments under the plasma influence. Droplets, due to their small size and spherical shape, experience a stronger deflection as the analytical investigation indicated.

The simplified model developed in the context of the present study provided a proof of principle explanation for the observed jet/drop deflection from the original trajectory in a simplified Tokamak environment. As a consequence, the results obtained corroborate the belief that employment of liquid metal drops/jets cannot be regarded as an optimal alternative plasma facing component mainly due to their strong deflection as they interact with the surrounding plasma. In addition, the results based on this first principle study reasonably conform to the findings of ISSTOK experiments, see also [115].

Institutional Repository - Library & Information Centre - University of Thessaly
23/04/2024 18:05:53 EEST - 18.189.2.122

7.2 Static arrangement of the CPS

The Capillary Porous System operates like a capillary pump replenishing the liquid metal on the interface with plasma by utilizing the capillary pressure. The static film thickness is an important parameter that will definitely affect the reliability of the CPS during plasma operation. In this PhD dissertation, estimation of the static configuration both at preparation phase and after depletion and replenishment of the liquid metal was accomplished using the finite element numerical methodology. More specifically, parametric studies were performed regarding the effect of reservoir overpressure and external field forces, namely the electric stresses and the Lorentz forces. Besides, the effect of the topography of the porous substrate on the static configuration was also taken into account, since the liquid metal film which is formed at near vacuum conditions is on the order of micrometers and sub-micrometers. As a consequence, in the vicinity of the three-phase contact line the film thickness approaches zero and thus the overlapping of the boundary layers results in the existence of surface forces. Hence, the micro-scale liquid-solid interactions were also considered.

7.2.1 Effect of reservoir overpressure
The parametric study pertaining to the effect of the reservoir overpressure on the static arrangement gave the following results:

- For relatively large overpressures, very small almost hemispherical drops are obtained and the governing force balance is between the pressure and surface tension forces. Consequently, as the reservoir overpressure decreases, the drop spreads out forming a liquid metal film.
- As the drop further spreads out, the liquid metal film gradually covers the entire CPS outer surface, while the importance of gravity increases and balances pressure forces in this regime. In the region near the contact point, capillary pressure balances pressure drop.
- As the pressure drop is further decreased (below 29 Pa), the contact length approaches exceed any reasonable wafer length and the numerical results indicated that such a balance cannot be maintained for fixed contact angle.
- By imposing a fixed contact point rather than a fixed contact angle, static solutions for even lower reservoir overpressures can be obtained until ΔP almost vanishes with the film achieving micron-size thicknesses and near zero contact angles.

7.2.2 Effect of the topography of the porous substrate
As was stressed above, at near vacuum conditions, namely considering slightly positive or negative reservoir overpressures, the film thickness reduces down to micron or even submicron sizes. We did not assume the classic partial wetting case, of liquid lithium with a dry substrate beyond the contact point. In this fashion, we are dealing with coatings rather than films and micro-scale liquid-solid interactions need to be accounted for. In particular, the cases with a purely repulsive and a long range attractive short range repulsive potential are investigated in order to model the effect of the topography and nature of the porous substrate on the static arrangement of the liquid metal.

The repulsive interaction potential was in the form of $W(\delta) = \dfrac{A}{12\pi\delta^2}$. Assuming that $P_r \approx$ P_{out} and a CPS thickness of 1mm and a pore size on the order of 30 μm:

182

- An almost uniform coating of size on the order of submicron's over the substrate, with an indentation in the pore region is obtained.
- As the strength of the repulsion increases, the liquid metal film thickness increases as well.
- Similarly, as the external overpressure increases the coating thickness decreases.
- For relative large external overpressures, the liquid metal-gas interface enters the pore region and the indentation seems to be bigger.
- No static solution is possible for positive reservoir overpressures, because this kind of interaction potential cannot counterbalance a positive pressure drop across the interface.
- As anticipated in real experiments, the presence of Lorentz forces may lead to positive and very large effective reservoir overpressures, in the form of magnetic pressure, especially during off-normal events. In such a situation a purely repulsive potential cannot exert a stabilizing attractive force that would pin the film onto the substrate. Thus, a purely repulsive potential is considered inappropriate for the real case of CPS static configuration.

On the other hand, in the absence of any reliable data, a long range attractive short range repulsive potential in the form of $W = W_{.0}\left[\left(\dfrac{\delta_A}{\delta}\right)^4 - 2\left(\dfrac{\delta_A}{\delta}\right)^2\right]$ gave us more useful results.

- As a general trend, as the interaction potential increases, the attraction between the liquid metal and the pore increases as well and the pore tends to drag the liquid metal inside it and, thus, a small indentation is noted in the vicinity of pore`s "mouth".
- Three main region are identified: the "inner region" (intermolecular forces balance pressure forces and as a result a precursor layer is formed), "the outer region" (surface tension forces balance pressure forces). Finally, the precursor layer is smoothly matched with the outer region via an intermediate regime, namely the "transition region" (intermolecular forces balance surface tension forces).
- It was shown by an asymptotic analysis of the above regions, in the subsection 6.4.2, that the angle at which the transition layer leaves the substrate to match the solution from the outer region is given by the relationship:

$$\cos\theta = 1 - \frac{W_{inner}(\delta)}{\gamma} = 1 - \frac{W_0}{\gamma}\left[2\left(\frac{\delta_A}{\delta}\right)^2 - \left(\frac{\delta_A}{\delta}\right)^4\right] \tag{7.1}$$

- The above equation applies for the case of liquid lithium resting on a prewet CPS for which a precursor layer is formed on the substrate surface that is prewet during the preparation process.
- For negative and non-zero values of ΔP in the pore region the dominant force balance between surface tension and pressure forces determines the curvature in that region via $2\gamma/\Delta P = R_m$.
- As the reservoir overpressure increases, the liquid metal layer that coats the pore assumes a static arrangement with a fixed contact point at the pore's edge.
- When the contact angle at the pore edge reaches a critical value predicted by the interaction potential between the liquid metal and substrate, a limit point arises and the solution family turns to lower overpressures. The coating assumes the

183

shape of a drop that has escaped the pore and coats the substrate with the above critical contact angle.

- Beyond the overpressure corresponding to the critical contact angle, depending on the strength of the interaction potential, a static arrangement does not exist and a transient analysis is necessary to describe the CPS response, possibly introducing the concept of dynamic contact angle.

7.2.3 Effect of external field forces
(a) Effect of electric field

Although the film generated is thin enough, it may be subject to instabilities and drop ejection in the presence of electromagnetic forces. As a first approach to capture the jxB effects on the static arrangement, an external electric field was applied. Using the static equilibrium obtained with the top of the porous matrix fully covered and gradually increasing the electric field intensity while keeping the mass of the liquid metal within the layer constant, a sequence of shapes was obtained. The main results related to this study are summarized as follows:

- The pole section of the layer is elongated in the field direction, as a result of the electric stresses while the contact angle at the equator decreases in order to maintain the same amount of liquid lithium.
- The liquid layer thickness increases away from the contact line and its curvature increases as well. Eventually, a conical angle tends to be formed at the pole and a solution could not be obtained for stronger electric fields. In this limit, gravity is balanced by electric stresses and this determines the size of the conical angle at the pole.
- It has been seen in the literature that jetting can be initiated at the pole region. This process is known to generate small droplets once the jet speed reaches a certain threshold. Thus, the present study may give a reasonable explanation for the experimentally observed drop ejection.

(b) Effect of Lorentz forces

In this consideration, the more relevant to fusion applications jxB effects are taking into account. The Lorentz forces are anticipated to generate an additional overpressure, depending on the magnitude and direction of the magnetic field and the electric current that enters the liquid metal layer. In this study, the externally applied magnetic field was considered to be in the azimuthal direction as a first attempt to find out under which circumstances drop ejection can be provoked. The effect of Lorentz forces is incorporated in the Maxwell stress that is decomposed in the magnetic pressure and the rotational part. The relative strength of Lorentz forces with respect to capillarity is determined by a magnetic Bond number, $Bond_m$, which acts as a dimensionless magnetic pressure:

$$Bond_m = \frac{B_0 J_r R_p^2}{\gamma} \tag{7.2}$$

As a first approximation, the micro-scale surface forces are not taken into account and as a result the precursor layer is neglected. The key results are highlighted as follows:

- For relatively small values of $Bond_m$ the rotational part of the stress is negligible and the effect of the magnetic pressure on the static arrangement is similar to the situation described above for the same overpressure.

- For small values of $Bond_m$ shapes with fixed contact point are obtained at the pore's edge with increasing contact angle and increasing protrusion into the plasma.

- Provided that the interaction potential with the substrate is known, in the presence of Lorentz forces, the critical contact angle is also known. Upon reaching this value for the contact angle at the pore's edge, the onset of shapes with fixed contact angle is anticipated for smaller values of $Bond_m$ as a result of a limit point in the parameter space that includes the interaction potential with the substrate.

- Static solutions with a fixed contact angle do not exist for larger magnetic pressures and a dynamic analysis is required in order to investigate the response at large electric currents or larger $Bond_m$.

- The above critical $Bond_m$ number is a first threshold for the establishment of a static arrangement. For fixed operating medium, e.g. liquid lithium, magnetic field intensity and strength of the interaction potential, the above critical value is achieved for larger electric current densities as the pore size decreases.

- Solutions can be obtained for larger values of $Bond_m$ but they require imposition of the fixed contact point condition. The stability of such solutions is questionable in the presence of transient effects.

- In order to investigate different dynamic patterns that occur at large $Bond_m$, the dynamic contact angle effects can be investigated during the spreading process of the liquid metal on the substrate.

- To this end, the proper interaction potential pertaining to the liquid metal and substrate has to be introduced.

7.3 Directions for future work

In this section, the future perspectives of the present research are presented. These perspectives are associated with the framework of the European fusion program [1] analyzed in subsection 1.1. In a nutshell, the possibility for a modified steady state to emerge in the pore level is intended to be investigated by Dr. Pelekasis and his colleagues. This steady state is going to take into account an external heat load, where a liquid metal flux out of the reservoir is established balancing evaporation at the interface with plasma. The effect of Lorentz forces will also be investigated via an extensive numerical study in the context of axisymmetry when the contact point between the liquid metal and the substrate is fixed at the pore mouth. Capturing the dynamic evolution of the interface, preliminary stability criteria for the loss of cohesion of the liquid metal protective coating and drop ejection will be obtained. Furthermore, the onset of a three dimensional swirling motion will be introduced, and its impact on the emerging steady state and heat transfer will be investigated, when an appreciable axial component of the magnetic field is present.

In order to assess the impact of adhesion in the dynamic response of a capillary porous system, the effect of intermolecular forces is going to be introduced in the above studies, in the context of axisymmetry. The onset of a dynamic contact angle will be examined and its impact on the nature of the final steady state or dynamic response will be captured. Pore replenishment will be examined on a more realistic basis and the range of validity of the stability threshold for the collapse of the interface and drop ejection, obtained assuming a fixed contact point, will be cross-checked and corrected.

More specifically, the proposed future work is focused mainly on three directions:

7.3.1 Axisymmetric analysis of flow and heat transfer in the pore level – Criteria for stability and drop ejection

As a continuation of the above studies, the assumption of isothermal conditions is intended to be relaxed. Instead, the introduction of an external heat load is intended to the static arrangement obtained thus far or the steady state that emerges in the presence of Lorentz and viscous forces, in the pore level. In this fashion, a modified steady state is anticipated to emerge in which evaporation is going to be balanced by the liquid metal being supplied from the reservoir. To this end, the assumption of fixed contact point and contact angle will be explored. The dynamic evolution towards the steady flow arrangement will also be investigated in order to assess criteria for destabilization and drop ejection, in the presence of intense jxB effects. The finite element methodology will be employed to this end with the spine method for mesh generation.

7.3.2 3-D analysis of flow and heat transfer in the pore level

The above steady flow arrangement and stability criteria will be obtained in the framework of axisymmetry assuming a planar magnetic field for the estimation of Lorentz forces. However, in the presence of an appreciable vertical magnetic field the onset of a strong swirling motion is anticipated as a result of an appreciable azimuthal force component that will consume a large portion of the kinetic energy of the liquid metal. There are indications for such flow effects in experiments with linear devices. Furthermore, assuming more realistic magnetic field arrangements will allow for a more accurate evaluation of the induced magnetic field and the resulting Maxwell stresses. Coupling, with heat transfer effects will assess the extent of temperature rise sustained by

the CPS in response to large external heat loads in the effect of evaporation and convection, at steady state conditions. This will require development of a three dimensional methodology that will couple the finite element method with the spectral method for capturing three dimensional variations of the unknown quantities. Parallelization strategies will also be employed in order to optimize CPU time and storing requirements.

7.3.3 Dynamic analysis of pore replenishment as a function of the overpressure and interaction potential with the substrate

In order to assess the validity of the fixed contact point or contact angle boundary condition and investigate the response pattern at large overpressures, dynamic simulations will be performed based on the static arrangement obtained in the absence of Lorentz forces or thermal loads. Introduction of the interaction potential will allow the study of dynamic evolution of the liquid metal coating over a large range of overpressures, and address the issue of different response patterns such as the stick-slip type of flow out of the pore, as well as the possibility for a finite time singularity to emerge that will destroy the coherence of the coating. In this context it is important to select an interaction potential that provides the good adhesion properties in terms of contact angle and allows for the formation coherent coatings. The finite element methodology will be employed in order to develop a solver for the Navier Stokes including the effects of intermolecular, viscous, capillary and pressure forces for axisymmetric geometry, coupled with elliptic mesh generation techniques in order to provide optimal domain decomposition pertaining to areas with varying intensity of the intermolecular forces. Such techniques were originally developed for coating problems and are appropriate for studying the dynamic evolution of the contact problem studied herein.

Finally, the schematics of the flow arrangements described above are illustrated in **Figs. 7.1-7.3**.
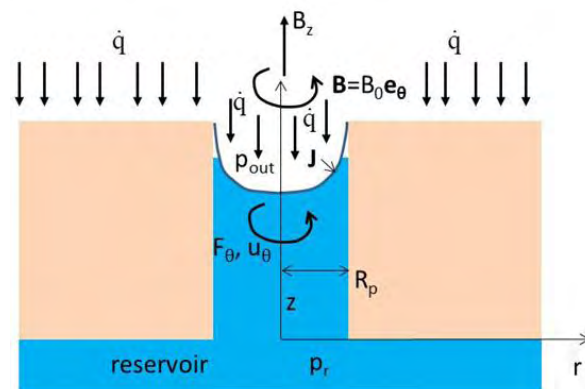

Fig. 7.1 Schematic of the flow arrangement in the pore level in the presence of heat and momentum transfer and Lorentz forces
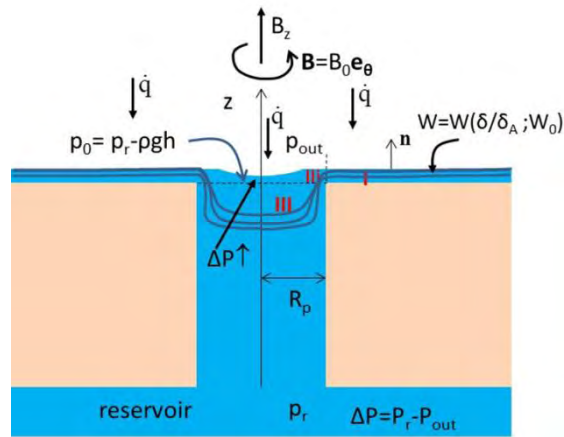
187

Fig. 7.2 Schematic of the onset of 3-D swirling motion for realistic magnetic fields
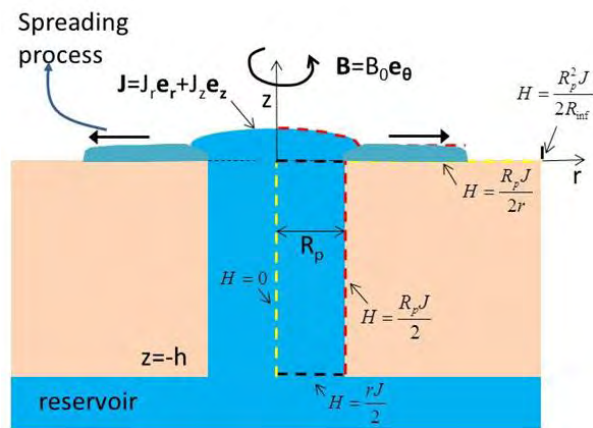

Fig. 7.3 Schematic of the spreading process in the pore level taking into account dynamic contact angle effects

188

References

[1]   EUROfusion: realising fusion electricity. Retrieved September 16, 2017, from https://www.euro-fusion.org/eurofusion/.

[2]   Generalfusion: Retrieved November 6, 2017, from generalfusion.com.

[3]   Helion Energy: Retrieved November 24, 2017, from helionenergy.com.

[4]   U. Shumlak, B.A. Nelson, E.L. Claveau, E.G. Forbes, R P. Golingo, M.C. Hughes et al., *Increasing plasma parameters using sheared flow stabilization of a Z-pinch*, Physics of Plasmas 24 (2017) 055702.

[5]   P.A. Bagryansky, A.G. Shalashov, E.D. Gospodchikov, A.A. Lizunov, V.V. Maximov, V.V. Prikhodko et al., *Threefold Increase of the Bulk Electron Temperature of Plasma Discharges in a Magnetic Mirror Device,* Physical Review Letters 114 (2015) 205001.

[6]   Y. Xu, *A general comparison between tokamak and stellarator plasmas*, Matter and Radiation at Extremes, Matter and Radiation at Extremes 1 (2016) 192-200.

[7]   M. Akiba and H. Madarame, Effects of plasma disruption on structural and plasma facing materials, Nuclear Materials 212-215 (1994) 90-96.

[8]   N.C. Christofilos, *Design for a high power-density Astron reactor*, Fusion Energy 8 (1989) 97.

[9]   F. L. Tabarés, *Present status of liquid metal research for a fusion reactor*, Plasma Physics Controlled Fusion 58 (2015) 014014 (8pp).

[10]   Y. Hirooka, G. Mazzitelli, S. Mirnov, M. Ono, M. Shimada and F. L. Tabarés, *A Review of the Present Status and Future Prospects of the Application of Liquid Metals for Plasma-Facing Components in Magnetic Fusion Devices*, Fusion Science and Technology 68 (2015) 477-483.

[11]   Y. Hirooka, G. Mazzitelli, S.V. Mirnov, M. Ono, M. Shimada and F.L. Tabarés, *Conference Report on the 1st International Workshop on Li-applications to Boundary Control in Fusion Devices*, Nuclear Fusion 50 (2010) No. 7.

[12]   M. Ono, M.G. Bell, Y. Hirooka, R. Kaita, H.W. Kugel, G. Mazzitelli et al. , *Conference Report on the 2nd International Symposium on Lithium Applications for Fusion Devices* , Nuclear Fusion 52 (2012) No. 3.

[13]   G. Mazzitelli, Y. Hirooka, J.S. Hu, S.V. Mirnov, R. Nygren, M. Shimada et al., *Conference Report on the 3rd International Symposium on Lithium Application for Fusion Devices*, Nuclear Fusion 55 (2015) No. 2.

[14]   F.L. Tabarés, Y. Hirooka, R. Maingi, G. Mazzitelli, V. Mirnov, R. Nygren et al., *Conference Report on the 4th International Symposium on Lithium Applications in Fusion*, Nuclear Fusion 56 (2016) No. 12.

[15]   M.A. Jaworski, T. Abrams, J.P. Allain, M.G. Bell, R.E. Bell, A. Diallo et al., *Liquid lithium divertor characteristics and plasma–material interactions in NSTX high-performance plasmas*, Nuclear Fusion 53 (2013) No. 8.

[16]   M.A. Jaworski, A. Brooks, R. Kaita, N. Lopes-Cardozo, J. Menard, M. Ono et al., *Upgrades toward high-heat flux, liquid lithium plasma-facing components in the NSTX-U*, Fusion Engineering and Design 112 (2016) 93-101.

[17]   R.E. Nygren and F.L. Tabarés, *Liquid surfaces for fusion plasma facing components-A critical review. Part I: Physics and PSI*, Nuclear Materials and Energy 9 (2016) 6–21.

[18]   I. Lyublinski, A. Vertkov, S. Mirnov and V. Lazarev, Protection of tokamak plasma facing components by a capillary porous system with lithium, Nuclear Materials 463 (2015) 1156–1159.

[19] J.W. Coenen, G. De Temmerman, G. Federici, V. Philipps, G. Sergienko, G. Strohmayer et al., *Liquid metals as alternative solution for the power exhaust of future fusion devices: status and perspective*, Physica Scripta (2014) No. T159 014037.

[20] M.A. Jaworski, N.B. Morley and D.N. Ruzic, *Thermocapillary and thermoelectric effects in liquid lithium plasma facing components*, Nuclear Materials 390–391 (2009) 1055-1058.

[21] J. C. Schmitt, R.E. Bell, D.P. Boyle, B. Esposti, R. Kaita, T. Kozub et al., *High performance discharges in the Lithium Tokamak experiment with liquid lithium walls*, Physics of Plasmas 22 (2015) 056112.

[22] Z. Chen, Y. Song, Q. Yang, J. Hu, G. Zuo, J. Ren et al., *Preliminary design and performance study of EAST liquid lithium limiter based on CPS*, Fusion Engineering and Design 89 (2014) 2685-2690.

[23] R. Kaita, H.W. Kugel, T. Abrams, J.P. Allain, M.G. Bell, R.E. Bell et al., *Characterization of fueling NSTX H-mode plasmas diverted to a liquid lithium divertor*, Nuclear Materials 438 (2013) S488-S492.

[24] R. Kaita, R. Majeski, T. Gray, H. Kugel, D. Mansfield, J. Spaleta et al., *Low recycling and high power density handling physics in the Current Drive Experiment-Upgrade with lithium plasma-facing components*, Physics of Plasmas 14 (2007) 05611.

[25] S. Mirnov, *Plasma-wall interactions and plasma behaviour in fusion devices with liquid lithium plasma facing components*, Nuclear Materials 390-391 (2009) 876-885.

[26] R.B. Gomes, R. Mateus, E. Alves, M.F. Montemor, C. Silva, H. Fernandes et al., *Saturation of hydrogen retention in gallium samples exposed to tokamak ISTTOK plasmas*, Nuclear Materials 438 (2013) S992-S995.

[27] V.A Evtikhin, I.E. Lyublinski, A.V. Vertkov, E.A. Azizov, S.V. Mirnov, V.B. Lazarev et al, *Main directions and recent test modeling results of lithium capillary-pore systems as plasma facing components*, Plasma Science and Technology 6 (2004) 2291-2295.

[28] M.L. Apicella, G. Mazzitelli, V. Pericoli Ridolfini, V. Lazarev, A. Alekseyev, A. Vertkov et al., *First experiments with lithium limiter on FTU*, Nuclear Materials 363-365 (2007) 1346-1351.

[29] J. Ren, J.S. Hu, G.Z. Zuo, Z. Sun, J.G. Li, D.N. Ruzic et al., *First results of flowing liquid lithium limiter in HT-7*, Physica Scripta (2014) No. T159 014033.

[30] F.L. Tabarés, E. Oyarzabal, D. Tafalla, A.B. Martin-Rojo, D. Alegre, A.de Castro et al., *First liquid lithium limiter biasing experiments in the TJ-II stellerator,* Nuclear Materials 463 (2015) 1142-1146.

[31] I.E. Lyublinski, A.V. Vertkov, M.Y. Zharkov, V.V. Semenov, S. V.Mirnov et al., *Status of design and experimental activity on module of lithium divertor for KTM tokamak*, Fusion Engineering and Design 88 (2013) 1862-1865.

[32] D.K. Mansfield, A.L. Roquemore, H. Schneider, J. Timberlake, H. Kugel, M.G .Bell et al*., A simple apparatus for the injection of lithium aerosol into the scrape-off layer of fusion research devices*, Fusion Engineering and Design 85 (2010) 890-895.

[33] G.Z. Zuo, J.S. Hu, S. Zhen, J.G. Li, D.K. Mansfield, B. Cao et al., *Comparison of various wall conditionings on the reduction of H content and particle recycling in EAST*, Plasma Physics and Controlled Fusion 54 (2012) No.1.

[34] E. Oyarzabal, A.B. Martin-Rojo, F.L.Tabarés, *Electron-induced secondary electron emission coefficient of lithium, tungsten and stainless steel surfaces exposed to low-*

pressure plasmas, Nuclear Materials 452 (2014) 37-40.

[35] M.Z. Kaudze and O.A. Lielausis, *Collision of a drop with the surface of a liquid metal in a magnetic field*, Magnetohydrodynamics New York 20, (1984) 30-35.

[36] B. Bazylev, I. Landman, A. Loarte, N.S. Klimov, V. L. Podkovyrov and V.M. Safronov, *Experiments and modeling of droplet emission from tungsten under transient heat loads*, Physica Scripta (2009) No. T138 014061.

[37] J.W. Coenen, V. Philipps, S. Brezinsek, B. Bazylev, A. Kreter, T. Hirai et al., *Analysis of tungsten melt-layer motion and splashing under tokamak conditions at TEXTOR*, Nuclear Fusion 51 (2011) 083008.

[38] R.B. Gomes, H. Fernandes, C.Silva, A. Sarakovskis, T. Pereira, J. Figueiredo et al., *Interaction of a liquid gallium jet with the tokamak ISTTOK edge plasma*, Fusion Engineering and Design 83 (2008) 102-111.

[39] R.B. Gomes, C. Silva, H. Fernandes, P. Duarte, I. Nedzelskiy, O. Lielausis et al., *ISTTOK tokamak plasmas influence on a liquid gallium jet dynamic behavior*, Nuclear Materials 415 (2011) S989-S992.

[40] L.G. Golubchikov, V.A. Evtikhin, I.E. Lyublinski, V.I. Pistunovich, I.N. Potapov and A.N. Chumanov, *Development of a liquid-metal fusion reactor divertor with a capillary-pore system*, Nuclear Materials 233-237 (1996) 667-672.

[41] S.V. Mirnov and V.B. Lazarev, *Li experiments at the tokamak T-11 M in field of steady state PFC investigations*, Nuclear Materials 415 (2011) S417-S420.

[42] V.A. Evtikhin, I.E. Lyublinski, A.V. Vertkov, S.V. Mirnov and V.B. Lazarev, *Technological aspects of lithium capillary-pore systems application in tokamak device*, Fusion Engineering and Design 56-57 (2001) 363-367.

[43] V.A. Evtikhin, I.E. Lyublinski, A.V. Vertkov, N.I. Yezhov, B.I. Khripunov, S.M. Sotnikov et al., *Energy removal and MHD performance of lithium capillary-pore systems for divertor target application*, Fusion Engineering and Design 49-50 (2000) 195-199.

[44] S.V. Mirnov, E.A. Azizov, V.A. Evtikhin, V.B. Lazarev, I.E. Lyublinski, A.V. Vertkov et al., *Experiments with lithium limiter on T-11M tokamak and applications of the lithium capillary-pore system in future fusion reactor devices*, Plasma Physics Controlled Fusion 48 (2006) 821.

[45] V.A. Evtikhin, I.E. Lyublinski, A.V. Vertkov, S.V. Mirnov, V.B. Lazarev et al., *Lithium divertor concept and results of supporting experiments*, Plasma Physics Controlled Fusion 44 (2002) 995.

[46] F.L. Tabarés, *Reactor plasma facing component designs based on liquid metal concepts supported in porous systems*, Nuclear Fusion 57 (2017) 016029.

[47] G. Mazzitelli, M.L. Apicella, A. Alexeyev and FTU Team, *Heat loads on FTU liquid lithium limiter*, Fusion Engineering and Design 86 (2011) 580-583.

[48] T.D. Rognlien and M.E. Rensink, *Interactions between liquid-wall vapor and edge plasmas*, Nuclear Materials 290-293 (2001) 312-316.

[49] D.I. Skovorodin, A.A. Pshenov, A.S. Arakcheev, E.A. Eksaeva, E.D. Marenkov and S.I. Krasheninnikov, *Vapor shielding models and the energy absorbed by divertor targets during transient events*, Physics of Plasmas 23 (2016) 022501.

[50] G. G. van Eden, T. W. Morgan, D. U. B. Aussems, M. A. van den Berg, K. Bystrov and M. C. M. van de Sanden, *Self-Regulated Plasma Heat Flux Mitigation Due to Liquid Sn Vapor Shielding,* Physical Review Letters 116 (2016) 135002.

[51] B.V. Deryaguin, N.V. Churaev and V.M. Muller (1987), *Surface Forces*, New York, NY: Plenum Press.

[52] S. Middleman (1995), *Modeling axisymmetric flows: dynamics of films, jets, and drops*, San Diego, California: CRC Press.

191

[53] V.M. Starov, M.G. Velarde and C.J. Radke (2007), *Wetting and spreading dynamics*, New York, NY: Academic Press.

[54] G.F. Teletzke, H.T. Davis ant L.E. Scriven, Wetting hydrodynamics, Review Physical Applied 23 (1988) No 6.

[55] X. Gan, W. Hu1, H. Deng, S. Xiao and F. Gao, *Comparison between the Fe(001) surface and the Fe(001)-Li solid-liquid interface under irradiation*, in 5th ISLA 2017: Moscow, Russia.

[56] M. W. Finnis and J. E. Sinclair, *A simple empirical N-body potential for transition metals*, Philosophical Magazine A, 50:1 (1984) 45-55.

[57] J.N. Israelachvili (2011), *Intermolecular and surface forces*, 3rd Edition, Amsterdam: Academic Press.

[58] M. Rauscher and S. Dietrich, *Nano-droplets on structured substrates*, Soft Matter 5 (2009) 2997–3001.

[59] I. Cantat, K. Kassner and C. Misbah, *Vesicles in haptotaxis with hydrodynamical dissipation*, The European Physical Journal E 10 (2003) 175–189.

[60] G. Karapetsas, N.T. Chamakos and A.G. Papathanasiou, *Efficient modelling of droplet dynamics on complex surfaces*, Journal of Physics: Condensed Matter 28 (2016) 16pp.

[61] M.J. Blount, M.J. Miksis and S.H. Davis, The equilibria of vesicles adhered to substrates by short-ranged potentials, Proceedings of the Royal Society A 469 (2013) 20120729

[62] N.T. Chamakos, M.E. Kavousanakis, A.G. Boudouvis and A.G. Papathanasiou, *Droplet spreading on rough surfaces: Tackling the contact line boundary condition*, Physics of Fluids 28 (2016) 022105.

[63] P. Filfis, W. Xu, D. Andruczyk, D. Curreli and D.N. Ruzic, *Wetting properties of liquid lithium on select fusion relevant surfaces*, Fusion Engineering and Design 89 (2014) 2827-2832.

[64] M.Z. Krause and O.A. Lielausys, Magnitnaya Gidrogynamika 1 (1984) 37; EFDA Report, 2012.

[65] S.V. Mirnov and V.A. Evtikhin, T*he tests of liquid metals (Ga, Li) as plasma facing components in T-3M and T-11M tokamaks*, Fusion Science and Technology 47 (2005) 698.

[66] H. Fernandes, C.A.F. Varandas, and J.A.C. Cabral, *Role of the Tokamak ISTTOK on the EURATOM Fusion Program*, Brazilian Journal of Physics 32 (2002) no. 1.

[67] Lord Rayleigh Sec. R.S. XVI, *On the instability of a cylinder of viscous liquid under capillary force*, Philosophical Magazine, 34:207 (1892) 145-154

[68] Lord Rayleigh Sec. R.S. XIX, *On the instability of cylindrical fluid surfaces, Philosophical Magazine*, 34:207 (1892) 177-180.

[69] K. Weber, Z. Angew, Applied Mathematics and Mechanics 11 (1931) 136.

[70] R.P. Grant and S. Middleman, *Newtonian jet stability*, A.I.Ch.E. Journal 12 (4) (1966) 669-678.

[71] I. M. Wallwork, S. P. Decent, A. C. King and R. M. S. M. Schulkes, *The trajectory and stability of a spiralling liquid jet. Part 1. Inviscid theory*, Fluid Mechanics 459 (2002) 43-65.

[72] J. D. Jackson (1962), *Classical Electrodynamics*, New York, NY: John Wiley and Sons Inc.

[73] E. Harper, G. Grube and I. Chang, *On the break-up of the accelerating liquid drops*, Journal of Fluid Mechanics 52 (1972) 565-591.

[74] Z. C. Feng and L. G. Leal, Translational instability of a bubble undergoing shape oscillations, Physics of Fluids 7 (1995) 1325.

[75] R. Natarajan and R. Brown, *The Role of Three-Dimensional Shapes in the Break-Up of Charged Drops*, Proceedings of the Royal Society A410 (1987) 209-227.

[76] S.V. Mirnov, E.A. Azizov, A.G. Alekseev, V.B. Lazarev, R.R. Khayrutdinov, I.E. Lyublinski et al., *Li experiments on T-11M and T-10 in support of a steady-state tokamak concept with Li closed loop circulation*, Nuclear Fusion 51 (2011) No. 7.

[77] M.L. Apicella, V. Lazarev, I. Lyublinski, G. Mazzitelli, S. Mirnov, A. Vertkov, *Lithium capillary porous system behavior as PFM in FTU tokamak experiments*, Nuclear Materials 386-388 (2009) 821-823.

[78] H.W. Kugel, J.P. Allain, M.G. Bell, R.E. Bell, A. Diallo, R. Ellis et al., *NSTX plasma operation with a Liquid Lithium Divertor*, Fusion Engineering and Design 87 (2012) 1724-1731.

[79] V.A. Evtikhin, L.G. Golubchikov, *Divertor of fusion reactor,* RF patent (1995) No. 2051430.

[80] V.A. Evtikhin, A.V. Vertkov, I.E. Lyublinski, B.I. Khripunov, V.B. Petrov and S.V. Mirnov, Research of lithium capillary-pore systems for fusion reactor plasma facing components, Nuclear Materials 307–311 (2002) 1664–1669.

[81] G. Mazitelli, M.L. Apicella, M. Marinucci, C. Mazzotta, V. Pericoli, O. Tudisco, et al., 21st IAEA Fusion Energy conference 2006: Chengdu, China.

[82] Management of Large Experiment Facilities (FTU). Retrieved October 10, 2017, from https://www.euro-fusion.org/eurofusion/.

[83] P. Rindt, *Conceptual design of pre-loaded liquid lithium divertor targets for NSTX-U,* (Master Thesis) University of Eindhoven, Netherlands, 2015.

[84] P. Rindt, N.J. Lopes Cardozo, J.A.W. van Dommelen, R. Kaita, M.A.Jaworski, *Conceptual design of a pre-loaded liquid lithium divertor target for NSTX-U*, Fusion Engineering and Design 112 (2016) 204-212.

[85] G.I. Taylor, *The force exerted by an electric field on a long cylindrical conductor*. Proceedings of the Royal Society A 291 (1966) 145–158.

[86] V. Philipps, Comments on the assessment of liquid metal solutions for DEMO (WPDTT1 Meeting LM-2), Frascati November 2015.

[87] E.W. Washburn, *The dynamics of capillary flow*, Physical Review Letters 17, (1921) 273.

[88] G.L. Batten, *Liquid imbibition in capillaries and packed beds*, Colloid and Interface Science 102 (1984) 513.

[89] R.J. Good and N.J. Lin, *Rate of penetration of a fluid into a porous body*, Colloid and Interface Science 54 (1976) 52.

[90] P. Joos, P. van Remoortere, and M. Bracke, *The kinetics of wetting in a capillary,* Colloid and Interface Science 136 (1990) 189.

[91] V.M. Starov, S.R. Kosvintsev, V.D. Sobolev, M.G. Velarde and S.A. Zhdanov, Spreading of Liquid Drops over Saturated Porous Layers, Colloid and Interface Science246 (2002) 372-379.

[92] S. N. Reznik, A. L. Yarin, A. Theron and E. Zussman, *Transient and steady shapes of droplets attached to a surface in a strong electric field*, Fluid Mechanics 516 (2004) 349–377.

[93] M. J. Miksis, *Shape of a drop in an electric field*, Physics of Fluids 24 (11) (1981) 1967-1972.

[94] N. Dubash, A.J. Mestel, *Behaviour of a conducting drop in a highly viscous fluid subject to an electric field*, Fluid Mechanics 581 (2007) 469–493.

[95] M.A. Jaworski, S.P. Gerhardt, N.B. Morley, T. Abrams, R. Kaita, J. Kallman et al., *Macroscopic motion of liquid metal plasma facing components in a diverted plasma*, Nuclear Materials 415 (2011) S985–S988.

[96] D. Gao and N.B. Morley, *Equilibrium and initial linear stability analysis of liquid metal falling film flows in a varying spanwise magnetic field*, Magnetohydrodynamics 38 (4) (2002) 359-375.

[97] N.B. Morley, S. Smolentsev and D. Gao, *Modeling infinite/axisymmetric liquid metal magnetohydrodynamic free surface flows*, Fusion Engineering and Design 63-64 (2002) 343-351.

[98] P.A Davidson (2001), *An Introduction to Magnetohydrodynamic*, New York, NY: Cambridge University Press.

[99] J.N. Reddy (1993), *An Introduction to the Finite Element Method*, 2nd Edition, New York, NY: Cambridge University Press. McGraw-Hill, Inc.

[100] N.A. Pelekasis, J.A. Tsamopoulos, and G.D. Manolis, *Equilibrium shapes and stability of charged and conducting drops,* Physics of Fluids A: Fluid Dynamics 2 (1990) 1328-1340.

[101] C. de Boor (1978), *A Practical Guide to Splines*, New York, NY: Springer.

[102] S. F. Kistler and L. E. Scriven, *Coating flow theory by finite element and asymptotic analysis of the Navier-Stokes system*, International Journal for Numerical Methods in Fluids 4 (1984) 207-229.

[103] E. Widjaja, Nai-Chi Liu, M. Li, R. T. Collins, O. A. Basaran and M. T. Harris, *Dynamics of sessile droplet evaporation: A comparison of the spine and the elliptic mesh generation methods*, Computers and Chemical Engineering 31 (2007) 219–232.

[104] D.P O' Leary, G.W. Stewart, *Computing the eigenvalues and eigenvectors of symmetric arrowhead matrices*, Computational Physics 90 (1990) 497-505.

[105] H. Binous, A.A. Shaikh, *Introduction of the arc-length continuation technique in the chemical engineering graduate program at KFUPM*, Computer Applications in Engineering Education 23 (2015) 344–351.

[106] N. Pelekasis, *A study on drop and bubble dynamics via a hybrid boundary – element finite element methodology,* (PhD Thesis) State University of New York at Buffalo, USA, 1991.

[107] A. Lytra, *Numerical & theoretical study of the static response of coated microbubbles subject to uniform and distributed load application on the estimation of the shell elastic properties*, (PhD Thesis) University of Thessaly, Greece, 2017.

[108] N. Pelekasis and L. Benos, *Static Arrangement of a Capillary Porous System (CPS): Modelling*, Fusion Engineering and Design 117 (2017) 180-187.

[109] S.J. Zinkle, *Summary of Physical Properties for Lithium, Pb-17Li, and (LiF)nBeF2 Coolants*, Technical report (1998) APEX study meeting, Sandia National Lab.

[110] E. Rillaerts and P. Joos., *The dynamic contact angle*, Chemical Engineering Science 35 (1980) 883.

[111] T.W. Morgan, D.C.M. van den Bekerom, G. De Temmerman, *Interaction of a tin-based capillary porous structure with ITER/DEMO relevant plasma conditions*, Nuclear Materials 463 (2015) 1256-1259.

[112] Starov and Velarde, *Surface forces and wetting phenomena*, Journal of Physics: Condensed Matter 21 (2009) 464121.

[113] Starov, *Surface forces action in vicinity of three phase contact line and other current problems in kinetics of wetting and spreading*, Advances in Colloid and Interface Science 161 (2010) 139-152.

[114] Orfanidis, *Numerical and theoretical analysis of a drop that adheres on a solid substrate via capillary and intermolecular forces*, (Diploma Thesis) University of Thessaly, Greece, 2017.

[115] N. Pelekasis, **L. Benos**, R. Gomez, *Deflection of a liquid metal jet/drop in a*

194

tokamak environment, Fusion Engineering and Design 89 (2014) 2930–2936.

Appendices

Appendix A: A dielectric sphere in a uniform electric field

A dielectric sphere of radius a and dielectric constant $\in$ is placed in an initially uniform electric field which at large distances from the sphere is directed along the z axis and has magnitude E_0 as illustrated in Fig. A.1:
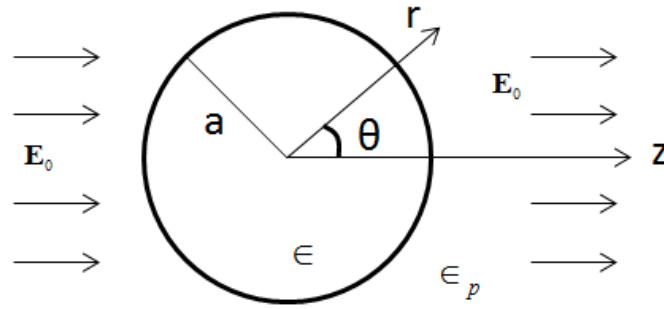
Fig. A.1 Schematic of a dielectric sphere placed in an initially uniform electric field

We take the solution to be of the form:

$$\varphi_{in} = \sum_{n=1}^{\infty} A_n r^n P_n \left(\cos \theta \right)$$ (A.1)

$$\varphi_{out} = \sum_{n=0}^{\infty} \left(B_n r^n + C_n r^{-(n+1)} \right) P_n \left(\cos \theta \right)$$ (A.2)

At infinity:

$$\varphi = -E_0 z$$ (A.3)

Due to the boundary condition described via Eq. A3, the only non-vanishing B_n is:

$$B_1 = -E_0$$ (A.4)

For n=1 Eqs A.1, A.2 result in:

$$\varphi_{in} = \sum_{n=1}^{\infty} A_1 r \cos \theta$$ (A.5)

$$\varphi_{out} = \left(-E_0 r + \frac{C_1}{r^2} \right) \cos \theta$$ (A.6)

The other coefficients are determined via the boundary conditions at r = a:

197

Tangential: $\left(E_{in}\right)_t = \left(E_{out}\right)_t$

$$-\frac{1}{a}\frac{\partial\varphi_{in}}{\partial\theta}\bigg|_{r=a} = -\frac{1}{a}\frac{\partial\varphi_{out}}{\partial\theta}\bigg|_{r=a}$$

(A.7)

Normal: $\left(D_{in}\right)_n = \left(D_{out}\right)_n$

(A.8)

$$-\frac{\in}{\in_p}\frac{\partial\varphi_{in}}{\partial r}\bigg|_{r=a} = -\frac{\partial\varphi_{out}}{\partial r}\bigg|_{r=a}$$

Substituting Eqs. (A.5, A.6) to Eqs. (A.7, A.8) the following equations are derived:

$$A_1 = -E_0 + \frac{C_1}{a^3}$$

(A.7)

$$C_1 = \frac{\dfrac{\in}{\in_p}-1}{\dfrac{\in}{\in_p}+2}E_0 a^3$$

(A.8)

Thus,

$$A_1 = -\frac{3}{\dfrac{\in}{\in_p}+2}E_0$$

(A.9)

As a consequence Eqs. A.5 and A.6 describing the electric potentials inside and outside the sphere result in:

$$\varphi_{in} = -\frac{3}{\in/\in_p+2}E_0 r\cos\theta$$

(A.10)

$$\varphi_{out} = -E_0 r\cos\theta + \frac{\in/\in_p-1}{\in/\in_p+2}\frac{E_0 a^3}{r^2}\cos\theta$$

(A.11)

The potential inside the sphere describes a constant electric field parallel to the applied one with magnitude:

$$E_{in} = \frac{3}{\in/\in_p+2}E_0$$

(A12)

Outside the sphere the potential is equivalent to the applied field plus the field of an electric dipole at the origin with dipole moment:

$$p = \frac{\in/\in_p-1}{\in/\in_p+2}E_0$$

(A.13)

198

oriented in the direction of the applied field. The dipole moment can be interpreted as the volume integral of the polarization **P**:

$$\mathbf{P} = \frac{\in / \in_p - 1}{4\pi} \mathbf{E} = \frac{3}{4\pi} \frac{\in / \in_p - 1}{\in / \in_p + 2} \mathbf{E_0} \qquad \text{(A.14)}$$

According to Jackson [72] an internal electric field is produced that is directed oppositely to the applied field as can be depicted in Fig. A.2.
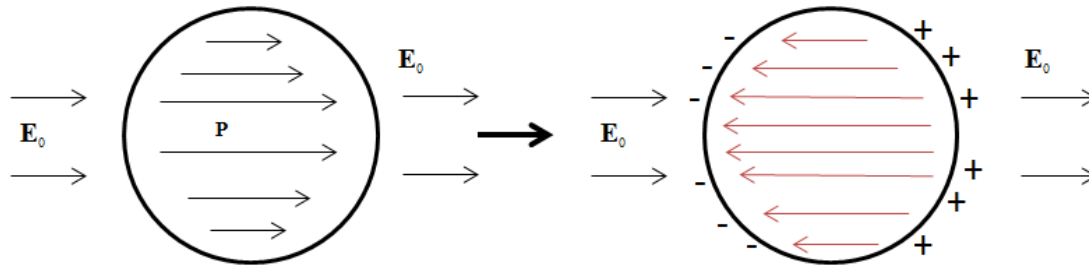

Fig. A.2 Dielectric sphere in a uniform electric field E_0, showing the polarization on the left and the polarization charge with its associated, opposing, electric field on the right

199

Appendix B: Cylindrical coordinates: Derivation of unit vectors and curvatures
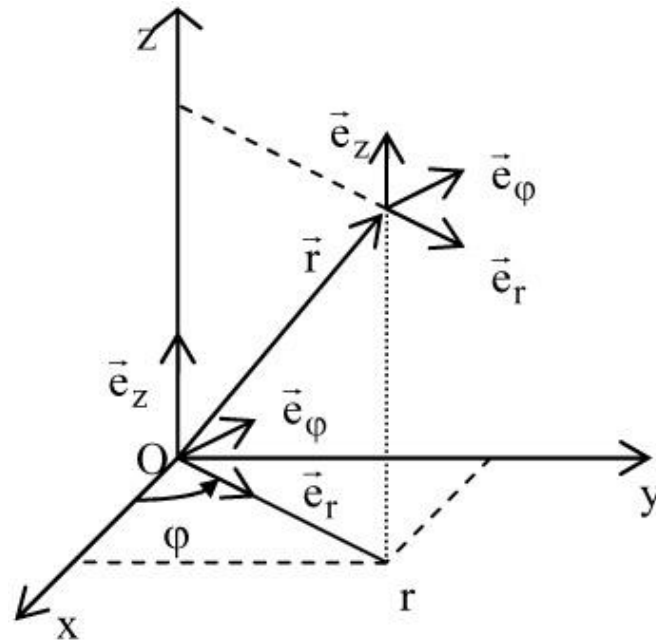

Fig. B.1 Cylindrical coordinate system

A cylindrical coordinate system is a three-dimensional coordinate system that specifies point positions by the distance from a chosen reference axis, the direction from the axis relative to a chosen reference direction, and the distance from a chosen reference plane perpendicular to the axis. The origin of the system is the point where all three coordinates can be given as zero. This is the intersection between the reference plane and the axis. The distance from the axis is called radial distance or radius, while the angular coordinate is sometimes referred to as the angular position or as the azimuth. The radius and the azimuth are together called the polar coordinates, as they correspond to a two-dimensional polar coordinate system in the plane through the point, parallel to the reference plane. The third coordinate may be called the height axial position.

Relationship between Cylindrical and Cartesian coordinates

For the conversion between cylindrical and Cartesian coordinates, it is convenient to assume that the reference plane of the former is the Cartesian xy-plane (with equation z = 0), and the cylindrical axis is the Cartesian z-axis. Then the z-coordinate is the same in both systems, and the correspondence between cylindrical (r, φ) and Cartesian (x, y) are the same as for polar coordinates, namely:

$$x = r\cos\varphi \tag{B.1}$$
$$y = r\sin\varphi \tag{B.2}$$

The line element is:

$$\mathbf{dr} = dr\mathbf{e_r} + rd\theta\mathbf{e_\varphi} + dz\mathbf{e_z} \tag{B.3}$$

where:

200

$$\mathbf{e_r} = \cos\varphi\,\mathbf{e_x} + \sin\varphi\,\mathbf{e_y} \tag{B.4}$$

$$\mathbf{e_\varphi} = -\sin\varphi\,\mathbf{e_x} + \cos\varphi\,\mathbf{e_y} \tag{B.5}$$

$$\mathbf{e_z} = \mathbf{e_z} \tag{B.6}$$

The surface element in a surface of constant radius is:

$$dA_r = r\,d\varphi\,dz \tag{B.7}$$

The surface element in a surface of constant azimuth φ is:

$$dA_\varphi = dr\,dz \tag{B.8}$$

Finally, the surface element in a surface of constant height z is:

$$dA_z = r\,dr\,d\varphi \tag{B.9}$$

Moreover, the volume element is:

$$dV = r\,dr\,d\varphi\,dz \tag{B.10}$$

Furthermore, the del operator in the cylindrical coordinate system leads to the following expression for the gradient:

$$\nabla f = \frac{\partial f}{\partial r}\mathbf{e_r} + \frac{1}{r}\frac{\partial f}{\partial \varphi}\mathbf{e_\varphi} + \frac{\partial f}{\partial z}\mathbf{e_z} \tag{B.11}$$

Derivation of unit vectors and curvatures (Eulerian specification)

The covariant tangent vectors along r and φ directions are defined as:

$$\mathbf{a_r} = \frac{\partial \mathbf{R}}{\partial r} = \frac{\partial\left(r\mathbf{e_r} + z(r)\mathbf{e_z}\right)}{\partial r} = \mathbf{e_r} + z_r\mathbf{e_z} \tag{B.12}$$

$$\mathbf{a_\varphi} = \frac{\partial \mathbf{R}}{\partial \varphi} = \frac{\partial\left(r\mathbf{e_r} + z(r)\mathbf{e_z}\right)}{\partial \varphi} = r\frac{\partial \mathbf{e_r}}{\partial \varphi} = r\mathbf{e_\varphi} \tag{B.13}$$

The normal unit vector is:

$$\mathbf{n} = \frac{\mathbf{a_r} \times \mathbf{a_\varphi}}{\left|\mathbf{a_r} \times \mathbf{a_\varphi}\right|} = \frac{-z_r\mathbf{e_r} + \mathbf{e_z}}{\sqrt{1 + z_r^2}} \tag{B.14}$$

The tangent unit vector is:

$$\mathbf{t} = \frac{\mathbf{e_r} + z_r\mathbf{e_z}}{\sqrt{1 + z_r^2}} \tag{B.15}$$

201

In addition, the contravariant vectors along r and φ directions are defined as:

$$\mathbf{a^r} = \frac{\mathbf{a_\varphi} \times \mathbf{n}}{\mathbf{a_r} \cdot \left(\mathbf{a_\varphi} \times \mathbf{n} \right)} = \frac{\mathbf{e_r} + z_r \mathbf{e_z}}{1 + z_r^2} \tag{B.16}$$

$$\mathbf{a^\varphi} = \frac{\mathbf{n} \times \mathbf{a_r}}{\mathbf{a_r} \cdot \left(\mathbf{a_\varphi} \times \mathbf{n} \right)} = \frac{1}{r} \mathbf{e_\varphi} \tag{B.17}$$

Thus, the surface gradient operator is:

$$\nabla_s = \mathbf{a^r} \cdot \frac{\partial}{\partial r} + \mathbf{a^\varphi} \cdot \frac{\partial}{\partial \varphi} \tag{B.18}$$

As a consequence:

$$\nabla_s \cdot \mathbf{n} = -\frac{z_{rr}}{\left(1 + z_r^2 \right)^{3/2}} - \frac{z_r}{r \sqrt{1 + z_r^2}} \tag{B.19}$$

The mean curvature (H_c) of a surface is an extrinsic measure of curvature that comes from differential geometry and that locally describes the curvature of an embedded surface in some ambient space such as Euclidean space.

For a surface defined in 3D space, the total curvature is related to a unit normal of the surface:

$$2H_c = \kappa_1 + \kappa_2 = \frac{1}{R_1} + \frac{1}{R_2} = -\nabla_s \cdot \mathbf{n} \tag{B.20}$$

The maximal curvature κ_1 and minimal curvature κ_2 are known as the principal curvatures of the surface. Moreover, R_1 and R_2 are the principal radii of curvature.

Therefore,

$$\frac{1}{R_1} = \kappa_1 = \frac{z_{rr}}{\left(1 + z_r^2 \right)^{3/2}} \tag{B.21}$$

$$\frac{1}{R_2} = \kappa_2 = \frac{z_r}{r \sqrt{1 + z_r^2}} \tag{B.22}$$

202

Lagrangian specification

Using Lagrangian representation for the interface:

$$r = r(\xi),\ z = z(\xi)\,, \tag{B.23}$$

As a consequence:

$$dr = r_\xi d\xi \tag{B.24}$$

$$z_r = \frac{\partial z}{\partial \xi}\frac{\partial \xi}{\partial r} = \frac{z_\xi}{r_\xi} \tag{B.25}$$

The normal unit vector becomes:

$$\mathbf{n} = \frac{-z_r\mathbf{e_r} + \mathbf{e_z}}{\sqrt{1+z_r^2}} = \frac{-\dfrac{z_\xi}{r_\xi}\mathbf{e_r} + \mathbf{e_z}}{\sqrt{1+\left(\dfrac{z_\xi}{r_\xi}\right)^2}} = \frac{-z_\xi\mathbf{e_r} + r_\xi\mathbf{e_z}}{\sqrt{r_\xi^2 + z_\xi^2}} \tag{B.26}$$

The tangent unit vector is:

$$\mathbf{t} = \frac{\mathbf{e_r} + \dfrac{z_\xi}{r_\xi}\mathbf{e_z}}{\sqrt{1+\left(\dfrac{z_\xi}{r_\xi}\right)^2}} = \frac{r_\xi\mathbf{e_r} + z_\xi\mathbf{e_z}}{\sqrt{r_\xi^2 + z_\xi^2}} \tag{B.27}$$

The total curvature using the Lagrangian representation is:

$$2H_c = -\nabla_s \cdot \mathbf{n} = \frac{z_{\xi\xi}r_\xi - z_\xi r_{\xi\xi}}{r_\xi^3\left[1+\left(\dfrac{z_\xi}{r_\xi}\right)^2\right]^{3/2}} + \frac{z_\xi}{r_\xi r\sqrt{1+\left(\dfrac{z_\xi}{r_\xi}\right)^2}} \Rightarrow$$

$$\Rightarrow 2H_c = \frac{r_\xi z_{\xi,\xi} - r_{\xi,\xi} z_\xi}{S_\xi^3} + \frac{z_\xi}{r S_\xi}\,,\ S_\xi = \sqrt{r_\xi^2 + z_\xi^2} \tag{B.28}$$

203

Appendix C: Spherical coordinates: Derivation of unit vectors and curvatures
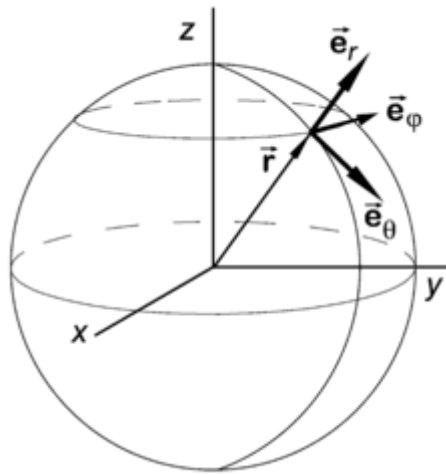

Fig. C.1 Spherical coordinate system

In mathematics, a spherical coordinate system is a coordinate system for three-dimensional space where the position of a point is specified by three numbers: the radial distance of that point from a fixed origin, its polar angle measured from a fixed zenith direction, and the azimuth angle of its orthogonal projection on a reference plane that passes through the origin and is orthogonal to the zenith, measured from a fixed reference direction on that plane. It can be seen as the three-dimensional version of the polar coordinate system. The radial distance is also called the radius or radial coordinate. The polar angle may be called colatitude, zenith angle, normal angle, or inclination angle. In the spherical coordinate system (r, θ, φ) gives the radial distance, polar angle, and azimuthal angle.

Relationship between Spherical and Cartesian coordinates

The spherical coordinates (r, θ, φ) of a point can be obtained from its Cartesian coordinates (x, y, z) by the formulae:

$$r = \sqrt{x^2 + y^2 + z^2} \tag{C.1}$$

$$\theta = \arccos\left(\frac{z}{\sqrt{x^2 + y^2 + z^2}}\right) \tag{C.2}$$

$$\varphi = \arctan\left(y/x\right) \tag{C.3}$$

Conversely, the Cartesian coordinates may be retrieved from the spherical coordinates:

$$x = r \sin\theta \cos\varphi \tag{C.4}$$
$$y = r \sin\theta \sin\varphi \tag{C.5}$$
$$z = r \cos\theta \tag{C.6}$$

204

These formulae assume that the two systems have the same origin and same reference plane, measure the azimuth angle φ in the same sense from the same axis, and that the spherical angle θ is inclination from the cylindrical z-axis.

The line element for an infinitesimal displacement from (r, θ, φ) to (r + dr, θ + dθ, φ + dφ) is:

$$\mathbf{dr} = dr\mathbf{e_r} + rd\theta\mathbf{e_\theta} + r\sin\varphi d\varphi\mathbf{e_\varphi} \tag{C.7}$$

where:
$$\mathbf{e_r} = \sin\theta\cos\varphi\mathbf{e_x} + \sin\theta\sin\varphi\mathbf{e_y} + \cos\theta\mathbf{e_z} \tag{C.8}$$
$$\mathbf{e_\theta} = \cos\theta\cos\varphi\mathbf{e_x} + \cos\theta\sin\varphi\mathbf{e_y} - \sin\theta\mathbf{e_z} \tag{C.9}$$
$$\mathbf{e_\varphi} = -\sin\varphi\mathbf{e_x} + \cos\varphi\mathbf{e_y} \tag{C.10}$$

are the local orthogonal unit vectors in the directions of increasing r, θ, and φ, respectively, and $\mathbf{e_x}$, $\mathbf{e_y}$, and $\mathbf{e_z}$ are the unit vectors in Cartesian coordinates.

The surface element spanning from θ to θ + dθ and φ to φ + dφ on a spherical surface at (constant) radius r is:

$$dA = r^2\sin\theta d\theta d\varphi \tag{C.11}$$

Moreover, the volume element spanning from r to r + dr, θ to θ + dθ, and φ to φ + dφ is:

$$dV = r^2\sin\theta dr d\theta d\varphi \tag{C.12}$$

Furthermore, the del operator in the spherical coordinate system leads to the following expressions for gradient, divergence and curl:

$$\nabla f = \frac{\partial f}{\partial r}\mathbf{e_r} + \frac{1}{r}\frac{\partial f}{\partial \theta}\mathbf{e_\theta} + \frac{1}{r\sin\theta}\frac{\partial f}{\partial \varphi}\mathbf{e_\varphi} \tag{C.13}$$

$$\nabla\cdot\mathbf{A} = \frac{1}{r^2}\frac{\partial\left(r^2 A_r\right)}{\partial r} + \frac{1}{r\sin\theta}\frac{\partial\left(\sin\theta A_\theta\right)}{\partial \theta} + \frac{1}{r\sin\theta}\frac{\partial A_\varphi}{\partial \varphi} \tag{C.14}$$

$$\nabla\times\mathbf{A} = \frac{1}{r\sin\theta}\left(\frac{\partial\left(A_\varphi\sin\theta\right)}{\partial \theta} - \frac{\partial A_\theta}{\partial \varphi}\right)\mathbf{e_r}$$

$$+\frac{1}{r}\left(\frac{1}{\sin\theta}\frac{\partial A_r}{\partial \varphi} - \frac{\partial\left(rA_\varphi\right)}{\partial r}\right)\mathbf{e_\theta}$$

$$+\frac{1}{r}\left(\frac{\partial\left(rA_\theta\right)}{\partial r} - \frac{\partial A_r}{\partial \theta}\right)\mathbf{e_\varphi} \tag{C.15}$$

205

Derivation of unit vectors and curvatures (Eulerian specification)

The covariant tangent vectors along θ and φ directions are defined as:

$$\mathbf{a_\theta} = \frac{\partial \mathbf{R}}{\partial \theta} = \frac{\partial \left(r(\theta) \mathbf{e_r} \right)}{\partial \theta} = r_\theta \mathbf{e_r} + r \mathbf{e_\theta} \tag{C.16}$$

$$\mathbf{a_\varphi} = \frac{\partial \mathbf{R}}{\partial \varphi} = \frac{\partial \left(r(\theta) \mathbf{e_r} \right)}{\partial \varphi} = r \frac{\partial \mathbf{e_r}}{\partial \varphi} = r \sin \theta \, \mathbf{e_\varphi} \tag{C.17}$$

The normal unit vector is:

$$\mathbf{n} = \frac{\mathbf{a_\theta} \times \mathbf{a_\varphi}}{\left| \mathbf{a_\theta} \times \mathbf{a_\varphi} \right|} = \frac{-r_\theta \mathbf{e_\theta} + r \mathbf{e_r}}{\sqrt{r_\theta^2 + r^2}} \tag{C.18}$$

The tangent unit vector is:

$$\mathbf{t} = \frac{r_\theta \mathbf{e_r} + r \mathbf{e_\theta}}{\sqrt{r_\theta^2 + r^2}} \tag{C.19}$$

In addition, the contravariant vectors along θ and φ directions are defined as:

$$\mathbf{a^\theta} = \frac{\mathbf{a_\varphi} \times \mathbf{n}}{\mathbf{a_\theta} \cdot \left(\mathbf{a_\varphi} \times \mathbf{n} \right)} \tag{C.20}$$

$$\mathbf{a^\varphi} = \frac{\mathbf{n} \times \mathbf{a_\theta}}{\mathbf{a_\theta} \cdot \left(\mathbf{a_\varphi} \times \mathbf{n} \right)} \tag{C.21}$$

Thus, the surface gradient operator is:

$$\nabla_s = \mathbf{a^\theta} \cdot \frac{\partial}{\partial \theta} + \mathbf{a^\varphi} \cdot \frac{\partial}{\partial \varphi} \tag{C.22}$$

The mean curvature (H_c) of a surface is an extrinsic measure of curvature that comes from differential geometry and that locally describes the curvature of an embedded surface in some ambient space such as Euclidean space.

For a surface defined in 3D space, the mean curvature is related to a unit normal of the surface:

$$2H_c = \kappa_1 + \kappa_2 = \frac{1}{R_1} + \frac{1}{R_2} = -\nabla_s \cdot \mathbf{n} \tag{C.23}$$

The maximal curvature κ_1 and minimal curvature κ_2 are known as the principal curvatures of the surface. Moreover, R_1 and R_2 are the principal radii of curvature.

Therefore,

206

$$\frac{1}{R_1} = \kappa_1 = \frac{1}{\sqrt{r_\theta^2 + r^2}} - \frac{r_\theta \cot\theta}{r\sqrt{r_\theta^2 + r^2}} \qquad\qquad (C.24)$$

$$\frac{1}{R_2} = \kappa_2 = \frac{r_\theta^2}{\left(r_\theta^2 + r^2\right)^{3/2}} - \frac{r r_{\theta\theta}}{\left(r_\theta^2 + r^2\right)^{3/2}} + \frac{1}{\sqrt{r_\theta^2 + r^2}} \qquad\qquad (C.25)$$

Appendix D: Derivation of $\nabla(B_i \cdot e_k)$ and $\tau_{\underline{v}}: \nabla(B_i \cdot e_k)$

D.1 Derivation of $\nabla(B_i \cdot e_k)$
z component:

$$\nabla\left(B_i \cdot \mathbf{e_z}\right) = \mathbf{e_r}\frac{\partial B_i}{\partial r}\mathbf{e_z} + \mathbf{e_r}\frac{\partial \mathbf{e_z}}{\partial r}\overset{0}{B_i} + \frac{\mathbf{e_\theta}}{r}\frac{\partial B_i}{\partial \theta}\overset{0}{\mathbf{e_z}} + \frac{\mathbf{e_\theta}}{r}\frac{\partial \mathbf{e_z}}{\partial \theta}\overset{0}{B_i} + \mathbf{e_z}\frac{\partial B_i}{\partial z}\mathbf{e_z} + \mathbf{e_z}\frac{\partial \mathbf{e_z}}{\partial z}\overset{0}{B_i}$$

$$\nabla\left(B_i \cdot \mathbf{e_z}\right) = \begin{bmatrix} 0 & 0 & \dfrac{\partial B_i}{\partial r} \\ 0 & 0 & 0 \\ 0 & 0 & \dfrac{\partial B_i}{\partial z} \end{bmatrix} \tag{D.1}$$

r component:

$$\nabla\left(B_i \cdot \mathbf{e_r}\right) = \mathbf{e_r}\frac{\partial B_i}{\partial r}\mathbf{e_r} + \mathbf{e_r}\frac{\partial \mathbf{e_r}}{\partial r}\overset{0}{B_i} + \frac{\mathbf{e_\theta}}{r}\frac{\partial B_i}{\partial \theta}\overset{0}{\mathbf{e_r}} + \frac{\mathbf{e_\theta}}{r}\frac{\partial \mathbf{e_r}}{\partial \theta}\overset{\mathbf{e_\theta}}{B_i} + \mathbf{e_z}\frac{\partial \mathbf{e_r}}{\partial z}\overset{0}{B_i} + \mathbf{e_z}\frac{\partial B_i}{\partial z}\mathbf{e_r}$$

$$\nabla\left(B_i \cdot \mathbf{e_r}\right) = \begin{bmatrix} \dfrac{\partial B_i}{\partial r} & 0 & 0 \\ 0 & \dfrac{B_i}{r} & 0 \\ \dfrac{\partial B_i}{\partial z} & 0 & 0 \end{bmatrix} \tag{D.2}$$

D.2 Derivation of $\underset{=}{\tau_v}: \nabla(B_i \cdot e_k)$

z component:

$$\underset{=}{\tau_v}: \nabla\left(B_i \cdot \mathbf{e_z}\right) = \begin{bmatrix} 2\dfrac{\partial u_r}{\partial r} & 0 & \dfrac{\partial u_z}{\partial r} + \dfrac{\partial u_r}{\partial z} \\ 0 & 2\dfrac{u_r}{r} & 0 \\ \dfrac{\partial u_z}{\partial r} + \dfrac{\partial u_r}{\partial z} & 0 & 2\dfrac{\partial u_z}{\partial z} \end{bmatrix} : \begin{bmatrix} 0 & 0 & \dfrac{\partial B_i}{\partial r} \\ 0 & 0 & 0 \\ 0 & 0 & \dfrac{\partial B_i}{\partial z} \end{bmatrix} =$$

$$= \frac{\partial B_i}{\partial r}\left(\frac{\partial u_z}{\partial r} + \frac{\partial u_r}{\partial z}\right) + 2\frac{\partial u_z}{\partial z}\frac{\partial B_i}{\partial z} \tag{D.3}$$

208

r component:

$$\underset{=}{\tau}_v : \nabla \left(B_i \cdot \mathbf{e_r} \right) = \begin{bmatrix} 2\dfrac{\partial u_r}{\partial r} & 0 & \dfrac{\partial u_z}{\partial r}+\dfrac{\partial u_r}{\partial z} \\[2ex] 0 & 2\dfrac{u_r}{r} & 0 \\[2ex] \dfrac{\partial u_z}{\partial r}+\dfrac{\partial u_r}{\partial z} & 0 & 2\dfrac{\partial u_z}{\partial z} \end{bmatrix} : \begin{bmatrix} \dfrac{\partial B_i}{\partial r} & 0 & 0 \\[2ex] 0 & \dfrac{B_i}{r} & 0 \\[2ex] \dfrac{\partial B_i}{\partial z} & 0 & 0 \end{bmatrix} =$$

$$= 2\frac{\partial u_r}{\partial r}\frac{\partial B_i}{\partial r} + \frac{\partial B_i}{\partial z}\left(\frac{\partial u_z}{\partial r}+\frac{\partial u_r}{\partial z} \right) + \frac{2u_r B_i}{r} \qquad\qquad\qquad\qquad\qquad\qquad (D.4)$$

209

Appendix E: Analytical solution within the pore assuming a rectangular geometry

In this subsection, a simplification is used for the pore problem described above and an analytical solution of $\nabla^2 H = \dfrac{H}{r^2} \Rightarrow \dfrac{\partial^2 H}{\partial r^2} + \dfrac{1}{r}\dfrac{\partial H}{\partial r} + \dfrac{\partial^2 H}{\partial z^2} = \dfrac{H}{r^2}$ is obtained. The simplified geometry is depicted in **Fig. E.1** along with the boundary conditions pertaining to H which were discussed in subsection 4.4.3.
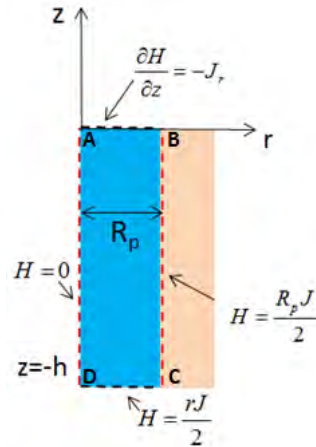

Fig. E.1 Schematic of the studied rectangular geometry and the boundary conditions pertaining to H

First of all, the following assumptions are made:

$$J_r, J_z = \text{constant} \tag{E.1}$$

$$\frac{\partial H}{\partial z} = -J_r, \quad J_z = \frac{1}{r}\frac{\partial(rH)}{\partial r} \tag{E.2}$$

$$z \to -\infty : H = \frac{rJ}{2}, \quad J = \frac{2\displaystyle\int_0^{R_p}\left(J_z - J_r z_r\right)r\,dr}{R_p^2}\Bigg|_{Int} \xrightarrow{z_r=0} J = J_z\big|_{Int}, \tag{E.3}$$

Thus,

$$z \to -\infty : \quad H = \frac{rJ}{2} + F(r,z) \tag{E.4}$$

with F(r,z) satisfying:

$$\frac{\partial^2 F}{\partial r^2} + \frac{1}{r}\frac{\partial F}{\partial r} + \frac{\partial^2 F}{\partial z^2} = \frac{F}{r^2} \Rightarrow$$

$$\Rightarrow \frac{\partial^2 F}{\partial r^2} + \frac{1}{r}\frac{\partial F}{\partial r} - \frac{F}{r^2} = -\frac{\partial^2 F}{\partial z^2} \tag{E.5}$$

$$z = 0 : \frac{\partial F}{\partial z} = -J_r, \quad z = -\infty : F = 0 \tag{E.6}$$

$$r = 0, \ r = R_p : F = 0 \tag{E.7}$$

210

F(r,z) can be expressed as:

$$F(r, z) = Z(z) \cdot R(r) \tag{E.8}$$

Hence,

$$\frac{R''}{R} + \frac{1}{r}\frac{R'}{R} - \frac{1}{r^2} = -\frac{\ddot{Z}}{Z} = -\lambda \tag{E.9}$$

$$\ddot{Z} - \lambda Z = 0 \tag{E.10}$$

$$r^2 R'' + rR' + \left(\lambda r^2 - 1\right)R = 0 \tag{E.11}$$

If $\lambda = k^2$, $\lambda \neq 0$:

$$r^2 R'' + rR' + \left[(kr)^2 - 1\right]R = 0, \ R(0) = R(R_p) = 0 \tag{E.12}$$

$$R_1(r) = AJ_1(kr) + BJ_1(kr) \tag{E.13}$$

$$R_1(r = 0) = 0 \Rightarrow B = 0 \Rightarrow R_1(r) = AJ_1(kr) \tag{E.14}$$

$$R_1(r = R_p) = 0 \Rightarrow J_1(kR_p) = 0 \Rightarrow kR_p = x_{1m} \Rightarrow$$

$$k_{1m} = \frac{x_{1m}}{R_p}, \ R_1(r) = AJ_1\left(x_{1m}\frac{r}{R_p}\right) \tag{E.15}$$

And

$$Z'' - k_{1m}{}^2 Z = 0 \Rightarrow$$
$$\Rightarrow Z = ce^{-k_{1m}z} + de^{k_{1m}z}, \ Z(z \to -\infty) = 0 \Rightarrow c = 0 \tag{E.16}$$
$$Z = de^{k_{1m}z}$$

Thus, substituting Eqs. E.15 and E.16 to Eq. E.8:

$$F(r, z) = \sum_{m=1}^{\infty} A' e^{\frac{x_{1m}}{R_p}z} J_1\left(x_{1m}\frac{r}{R_p}\right) \tag{E.17}$$

However,

211

$$\frac{\partial F}{\partial z}(r,\, z=0) = -J_r \Rightarrow -J_r = \sum_{m=1}^{\infty} A_m{}' \frac{x_{1m}}{R_p} J_1\left(x_{1m}\, \frac{r}{R_p}\right) \Rightarrow$$

$$\Rightarrow -\frac{J_r R_p}{x_{1m}} = \sum_{m=1}^{\infty} A_m{}' J_1\left(x_{1m}\, \frac{r}{R_p}\right) \Rightarrow \text{Orthogonality of Bessel Functions}$$

$$A_m{}' = \frac{\displaystyle\int_0^{R_p}\left(\frac{-J_r R_p}{x_{1m}}\right) J_1\left(\frac{x_{1m}r}{R_p}\right) r\,dr}{\displaystyle\int_0^{R_p} J_1^2\left(\frac{x_{1m}r}{R_p}\right) r\,dr} \Rightarrow A_m{}' = \left(\frac{-2J_r}{R_p x_{1m}}\right) \frac{\displaystyle\int_0^{R_p} J_1\left(\frac{x_{1m}r}{R_p}\right) r\,dr}{J_2^2\left(x_{1m}\right)}$$

(E.18)

Hence Eq. E.4 results in:

$$H(r,z) = -\frac{Jr}{2} - \sum_{m=1}^{\infty} \frac{2J_r \displaystyle\int_0^{R_p} J_1\left(\frac{x_{1m}r}{R_p}\right) r\,dr}{x_{1m}R_p J_2^2\left(x_{1m}\right)} e^{\frac{x_{1m}}{R_p}z} J_1\left(\frac{x_{1m}r}{R_p}\right) \Rightarrow$$

$$\begin{array}{l} \hat{r}=r/R_p \\ \hat{z}=z/R_p \\ \hat{H}=H/(J_r R_p) \end{array} \Rightarrow \quad \hat{H}(\hat{r},\hat{z}) = -\frac{J\hat{r}}{J_r 2} - \sum_{m=1}^{\infty} \frac{2}{x_{1m}} \frac{\displaystyle\int_0^1 J_1\left(x_{1m}\hat{r}\right) \hat{r}\,d\hat{r}}{J_2^2\left(x_{1m}\right)} e^{x_{1m}\hat{z}} J_1\left(x_{1m}\hat{r}\right)$$

(E.19)

Based on the above solution, when $J_z=J=0$ the magnetic pressure is:

$$P_m = B_0 \overset{=0}{\overbrace{\frac{rJ}{2}}} - B_0\, \mathrm{H}\big|_{Int} = 2B_0 J_r R_p \sum_{m=1}^{\infty} \frac{1}{x_{1m}} \frac{\displaystyle\int_0^1 J_1\left(x_{1m}\hat{r}\right) \hat{r}\,d\hat{r}}{J_2^2\left(x_{1m}\right)} J_1\left(x_{1m}\hat{r}\right) \xrightarrow{x_{1m}\hat{r}=s}$$

(E.20)

$$P_m = 2B_0 J_r R_p \sum_{m=1}^{\infty} \frac{1}{x_{1m}^3} \frac{\displaystyle\int_0^{x_{1m}} J_1\left(s\right) s\,ds}{J_2^2\left(x_{1m}\right)} J_1\left(x_{1m}\hat{r}\right)$$

Plots of dimensionless $\mathrm{H}\left(\hat{H} = \frac{H}{J_r R_p}\right)$ and magnetic pressure $\mathrm{P_m}\left(\hat{P}_m = \frac{P_m}{B_0 J_r R_p}\right)$ are provided in **Figs. E.2a,b**, respectively, when $J = 0$ for reference.

212
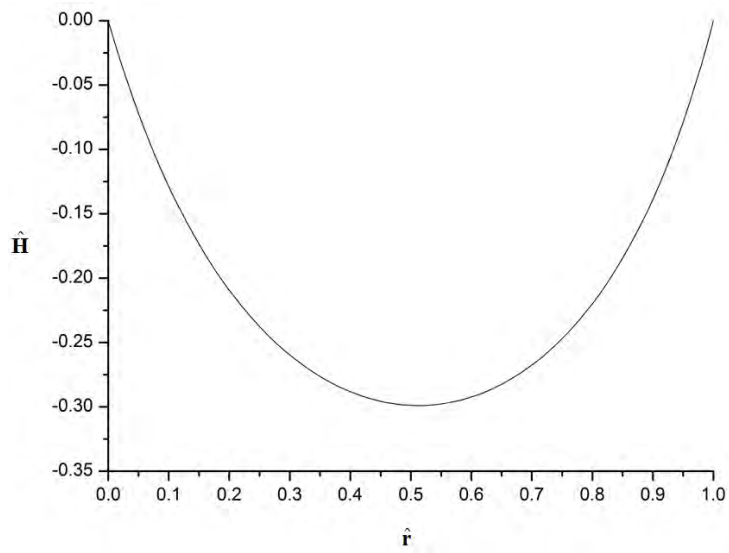
(a)
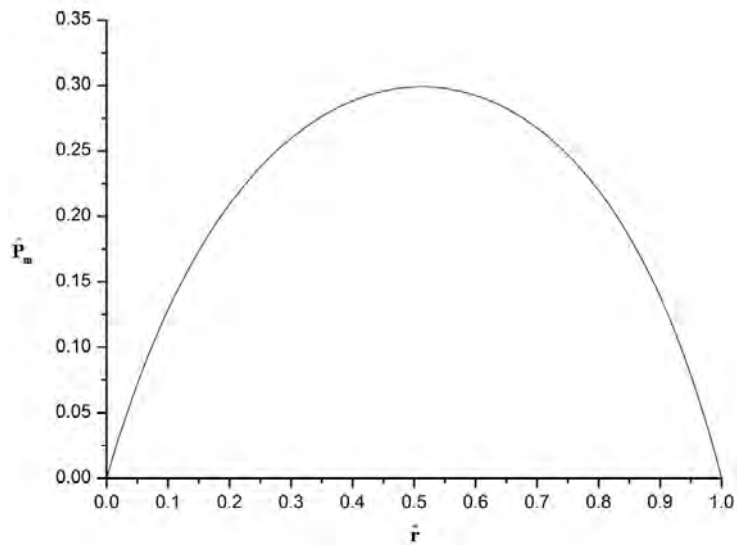
(b)

Fig. E.2 (a) Dimensionless H and (b) M11agnetic pressure for a rectangular domain when J_z=0

213